UNIVERSITY OF CRETE
SCHOOL OF SCIENCES AND ENGINEERING
MATERIALS SCIENCE AND TECHNOLOGY

Synthesis of Mesoporous Networks of Metal-Chalcogenide Nanocrystals for Photocatalytic Applications and Hydrogen Fuel Production

Ph.D. Thesis

IOANNIS VAMVASAKIS

Supervisor: **Gerasimos S. Armatas**

Heraklion 2020

ΠΑΝΕΠΙΣΤΗΜΙΟ ΚΡΗΤΗΣ
ΣΧΟΛΗ ΘΕΤΙΚΩΝ ΚΑΙ ΤΕΧΝΟΛΟΓΙΚΩΝ ΕΠΙΣΤΗΜΩΝ
ΤΜΗΜΑ ΕΠΙΣΤΗΜΗΣ ΚΑΙ ΤΕΧΝΟΛΟΓΙΑΣ ΥΛΙΚΩΝ

Σύνθεση Μεσοπορώδων Πλεγμάτων από Νανοκρυστάλλους Μετάλλου-Χαλκογονιδίου για Φωτοκαταλυτικές Εφαρμογές και Παραγωγή Καυσίμου Υδρογόνου

Διδακτορική Διατριβή

ΙΩΑΝΝΗΣ ΒΑΜΒΑΣΑΚΗΣ

Επιβλέπων καθηγητής: **Γεράσιμος Αρματάς**

Ηράκλειο 2020

Abstract

Synthesis of mesoporous (pore size from 2 to 50 nm) assembly architectures of well-defined inorganic nanocrystals (NCs) represents an important challenge in material science and chemical nanotechnology. Such self-assembled materials can incorporate complementary functionalities into the framework, such as nanoporosity and photocatalytic and quantum-confined electronic properties of individual NCs. These characteristics may endow them enhanced applications for photocatalysis, solar energy conversion, chemical sensing and size-selective adsorption and separation. Although great progress in the synthesis of nanoporous frameworks of metal and metal oxide nanoparticles with highly accessible pore surface and ordered mesoscale structure has been achieved, synthesis of assembled three-dimensional (3D) mesostructures of metal-chalcogenide NCs is still challenging.

In this dissertation, a new and cost-effective synthetic strategy for preparing mesoporous networks of interconnected metal-sulfide NCs has been successfully developed and demonstrated. By utilizing a simple polymer-templated oxidative polymerization process, the resulting self-assembled mesostructures comprise a unique combination of light-emitting metal-chalcogenide NCs and a 3D open-pore structure with large internal surface area and uniform mesopores. Through appropriate selection of the synthetic components, this assembly process provides the advantage of preparing mesoporous materials from metal chalcogenide NCs with various sizes and compositions, allowing the design and creation of tailored characteristics and desirable functionalities. Due to the large and accessible surface area and visible-light response, the present mesoporous NC-based assemblies (NCAs) were studied as potential catalysts, particularly in the challenging field of photocatalysis and photochemical water reduction for hydrogen evolution. Notably, the construction of mesoporous nanocomposite materials with different composition (e.g., CuS/CdS) or the deposition of active co-catalyst nanoparticles such as Pt and $Ni(OH)_2$ on the CdS NCAs surface synergistically improve the photoactivity of the mesostructures through the formation of efficient nano-heterojunctions; such heterojunctions can facilitate better separation and transfer of the photogenerated charges. We found that the hydrogen production activity and stability of all the examined mesoporous NCAs composites is remarkably enhanced, outperforming other reported CdS-based photocatalysts and demonstrating their potential for practical use in photocatalytic hydrogen evolution. Overall, this research work wishes to contribute to the creation of new opportunities for designing and synthesizing novel metal-chalcogenide functional nanomaterials and to a better in-depth understanding of some key features for efficient solar-to-hydrogen energy conversion.

Περίληψη

Η σύνθεση μεσοπορώδων (μεγέθους πόρων από 2 έως 50 nm) δομημένων υλικών από ανόργανους νανοκρυστάλλους (NCs) αποτελεί μια σημαντική πρόκληση στην επιστήμη των υλικών και στη χημική νανοτεχνολογία. Τέτοια αυτο-οργανωμένα υλικά έχουν την ικανότητα να ενσωματώνουν συμπληρωματικές ιδιότητες στην δομή τους, όπως το νανοπορώδες και οι φωτοκαταλυτικές και ηλεκτρονιακές ιδιότητες των επιμέρους νανοκρυστάλλων. Αυτά τα χαρακτηριστικά μπορεί να τους προσφέρουν ενισχυμένες εφαρμογές για φωτοκατάλυση, μετατροπή ηλιακής ενέργειας, χημικούς αισθητήρες και εκλεκτική προσρόφηση και διαχωρισμό. Αν και έχει επιτευχθεί μεγάλη πρόοδος στη σύνθεση πορωδών υλικών από νανοσωματίδια μετάλλων και οξειδίων μετάλλων με υψηλή επιφάνεια και οργανωμένους μεσοπόρους, η σύνθεση τρισδιάστατων μεσοπορώδων πλεγμάτων από νανοκρυστάλλους χαλκογονιδίων-μετάλλων εξακολουθεί να αποτελεί πρόκληση στην επιστήμη υλικών και στη χημική νανοτεχνολογία.

Στην παρούσα διδακτορική διατριβή αναπτύχθηκε με επιτυχία και παρουσιάζεται μία νέα και αποδοτική στρατηγική σύνθεσης μεσοπορώδων δομών από διασυνδεδεμένους νανοκρυστάλλους σουλφιδίου-μετάλλου. Με χρήση μιας απλής μεθόδου, η οποία περιλαμβάνει οξειδωτικό πολυμερισμό κολλοειδών νανοσωματιδίων παρουσία οργανικού πολυμερικού εκμαγείου, μπορούν να παρασκευαστούν αυτο-οργανωμένες μεσοδομές οι οποίες αποτελούνται από νανοκρυστάλλους χαλκογονιδίου-μετάλλου και εμφανίζουν τρισδιάστατη δομή ανοιχτού πόρου με μεγάλη επιφάνεια και ομοιόμορφους πόρους. Με κατάλληλη επιλογή των αρχικών δομικών μονάδων, αυτή η μέθοδος σύνθεσης μπορεί να οδηγήσει στην ανάπτυξη μεσοπορώδων υλικών από νανοσωματίδια χαλκογονιδίων-μετάλλων διαφορετικής χημικής σύστασης και μεγέθους, επιτρέποντας έτσι τον σχεδιασμό και τη δημιουργία προσαρμοσμένων χαρακτηριστικών και επιθυμητών λειτουργιών. Λόγω της υψηλής και προσβάσιμη εσωτερικής επιφάνειας και της ικανότητας απορρόφησης ορατής ακτινοβολίας, τα παρόντα μεσοπορώδη νανοδομημένα υλικά (NCAs) μελετήθηκαν ως πιθανοί καταλύτες, ιδιαίτερα στον τομέα της φωτοκατάλυσης και της φωτοχημικής αναγωγής του νερού προς παραγωγή υδρογόνου. Συγκεκριμένα, η παρασκευή μεσοπορώδων σύνθετων νανοϋλικών διαφορετικής σύνθεσης (π.χ. CuS / CdS) ή η εναπόθεση ενεργών συγκαταλυτών όπως νανοσωματίδια Pt ή $Ni(OH)_2$ στην επιφάνεια του μεσοπορώδους CdS NCAs συνέβαλλαν στην συνεργιστική αύξηση της φωτοκαταλυτικής δράσης των υλικών αυτών λόγω του σχηματισμού αποτελεσματικών νανο-συζεύξεων – αυτές οι νανοεπαφές μπορούν να ενισχύσουν το διαχωρισμό και τη μεταφορά των φωτο-παραγόμενων φορτίων. Όλα τα σύνθετα μεσοδομημένα υλικά που εξετάστηκαν παρουσιάζουν αυξημένη σταθερότητα και αξιοσημείωτη φωτοκαταλυτική δραστικότητα στην παραγωγή υδρογόνου, υπερβαίνοντας σε απόδοση άλλους αναφερόμενους φωτοκαταλύτες με βάση το CdS,

επιδεικνύοντας έτσι την δυνατότητά τους για πρακτική εφαρμογή στην φωτοκαταλυτική παραγωγή υδρογόνου. Συνολικά, το ερευνητικό αυτό έργο επιθυμεί να συμβάλει στη δημιουργία νέων δυνατοτήτων για το σχεδιασμό και τη σύνθεση καινοτόμων λειτουργικών υλικών από χαλκογονίδια-μετάλλων και στην καλύτερη κατανόηση ορισμένων βασικών χαρακτηριστικών για την αποδοτική μετατροπή της ηλιακής ενέργειας σε υδρογόνο.

Acknowledgements

First of all, I would like to thank the Department of Materials Science and Technology, University of Crete, for providing me the precious opportunity to pursue a higher degree of education in this amazing institution.

Subsequently, I would like to express my gratitude to several people, without whom it would have not been possible for me to carry out this academic research endeavor.

In the very first place, I am deeply grateful to my supervisor Prof. Gerasimos. S. Armatas for his continuous support, encouragement, insightful guidance, and constructive expert supervision during the course of my doctoral studies at this University.

I am also thankful to Prof. George Kioseoglou, Prof. George Kopidakis, Prof. Pantelis Trikalitis, Prof. Maria Vamvakaki, Prof. Constantinos Stoumpos, and Prof. Constantinos Milios, for accepting to be members of my doctoral committee and for their insightful evaluation.

My sincere thanks to the collaborators, Prof. Mercouri G. Kanatzidis (NU, USA), Prof. Bin Liu (NTU, Singapore), Prof. Stella Kennou (UoP, GR) and Prof. Stelios A. Choulis (CUT, CY), who provided important contributions in the collaborated publications during my Ph.D. study. Many thanks to Dr. Ioannis T. Papadas (CUT, CY) for the electrochemical measurements, Dr. Jianwei Miao (NTU, Singapore) for XPS and EIS measurements, Dr. Kota S. Subrahmanyam (NU, USA) for the SAXS measurements, and MSc Charalampos Drivas (UoP, GR) for XPS measurements.

Moreover, I would like to thank all former and present members of ChemMater Lab that contributed in different ways throughout these years. In particular, the graduates Adelais Trapali and Theocharis Tzanoudakis for their contribution to a considerable part of the experimental work of this dissertation, as well as Stelios Papadogiorgakis, Ioannis Daskalakis, Konstantina Giovanopoulou and Chrysanthi Patriarchea for continuing the development of this research work. Also, special thanks to Dr. Evangelia Skliri, M.Sc. Eirini Koutsouroubi, M.Sc. Ioannis Tamiolakis, M.Sc. Ioannis Kornarakis, Dr. Alexandra Xylouri, Dr. Georgia Velegraki, Dr. Ioannis Papadas and Dr. Alexia Agiomyrgianaki, for their valuable help and collaboration since my first steps in the lab, and for the opportunity to build beautiful friendships.

Last but not least, I would like to express my deepest gratitude to my loving and understanding parents, my brother, and to my partner Foteini, who are always there for me and give me faith and care to achieve the best I can do.

The present reasearch work has been co-financed by the Greek Ministry of Education (Greek Secretariat of Research and Technology – GSRT) and the European Union (European Social Fund – ESF) under the ERC grant shemes (ERC-09) and the Special Account for Research Funds of University of Crete (SARF UoC).

FUNDING

University of Crete
School of Sciences and Engineering
Materials Science and Technology

Laboratory of
Advanced Materials Chemistry

Synthesis of Mesoporous Networks of Metal-Chalcogenide Nanocrystals for Photocatalytic Applications and Hydrogen Fuel Production

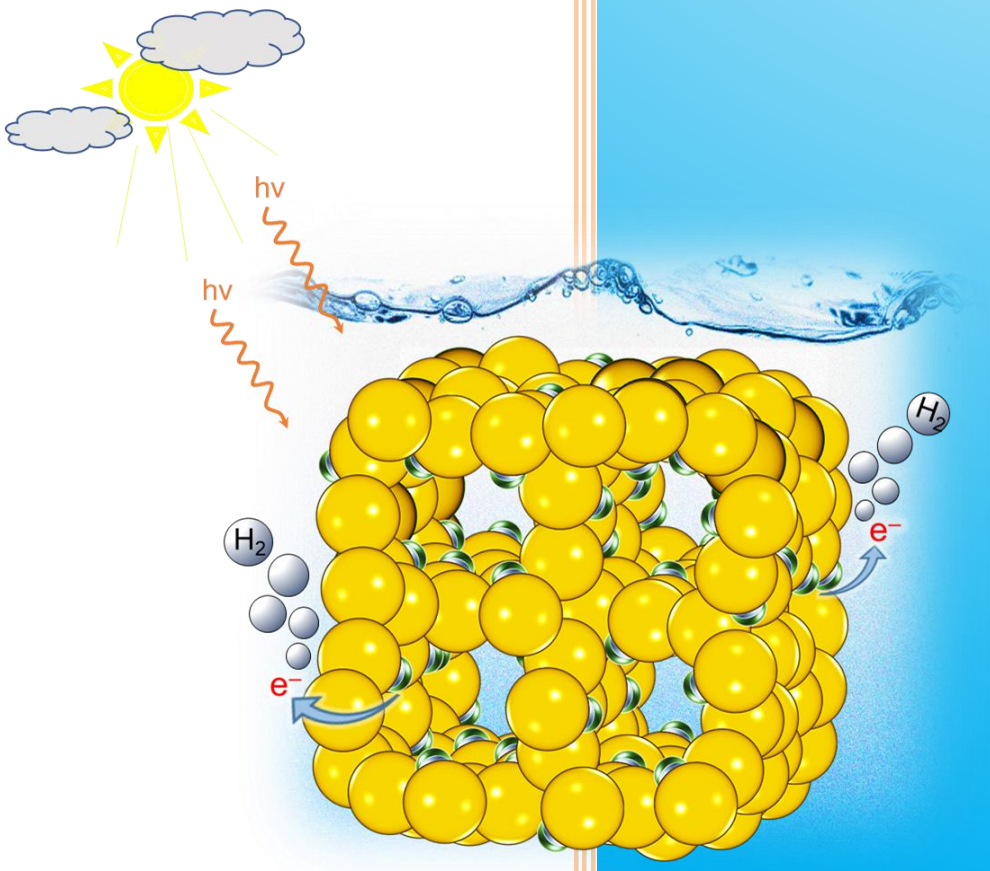

Ioannis Vamvasakis

Supervisor: Gerasimos S. Armatas

Ph.D. Thesis

Heraklion 2020

Contents

Chapter 1: General Introduction

1. Brief overview to ordered porous materials

1.1 Nanoporous materials

In recent years, nanostructured materials — i.e., materials with grain size, layer thickness, or with any external or internal dimension in the range of 1–100 nm — have gained immense attention in nanoscience and nanotechnology, an ever-growing multidisciplinary field of study that attracts tremendous interest and efforts in research and development around the world. The nanoscale is fascinating because, on this scale, the atoms or molecules interact and assemble into structures that possess unique physicochemical properties. Indeed, these properties are dependent on the size and shape of the building block units. Most importantly, at this scale the molecular interactions, processes, and phenomena can be also controlled and directed to form desired material geometries and endow desirable functionalities.

Nanoporous materials, as a subset of nanostructured materials, possess unique surface, structural, and bulk properties that underline their important uses in various fields of technology, such as ion exchange, molecular separation, catalysis, chemical sensing, biological molecular isolation, and purification. Nanoporous materials are of scientific and technological importance because of their ability to adsorb and interact with atoms, ions and molecules on their large interior surface within nanometer-sized pore spaces. [1] Generally, porous materials are solids that contain void spaces (pores) within their structure. There are varieties of porous materials having different structures, composition, and pore size and geometry, but they all share a common trait: a significant volume ratio of pore space to the total volume of the material (i.e., porosity). The presence of pores in materials provides increased surface area per unit mass ratios (i.e., large specific surface area), and thus render novel properties and functionalities that are not present in dense solids with highly close-packed structures.

According to the International Union of Pure and Applied Chemistry (IUPAC), porous solids can be distinguished in various ways depending on their size, shape (geometry) and accessibility of pores. [2] One classification is usually done by describing their accessibility to an external fluid. Pores that are isolated from their neighbors and from the external surface are called closed pores. These pores influence the macroscopic properties of the solid (e.g. mechanical stability), but they are inactive in terms of functional applications such as adsorption, catalysis and sensing. On the other hand, pores which are open to the external surface on one end (blind or dead-end pores) or multiple ends (through pores) are called open pores. The latter ones are necessary to ensure mass transport

through a material, as required for example in applications including chromatography (separation), catalysis, filtration etc. In addition, pores may also be classified according to their shape, which may vary from cylindrical, to ink-bottle-shaped, funnel-shaped or slit-shaped. However, the most prominent classification of pores (and hence porous solids) is mostly based on their size, i.e., pore diameter or width. In this respect, in line with the IUPAC definition, porous materials can be divided into three main categories:

- *Microporous materials* — with pore widths smaller than 2 nm.
- *Mesoporous materials* — with pore widths between 2 and 50 nm.
- *Macroporous materials* — with pore widths larger than 50 nm.

For most technological applications, though, pore sizes normally do not exceed 100 nm and therefore in the field of functional porous materials the term "nanoporous" is consistently used to refer to this class of materials, namely, materials having large porosity and pore size between 1–100 nm.

In this context, inorganic nanoporous materials can be envisaged as solids that contain a nanoscale porous structure within an inorganic framework. The framework can be either amorphous, semi-crystalline or may consist of either a continuous crystalline phase (monocrystalline framework) or nanoscale crystalline grains (polycrystalline framework). In addition, with regard to the pore structure, nanoporous materials may exhibit long-range pore periodicity (periodically ordered structures) or disordered structure with uniform/or random pore morphologies and narrow/or wide pore-size distributions. As an example, nanoporous carbons, such as active carbons, have an amorphous very disordered structure, as revealed by various proposed model structures (**Figure 1-1a**). [3-6] Although the models differ in detail, the essential feature of all of them is a twisted network of carbon chains or defective carbon layer planes, which are cross-linked by aliphatic bridging groups. They usually have high surface areas (typically 1000–2000 m^2 g^{-1}) and there is considerable microporosity in the form of an interconnected network of slit-shaped pores between the carbon stacks. [7] Moreover, typical examples of crystalline framework solids with ordered pore structure are zeolites. [8] Zeolites are open-framework microporous materials with ordered atomic arrangement in their inorganic framework, encompassing a network of well-organized pore channels and cages of strictly regular dimensions ranging from 0.2 to 1.5 nm (**Figure 1-1b**). Because of their high porosity and surface area, and the possibility of controlling their adsorption capacity as well as tailoring their surface functional centers (active sites), zeolites became the most widely used materials in the industry, serving as catalysts and molecular sieves. [9] However, in spite of the large number of zeolite structures and other novel microporous materials synthesized so far [10, 11], the size of their pores remains a strong limitation for applications involving absorption and separation of large bulky molecules. Hence there has been an ever-growing interest in expanding the pore size of microporous molecular sieves from the micropore to mesopore region.

1.2 Ordered mesoporous structured materials

Roughly speaking, most of the nanostructured materials synthesized by common methods, such as hydrothermal reactions, have mesoporosity. However, this random mesoporosity does not usually serve any functional expectation since the mesopores are not ordered, and hence, the diffusion pathway is not straightforward; the pores might be blocked in the random arrangement. The answer to this problem came with the discovery of ordered mesoporous structured materials, which combine the ordered porous structure (similar to zeolites) with the advantage of tailoring the pore dimensions in the range of mesopores. Originally, the synthesis of an ordered mesoporous material was described in a patent in 1971 where Chiola and co-workers [12] reported on the formation of low-bulk density silica, while in 1990 Yanagisawa et al. [13] synthesized a kanemite-based (silica) mesoporous material. Nevertheless, due to an only limited description of the synthesis and material characteristics, the synthesis and the structural characteristics of these materials did not lead to any significant recognition until some years later. [14-16] The major breakthrough came in 1992 by Mobil group scientists, who described a generalized pathway to produce ordered mesoporous silicate materials. [17, 18] Mobil researchers proposed a self-assembling supramolecular templating mechanism in which ordered surfactant micellar structures served as structure-directing agents (SDAs) to direct the formation of SiO_2 mesostructures. This is an important synthetic advance leading to the discovery of a new class of ordered mesoporous molecular-sieves designated as M41S. Among the members of this group, the MCM-41 (Mobil Composition of Matter No. 41) phase — with ordered hexagonally-packed pore channels (**Figure 1-1c**), a surface area of approximately 1200 m^2 g^{-1} and uniform pores that can be tailored from 1.5 to 10 nm in diameter — has received the most attention and is the most widely studied mesostructure. [19] In addition to the two-dimensional (2-D) hexagonal MCM-41 pore structure, other known mesophases of the M41S family are the three-dimensional (3D) cubic MCM-48 and the more unstable lamellar MCM-50 materials (**Figure 1-1c**). These different mesophases, which were obtained by simply altering the surfactant concentration, were discovered several months later as a result of a detailed study investigating the effect of the surfactant/silica molar ratio on the formation of M41S. [20, 21] This clearly indicated the versatility of the proposed supramolecular templating mechanism in designing and constructing ordered mesoporous materials with tailored mesostructure geometries and desirable pore size characteristics.

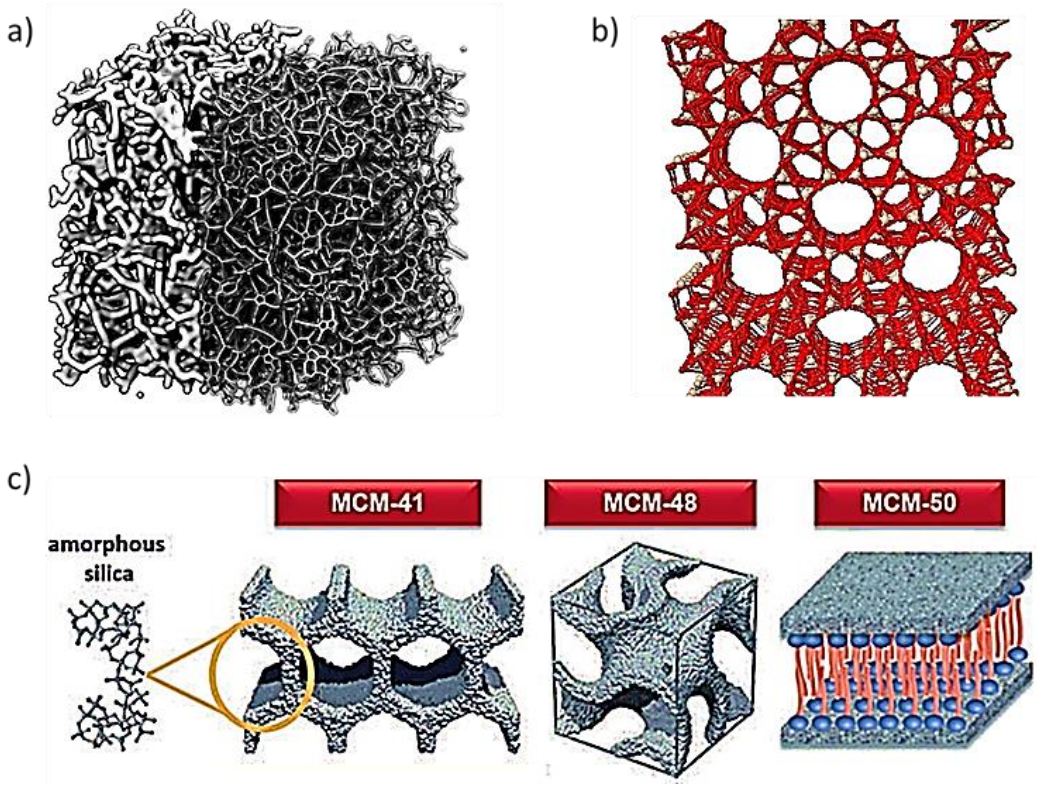

Figure 1-1: a) Model structure example of amorphous disordered nanoporous carbon, reproduced from ref. [6]. b) Example of crystalline zeolite (ZSM-5) ordered microporous structure with estimated pore size 0.54-0.56 nm (Copyright © Karl Harrison 3DChem.com). c) Members of the M41S family of ordered mesoporous structured materials: MCM-41 (hexagonal), MCM-48 (cubic) and MCM-50 (lamellar with the presence of surfactant molecules between lamellae). Adapted from ref. [22] with permission from Springer (Copyright © 2017, Springer International Publishing AG).

Consequently, these results have triggered an interesting research line on the synthesis of new mesoporous materials, by using surfactants of various nature (cationic, anionic, non-ionic, block copolymers) in different synthesis conditions. This led to the preparation of a large number of families of mesoporous materials with different porous characteristics and physicochemical properties, some of the most representative being: SBA-15 (hexagonal, with controllable pore size from 5 to 30 nm, micropores connecting the mesopore channels and wall thicknesses of 3–6 nm) [23], SBA-16 (cubic) [24], HMS (hexagonal) [25], KIT-6 (cubic with a mesophase similar to MCM-48) [26], MSU-X (mesostructures with regular diameter pore-channels but lacking long-range pore ordering) [27], and others. Note that the acronyms for the aforementioned mesoporous materials generally represent the research institutes that they were discovered or some peculiarity of each material. For example, MCM is the acronym for the series of Mobil Composition of Matter type materials, the acronym SBA means Santa Barbara Amorphous, KIT indicates the Korea Institute of Technology, HMS means hexagonal mesoporous silica, and MSU means Michigan State University. A time scale with the chronologically-ordered discoveries of some representative mesoporous structures is presented in **Figure 1-2**. [28]

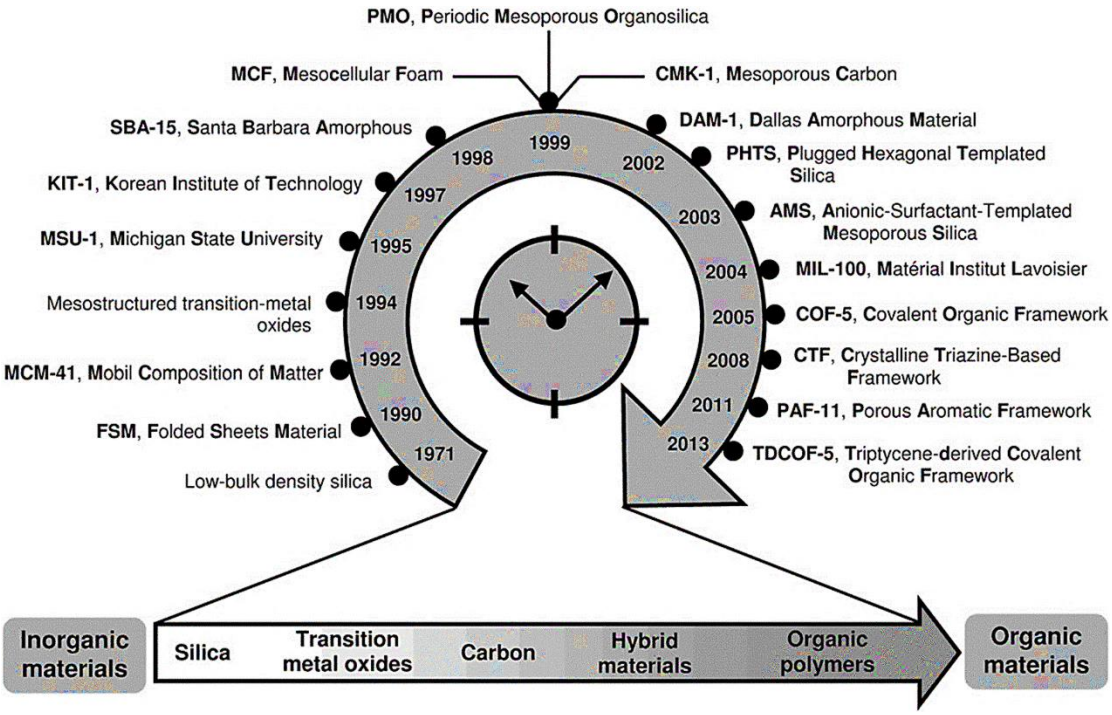

Figure 1-2: Time scale with the discoveries of some representative mesoporous materials. Adapted with permission from ref. [28]. Copyright © 2014 Elsevier B.V. All rights reserved.

1.3 Synthesis strategies for ordered mesostructured materials

The synthesis of ordered mesostructured materials can be considered an evolution of that of zeolites. In fact, the crystallization of microporous materials requires templates (or more properly defined as structure-directing agents, SDAs), that is, either organic molecules or hydrated inorganic cations (alkali or less commonly earth alkali metal ions) around which the (alumino)silicate species are polymerized to form 3D zeolite structures. Upon removal of the template by calcination or ion exchange, the porous structure becomes accessible to other molecules and ions. In a simplified view, the single SDA organic molecule/hydrated-cation determines the size of the pores, which in the vast majority of cases remains in dimensions lower than 1.5 nm. In the case of mesostructured materials, however, the concept of template moves from the single molecule to that of aggregates of surfactants, namely of micelles. [29] Surfactants are amphiphilic molecules containing a hydrophilic polar head group (either ionic or non-ionic) and a lipophilic non-polar chain. When dissolved in a polar medium (e.g. water) they aggregate to form micelles, constituted by a liquid-like core of non-polar chains and an outer rim (corona) of polar groups. It should be noted that micelles form when the surfactant concentration in solution exceeds a well-defined value, i.e. the critical micellar concentration (cmc). Only above this value micelles are created — with the driving force being the necessity of reducing the exposure of non-polar chains to the surrounding polar medium — forming various configurations

(spheres, rods or bi-layers) depending on the concentration and on the geometric characteristics of the particular surfactant. [30] Spherical micelles are considered to form first and as the surfactant concentration increases they approach each other until the stability limit is reached. After that, cylindrical micelles are formed so that the area/volume ratio decreases. Cylindrical micelles organize themselves into a liquid crystalline phase, forming a hexagonal array of parallel rods. A further increase of the surfactant concentration (beyond the stability limit of the cylindrical micelles) leads to a transition, first to the cubic and finally to the lamellar mesophases.

In general, the ability of micelles to form liquid-crystalline mesophases is the determining factor that leads to the synthesis of inorganic materials with ordered mesoporosity. However, unlike a simple surfactant-in-water system where the geometry and concentration of the surfactant molecules dominate their packing mode, mesoporous materials are usually synthesized in a surfactant/water/inorganic multicomponent system. In this context, the involvement of inorganic species increases the complexity of the surfactant self-assembly in solution because the different interactions between the surfactant and inorganic species. Many studies have investigated the formation of mesoporous structures on the basis of surfactant/inorganic species interactions under various conditions (temperature, pH, concentration), but the general concept in all of them involves the condensation and polymerization (cross-linking) of the inorganic components on the surface of self-assembled micellar structures. These physico-chemical processes lead to the formation of intermediate hybrid organic-inorganic mesostructures. [31] Eventually, upon removal of the organic template by calcination or solvent extraction, the final ordered mesoporous material can be obtained with pore structure that resemble the structure of the liquid-crystal mesophase. To this general supramolecular templating strategy, the so-called "*soft-templating*", three main pathways have been so-far proposed for the effective construction of ordered mesoporous materials: (i) the *cooperative self-assembly (CSA)* [32, 33], (ii) the *true liquid-crystal templating* (TLCT) [17, 34], and (iii) the *evaporation-induced self-assembly* (EISA) [35, 36], as illustrated in **Figure 1-3a-c**. [37]

1.3.1 Soft-templating

Cooperative self-assembly

The "cooperative" aspect of this mechanism, termed *cooperative self-assembly (CSA)* or *precipitation*, derives its name from the observation that both inorganic and organic components are essential to achieve ordered mesostructures. According to this mechanism, it is unnecessary to have pre-formed liquid-crystalline mesophases to serve as templates for inorganic species polymerization. Instead, the ordered mesostructures can be formed in lower surfactant concentrations (usually around

the cmc value) via the simultaneous self-assembly of the inorganic precursors and surfactant molecules (**Figure 1-3a)**. Briefly, the major points of this mechanism include the following: (i) preformed ordered arrays of surfactants are not necessary (i.e., the liquid-crystalline phase is formed after the addition of the inorganic species), (ii) interactions between the organic surfactant molecules and inorganic species are needed to facilitate the "cooperative assembly", and (iii) the organic–inorganic interactions, along with the hydrophobic interactions of the surfactant non-polar chains, determine the surfactant's self-assembly behavior and, thus, the arrangement of the resultant mesostructure. From the viewpoint of the organic-inorganic interactions, the synthesis of ordered mesostructures can be achieved through either (i) electrostatic pathways, based on supramolecular assembly of ionic surfactants with charged inorganic precursors, or (ii) neutral pathways, in which other types of interactions such as hydrogen bonds or covalent bonds are responsible for the cooperative assembly of the surfactant and inorganic precursors. [31, 38] Another requirement for making the cooperative self-assembly possible is that the condensation of inorganic species cannot be too fast relative to the organization of the surfactant aggregates, otherwise phase separation would occur. Specifically, if condensation takes place to an appreciable extent before the liquid-crystalline phase is formed, precipitation of untemplated precursors may occur forming a disordered mesostructure. Since the condensation of silicates can be easily controlled, most mesoporous structures were originally fabricated with silica and the CSA mechanism was first suggested as a probable synthetic pathway by Beck et al. and Stucky's group immediately after the discovery of MCM-41 [18, 23, 24, 25, 27, 32, 33, 39, 40]. However, extension of this method to other non-siliceous compositions of mesoporous materials, such as transition-metal oxides, has proven to be more challenging due to the fact that the hydrolysis and condensation rates for most transition-metal oxide precursors are generally much faster than they are for silica. Thus, special attention has to be paid to hydrolysis rates, redox reactions and phase transformations during the formation of the mesostructure. For instance, early attempts to synthesize stable mesoporous metal oxides, although led to the formation of ordered organic/inorganic composite mesostructures, result in poorly ordered materials mainly due to changes in crystallinity and/or redox reactions that occurred during the thermal decomposition of template. [33, 41] Since then, most of these difficulties have been largely overcome and a wide variety of non-siliceous mesoporous oxides including aluminum, zirconium, hafnium, molybdenum, manganese, tantalum, tungsten, niobium, tin, titanium oxides etc., as well as numerous mixed oxides such as alumino-, vanadophosphates, heteropolyoxides and chalcogenide composites, have been successfully prepared via the SCA route described above. [42-44]

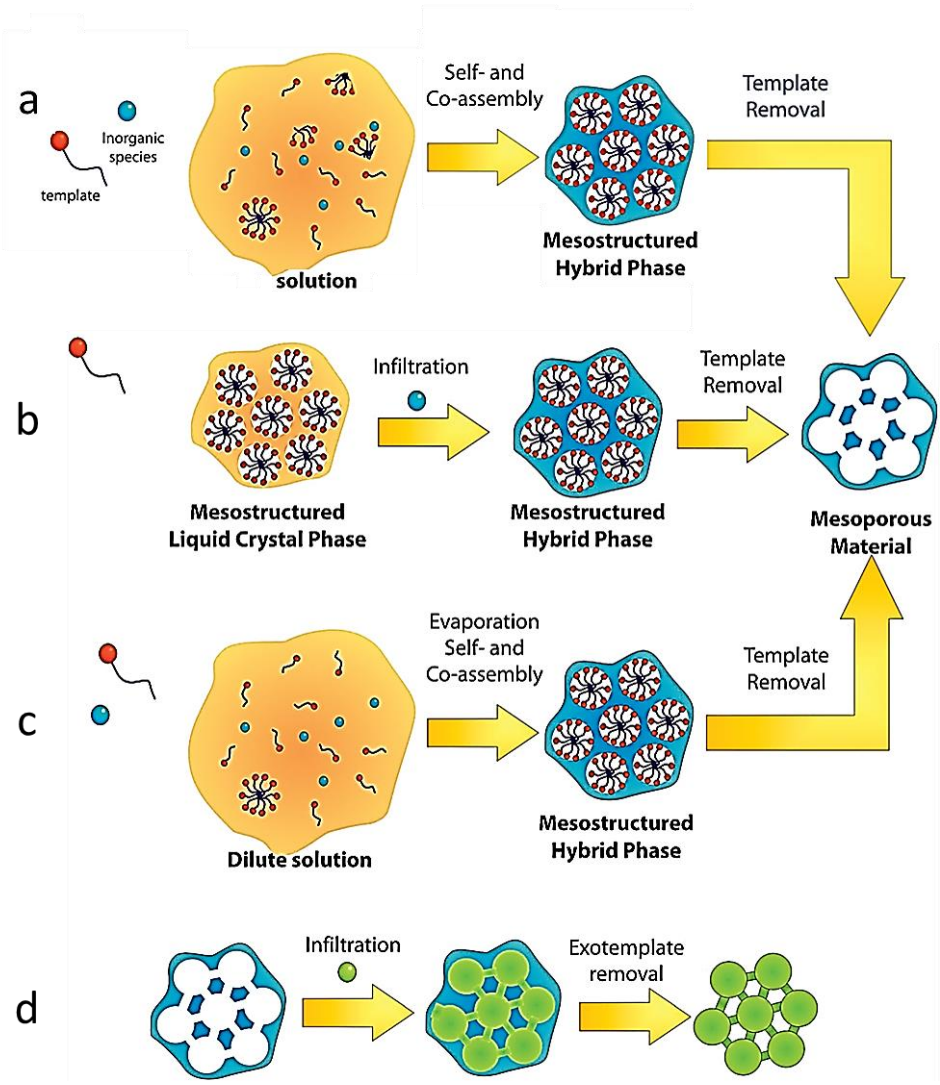

Figure 1-3: Scheme of the main synthesis routes to mesoporous materials. (a-c) Soft-Templating methods: (a) Cooperative Self-Assembly (CSA), (b) True Liquid Crystal Templating (TLCT), (c) Evaporation-Induced Self-Assembly (EISA); and (d) Hard-Templating method or nanocasting. Adapted from ref. [37] with permission from The Royal Society of Chemistry.

True liquid-crystal templating

The second way to prepare ordered mesostructures is the "true liquid crystal templating" (TLCT) pathway (**Figure 1-3b**). Although the formation of a liquid-crystal mesophase is always involved at some point in a soft-templating synthesis route to mesoporous materials, the word "true" is used to describe the direct templating pathway by preformed lyotropic liquid-crystal phases; these organic mesophases are prepared under high surfactant concentrations (generally >20 wt.%). After the first suggestion of the liquid-crystal templating mechanism by Mobil scientists [17], the TLCT route was developed by Attard et al. [34, 45] and further investigated by Göltner and Antonietti et al. [46-48] by utilizing high concentrations of non-ionic surfactants or amphiphilic block-copolymers for the formation of the lyotropic mesophases. In general, this mechanism implies three steps: (i) the

surfactant molecules self-assemble to form a liquid-crystalline mesophase, (ii) the inorganic precursors are "cast" (deposit) on the surface of the preformed liquid-crystal template and (iii) the inorganic species interconnect to a continuous network forming the inorganic walls between the micelles. After removing the template, a highly ordered mesoporous inorganic structure can be obtained. In this case the pore size and the structure of the recovered materials can be predicted based on known surfactant/water phase diagrams, since the preformed lyotropic mesostructure is not affected by the presence of inorganic species and is preserved throughout the whole process. In some cases, however, the release of low weight alcohols upon hydrolysis and condensation of inorganic alkoxide precursors can disrupt the initial lyotropic liquid-crystal mesophase, limiting the applicability of the method. Also, significant inhomogeneities can result, either by inadequate diffusion of the inorganic components within the preformed liquid-crystal phase, or by uncontrolled phase separation due to inorganic polymerization taking place in viscous liquid-crystal media. Nevertheless, this path has led so far to the synthesis of new mesostructured hexagonal, cubic or lamellar silica materials, prepared in various forms such as gels, cast monoliths or films. Also, beside silica-based mesoporous materials, a wide variety of ordered mesostructured and mesoporous non-silica materials, including crystalline oxides [49, 50] and especially metals and metal alloys, oxides and complexes [51-57], as well as chalcogenides [58-64], have been successfully prepared using the TLCT mechanism.

Evaporation-induced self-assembly

Another important route of the soft-templating strategy is the evaporation-induced self-assembly (EISA) process. The EISA denomination was first introduced by Brinker et al. to describe the synthesis methods used to produce mesostructured materials from solutions, upon solvent evaporation conditions. [35] This method is based on the formation of an organic-inorganic hybrid mesostructured phase after solvent evaporation from a dilute solution containing the inorganic precursors, the templating agent (surfactants or block-copolymers) and other additives (**Figure 1-3c**). In general, dilute solutions below the critical micellar concentration (cmc) permit to obtain materials with excellent homogeneity. Specifically, high dilutions discourage inorganic condensation, whereas the evaporation of volatile solvents (e.g., ethanol, water) promotes the co-assembly of both the organic and inorganic precursors into a hybrid liquid-crystalline mesophase, as the solution becomes more concentrated and the cmc is reached. Therefore, EISA can be understood as a TLCT-related method, although additional interactions (like those at the solid–liquid interface) are also impact the process. [36, 65] This evaporation-based procedure offers the opportunity to avoid the diffusion problems (commonly found in TLCT method) encountered when infiltrating a real liquid-crystal

structure with inorganic precursors. Also, the organic-inorganic hybrid mesophase formed upon solvent evaporation is flexible enough (the so-called tunable steady-state condition) due to the incomplete inorganic polymerization. Aging of these hybrid mesophases under controlled humidity conditions helps to improve the ordering of the final mesostructure. [65-67] Inorganic condensation-polymerization can be "turned on" in a subsequent step by thermal or chemical treatment, which leads to the formation of a robust inorganic framework. A last step may also be needed for the removal of the organic template, the stiffening of the inorganic network and eventually the crystallization of the inorganic structure, usually by calcination. However, if the condensation reaction takes place too fast, large crystallites may grow within the inorganic structure and precipitation of untemplated material may occur (resulting to a dense structure). [68] This procedure permits materials to be processed in various forms, such as powders, gels, monoliths and thin films. The solution can be casted in order to form mesostructured gels or can be dip- or spin-coated to form mesoporous films. Except silica mesoporous films [69, 70], monoliths [71, 72] and particles [73], the EISA method is particularly interesting to work with non-silica systems, where condensation has to be thoroughly controlled. Over the past years, various EISA-based methods have been developed to produce porous metal oxides, as powders (xerogels) [74-76], thin films [77, 78] or microparticles [79].

1.3.2 Hard-templating

In all the soft-templating routes outlined above (CSA, TLCT and EISA), the interplay of a number of physical and chemical factors (e.g. organic/inorganic interactions, condensation rates, surfactant concentration, humidity, temperature, crystallization, evaporation conditions etc.) has to be considered and carefully controlled in order to design inorganic mesostructured frameworks with ordered mesoporosity. To overcome this complexity and its limitations, a "hard-templating" strategy referred to as nanocasting [80, 81] or exotemplating [82] has also been developed, using porous materials as hard templates to create replicas. The principle of the nanocasting strategy is shown schematically in **Figure 1-3d**. First, a hard template is synthesized, usually a highly ordered mesoporous silica with interconnected porous structure, such as SBA-15. In the second step, the porous hard template is impregnated with a suitable precursor (e.g., an organic compound or a metal salt), followed by thermal treatment under inert or reactive atmosphere. The precursor infiltration may be repeated to achieve high loadings, as this will facilitate the rigidification of the templated framework. Finally, when sufficient solidification has been achieved within the host pore system and eventual heat treatment has been carried out to form the desired phase, the exotemplate can be selectively removed (usually by HF or NaOH solutions) to give the final structure as a "negative"

replica of the initial porous structure. The first report on this method by Ryoo's group in 1999 described the synthesis of mesoporous carbon with an ordered structure. In this synthetic protocol, the replication of the MCM-48 structure led to the formation of a new type of ordered mesoporous carbon material called CMK-1. [83] Soon after, a new family of ordered mesoporous carbons with various pore structures was created by Ryoo and coworkers, designated as CMK-n (Carbon Mesostructured by KAIST), using mesoporous silicas or aluminosilicate templates with 3D pore connectivity. [84-86] In addition to ordered mesoporous carbons, the nanocasting method has been extended and proven to be a useful strategy for the preparation of various crystalline nanoporous materials, such as ordered mesoporous metals, and metal oxides, nitrides, carbides and sulfides [87], which are usually difficult to synthesize by conventional soft-templating processes due to their poor thermal and/or redox stability upon the template removal process.

1.4 Mesoporous frameworks from colloidal nanocrystals

Since the beginning of the 21st century, the push to develop new efficient materials for catalysis and other environmental and energy-related applications has produced a surge of interest in constructing mesoporous architectures from functional nanomaterials. As this field is continuously evolving, framework structural components are evolving as well. Today, although the preparation of porous frameworks from molecular precursors remains attractive, there is a growing interest to do synthesis using pre-formed nanocrystalline colloids. While, in most soft-templated nanoporous materials, the use of molecular precursors as building components provides nice control of the architecture in the nanometer-scale, there is much less control of the atomic-scale structure (e.g. crystallinity). For instance, since for many crystalline mesoporous materials (such as transition-metal oxides) the pore walls can be crystallized by thermal processing, in many cases, they do not fully crystallize resulting in semi-crystalline or amorphous pore walls. [78, 88] Moreover, the lack of control in crystal growth during the crystallization process can result in the destruction of the porous structure. To achieve good crystallinity special reinforcement is often needed to strengthen the inorganic structure so that the porosity is preserved without collapsing during the thermal treatment process. [89] Therefore, by using pre-formed nanocrystals (NCs) as building-units, the problems associated with the crystallization of the inorganic framework can be mitigated, and thus crystalline nanoporous architectures can be produced in a controllable and reproducible manner. Because thermal processing is needed only to remove the organic template and fuse the assembled NCs into a tightly connected network, the open-pore structure is well retained in the final product. The resulting materials exhibit a unique combination of an interlinked colloidal NC network with large and highly accessible pore surface. Another important advantage in using colloidal NCs as building blocks,

rather than molecular precursors, is that their physiochemical properties can be precisely controlled (through synthesis) prior to their assembly into a framework configuration. Recent advances in material chemistry now allow the synthesis of colloidal NCs with a diverse range of compositions and precise control over the size, shape and uniformity. [90-100] These characteristics can be deliberately configured to suit a particular application, thus offering tailored properties not available to conversional porous structures derived from small-molecule precursors.

The prospect of tuning the optical, electronic and surface properties with size, shape and composition is a fascinating feature of small-sized NCs (typically 1–20 nm in diameter). This prospect greatly expands the applicability of these nanomaterials to a wide variety of technological fields, ranging from catalysis and photovoltaic cells to optoelectronic devices, as well as chemical, biological and biomedical applications. [101-107] For example, the tunable energy bandgap and size-dependent optical absorption and luminescence are some of the intrinsic characteristics of small semiconductor NCs, explained by quantum mechanical effects; quantum confinement effects essentially arise from the presence of discrete, atom-like electronic states within the electronic band structure. [108] Nevertheless, despite their unique properties, individual NCs and most NC-based superlattice assemblies face several limitations for practical use in applications that that involve charge or energy transfer, such as catalysis and chemical sensors. One of the main problems is that colloidal NCs (and their resulting superlattice assembled structures) are coated with organic ligands adsorbed to the NC's surface; such ligands are used to control their size and shape during the synthesis process and to provide colloidal stability [109] as well as to enable control over their self-assembly into desirable NC-ensembles [107, 110, 111]. However, these large organic surface molecules separate the inorganic components and create an insulating effect, thus restricting, for example, electromagnetic coupling and interparticle charge transfer processes, resulting in poor interparticle interactions. Typically, to improve conductivity between particles, the original surface ligands are either removed in-situ or replaced by small molecules. However, with this approach NC aggregates are usually obtained as close-packed superlattices or random NC networks with irregular morphology and porosity due to the strong tendency of small NCs to agglomerate. [112-115]

Consequently, one of the most effective approaches to exploit the unique chemical, optical and electronic properties of colloidal NCs is to integrate them into extended network architectures, such as three-dimensional (3D) porous mesostructures. These materials — as a result of the combination of the inherent properties of the framework's NC-constituents and the mesoscale pore structure — can exhibit high chemical reactivity and electrical conductivity, by providing a large number of active sites and allowing molecular diffusion within the pores. [116, 117] Such characteristics are expected to impart unique functionalities for various technological processes, especially those involving mass transport-related phenomena such as ion exchange, separation and catalysis, that substantially deviate

from those of starting materials (i.e., individual NCs) and conventional porous solids. However, the construction of ordered mesoporous frameworks from colloidal NCs is still a grand challenge for synthetic chemists. The major problem lies in the complexity of the overall process, where the assembly of the NC building blocks into ordered mesoscopic architectures requires precise control over their spatial organization at the nanoscale. In general, conventional supramolecular self-assembly methods which rely on weak intermolecular interactions (e.g., hydrogen bond or van der Waals forces) are not as effective for colloidal nanoparticles (as they are bigger than molecular precursors), offering limited control over their spatial arrangement.

1.4.1 Arranging colloidal nanocrystals in mesoporous architectures

Polymer templating of inorganic materials has been regarded as an effective method to produce mesostructured frameworks with high surface area and uniform pores. This approach, initially proposed for the synthesis of ordered mesoporous metal oxides using molecular compounds, has also proven to be well-suited for self-assembling colloidal NCs into mesoporous structures. [118] This method manipulates well-dispersed colloidal nanoparticles as functional building units and relies on their controlled arrangement into mesostructured morphologies, with the aid of amphiphilic block-copolymers (BCPs) serving as structure-directing agents (SDAs). The general idea includes the incorporation of uniform NCs within the polar domains of BCP micelles in order to produce nanostructured BCP/NC hybrid composites. The co-assembly of NCs with BCP templates occurs through supramolecular and colloidal interactions, often assisted by an EISA-based process. Namely, in this process, the evaporation of solvent drives the aggregation-assembly of the BCP/NC composites into a hybrid mesostructure. Finally, the organic components can be removed from the hybrid mesostructure by calcination or chemical/solvent extraction. If the concentration of NCs is sufficiently high at the BCP micellar interface, this process makes it possible to produce well-connected NC networks that maintain their structural integrity and porosity after the template removal process. Indeed, the obtained mesostructure can be viewed as a negative replica of the BCP aggregates.

A key aspect of this method is the surface functionalization of NCs with appropriate surface ligands (usually small organic molecules with functional groups or ions). In particular, the ligands attached to the NC surface must prevent the flocculation of NCs in the desired solvent (i.e., stabilize the colloidal solution), while promoting favorable enthalpic interactions with the BCP micelle interface during self-assembly. Generally, the thermodynamic and kinetic factors that govern the interfacial self-assembly can be manipulated by modulating the NC's surface (with suitable ligands) or/and designing BCP polymers to enhance their enthalpy of interaction. More specifically, the

polyvalent NC-BCP interactions — that confine the NCs within a specific domain of the BCP matrix (usually within the polar segments) and drive the assembly process — primarily include molecular and nanoscale forces, such as van der Waals, hydrogen bonding and electrostatic forces. [119] Interfacial interactions based on van der Waals forces are generally too weak and inherently limit the inorganic volume fraction in the BCP/NC interface. [120] In these case, there are few NCs to stabilize the framework, which may collapse during the thermal treatment. [121] Interfacial hydrogen bonding solves this problem to some extent by enhancing the interaction strength between NC and BCP aggregates. [122-126] Even so, ordered framework mesostructures can still be difficult to achieve using certain combinations of NCs and polymeric SDAs. To date, the most successful NC assembly schemes to ordered mesoporous frameworks have employed electrostatics or ionic interactions (e.g., acid-base, ion-induced dipole, etc.) as an efficient interfacing strategy. In this case, the surface of NC components are ionic in character and, therefore, both ligand-coated or ligand-free ("stripped") NCs can interact and assemble with BCP templates with suitable NC-tethering domains. [127]

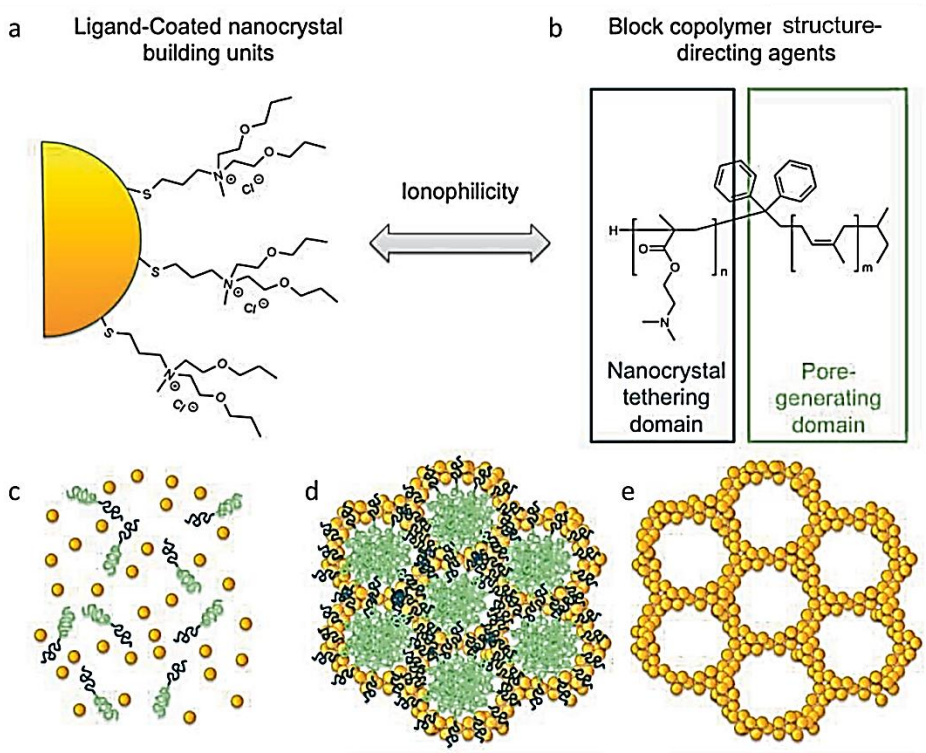

Figure 1-4: Assembly of ligand-coated NCs with BCP template through ionic interactions (ionophilicity) as an interfacing strategy for the formation of NC-network mesostructures under thermodynamic control. The co-assembly of ligand-stabilized Pt nanoparticles and BCP-template from ref. [128] is used here as example. (a) ligand (N,N-di-2-propoxyethyl-N-3-mercaptopropyl-N-methylammonium-chloride) stabilized Pt NCs and (b) polyisoprene-*block*-poly(N,N-dimethylaminoethyl-methacrylate) BCP-template with appropriate NC-tethering domain. In order to achieve thermodynamic control, the BCPs are initially un-aggregated (c). With solvent evaporation, the Pt NCs sequester throughout the polar domains of the hexagonally organized BCP-micelle mesophase (d), yielding a well-ordered mesoporous colloidal Pt NC-framework upon thermal processing (e). Adapted with permission from ref. [127]. Copyright © 2015 WILEY-VCH Verlag GmbH & Co. KGaA, Weinheim.

For ligand-coated NCs, careful selection or design of the surface ligands, BCP templates and colloidal particle size are important factors that affect the assembling process and the structural characteristics of the final mesostructure. The ligands must have appropriate functional groups that allow them to bind to the NC surface and induce productively leverage interactions (electrostatic or ionic) with the polar domains of the polymer template. Regarding BCP templates, the composition of the NC-tethering domain should also be chosen to be complementary to the NC surface chemistry. Moreover, in order to achieve high NC loadings in the BCP/NC interface, the size of the colloidal particles should be below a critical limit relative to the size of the polar groups; this size is approximated by the root-mean-square end-to-end distance of the hydrophilic block of BCP. [129] Therefore, by meeting these criteria it is possible to control the BCP/NC assembly and maintain the structural integrity of the resulting mesoporous NC-linked frameworks after thermal processing (see **Figure 1-4**). Using this approach, the synthesis of ordered mesoporous networks from metal nanoparticles [128, 130] as well as metal-oxide NCs with various compositions [131-133] has already been achieved. All these materials feature an interconnected pore structure with large surface area and uniform mesopores.

On the other hand, direct interactions between "naked" NC surfaces and BCP micelles may offer new opportunities for the construction of novel NC-assembled materials with well-ordered pore structures. As a result of the high loading and close proximity of colloidal nanoparticles at the BCP micelle surface, the templating self-assembly of ligand-stripped NCs can be accounted as a facile and efficient way to prepare mesoporous NC-based frameworks. Indeed, in these materials the well-linked network of NCs can provide high electronic conductivity throughout the whole structure and mechanical stability. A nice example of using ligand-free nanoparticles and BCP-template to produce highly stable and catalytically active porous frameworks can be found in a recent work, in which an ordered mesoporous NC-based titania structure was successfully synthesized. [134] In this work, the use of a polyoxoethylene-cetyl-ether diblock copolymer template (denoted as POE(20)-C16 or Brij 58), with a high hydrophilic-to-lipophilic ratio, favored the strong enthalpic interactions between the hydrophilic POE moieties and the ligand-free TiO_2 nanoparticles, thus directing their assembly within the micelles' hydrophilic domains and eventually organizing them into a 3D mesostructured NC-network. Importantly, the mesostructure remained thermally stable upon calcination and become catalytically active after template removal. Besides that, another interesting synthetic methodology to prepare NC-based porous thin films of different particle sizes and compositions was recently developed by the Milliron group, using ligand-stripped colloidal NCs as building blocks. [114, 135, 136] In particular, they used nitrosonium tetrafluoroborate ($NOBF_4$) or Meerwein's salt ($ROBF_4$) as reactive stripping agents to replace the native ligands attached to the NC surface (e.g., carboxylate, phosphonate, or amine passivating ligands) with weakly coordinating inorganic BF_4^- anions. This

exchange process gives ligand-stripped NCs with open coordination sites (cationic sites) at their surface, which are electrostatically stabilized by BF_4^- ions. [137, 138] The BF_4^-–stabilized NCs can then be readily dispersed in various polar solvents, such as ethanol and DMF, to form stable colloidal dispersions, while their cationic naked surfaces are available to interact with the polar segments of the BCP template, as illustrated in **Figure 1-5** and **Figure 1-6 (a-b)**. Upon evaporation of the solvent, the bare NCs can preferentially segregate into the hydrophilic domains of the BCP micelles (see **Figure 1-5)**, producing ordered mesostructured organic-inorganic films. Next, these hybrid films can be thermally treated to obtain mesoporous NC-frameworks with high volume fractions of NCs, as shown in **Figure 1-6 (c-e)**. Therefore, the selection of ligand-stripped NCs as starting materials has introduced further opportunities for constructing new types of functional mesoporous NC-networks, with various morphologies (e.g. thin films, xerogels and powders) and a broad range of compositions, such as oxides (e.g., Sn-doped In_2O_3 or ITO, CeO_2, TiO_2, Mn_3O_4, $MnFe_2O_4$, Fe_2O_3, Co-doped Fe_2O_4, CoO and Ni-doped CoO) [135, 139-144], fluorides (e.g., Yb,Er-doped $NaYF_4$) and metals (e.g., FePt) [135].

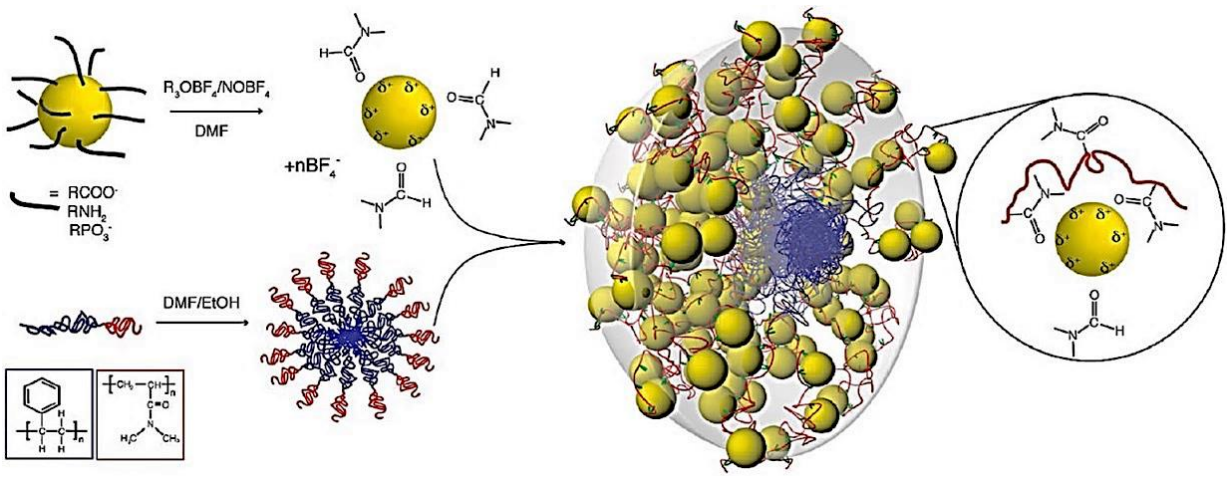

Figure 1-5: A co-assembly example between DMF dispersed ligand-stripped (BF_4^-–stabilized) NCs and BCP [poly(*N,N*-dimethylacrylamide)-*block*-polystyrene, PDMA-*b*-PS] micelles. The stripped colloidal NCs are dynamically adsorbed within the polar PDMA domain of the BCP micelle. Reproduced from ref. [135] with permission. Copyright © 2012, American Chemical Society.

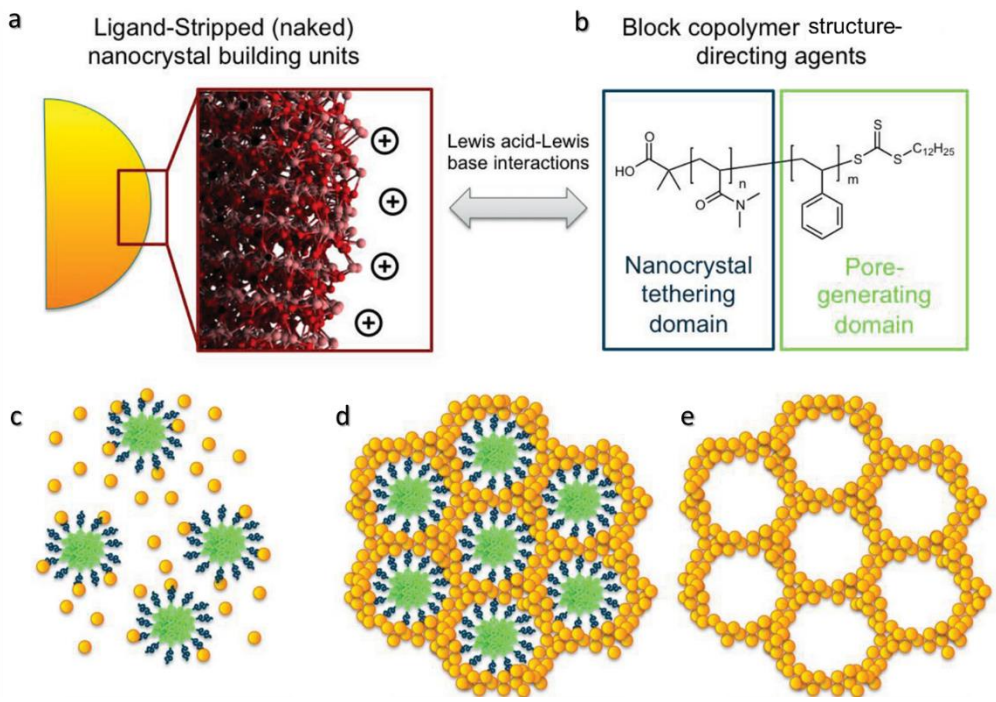

Figure 1-6: Leveraging Lewis acid–base interactions as an interfacing strategy for assembling colloidal-NC networks under kinetic control (a, b). The assembly process of ligand-stripped ITO NCs with a poly(*N*,*N*-dimethylacrylamide)-*block*-polystyrene (PDMA-*b*-PS) BCP-template from ref. [135] is shown here as example. The BCP-template is present in the dispersion as kinetically frozen micelles, which are gradually coated with ITO NCs due to the attractive interactions between their naked cationic NC surfaces and the PDMA NC-tethering domains of the BCP-template (c). Once deposited onto a substrate and the dispersant is evaporated, colloidal packing rules govern their mesostructural organization and a hybrid organic-inorganic composite film is obtained (d). Finally, ordered mesoporous ITO NC-framework films can be obtained after thermal processing for template removal (e). Reproduced with permission from ref. [127]. Copyright © 2015 WILEY-VCH Verlag GmbH & Co. KGaA, Weinheim.

1.4.2 Mesoporous networks of metal-chalcogenide nanocrystals

In general, metal-chalcogenides are chemical compounds containing in their structure at least one chalcogen atom, such as sulfur (S), selenium (Se), and tellurium (Te), often exhibiting semiconducting properties. In recent years, metal-chalcogenide NCs have progressively attracted research attention because of their interesting size-dependent semiconducting behavior and tunable optical and electronic properties, making them promising building blocks for optoelectronic and semiconductor devices [145-152], as well as for electrochemical and photochemical (i.e., photoelectrochemical and photocatalytic) cells [153-156]. Moreover, this trend has been encouraged by the significant advances in chemical synthesis of robust and easily processable metal-chalcogenide NCs with a wide range of sizes, shapes and compositions. [157-166] Similar to many metal and metal-oxide colloidal nanoparticles, the vast majority of these syntheses employ large passivating (organic) ligands on the metal-chalcogenide NC surface, which stabilize the NCs and prevent aggregation. Monodisperse colloids of this type can be self-assembled into ordered superlattices, which may

contain one or more different types of NCs. [167-169] However, although compositionally and topologically diverse materials can be created in this way, they are often neither conductive (i.e., due to the insulating nature of the native surface-ligands) nor porous, thus preventing their practical use in many relevant technological applications. In many cases, the conductivity problems have been partially resolved by depositing a dense film of NCs and exchanging their native insulating ligands with smaller functional molecules. [170-172] In addition, various NC-based metal-chalcogenide materials have also been synthesized by using metal-chalcogenide complexes as inorganic surface ligands that can be thermally processed to produce NCs embedded in a conductive matrix. [115, 173-175] While these methods may somewhat solve the conductivity problem, the resulting metal-chalcogenide materials are mostly dense superstructures, thereby inhibiting access to their intrinsic interfacial area. Consequently, the key to their further development in various nanotechnological areas, such as catalysis and energy conversion, is the introduction of mesoscale porosity into their structures.

Integrating metal-chalcogenide NCs into mesoporous framework architectures with a high and accessible surface area allows the semiconductor NC-based networks to interact chemically with infiltrating species, thus enabling new functionalities to be developed. To this end, even though polymer templating techniques for creating mesoporous metal (e.g., Pt) and metal oxide (e.g., Mn_3O_4, Fe_2O_3, TiO_2, CeO_2) NC-based networks have progressed markedly (as described earlier), the synthesis of ordered mesoporous architectures from metal-chalcogenide NCs is still challenging. Contrary to metal-oxide systems, thermal processing cannot be considered as a reproducible way to remove the polymer template and fuse the metal-chalcogenide NCs into an extended 3D mesostructure. One of the main reasons is that most chalcogenide NCs are thermally and oxidatively unstable at the elevated temperatures required for the degradation of polymer templates (usually > 400 ^{o}C). At these conditions, chalcogenide NCs may undergo thermal oxidation (forming unwanted metal-oxides) or coalesce into larger particles (thermal coarsening or Ostwald ripening). [176, 177] Such structural transformations may lead to mechanical deformation and fracture of the porous NC-framework or to unwanted changes in the optical, electronic and semiconducting properties of constituent NCs.

Therefore, previous efforts to assemble porous networks from metal-chalcogenide NCs have employed template-free sol-gel synthetic routes, which have resulted in NC-based aerogels. [178-187] Briefly, the methodology for aerogel formation is simple, comprising three major steps as illustrated in **Figure 1-7**: (i) Nanoparticle formation and thiolate-capping to stabilize the colloidal sols in polar solvents, (ii) oxidative condensation-aggregation (gelation) of the colloidal nanoparticles, through controlled surface-ligand loss, to form an extended NC-linked structure and (iii) supercritical CO_2 drying to remove the solvent from the wet-gel while maintaining the open pore

structure. [182] With this strategy, highly porous aerogels have already been produced from various preformed chalcogenide NCs, including CdS [181, 182], CdSe [182, 187], CdTe [178, 183], PbS [182], ZnS [182] and Ag_2Se [179], as well as core/shell CdSe/ZnS quantum-dots [186]. Nevertheless, although these inorganic NC polymers feature large surface areas (up to 250 m^2 g^{-1}) and physicochemical properties similar to those of the individual NCs, they show poor ordering with a "pearl-necklace" framework morphology and a broad pore-size distribution ranging from micropores to meso- and macropores as shown in **Figure 1-7**.

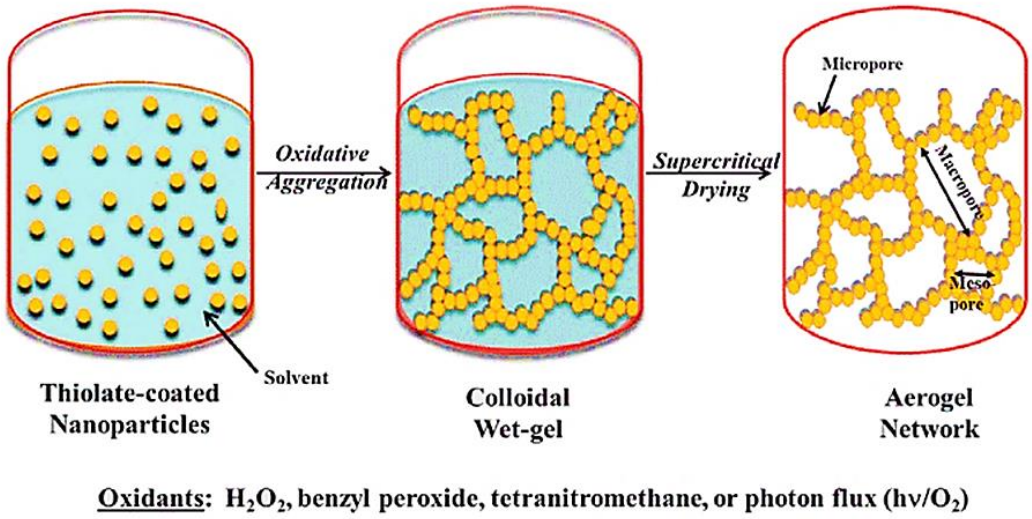

Figure 1-7: Schematic representation of the direct self-assembly of semiconductor nanoparticles into aerogel frameworks via a nanoparticle condensation strategy. Concentrated colloidal sols of thiolate-capped nanoparticles are prepared in polar solvents and the gel formation is induced by oxidative removal of the surface-ligands over 1-21 days. The resulting wet-gel structures are dried under CO_2 supercritical conditions to remove the solvent and form highly porous superstructures (aerogels) with a broad pore-size distribution (ranging from micro- to macropores) and a "pearl-necklace" morphology composed entirely of nanoparticle networks. [180]

Beyond the pioneering template-free assembling methods, attempts to create ordered porous networks of metal-chalcogenide NCs through polymer templating routes have so far met with limited success. For instance, Tolbert and co-workers have recently demonstrated a method to effectively assemble ligand-stripped CdSe NCs into stable mesoporous films, using appropriate BCPs as structure directing templates. [188] Upon deposition onto a substrate and solvent evaporation, the ligand-stripped NCs co-assemble with the polymer micelles and form hybrid organic/inorganic mesostructured films. Typically, these hybrid films are then heated at 400 ^{o}C under inert conditions — in order to remove the polymer template without oxidizing the chalcogenide NCs — leaving behind an open porous network. For this purpose, they used a carefully selected poly(butylene-oxide)-*block*-poly(ethylene-oxide) (PBO-*b*-PEO) diblock copolymer, which can be decomposed under non-oxidizing conditions to prevent oxidation of CdSe NCs to CdO and SeO_2. With this approach, the partial sintering of the NCs during thermal processing provided mechanical robustness, which

prevented the porous structure from collapsing. However, XRD analysis of the produced porous CdSe films showed the presence of both small-sized grains (~5 nm), which corresponded to the size of the starting NCs, and large domains (~18 nm in size) possible formed by the thermal fusion of NCs. This grain growth in the annealed films caused a bathochromic shift (i.e., a shift to longer wavelengths) in their optical absorption spectrum, which is indicative of a loss of well-defined NC size. Furthermore, a similar co-assembly and thermal treatment process has also been reported by Milliron's group, using ligand-stripped CdSe NCs and BCP template to control the porosity of the resulting films. The BCP template used in this work was obtained by chemically modifying the PDMA (poly(N,N-dimethylacrylamide)) domain of a PDMA-*b*-PS (PS = polystyrene) diblock copolymer with 10% acrylic acid to produce a new PDMA-*r*-PAA-*b*-PS (PAA = poly(acrylic acid)) structure directing agent. They found that this new BCP template strengthened the polymer-NC interactions, resulting in the formation of polymer/NC hybrid films with a high degree of mesoscale order. Nevertheless, a partial loss of order was observed after annealing (at 350 ^{0}C under inert conditions to decompose the polymer template), although the final films retained much of the mesoscale ordering and mesoporosity (pore diameter ~38 nm). Also, it was demonstrated that the framework composition of the porous films can be varied through chemical transformations, where the original mesoporous CdSe film could transform into porous films of different composition (PbSe, Cu_2Se, and Ag_2Se) via cation exchange, during which the porous morphology remained intact. However, some grain growth in the original CdSe NC size and a redshift in optical absorption was also observed after the heat treatment procedure. Therefore, while these current methods for producing ordered mesoporous films from colloidal chalcogenide NCs can provide exquisite control over film morphology, the effects of thermal processing can be detrimental to other material attributes, such as the grain size and crystallinity. In addition, the often complicated and tedious synthesis of specific BCP templates with appropriate NC-tethering domains — to enhance the interactions between the BCPs and ligand-stripped NCs and improve the conformation stability of the co-assembled structures — is also a downside for the widespread application of these methods. In this regard, it should be stressed that it would be very practical to use BCP templates that have a facile preparation method or are commercially available.

To overcome the deleterious effects of thermal processing on the NCs' grain size, Tobelt and co-workers developed an alternative method to form stable mesoporous films of chalcogenide NCs. [189] In this method, ligand-stripped NCs are first assembled with an appropriate BCP template and the resulting hybrid films are then soaked in a solution containing small organic bidentate ligands. As shown in **Figure 1-8**, these ligands serve as binding agents that cross-link the NCs into a continuous structure, thus forming a robust NC-linked network. Due to the well cross-linked structure

of the obtained composite, the polymer template between the NCs can be gently removed by solvent extraction, leaving behind a porous film of connected NCs.

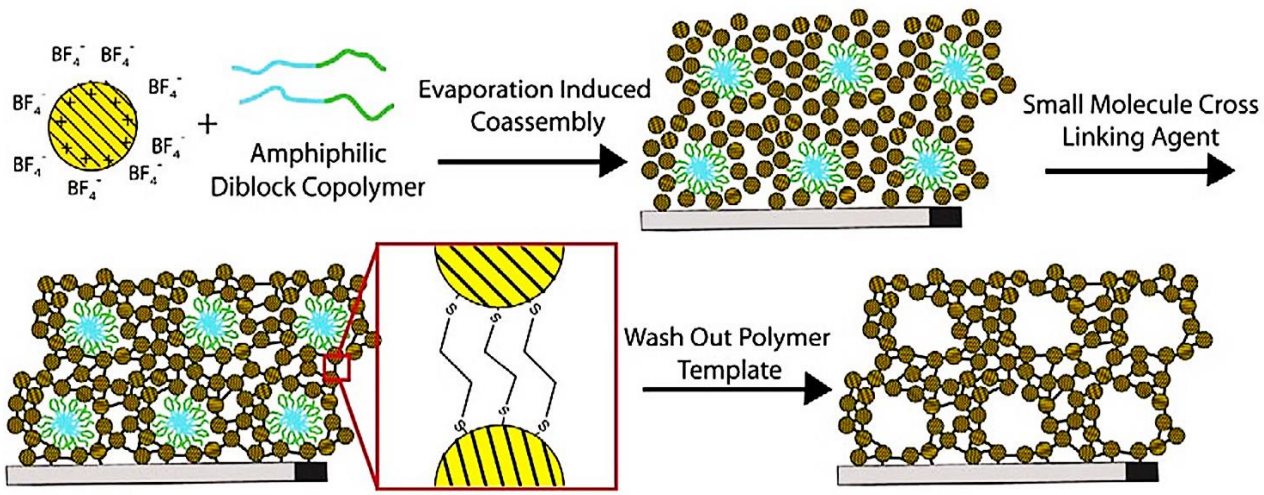

Figure 1-8: Schematic representation of the polymer templated assembly of metal-chalcogenide nanocrystals into porous thin films by a solution-phase cross-linking method. Ligand-stripped (BF_4^-–stabilized) NCs in a polar solvent (e.g. DMF) interact with the BCP template and form a hybrid organic/inorganic film via evaporation induced co-assembly. The NCs in the organized hybrid mesostructure are then cross-linked with the help of small cross-linking molecules (ethanedithiol is shown here) to form a robust NC-network. The final mesoporous film can be obtained after washing out the polymer template. Reprinted with permission from ref. [189]. Copyright © 2016, American Chemical Society.

The films produced by this method showed disordered but homogeneous porosity and optical properties very close to those of the starting NC building blocks, indicating that the initial NC size is preserved in the final structures. In this case, however, the small organic molecules used to cross-link the NCs coated the surface of the inorganic pore walls, thereby reducing the solvent-accessible pore volume of the films. [189] Also, the presence of an organic coating on the surface of NCs may have a detrimental effect on their chemical and catalytic reactivity. Generally, catalysis on solid surfaces occurs at surface active-sites that cause a reaction to take place through a specific reaction pathway at lower activation energy. To interact with the catalytically active sites, however, the reactants need first to reach the surface by diffusing through the boundary layer surrounding the solid catalyst. Therefore, the coating of the NCs' surface with such organic molecules, although may allow interparticle electronic coupling and electrical conductivity, it could block the surface active-sites and prevent their direct interaction with adsorbate molecules, thereby limiting catalytic activity. Therefore, the synthesis of 3D mesoporous architectures from chalcogenide NCs with controlled porosity and catalytically active structure is still a great challenge. Such nanomaterials are expected to have a key role in the development of new functional catalysts, which could help us to tackle current environmental and energy challenges.

1.5 The hydrogen issue and prospect of photocatalysis

1.5.1 Energy and sustainability challenges

It is an undeniable fact that Human activity fundamentally changes the characteristics of the planet on which we live, in a way that until recently could only happen in geological time or through cataclysmic natural events. Overconsumption of natural resources, large-scale pollution and gas emissions of our modern civilization are persistently altering the natural cycles, causing biologic changes and affecting the chemical composition of soil, water and atmosphere (**Figure 1-9**). [190] This human-dominated time period has been called by many scientists as the "Anthropocene". [191]

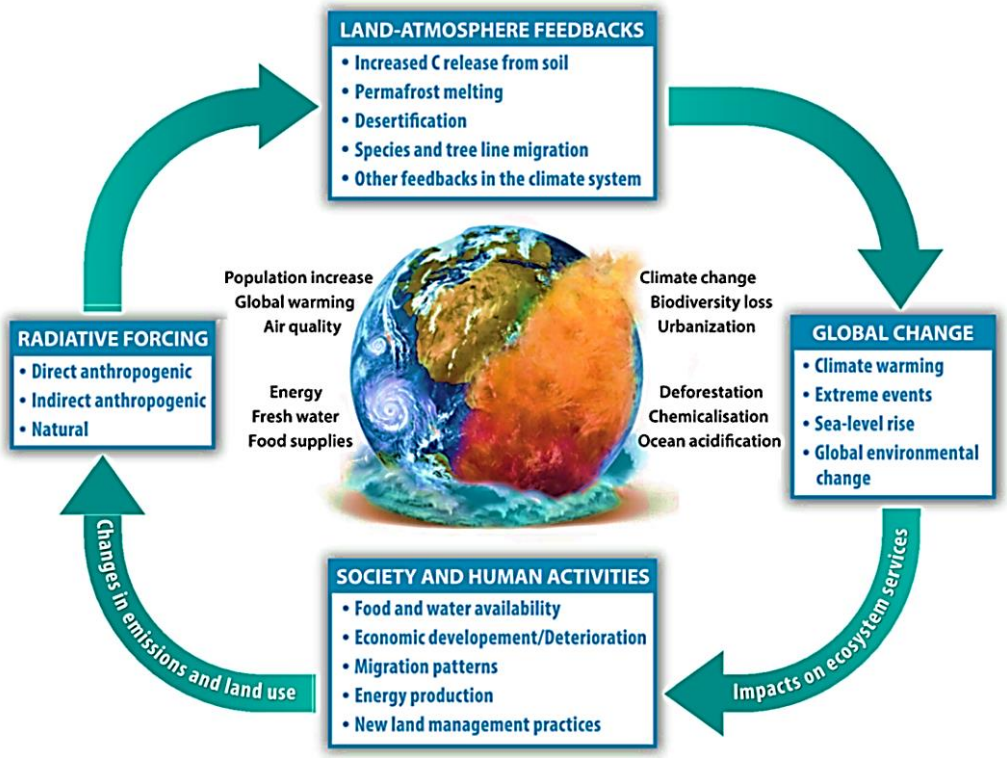

Figure 1-9: The land–water-atmosphere processes under anthropogenic global change. [190]

One of the primary attributes determining the Anthropocene is the linkage of human society with energy. For humans, the key not only of our survival through millennia but also for the realization of our well-being and the evolution of civilization has been inextricably linked to forms of energy that have enabled us to move beyond the energy outputs of our biophysical bodies. From the primitive fire regimes of the hunter-gatherer era to the pyro-technological advances of the agricultural revolution, the discovery and use of fossil fuels – the stored "ancient sunlight" [192] – have revolutionized once more the human way of being. Fossil fuels, comprising oil, coal and natural gas, are extremely attractive because they are highly concentrated, enabling large amounts of energy to

be stored in relatively small volumes that are practically easy to distribute. For these reasons, the utilization of fossil fuels has provided incredible benefits and opportunities to humankind during the last centuries (18th - 20th century). Indicators like life expectancy, population, economic growth and living standards increased dramatically after fossil fuels became the main source of energy [193], consequently creating the belief that they could provide humanity with unlimited potential for ever-expanding growth and living standards. However, although fossil fuels have offered such benefits, especially in the rich countries of the western world, the aforementioned belief has been totally disproved in the 21st century. As our population approaches 7.8 billion people (projecting at an estimated 9.8 billion by 2050) [194], the energy problem is becoming one of the most important issues [195] and mankind is now called upon to confront major challenges arising from the excessive exploitation of fossil fuels.

Currently, our civilization is supplied by more than 18 Terawatts (TW) of power (statistics for 2015) [196] and the demand is expected to nearly double by 2050. [197] This power is generated today from all sources of energy, namely fossil fuels and alternative sources (e.g., biofuels, solar, wind, hydropower and other), with the overall share of fossil fuel still reaching, however, around 81% [198]; a level that has remained stable for more than three decades despite the strong growth in renewables. So, from the energy generation perspective, our current society is still largely based on a carbon-fuel economy, which displays many weak points and challenges related to social, economic and environmental issues. First of all, fossil energy sources are nonrenewable. This means that the rapidly growing world population and the reasonable desire of less developed countries to increase their energy demand are now contributing to a faster depletion of the finite fossil fuel reserves, making them even more scarce and costly, exposing humanity to the risk of facing energy shortage soon. Moreover, a crucial challenge of our century is the pollution produced by the ever-increased use of carbon-fuels, which is considered one of the major causes of global warming and climate change. [199, 200] In particular, the current combustion rates of fossil fuels lead to vast emissions of trace greenhouse gases (GHGs) into the atmosphere (i.e. CO, CH_4, NO_x, SO_x, CO_2) and to huge production of other pollutants, including volatile organic compounds (VOCs), heavy metals and particulate matter, that cause adverse effects on human health [201]. Also, such pollutants are directly related to immense environmental problems, such as acid rain, ocean acidification and the enhanced greenhouse effect, associated with the accelerated global warming and climate change. [202, 203]

The increasing awareness for the energy and environmental risks posed from the extensive use of fossil fuels have triggered governments and scientists around the world to search for new energy strategies. [197, 204, 205] In this context, although there is not a unique solution to answer all the energy-related problems, it is clear that any successful energy strategy in the 21st century must include the fundamental principles of energy conservation (more rational use of energy) and the use of

renewable resources. In addition, this cannot be separated from social and economic issues, as a primary energy source must be also abundant, free of monopolies and available for all at a low cost. All these requirements can be grouped under the concept of sustainability [206] and only a solution that meets these requirements can be considered as truly sustainable. In this regard, technologies that use wind-, solar-, wave-, hydro-, tidal-, biomass-, geothermal power, etc., appear to be very attractive solutions as they account for renewable and CO_2 emission-free energy sources with acceptable efficiency. Nevertheless, despite their renewable potential, critical problems lie in their stochastic nature, high cost and construction limitations. With an intermittent and fluctuating energy supply and highly diffused spatial and temporal availability over the Earth, most of these renewable energy technologies either provide a poor ability to match the on-demand energy consumption, or have adverse impacts on local ecosystems and communities due to the necessity of capturing large areas in order to increase their energy supply. [207, 208] Therefore, in addition to the abundance and renewable nature of an energy source, it is essential from a sustainability viewpoint to be also easily storable, manageable, distributable and constant.

1.5.2 *Future fuel — Hydrogen*

Identifying and building a sustainable energy system is perhaps one of the most critical issues that today's society must face. Replacing our current fuels with a sustainable energy carrier is one of the key pieces in that system. From this perspective, hydrogen (H_2) fuel has attracted a great deal of attention as a promising alternative to fossil fuels that could contribute to tackling the current energy crisis and environmental pollution issues. [209] This conception stems from the fact that H_2 possess the highest energy content (120-142 MJ kg^{-1}) among the commonly used fuels [210] and because it has a clean reaction with oxygen, exhibiting a high specific enthalpy ($\Delta_f H^0$ ~ 242 kJ mol^{-1}) and yielding water vapor as only byproduct, according to the following equation (**eq.1**).

$$2H_2(g) + O_2(g) \rightarrow 2H_2O(g) + \text{energy } (\Delta_f H^0 = -241.8 \text{ kJ mol}^{-1} \text{ of } H_2) \qquad \textbf{(eq.1)}$$

Therefore, hydrogen provides the opportunity to be used as a non-polluting fuel either in internal combustion engines like other fossil fuels or in electrochemical cells (hydrogen fuel cells), which can convert the chemical potential energy of H_2 and O_2 directly into electrical work. [211] In addition to the high energy potential, hydrogen provides also the ability to be stored in gaseous, liquid or solid (e.g. in metal hydrides) form, enabling its efficient distribution and management over large distances. [212] However, although hydrogen is one of the most abundant elements on Earth (~0.9% by weight of the Earth's surface) [213], it does not occur in nature in the molecular form but is found mainly as

an element in chemical compounds (like water, biomass or hydrocarbons). So, unlike coal, hydrogen is not considered as a primary energy source itself, but rather as an “energy vector” or “energy carrier” (like electricity), with a capacity to store or deliver a great amount of energy.

Historically, after its identification as a distinct element by Henry Cavendish in 1766 [214], the idea of the potential use of hydrogen as fuel dates back to 1874 in the “Mysterious Island” by Jules Vern. Moreover, the concept of renewable hydrogen energy did not appear until 1923 (proposed by the geneticist J.B.S. Haldane [215]), while the perspective of a “hydrogen economy” was firstly coined by John Bockris in the 1970s [216]. Yet, a shift to a hydrogen economy is not a fictional break from the reality of mankind's energy history. On the contrary, it follows a rational trend that seems to accompany the evolution of energy sources over the centuries. Indeed, as shown in **Figure 1-10a**, there is a gradual transition over time, from solid-fuels (e.g., wood, coal) to liquid (e.g., petroleum) to gaseous fuels (e.g., propane, methane). [217] Surprisingly, as the energy studies during the past two decades reveal, the underlying process in all of these transitions is “decarbonization”, since the fuel molecules are progressively becoming smaller, leaner in carbon, and richer in hydrogen. [218, 219] As shown in **Figure 1-10b**, from wood to coal to oil, the ratio of hydrogen (H) to carbon (C) in the molecule of each successive source is increasing (H/C ratio: wood ~0.1 ; coal ~0.5–1 ; oil ~2), while the last major transition is to natural gas (methane), which has a ratio H/C = 4 and is currently the fastest-growing fossil fuel; as it is cleaner, lighter and burns more efficiently than gasoline. Consequently, the next logical step in this progression is expected to be hydrogen (**Figure 1-10a** and **c**), which has an H/C ratio of infinite and therefore could significantly contribute to a near-zero carbon economy.

Still, before the World can face a new hydrogen-based energy scenario, there are several scientific, technical, and socio-economic challenges that need to be overcome. In this respect, the most crucial step is the realization of efficient H_2 production processes. Ideally, such methods must take into account the long-term supply of the hydrogen source and the cost-effective production of hydrogen. In addition, although the use of hydrogen as fuel has a negligible contribution to environmental pollution, its indirect environmental “footprint” from its production and management methods may be significant. This means that to have an overall environmental impact close to zero, hydrogen must also be produced and managed in a clean, renewable and sustainable way. [220]

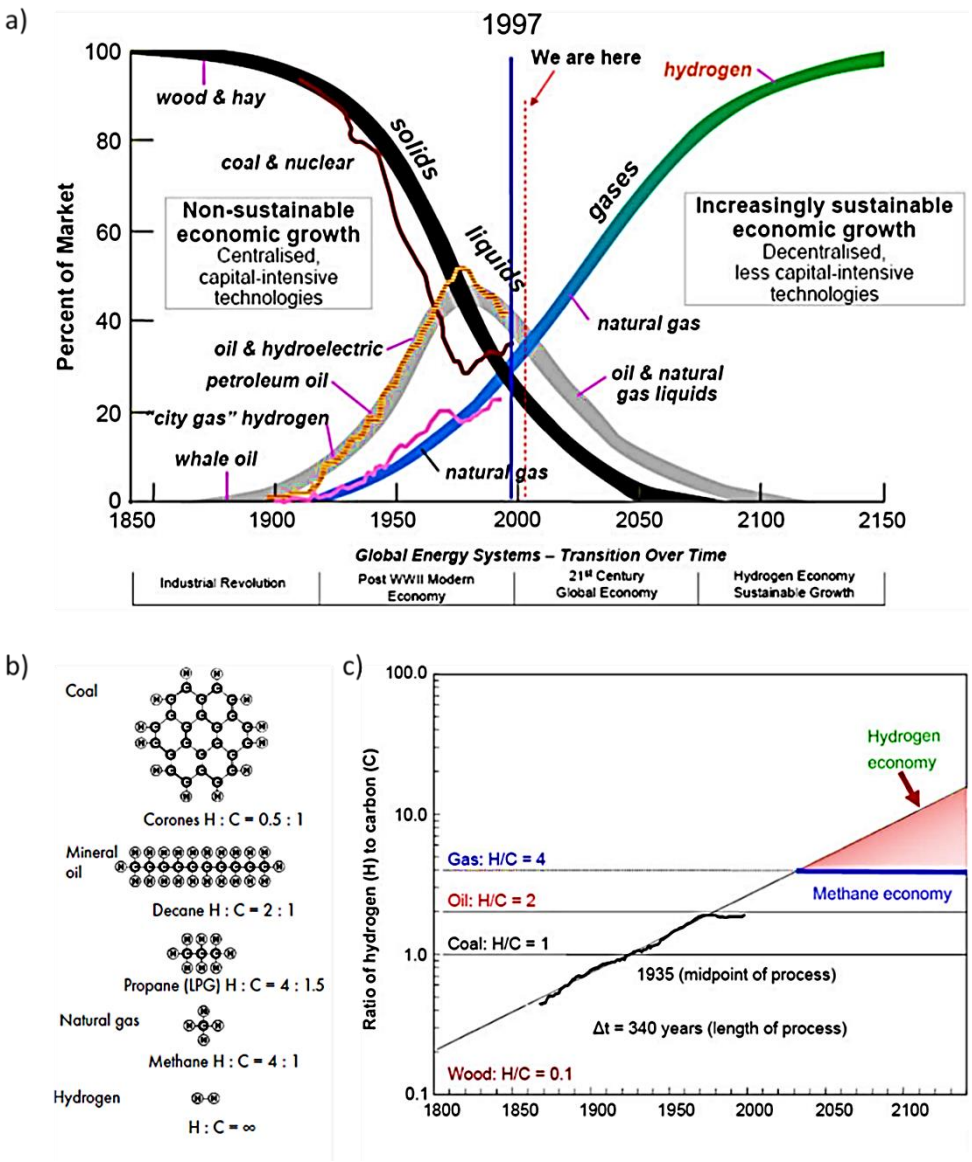

Figure 1-10: a) Global energy system transition 1850-2150; b) Atomic structure of typical molecules of coal, oil, and gas and their ratio of hydrogen (H) to carbon (C) atoms; (c) Evolution of the decarbonization process observed in the H/C ratio of the world fuel mix. [218, 219]

In relation to hydrogen production, H_2 can be produced in many ways from a broad spectrum of initial raw materials including carbon-based feedstocks (e.g. fossil fuels, biomass, wastes) as well as water as a primary hydrogen source. [221, 222] Nowadays, although H_2 is produced in large quantities for various industrial and commercial purposes (e.g., ammonia and fertilizer production, petrochemical refining industry, etc.), the vast majority of it (~96%) is currently obtained from fossil fuels: 48% from natural gas (methane); ~30% from oil; ~18% from coal, whereas other (renewable) sources like water and biomass had and still have a minimal contribution (**Figure 1-11**). [223, 224]

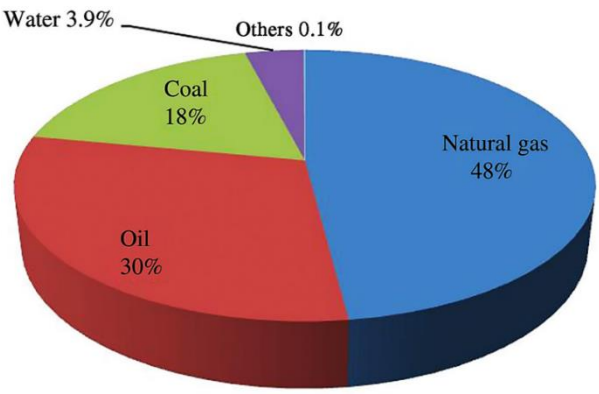

Figure 1-11: Feedstock used in the present global production of Hydrogen (data from Ref. [223]).

Regarding carbon-based sources, there are several industrial processes for producing H_2 from fossil fuel or biomass feedstocks, including steam methane reforming (SMR), auto-thermal reforming (ATR), fuel oil or gas partial oxidation (POX), coal or biomass gasification and other, as shown in **Figure 1-12**. [225] Among them, steam reforming of natural gas followed by the water-gas shift reaction (WGS) — which makes use of the produced CO in the first step to maximize H_2 production — is to date the most commonly and widely used industrial process, responsible for the majority of the world's production of H_2 and synthesis gas (Syngas, i.e., a mixture consisting primarily of H_2, CO and CO_2).[224]

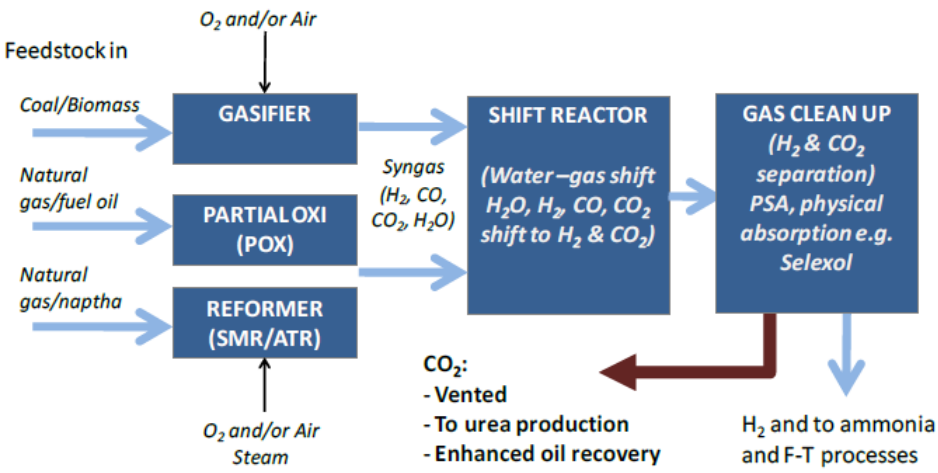

Figure 1-12: Generalized process flow for industrial hydrogen and syngas production. (SMR = Steam methane reforming; ATR = Auto thermal reforming; POX = Partial oxidation). [225]

However, these approaches cannot be considered sustainable on a long-term scale because of the non-renewable nature of fossil fuels and the limited supply of biomass for energy purposes (i.e., due to competition with food production), as well as the unavoidable production of GHGs (CO_2, CO, NO_x, SO_x) and other pollutants from the (thermo)chemical processing of carbon-based materials. In

addition, most of these methods require harsh operating conditions (e.g., high pressures and temperatures) and face several limitations associated with low efficiency and high demand for energy. Other approaches for H_2 generation such as enzymatic conversion of sugars [226, 227] or electrochemical, thermochemical and photobiological water-splitting [228-231] also suffer from low efficiencies or the need for high energy inputs in the form heat or electric power. Therefore, in order to achieve the benefits of a sustainable hydrogen economy, H_2 must be produced in a cost-effective way using renewable carbon-free resources, such as water, and a renewable energy source.

Owing to its abundance, solar energy is by far the most important renewable energy source. The incident solar power on the surface of the Earth is over 1.3×10^5 TW, which is roughly four orders of magnitude greater than the global energy consumption rate. [232] Thus, the utilization of only a small amount of this energy (i.e. around 0.01–0.03 %) could meet the current and future human energy demands. From this perspective, solar-activated routes combined with renewable water resources are presenting obvious advantages and have gained significant attention over the last years, as potentially sustainable methods for converting and storing the intermittent solar energy into solar fuels such as H_2. [233] For these processes, two general approaches are so far available:

a) “Indirect” solar-to-hydrogen production, which uses conventional solar panels combined with conventional electrolysers to run photovoltaic (PV)-assisted water electrolysis (PV-electrolysis systems).

b) “Direct” solar-to-hydrogen production, corresponding to a direct free-standing process of performing both solar-light harvesting and photochemical water-splitting at the same time (photoelectrochemical (PEC) cells or photocatalytic (PC) systems).

In brief, the indirect approaches benefit from the use of conventional and widely tested technologies, but they suffer from efficiency losses and high costs, owing to the additional step involved, that is, electricity has to be generated in photovoltaic cells first and then consumed in a subsequent electrolysis step in a separate device. [234] Instead, the direct solar-to-fuel methods are considered to perform “artificial photosynthesis” [235], a stand-alone process where solar energy can be directly captured, converted and stored as chemical energy in a product (e.g. H_2) with the help of suitable catalysts. Although this technology is currently less efficient than the indirect processes and still far from practical industrial application [233, 234], the simplicity of the direct exploitation of sunlight to generate hydrogen from natural renewable resources, such as water and/or aqueous biomass components/derivatives [236, 237], makes it an extremely promising future strategy for sustainable H_2 production.

1.5.3 *Sustainable hydrogen production — Photocatalysis*

Since the pioneering discovery of water photoelectrolysis in a photoelectrochemical water-splitting cell by Fujishima and Honda in 1972 [238] — using TiO_2 (photoanode) and Pt (cathode) electrodes to decompose water into H_2 and O_2 under ultraviolet irradiation — water splitting via heterogeneous artificial photosynthesis (i.e., using semiconducting solid-state materials instead of homogeneous molecular systems) [235, 239] has gained immense attention as a direct and effective way to convert and store solar energy into chemical fuel. As a result, during the past several decades significant research efforts have been undertaken to make the PEC approach more efficient and cost-effective. [240-243] Nonetheless, some years after the discovery and alongside the photoelectrolysis method, the direct photocatalysis route has also started to evolve. After the demonstration of direct photochemical water-splitting on a single platinized-TiO_2 photoelectrode in 1977 [244], Arthur Nozik formulated the concept of "photochemical diodes" [245] and Bard extended the principles of PEC cells to a design of a photocatalytic water-splitting system, which directly uses semiconductor particles suspended in water instead of fixed photoelectrodes immersed in aqueous electrolytes. [246-248]

Essentially, heterogeneous photocatalysis is defined as the process of catalysis induced by photo-irradiation in the presence of solid semiconductor materials serving as light-absorbing catalysts. Such photocatalytic materials are able to facilitate and accelerate photochemical reactions with the help of a light source (e.g. sunlight), without being consumed or transformed. On this basis, the use of dispersed photocatalyst particles for water-splitting, instead of fixed photoelectrodes, is the simplest method as shown in **Figure 1-13**. In general, the basic operating concept of photocatalytic H_2 production is simple. In a process that mimics photosynthesis, photocatalyst powders dispersed in water absorb solar energy and utilize it to promote photochemical redox reactions, converting water into H_2 and O_2 according to the basic water-splitting reaction (**eq. 2**).

$$\mathrm{H_2O}(l) \rightarrow \mathrm{H_2}(g) + \frac{1}{2}\mathrm{O_2}(g) \quad (\Delta G^o = +237\ \mathrm{kJ\ mol^{-1}\ of\ H_2}) \qquad \textbf{(eq. 2)}$$

As shown in the energy profile diagram in **Figure 1-13,** photocatalytic water-splitting converts solar energy into chemical energy through a thermodynamically unfavorable "uphill" reaction, with a large positive change in the Gibbs free energy ($\Delta G^0 = 237$ kJ mol^{-1}). This reaction resembles the endergonic ($\Delta G > 0$) photosynthetic processes by green plants, which is the reason why photocatalytic water-splitting is designated as an artificial-photosynthesis process. [249]

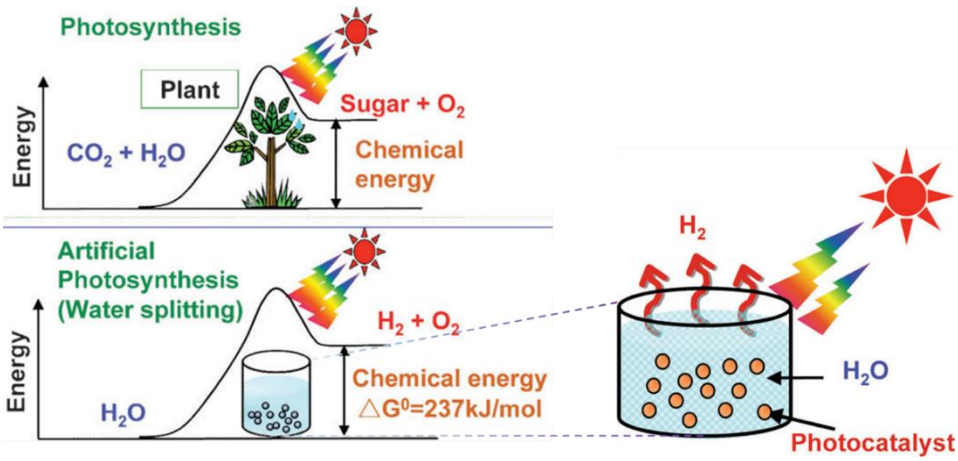

Figure 1-13: Photosynthesis by green plants and photocatalytic water splitting as artificial photosynthesis for solar H_2 production using powdered photocatalyst. Modified from ref. [237] with permission from the Royal Society of Chemistry.

The photocatalytic water-splitting approach shows generally the following advantages: (i) reasonable solar-to-hydrogen efficiency, (ii) low cost, (iii) the ability to achieve separate hydrogen and/or oxygen generation during reaction, and (iv) simple reactor systems suitable either for household or large-scale applications. [237, 250, 251] In this respect, recent techno-economical analyses between basic PEC and dispersed-photocatalyst systems have also indicated that the latter can be more economically advantageous for H_2 generation. [252, 253] Therefore, owing to the simplicity and lower cost of generating H_2 by using dispersed photocatalyst particles and water in simple reactor designs (without the need of fabricating complex electrodes and circuits), the photocatalytic water-splitting technology is expected to be a key solution to sustainable H_2 production in the future, if higher photocatalyst performance targets are met. [251, 254]

1.5.3.1 Fundamentals of semiconductor Photocatalysis

1.5.3.1.1 Band structure and electronic properties of semiconductors

For photocatalytic materials to be active, they must foremost possess the ability to absorb energy from light and use it to promote chemical reactions. For this purpose, solid semiconductor materials and their electronic band electronic structure play an essential role in the mechanism of photocatalysis. In general, solid materials are formed from a large number (*N*) of densely packed atoms, which interact intensely. These interactions produce the mechanical, thermal, electrical, magnetic and optical properties of solids. According to the band theory, when *N* atoms come close together to form a solid material, their atomic orbitals overlap and each electron energy state is perturbed by the electrons and nuclei of the adjacent atoms. [255] Since the Pauli exclusion principle dictates that it is impossible for two electrons to have the same quantum numbers in a molecule, the

N overlapping atomic orbitals split into *N* discrete molecular orbitals (MOs), each with a different energy level:

- *Bonding MOs*, which are lower in energy than the atomic orbitals that combine to produce them.
- *Antibonding MOs*, which are higher in energy than the atomic orbitals that combine to produce them.

So, as the number of atoms increases in the material, the number of MOs also increases and thus the energy levels are becoming denser. When the number of atoms becomes very large (N~10^{22}), such as in a macroscopic solid, the accumulated orbital energy levels are so closely spaced (in the order of 10^{-22} eV) that it is possible to consider them as a continuum of energetic states, forming what is termed an *energy band*. As an example**, Figure 1-14** shows the evolution in the electronic structure of a solid semiconductor from a distinct atomic orbital to the formation of broad energy bands, as the number N of atoms increases from unity (isolated atom) to solids of more than 2000 units. [256, 257]

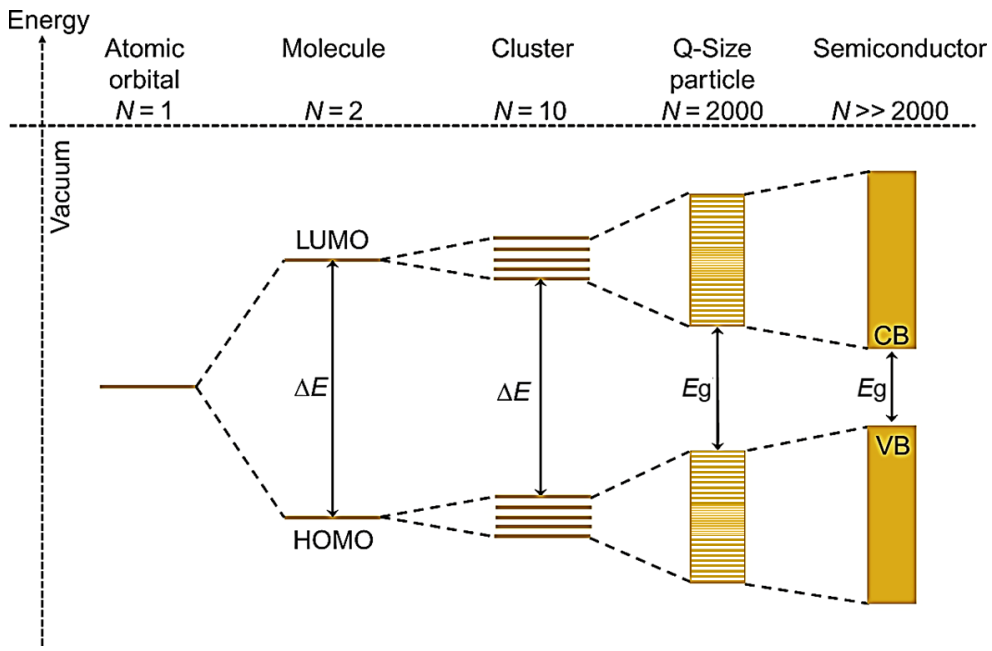

Figure 1-14: Schematic example of the change in the electronic structure of a solid semiconductor material by increasing the number of monomeric units (N). N=1 corresponds to a distinct atomic orbital. For N=2 the two atomic orbitals overlap to form two molecular orbitals of different energy (HOMO-LUMO). As N increases from 2 to more than 2000 units, orbitals in the material become denser and eventually form continuous energy bands composed of very closely-spaced orbitals. (HOMO = highest occupied molecular orbital, LUMO = lowest unoccupied molecular orbital, VB = valence band, CB = conduction band, and ΔE = energy gap, Eg = band gap). Adapted with permission from ref. [256]. Copyright © 1995, American Chemical Society.

Similar to isolated atoms where electrons are restricted to orbits with allowed energy levels, electrons in a solid are confined to a number of permitted energy bands, and forbidden from other regions. The inner energy bands are usually very narrow because the inner shell atomic orbitals

usually do not overlap to a significant degree. So, the formation of broad energy bands is mostly a feature of the atoms' outermost electron shells (valence electrons), which are the ones involved in chemical bonding and electrical conductivity. These uppermost energy bands are of particular importance, since they are the ones associated with the various chemical, electrical and optical properties of solid materials. Taking the energy of an electron in the vacuum level as a reference, the higher energy band is called the *conduction band* (CB) and the one of lower energy is known as the *valence band* (VB), as shown in **Figure 1-14**. At ground state conditions (i.e., absolute zero temperature, T = 0 K) the VB is usually filled with electrons (valence electrons), whereas the CB is empty. Note that the filling of the bands in a solid is governed by the Pauli exclusion principle, thus each band may contain maximum 2N electrons, where N is the number of energy levels in a band. As in molecular compounds the energy levels of interest are the highest occupied molecular orbitals "HOMO" and the lowest unoccupied molecular orbitals "LUMO" (see **Figure 1-14**), the highest (occupied) energy level of the VB is called the valence band maximum "VBM" (i.e., the top edge of the VB) and the lowest (unoccupied) energy level of the CB is the conduction band minimum "CBM" (i.e., the bottom edge of the CB). In terms of energy, between the valence and conduction band edges of semiconductors exists a forbidden region (energy gap, ΔE) called the *bandgap* (E_g), within which energy states do not exist (see **Figure 1-14)**. Moreover, the filling of bands is also correlated to another important quantity in the band theory called the *Fermi level* (E_F), or otherwise described as the chemical potential of materials and chemical species. The Fermi level is a theoretical thermodynamic quantity and is defined as the level of energy states that has a 50% probability of being occupied by electrons. Essentially, assuming a material with a single broad energy band (i.e., a continuum of energetic states without bandgap) the Fermi level represents the highest energy level in the solid that is filled at the ground state (T = 0 K), as all electronic energy levels below E_F are occupied and those above E_F are likely to be empty. [258]

The size of the bandgap as well as the degree of band-filling determine the electronic characteristics and consequently most of the physicochemical properties of solid materials. Considering electronic conduction (i.e., the flow of free electrons through the material), together E_F and E_g distinguish three basic classes of materials: conductors (or metals), semiconductors and insulators. Note that for an electron to become free, it must be promoted or excited into one of the empty and available energy states above E_F. [255] As shown in **Figure 1-15,** the Fermi level in conductors (like metals) is located within the VB, which is either partially filled or overlaps with the CB to form a single (E_g=0) partially filled band. So, electrons can easily become free to flow through the material when an electric field is applied (i.e., sufficiently small excitation), thus making metals excellent electron conductors. On the contrary, E_F of semiconductors and insulators lies in the forbidden gap (bandgap), the size of which is typically in the region of ~1–4 eV for a semiconductor

and above 4 eV for an insulator, and hence at T= 0 K both have a filled VB and a completely empty CB (see **Figure 1-15)**. This means that there is not enough energy to create free electrons, resulting in a non-conductive behavior for both insulators and semiconductors at absolute zero. However, unlike the prohibitively large E_g of insulators, the bandgap in semiconductors is relatively small and can be bridged by excited electrons of sufficient energy. [255] For the bandgap bridging, the excitation of electrons can be realized either thermally (thermal excitation) or optically (photoexcitation). Under thermal excitation, lattice vibrations from heat absorption (phonons) can provide enough energy to promote electrons from the filled VB to the empty CB; especially in narrow E_g semiconductors or the ones containing a large number of impurities (doped semiconductors). Similarly, under optical bandgap excitation, photons with energy greater than E_g (emitted by a light source) can be absorbed by the semiconductor and transfer their energy to the VB electrons, exciting them into the CB. In each case, the promotion of negatively charged electrons (e^-) to the CB leaves behind positively charged vacancies in the VB, which are referred to as *electron-holes* or simply *holes* (h^+). The holes can be viewed as positively charged quasiparticles (like positively charged free electrons) moving through the material and therefore, like electrons, are considered to be mobile charge-carriers. [255]

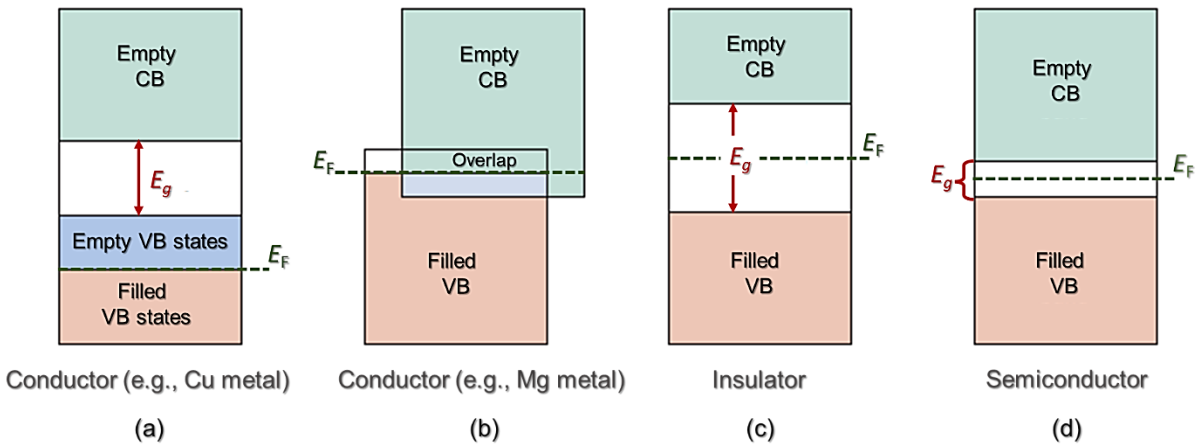

Figure 1-15: The various possible electron band structures in solids at T=0 K. (a) The electron band structure found in metals such as copper, in which E_F lies within the VB and so empty states are available above and adjacent to filled VB states. (b) The electron band structure of metals such as magnesium, where there is an overlap of filled and empty bands and E_F lies within the overlap region. (c) The electron band structure characteristic of insulators showing the E_F position within the bandgap. The filled VB is separated from the empty CB by a relatively large band gap (E_g > 4 eV). (d) The electron band structure found in semiconductors, which is the same as for insulators except that the band gap is relatively narrow (E_g < 4 eV). (VB = valence band, CB = conduction band, E_F = Fermi level, E_g = bandgap). Adapted with permission from ref. [255]. Copyright © 2018, John Wiley and Sons.

Besides bandgap excitation, a common strategy to create or increase mobile charge-carriers in semiconductors is to introduce impurities known as dopants. A pure, undoped semiconductor is called intrinsic (i.e., has equal number of electrons and holes), while a doped is referred to as an extrinsic semiconductor. In extrinsic semiconductors, doping can be realized either by the addition of a different element (e.g., with different number of valence electrons) into the semiconductor or by a deviation from stoichiometry in compound semiconductors (i.e., composed of two or more different chemical elements), thus generating more electron-rich or deficient states within their band structure. Typically, dopants create allowed energy states within the bandgap that lie close to the energy band corresponding to that particular dopant type (see **Figure 1-16**). When more electron deficient dopants (relative to the host material) create states near the VB, they can easily accept thermally excited (even at room temperature) VB electrons and thus produce more mobile holes than electrons (i.e., holes are the majority charge carriers and electrons the minority). These semiconductors are known as positive-charge doped (*p*-doped) or *p*-type and have a better hole conductivity. Conversely, when more electron-rich dopants create states near the CB, they can easily donate excited electrons to the CB and thus create more mobile electrons than holes. In this case they are referred to as negative-charge dopants and the semiconductors are called *n*-doped or *n*-type, which have better electron conductivity (electron conductors). For high doping densities, the introduction of intragap states can also modify the band structure and optical properties of the semiconductors, as shown in **Figure 1-16**. More specifically, because of the equal densities of electron and holes in intrinsic semiconductors, their E_F is placed at the mid-point of the bandgap (1/2 E_g). However, the presence of acceptor states (acceptor level) in *p*-type semiconductors increases the density of holes in the VB and shifts E_F closer to the VB, whereas donor states (donor level) in n-type semiconductors increase the density of electrons in the CB and cause E_F to shift just below the CB. In both cases, the new intragap states could narrow the effective bandgap of the semiconductors and create new optical-absorption transitions, consequently affecting their photoexcitation properties. [259]

It should be noted that the charge-carrier density connection with the Fermi level position, as described above, represents what is expected under equilibrium conditions. However, when a semiconductor is placed in close contact with another phase or undergoes excitation, the redistribution of charge-carries with the other phase (electrostatic interactions) or the electron excitation by the energy delivered could change the mobile charge-carrier equilibrium in the semiconductor, and thus affect the Fermi and band-edge energy levels. [260]

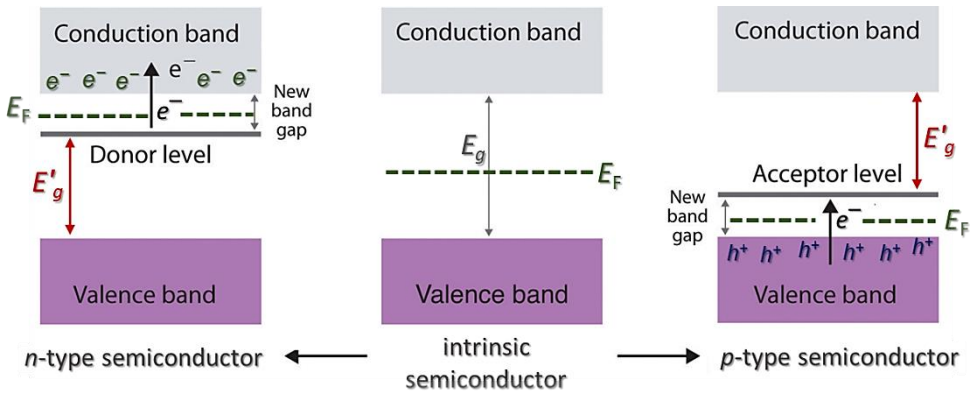

Figure 1-16: Electronic band structures of intrinsic and doped semiconductors. Intrinsic (undoped) semiconductors have equal densities of electrons and holes and E_F lies in the midpoint of E_g. Donor dopants in *n*-type semiconductors create filled states (donor lever) near the conduction band where electrons can be easily excited, thus increasing the electron density and causing E_F to shift below the conduction band. In *p*-type semiconductors acceptor dopants create electron-deficient states near the valence band (acceptor level) and electrons can be easily excited from the valence band to the acceptor level, thus increasing the density of holes and shifting E_F closer to the valence band. In both doping cases, the effective band gap (E'_g) is decreased, and the electrical conductivity at a given temperature increases significantly.

1.5.3.1.2 Interfacial Interactions in Semiconductor Junctions

One of the key features of semiconductors is the ability to develop a built-in electric field when they come in close contact with another phase (junction). The presence of an internal electric field can facilitate the separation and transfer of charge-carriers, by allowing for example one carrier (electrons or holes) to flow in one direction and the other to move in the opposite direction. In general, junctions are formed between a semiconductor and a second phase when an initial difference in Fermi levels (or chemical potential of electrons) exists between the two phases, such that majority charge-carriers are transferred to the second phase to equalize the Fermi levels and establish a thermo-dynamic equilibrium. Since photocatalysis involves (photo)electrochemical interface interactions between solid semiconductor photocatalysts and water (or aqueous electrolytes), the semiconductor/electrolyte junction is a fundamental aspect of heterogeneous photocatalysis.

To better describe the energetics of these electrochemical interactions, it is useful to utilize first the concepts of work function, electron affinity and ionization energy. The work function (Φ) is defined as the energy difference (usually measured in eV) between the Fermi level and the electrostatic potential energy in the vacuum level (E_{vac}). Note that the electrochemical potential level of the electrolyte (E_{redox}) is generally considered analogous to the Fermi level (E_F) of the semiconductor. The vacuum is taken as a reference of zero energy value (E_{vac} = 0 eV), since the kinetic energy of free electrons in vacuum is zero. Accordingly, the electron affinity (χ) is defined as the energy difference (in eV) between the electrochemical potential level of the conduction band edge

(E_C) and the electrostatic level just outside the semiconductor (E_{vac}), whereas the ionization energy (E_i) refers to the energy potential difference (in eV) between E_{vac} and the electrochemical potential level of the valence band edge (E_V). [261] Because in electrochemical systems the values of the E_F, E_{redox}, E_C and E_V levels are usually measured as redox potentials (in V) with reference to the normal hydrogen electrode (NHE), the following relationship (**eq. 3**) is used to convert the NHE scale (in V) to the absolute vacuum energy scale:

$$E_{[abs]} = -4.5\ \text{eV} - e_0 V_{[NHE]} \qquad \text{(eq. 3)}$$

where, $E_{[abs]}$ is the corresponding energy value vs the vacuum scale (in eV), $V_{[NHE]}$ is the respective redox potential vs the NHE scale (in V), e_0 is the elementary electronic charge and –4.5 eV is the work function (or Fermi level) of the NHE with respect to vacuum.

So, considering for simplicity an *n*-type semiconductor immersed in an electrolyte solution (e.g., water), if the initial semiconductor Fermi level (E_F) lies above the electrochemical potential (E_{redox}) of the electrolyte (or accordingly $\Phi_S < \Phi_{redox}$) then equilibration of the two electrochemical potentials ($E_F = E_{redox}$) occurs by transfer of electrons from the semiconductor to the electrolyte. This transfer of electrons leaves behind positively charged immobile donor-states in the semiconductor near the surface, which are compensated by negative charges that accumulate at the surface outer-layer, thus forming an electrical double-layer in the semiconductor. The positive charge built-up effect inside the semiconductor is most pronounced at a region with a width (W) ~100-1000 nm near the surface, called the *space-charge region* or the *space-charge layer* — also called a *depletion layer* since the region is depleted of majority charge-carriers — while at a distance sufficiently far away from the surface (i.e., in the bulk semiconductor) the effect diminishes. [260] In general, due to the oppositely charged regions developed in the double-layer, a built-in electric field is formed inside the semiconductor that causes a shift in the electrostatic potential and thus a "deformation" of the band structure across the space charge region. This deformation is manifested by a bending of the valence and conduction band levels denoted as *band bending*. [262, 263] Since the valence and conduction band levels are pinned at the surface of the semiconductor (due to interactions with the electrolyte), the corresponding potential drop between the positively charged depletion region and the negatively charged surface (induced by the adsorption of anions from the electrolyte or/and the trapping of electrons at surface-states) is reflected here in an upward bending of the bands towards the surface (*upward band bending*), as shown in **Figure 1-17a**. In this case, the upward band bending forms a potential barrier at the interface (Φ_{SC}) that prevents the further flow of electrons from the semiconductor into the electrolyte, which is often referred to as "pseudo" *Schottky barrier*. [260, 264] At equilibrium, the direction of the formed electric field at the interface (i.e., from the semiconductor

to the electrolyte) is such that the minority carriers (holes in this case) are driven to the semiconductor surface, while electrons move to the opposite direction away from the surface and towards the bulk.

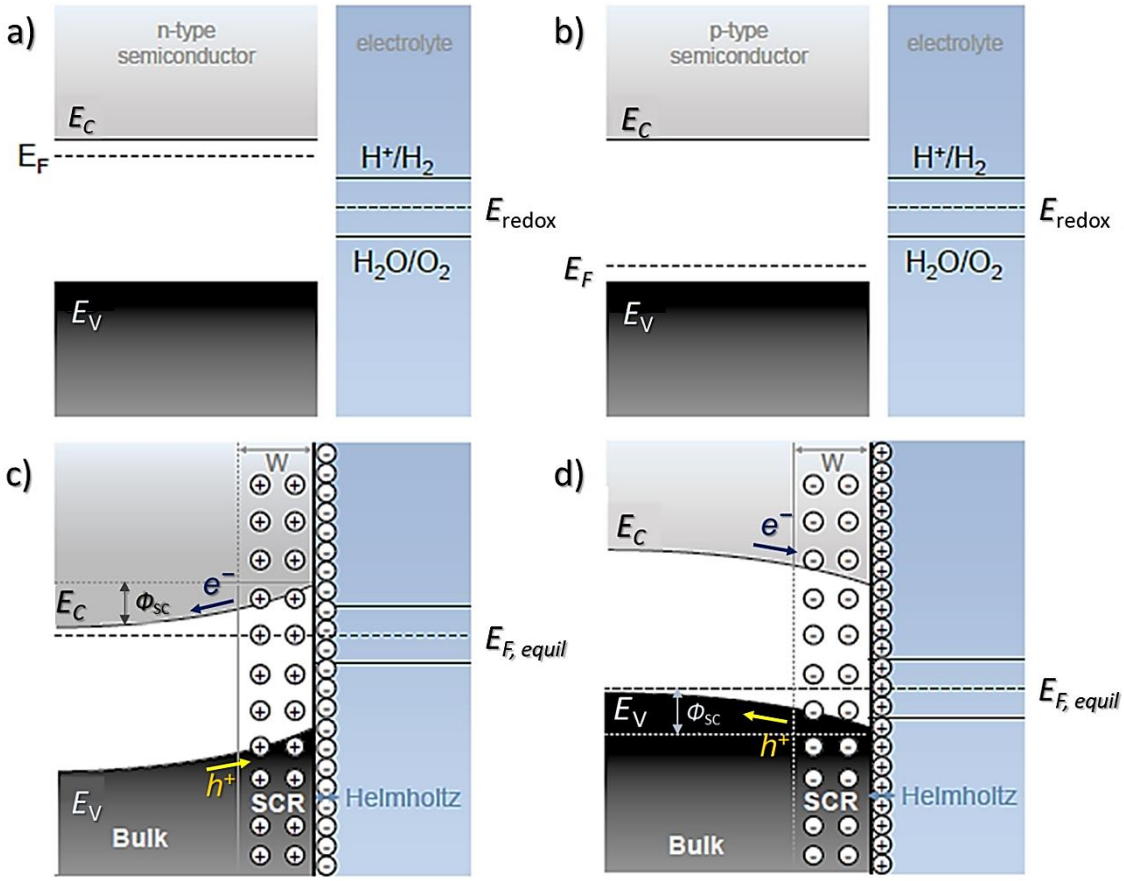

Figure 1-17: Semiconductor/electrolyte junction formation for n-type and p-type semiconductors. a) and b) represent an *n*- and p-type semiconductor before contact with the electrolyte, showing the different initial positions between the respective semiconductor Fermi level (E_F) and the electrochemical potential (E_{redox}) of the electrolyte. c) and d) shows the different charge distribution outcomes at the interface, after equilibration of the Fermi levels ($E_{F, equil}$). In the n-type semiconductor the valence and conduction band levels bend upwards across the space charge region (SCR), while in the p-type semiconductor a downward band bending is observed, both forming a potential barrier (Φ_{SC}) at the interface. Reproduced from ref. [265]

Note that the inverse but analogous situation occurs with p-type semiconductors having an initial E_F usually below E_{redox} (or accordingly $\Phi_S > \Phi_{redox}$), and so electrons are transferred from the electrolyte into the semiconductor. The space charge region is then associated with a negative charge, compensated by a positive charge at the surface, thus causing a downward band bending towards the surface (**Figure 1-17b**) and forming a potential barrier (Φ_{SC}) against further electron transfer from the electrolyte. For p-type semiconductors, the space charge region is also depleted of majority charge-carriers (i.e., holes) upon contact with the electrolyte and hence it is also referred to as a depletion layer. Also, the direction of the internal electric field in this case is from the electrolyte to

the semiconductor, thus driving electrons to the surface whereas holes flow towards the bulk semiconductor.

On the other hand, a charged double layer is also formed in the electrolyte side of the interface, corresponding to the *Helmholtz layer* (HL), which is followed by the diffuse *Gouy-Chapman layer*. The Helmholtz double layer is considered to be composed of two planar sheets of charges: (i) the inner Helmholtz plane (IHP) close to the semiconductor surface that consisted of charged surface-states and adsorbed ions and/or solvent dipole molecules from the electrolyte, and ii) the outer Helmholtz plane (OHP), a layer of solvated electrolyte ions of opposite sign to the IHP that are more loosely bound, see **Figure 1-18**. In electrolytes with high ionic strength, the dielectric Helmholtz layer is considered to be compact (also called Stern layer) with a width of a few Angstroms (10–100 Å), and creates a surface charge at the semiconductor of opposite sign to the charge induced within the semiconductor space charge region. In electrolytes of low ionic strength, there may be insufficient ions available at the OHP to compensate all adsorbed charges at the surface and the excess charge is then compensated by solvated ions, forming a diffuse ion layer that extends much beyond the OHP, the so-called Gouy-Chapman layer. [245, 260, 266, 267] Due to the charge distribution between the specifically adsorbed ions on the semiconductor surface layer (IHP) and the counter ions in OHP, a potential drop may also occur across the Helmholtz double layer. For many semiconductors in aqueous electrolytes, H^+ and OH^- are the dominant adsorbed species at the surface and therefore the Helmholtz potential drop (V_H) changes systematically with pH; usually by 59 mV per unit pH at 25 °C (Nernstian response) according to the relationship in **eq. 4**. [245, 260, 266] In **eq. 4** the term PZC refers to the point of zero charge of the semiconductor surface, which in aqueous electrolytes corresponds to the pH where $V_H = 0$.

$$\mathrm{V_H\ [V]} = 0.059\ (\mathrm{PZC} - \mathrm{pH}) \qquad \text{(eq. 4)}$$

Depending on the pH and composition of the electrolyte solution, the Helmholtz potential drop markedly affects the semiconductor band-edge positions at the interface (i.e., positive or negative shift in the potential of the E_C and E_V levels) and therefore affects the extent of band bending induced in the semiconductor space-charge region. As shown in the band diagram in **Figure 1-18**, V_H has an additional effect to the a priori work function difference of the two phases (i.e., $\Delta\Phi_{SC} = \Phi_S - \Phi_{redox}$). [245, 260] Taking the NHE energy scale as a reference, the total potential drop in the semiconductor (V_{BB}) after equilibrium with the electrolyte is given by the relationship:

$$\mathrm{V_{BB}\ [NHE]} = -(\Delta\Phi_{SC} + \mathrm{V_H}) = (\Phi_{redox} - 4.5) - (\Phi_S - 4.5 + \mathrm{V_H}) = \mathrm{V_{redox}} - \mathrm{V_{FB}} \qquad \text{(eq. 5)}$$

where V_{BB} is the total potential drop (total band bending) in the semiconductor (in V *vs* NHE), $\Delta\Phi_{SC}$ is the work function difference between the semiconductor and the electrolyte ($\Delta\Phi_{SC} = \Phi_S - \Phi_{redox}$), V_H is the potential drop across the Helmholtz layer (in V *vs* NHE), 4.5 is the NHE scale factor relating

the H^+/H_2 redox potential to vacuum, the part "Φ_{redox} - 4.5" refers to the potential (in V *vs* NHE) of the redox couple in the electrolyte (V_{redox}) and the part "$\Phi_S - 4.5 + V_H$" corresponds to the so-called *flat-band potential* (V_{FB}).

The flat-band potential is the measured potential with respect to a reference electrode, at which the semiconductor bands are flat (zero space-charge condition). [245] Hence, the effect of the Helmholtz layer on the total potential drop in the semiconductor is related within the flat-band potential, according to the relationship:

$$V_{FB}\,[\mathrm{NHE}] = (\Phi_S - 4.5 + V_H) \qquad \text{(eq. 6)}$$

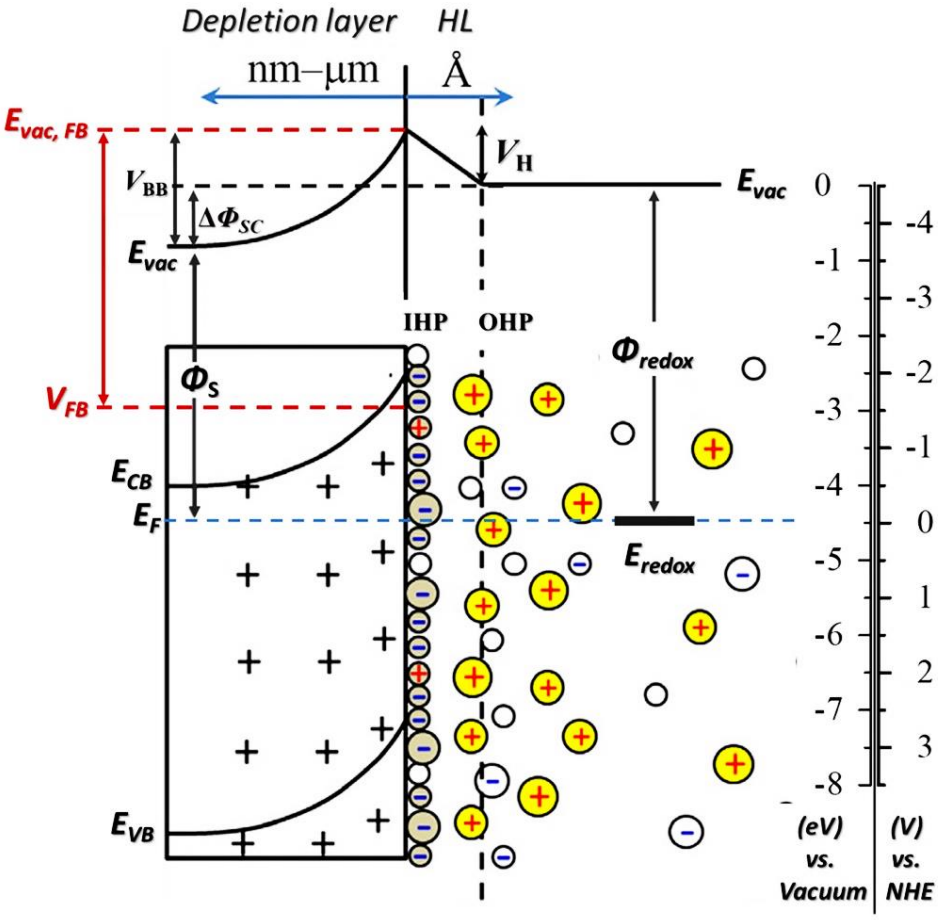

Figure 1-18: Band diagram for an n-type semiconductor/electrolyte junction under equilibrium, illustrating the Helmholtz layer (HL) and the Depletion layer formed at the junction interface. IHP and OHP are the inner and outer Helmholtz planes respectively. The Helmholtz layer potential drop (V_H), total band bending (V_{BB}), and the work function difference ($\Delta\Phi_{SC}$) of the semiconductor (Φ_S) and electrolyte (Φ_{redox}) with respect to the vacuum level (E_{vac}) are also shown. Note that E_{vac} follows the potential changes that occur in the system. The red dashed lines correspond to the vacuum level at the flat-band situation ($E_{vac,\,FB}$) and to the position of the flat-band potential (V_{FB}). Modified with permission from ref.[260]. Copyright © 2017, Elsevier Inc. All rights reserved.

Essentially, the measured flat-band potential denotes the initial position of the semiconductor Fermi level at the flat band situation (i.e., with zero band bending). This means that in the case of an n-type doped semiconductor, V_{FB} will be slightly below the conduction band edge and hence it can accurately reflect the position of the CB edge (or the position of the VB edge in the case of a p-type semiconductor) at a given set of conditions (solution pH, redox concentration, etc.). [266] From **eqs. 4** and **6** it is clear that the V_{FB} will also change systematically with pH, following the same trend as V_H. [245, 260, 266] Note that the aforementioned Nernstian dependence of V_{FB} with pH (i.e., 59 mV per unit pH) is accurate mostly for metal-oxide semiconductors, but other non-oxide semiconductors (such as chalcogenides) may have a different response. Also, for semiconductors with moderate doping level, V_H is usually negligible compared to $\Delta\Phi_{SC}$, and hence has an insignificant effect on the V_{FB} position and the total band bending (i.e., $V_{BB} \sim \Delta\Phi_{SC}$). But for higher doping levels (e.g., 10^{19} cm^{-3}) or high density of surface-states (i.e., localized electronic states at the semiconductor surface with energy levels that differ significantly from the allowed levels of the bulk), the Helmholtz potential drop can be considerable ($V_H \sim 0.1 - 0.5$ V) and should be taken into account. [268, 269] In this respect, if the density of surface-states is relatively high (> 10^{15} cm^{-2}) compared to that of the bulk dopant states ($\sim 10^8 - 10^{12}$ cm^{-2}), the Fermi level of the semiconductor becomes almost independent from the allowed energy levels of the bulk and is essentially "pinned" at the energy level of the surface-states (see **Figure A-1** in the Appendix). This situation is known as *Fermi level pinning*. [263, 269] This shift of the Fermi level to the level of the surface-states can affect the charge equilibrium in the semiconductor, by the transfer of majority charge-carriers from the bulk to the surface-states, thus inducing the formation of a space charge layer and a potential drop (band bending) near the surface (i.e., *surface-state-induced band bending*). The result is a semiconductor with an amount of band bending (and potential barrier Φ_{SC}) that is determined by the work function of the surface-state layer. Therefore, in the case of large concentration of surface-states, the semiconductor Fermi level will be pinned at the level of the surface-states and the contact of the semiconductor surface with an electrolyte will not alter the amount of band bending. In this case, the additional potential drop from the semiconductor/electrolyte equilibration will occur exclusively across the Helmholtz layer, reflected in a shift (negative or positive) of the band edge potentials while band bending remains fixed. [269] In addition, this situation can also influence the measured flat-band potential, which due to Fermi level pinning would correspond to the potential of the charged surface-states rather than the real Fermi level at the flat-band situation, resulting in an inaccurate estimation of the actual semiconductor band-edge positions. [270, 271]

Considering the contact phase, other important cases besides the semiconductor/electrolyte junction include the metal/semiconductor (M-S) junction and the semiconductor/semiconductor (S-S) heterojunctions. In all these cases, the same principles as with the semiconductor/electrolyte

junction — in the formation of an electric field, space-charge layer and potential barrier at the interface — apply, and thus will not be discussed here in detail for each separate case. Nevertheless, one of the most important features of M-S junctions is that the Fermi level of the semiconductor will be "pinned" to that of the metal due to the much higher electron density in metals (see **Figure A-2** in the Appendix). For a given semiconductor-metal combination, this creates a constant potential barrier (Schottky barrier) at the junction interface [263], irrespective of whether the junction is in contact with an electrolyte or not. Consequently, when a metal/semiconductor Schottky junction is in contact with an electrolyte, the potential barrier and band-bending in the semiconductor remain constant (fixed band-bending), while the additional potential drop due to charge equilibration with the electrolyte will occur across the Helmholtz layer at the metal/electrolyte interface. [272] This situation also causes discrepancies in the estimation of the actual semiconductor band-edge positions from flat-band potential measurements, because the apparent V_{FB} measured in this case will be the Fermi level of the contact metal. In typical M-S Schottky junctions, the electric field formed at the interface facilitates charge-carrier separation, where minority carries are transferred to the interface and majority carries are driven towards the bulk region of the semiconductor. However, this charge-carrier separation condition is considered to be slightly different for small semiconductor particles in contact with nanosized metal particles, where it has been observed that electrons can be injected into the metal nanoparticles (which act as electron "sinks") and holes remain in the semiconductor and transfer at the surface. [273-275]

In the case of S-S heterojunctions, numerous different semiconductor contact situations can be inferred. Generally, heterojunctions can be formed by dissimilar crystalline phases of the same chemical composition (with different bandgaps), or by semiconductors with different chemical composition (heterostructures). Additionally, depending on the type of semiconductor (p-type or n-type), the S-S heterojunctions can be categorized into p-p, n-n, and p-n type (or widely known as p-n junctions), while according to the alignment of their band-edge positions at the interface there are three different types of heterojunctions (see **Figure A-3** in the Appendix): Type-I (straddling gap), Type-II (staggered gap) and Type-III (broken gap). Moreover, based on the three different types of band alignment and the various situations of different E_F positions between the semiconductors, S-S heterojunctions may be further categorized into five main types (see **Figure A-4** in the Appendix), each with particular band structure and charge-separation characteristics. [276] Nevertheless, the common trait in all of them is the formation of a space-charge layer in each side of the junction, with band bending occurring in each semiconductor. This causes an internal electric field to form at the junction interface, in which the flow of charge-carriers is facilitated in one direction but hindered in another direction.

Overall, understanding and manipulating band bending in semiconductor junctions offer the ability to control the separation and transfer of charge-carriers from the semiconductor to the electrolyte or surface absorbed species, and thus can provide new opportunities for the better design and utilization of semiconductor-based materials, particularly for applications involving electrochemical processes such as catalysis and photocatalysis.

1.5.3.1.3 Basic mechanism of heterogenous photocatalysis

The fundamental working principle for semiconductor photocatalysis is generally based on the generation of photoexcited charge-carriers. In this regard, the band gap (E_g) of a semiconductor plays a crucial role in photocatalysis, since the energy of the incident photons from the light source (hv) must be equal or higher than E_g for the necessary excitation and activation of the photocatalyst to take place. More specifically, the basic processes of photocatalysis on a semiconductor particle, which are essentially similar to a photoelectrochemical (PEC) cell, can be described in five main steps as shown in **Figure 1-19**: (I) light absorption, (II) charge formation, (III) charge separation and migration, (IV) charge recombination and (V) redox reactions. [277]

The first two steps (I and II) in **Figure 1-19** involve the generation of photoexcited charge-carriers by light absorption from the semiconductor photocatalyst (SC). If the condition of the photon-energy (hv) ≥ band-gap (E_g) is reached, a photon is absorbed by the SC (step I) and an electron (e^-) is excited from the VB into the CB leaving behind a positive charged hole (h^+) in the VB, thus resulting in the formation of excited electron/hole pairs (e^-/h^+) called excitons (step II). This femtosecond (10^{-15} s) charge-carrier formation process is followed by relaxation of the electron and hole to lower excited states (radiationless internal conversion), namely to the bottom of the CB (CBM) and to the top of the VB (VBM) respectively (see **Figure 1-20b**), on a similar timescale (10^{-14} to 10^{-12} s). [262, 278] Depending on the degree of band-bending and electrostatic interactions, as a result of the contact interfaces formed between the SC and other phases (solution, metal or other semiconductors as described previously), the photoexcited charge-carriers can separate and migrate to the photocatalyst surface (step III in **Figure 1-19**) on a ps to µs timescale (10^{-12} to 10^{-6} s). The photoexcited e^-/h^+ pairs can then be consumed by participating in redox reactions (step V in **Figure 1-19**) with reactants adsorbed on the surface active-sites, on timescales usually longer than microseconds (>10^{-6} s) according to **Figure 1-20a.** At the surface, the SC can donate photogenerated electrons to reduce an electron acceptor (reduction pathway A in **Figure 1-19**), while a hole can combine with an electron from a donor species adsorbed on the surface, and thus cause oxidation of the donor reactants (oxidation pathway D in **Figure 1-19**). The probability and rate of the charge-

transfer processes for electrons and holes depends greatly on the respective positions of the SC conduction and valence band edges and the redox potential levels of the adsorbed species.

However, not all the photogenerated charge-carriers can be collected and finally contribute to chemical reactions. In fact, a portion of the photogenerated electron and holes is subjected to recombination (step IV in **Figure 1-19)** in the bulk due to poor e^-/h^+ separation or at the photocatalyst surface where trapped e^- and h^+ at surface-states may accelerate their recombination. Recombination dissipates the energy of the photoexcited charge-carries either thermally by creation of heat (non-radiative recombination) or optically by spontaneous photon emission (radiative recombination or photoluminescence). [279] Therefore, charge recombination is considered to be a major loss of the photoexcited charge-carriers and a critical factor that hinders the photocatalytic efficiency of semiconductor photocatalysts. Usually, charge-carrier recombination occurs at an average time-scale on the order of 10^{-9} s (see **Figure 1-20b)**, while the charge-transfer and redox reaction processes occur in similar and longer time scales ranging from ps to ms, as shown in **Figure 1-20a**. [35, 262, 277, 280]

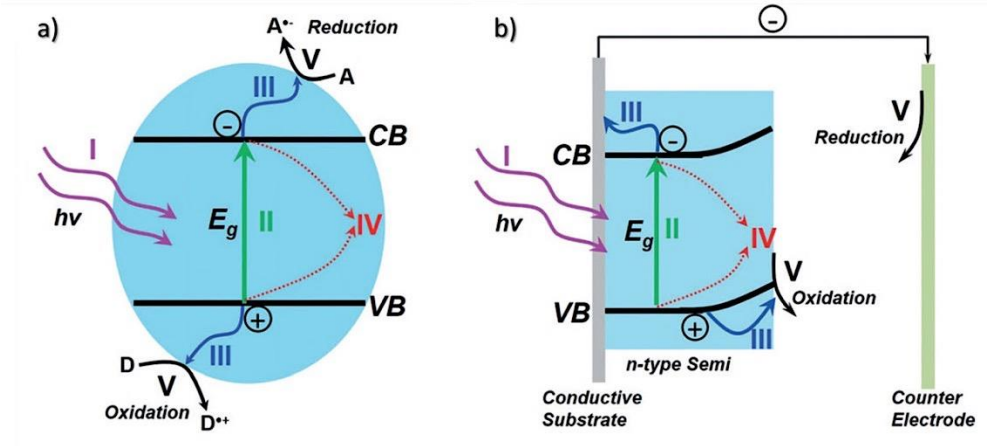

Figure 1-19: Scheme illustration of a particulate photocatalyst. Note: (I) light absorption, (II) charge separation, (III) charge migration, (IV) charge recombination and (V) redox reaction. CB = conduction band, VB = valence band, Eg = band gap, A=acceptor, and D = donor. Reproduced from Ref. [277] with permission from the Royal Society of Chemistry.

Over the last decades, heterogeneous photocatalysis has appeared as an emerging and promising "advanced oxidation process" (AOP), with more than 2000 recent publications on the subject. [281] Moreover, it has become increasingly attractive as an efficient method for green-chemistry processes in selective and synthetically useful transformations of specific organic compounds and in emerging AOPs. [280, 282-288] In most of these studies, the usual electron acceptor participating in the reduction reaction pathway is oxygen, which is usually present as dissolved O_2 in an aerated reaction mixture. It is generally admitted that photogenerated electrons can reduce molecular oxygen to

superoxide anion radical ($O_2^{\bullet-}$), which can be subsequently transformed into other chemical species, such as $HO_2^{\bullet}$, HO_2^{-}, H_2O_2, and possibly $HO^{\bullet}$ radicals. These activated oxygen species may take part in oxidation of electron-donor reactants (i.e., organic or inorganic compounds). On the other hand, photogenerated holes can also oxidize the electron donor (also referred to as the "*hole scavenger*"), either via the formation of reactive species, such as surface-bound hydroxyl radicals ($HO^{\bullet}$), or through direct reaction with the adsorbed molecules. Together, these reactions can ultimately result in either complete degradation of organic compounds (e.g., photo-mineralization of pollutants) or to more selective oxidation and transformation of the target electron-donor molecules, depending on a variety of thermodynamic and kinetic factors that govern these charge-transfer and redox reaction processes.

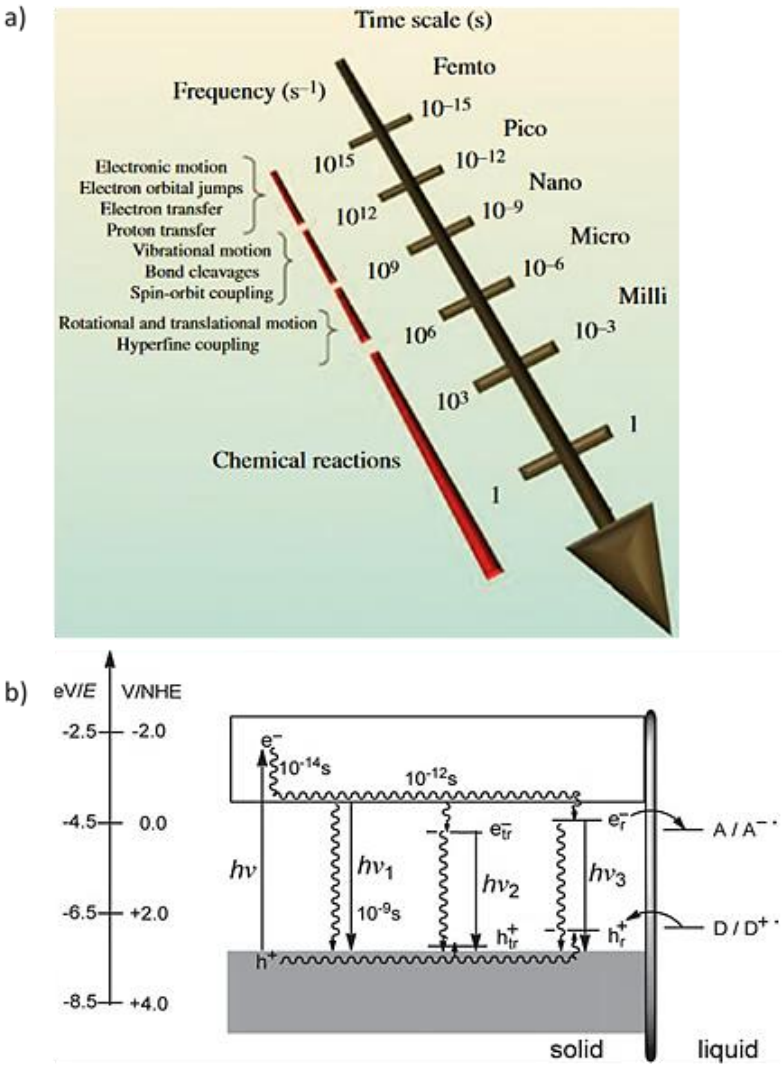

Figure 1-20: a) Timescales for photoinduced reaction steps; b) Primary photo-processes at the semiconductor/liquid interface (thick vertical bar). Note: After photoexcitation, radiative and nonradiative recombination can occur, depicted by straight and waved lines respectively. Electrons and holes gain stability when moving down and up in this scheme, respectively. The depicted band positions apply for TiO_2 in contact with water at pH 7. The electron energy (eV) is given relative to the vacuum level (0 eV); e^-_{tr} = electron trap, h^+_{tr} = hole trap, e^-_r = reactive electron surface site, h^+_r = reactive hole surface site. Reproduced with permission from Ref. [35, 280]. Copyright © John Wiley & Sons.

1.5.3.2 Photocatalytic water-splitting: Requirements and challenges

From a thermodynamic point of view, based on the Gibbs free energy change of reactions, the aforementioned photooxidation processes (i.e., degradation of organic pollutants or photooxidation of organic compounds) are generally considered to be "downhill" reactions ($\Delta G^0 < 0$). This means that these reactions may proceed irreversibly, once the proper amount of activation energy is delivered. On the other hand, as mentioned previously, the chemical dissociation of water into H_2 and O_2 is classified as a thermodynamically "uphill" reaction ($\Delta G^0 > 0$). This means that water-splitting requires a high energy input to meet the Gibbs free energy of the reaction, which is needed to rearrange the valence electrons and make the formation of H_2 and O_2 possible. In this respect, the full water-splitting reaction is an energy demanding multi-electron process, where two hydrogen molecules and one oxygen molecule (in 2:1 stoichiometric ratio) are produced, as follows:

$$2H_2O(l) \rightarrow O_2(g) + 2H_2(g) \qquad \begin{matrix} (\Delta G^o = 474 \text{ kJ mol}^{-1} \text{ of } O_2) \text{ or} \\ (\Delta G^o = 237 \text{ kJ mol}^{-1} \text{ of } H_2) \end{matrix} \qquad \textbf{(eq. 7)}$$

According to **eq. 7**, four valence electrons of two water molecules have to be dislocated, requiring a total energy input of 474 kJ or ~ 4.9 eV. This energy can theoretically be produced by either one photon of ultraviolet (UV) light with a wavelength shorter than 253 nm or by two photons of 2.46 eV in the visible spectrum with $\lambda < 504$ nm or by four infrared (IR) photons of at least 1.23 eV ($\lambda < 1008$ nm) energy. [289] **Figure 1-21** presents the photon energy *vs* wavelength as a function of number of photons needed for the full water-splitting reaction to occur, i.e., the generation of one molecule of oxygen and two molecules of hydrogen. Concerning UV-light, the energy needed for direct decomposition of water molecules by light radiation (direct water photolysis) corresponds mainly to wavelengths in the UV-C region (100–250 nm) that are naturally absorbed by the stratospheric gases (ozone), and thus are not present at the Earth's surface. Moreover, although infrared light makes up ~49% of the solar spectrum reaching the biosphere, pure water absorbs only few frequencies and most of this IR radiation has not enough energy to split water molecules. Thus, the most useful energy of solar-light reaching the Earth's surface is in the part of UV-A (320-400 nm, ~3-4% of the solar energy), the near-infrared (NIR) from 700–1000 nm, and particularly the visible spectrum (from 400 to 700 nm) that has an energy content representing ~43% of the whole spectrum. However, because water is transparent to the wavelength span from 300 to 1000 nm, it cannot be decomposed directly under normal conditions. [238] All of the above are critical energetic and kinetic limitations that prevent water photolysis from occurring naturally, and hence make the use of a photocatalyst necessary. To this end, it is rational to employ photocatalysts that can "harvest" sunlight in a wide

spectrum range in order to utilize solar-energy efficiently. Particularly in the visible range, two or three photons are ideally necessary to conduct the water-splitting reaction, as shown in **Figure 1-21**. Therefore, developing visible-light-responsive photocatalysts is energetically and kinetically favorable for water-splitting and crucial for achieving high energy-conversion efficiencies.

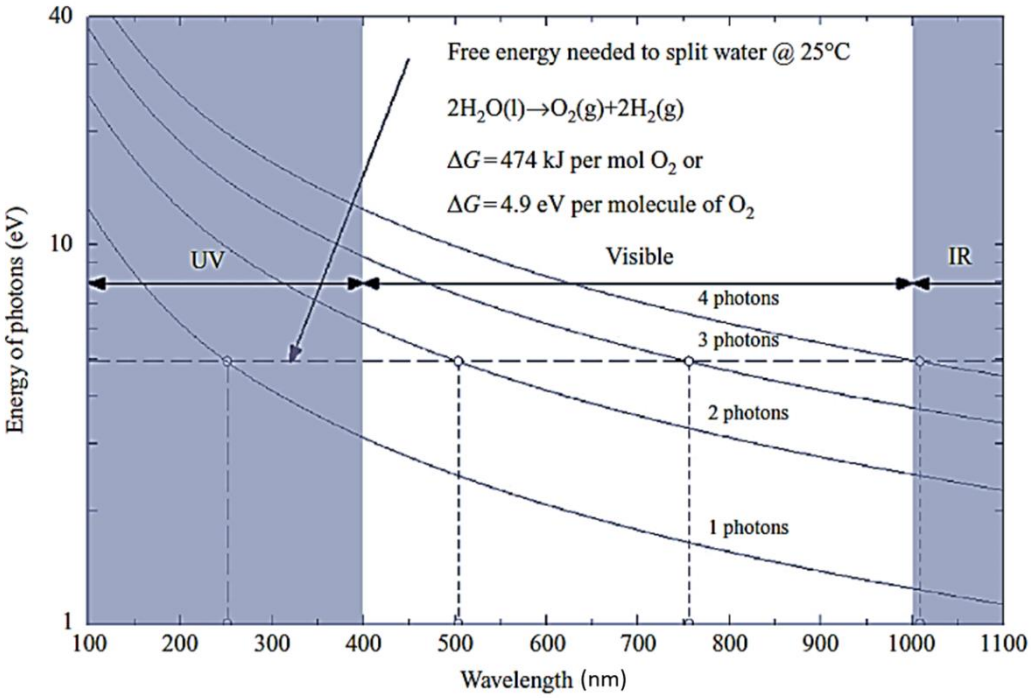

Figure 1-21: Energy of photons (eV) versus wavelength (nm), indicating the free energy (Δ*G*) as a function of number of photons needed for the full water-splitting reaction. Reproduced with permission from Ref. [289]. Copyright © 2016 Elsevier Inc. All rights reserved.

The overall process of photocatalytic water-splitting can be envisaged as two half redox reactions: (i) the water reduction or *hydrogen evolution reaction* (HER), and (ii) the water oxidation or *oxygen evolution reaction* (OER). Depending on whether the reaction occurs in acidic or alkaline solution conditions, the basic half-reactions and their corresponding standard redox potentials E^0 (in V *vs* NHE) can be written as follows (**eq. 8-12**):

pH=0	(HER)	$2H^+ + 2e^- \rightarrow H_2(g)$	$[E^0_{red} = 0.0\ V]$	(eq. 8)
	(OER)	$2H_2O(l) + 4h^+ \rightarrow O_2(g) + 4H^+$	$[E^0_{ox} = 1.23\ V]$	(eq. 9)
pH=14	(HER)	$2H_2O(l) + 2e^- \rightarrow H_2(g) + 2OH^-$	$[E^0_{red} = -0.826\ V]$	(eq. 10)
	(OER)	$4OH^- + 4h^+ \rightarrow O_2(g) + 2H_2O$	$[E^0_{ox} = 0.404\ V]$	(eq. 11)
Overall water-splitting		$2H_2O(l) \xrightarrow{catalyst} 2H_2(g) + O_2(g)$	$[\Delta E^0 = 1.23\ V]$	(eq. 12)

Regarding the redox potentials, it is well known that the standard reduction (E^0_{red}) and oxidation (E^0_{ox}) potentials of water are pH dependent, following the Nernst relation with pH according to the following equations (**eq. 13 and 14**):

$$E^0_{red} = -0.059\ V \cdot pH \quad (vs.\ NHE) \qquad \text{(eq. 13)}$$

$$E^0_{ox} = 1.23\ V - 0.059\ V \cdot pH \quad (vs.\ NHE) \qquad \text{(eq. 14)}$$

Surprisingly, as mentioned before, the flat-band potential and the band-edge potentials for many semiconductor materials (mostly metal oxides) in aqueous solutions exhibit the same linear pH dependence with a slope of 0.059 V per pH. [290, 291] This means that the necessary matching of the CB and VB levels of the photocatalyst with the redox potentials of the H_2 and O_2 evolution reactions is usually independent of the solution pH, and thus it is an a priori thermodynamic requirement that has to be met in order to achieve overall water-splitting. More specifically, the photocatalyst CB edge (or the flat-band potential) must be located at a more negative position than the reduction potential of H^+ to H_2 (e.g., −0.41 V *vs* NHE at pH 7), while the VB edge must be more positive than the oxidation potential of H_2O to O_2 (e.g., 0.82 V *vs* NHE at pH 7), as shown in **Figure 1-22**.

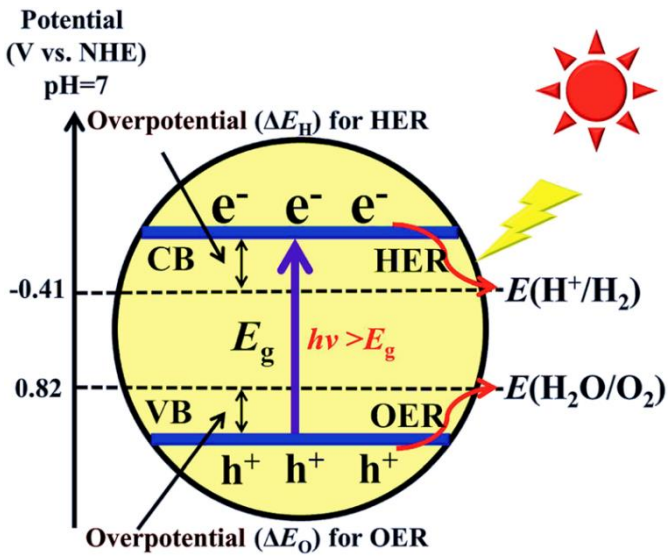

Figure 1-22: Basic thermodynamic requirements of overall water-splitting on a SC-photocatalyst particle. Dashed lines show the water redox levels in V *vs* NHE at pH 7. The necessary reduction (ΔE_H) and oxidation (ΔE_O) overpotentials of the photocatalyst CB and VB levels to drive the H_2 and O_2 evolution reactions (HER and OER respectively) are also shown. Reproduced from Ref. [292] with permission from the Royal Society of Chemistry.

Moreover, since the standard potential difference (ΔE^0) for the overall water-splitting reaction is 1.23 V (**eq. 12**), the minimum bandgap (E_g) of the photocatalyst should axiomatically be at least 1.23 eV to be able to convert the energy into H_2 and O_2. However, by taking into account various thermodynamic losses (~0.3–0.5 eV) and increased energy requirements to ensure sufficiently fast

reaction kinetics (~0.4–0.6 eV), some overpotentials are practically necessary to drive the H_2 evolution (ΔE_H in **Figure 1-22**) and O_2 evolution (ΔE_O in **Figure 1-22**) reactions. Thus, the optimum E_g of a single photocatalyst should be in the range of 1.8–2.5 eV for water-splitting. [277, 292] Nevertheless, even if semiconductor photocatalysts meet the bandgap and band-edge thermodynamic requirements, photocatalytic overall water-splitting into H_2 and O_2 is difficult to proceed due to the kinetical complexity of the multi-charge-transfer processes. Specifically, compared to the two-electron H_2-evolution reaction (**eq. 8** and **10**) the oxidation of water is much more challenging because the formation of one O_2 molecule requires at least four holes (**eq. 9** and **11)** and occurs on a timescale approximately five orders of magnitude slower than H_2 evolution. [293] By means of spectroscopic techniques, the four-hole water oxidation process has been shown to be the rate determining step during water-splitting (timescale of seconds) and competes with recombination, which takes place on the order of ns to μs. Also, because the products have a higher free energy than the reagents, the reverse reaction is thermodynamically favored ($\Delta G < 0$). This means that water-splitting photocatalysts must also be able to suppress the back reaction between O_2 and H_2 to produce H_2O, thus making photocatalytic water-splitting a very challenging process.

So, in addition to the energy band structure of semiconductors, other bulk and surface properties that strongly affect the chemical reactivity and the recombination process of photogenerated electrons and holes should be taken into consideration. [294] For instance, because structural or surface defects in semiconductor photocatalysts can act as recombination sites, developing highly crystalline semiconductor materials with a low number of defects can be beneficial for water-splitting applications. Nevertheless, in large crystal-size photocatalysts (e.g., defect-free single crystals), charge recombination (step IV in **Figure 1-19)** in the bulk can be significant due to the non-directional and long-distance migration of excitons from the bulk to the surface, thus decreasing the photocatalytic efficiency.[295] On the other hand, reducing the photocatalyst particle size increases the surface-to-volume ratio (i.e., surface area) and the number of surface active-sites and reduces the diffusion distances for excited electrons and holes to travel from the interior to the surface, thus improving the interfacial charge-transfer and photocatalytic performance. [296-298] However, these beneficial effects of small particle size are also offset by several disadvantages:

(i) The interfacial space-charge region and band bending that tends to separate electrons and holes could be limited when the dimensions of the particle are comparable to the width of the space charge layer. [299] When particles become small enough, e.g., smaller than the width of the space charge region present for a bulk material, the bands do not completely relax to the bulk level and thus the potential drop (band bending) and internal electric field will be significantly smaller for small nanoscale particles. [263, 297] This can limit the electric-field-induced e^-/h^+ separation in the semiconductor photocatalyst and increase their recombination probability.

(ii) In small semiconductor particles, an increase in their bandgap is usually observed because of quantum confinement. [262, 296, 300, 301] With regards to photocatalysis, although quantum size effects may favorably modify the band edge positions of the photocatalyst (i.e., by shifting the CB level to more reducing and the VB to more oxidizing potentials), the increase in the bandgap limits their light absorption range, which means that less solar energy is harvested.

(iii) Due to the lower particle volume, the reaction products (H_2 and O_2) are produced in close proximity on the surface of the particles and this makes the surface back reaction into H_2O more likely. [297]

(iv) Respectively, because of the high surface-to-volume ratio, surface defects may become dominant in small semiconductor nanoparticles, which can result in a significant increase of the e^-/h^+ recombination rates, especially when there is a lack of suitable active-sites for water splitting at the surface. [302, 303]

Taken together, all of these key parameters (i.e., optical absorption, bandgap, band edge positions, water-splitting kinetics, surface-back-reaction, charge separation and transfer, crystallinity and particle size) must be comprehensively considered and optimized in order to develop highly efficient photocatalysts for water-splitting. The current obstacle for the practical application of photocatalytic water-splitting and H_2 production still lies in the low energy-conversion efficiency of photocatalysts, which is strongly influenced by all the aforementioned factors. In addition, the lack of long-term structural and photochemical stability of photocatalysts is also a very important issue affecting their activity and practical use. [304] Therefore, the complexity of optimizing the bulk and surface properties and the electronic structure of a photocatalyst to meet the thermodynamic and kinetic requirements for overall water-splitting, makes so far the development of efficient and stable water-splitting photocatalysts one of the most challenging tasks in photocatalysis.

To address these challenges, intense efforts have been devoted to the continuous development of new efficient photocatalysts as well as the modification of existing photocatalysts. [292, 305] For example, aiming to achieve the balance between the thermodynamic and kinetic requirements for photocatalytic water-splitting, engineering strategies for better light-harvesting (e.g., bandgap engineering), boosting the charge-carrier separation and transfer (e.g., M-S or S-S heterojunction formation), and increasing the surface active-sites by nanostructuring or introducing co-catalysts, have been proposed and investigated. Among the various different engineering strategies, particularly the modification of base photocatalysts with co-catalysts that efficiently promote water-splitting has been extensively studied and reviewed. [237, 251, 277, 292, 305-309] In general, co-catalysts can be either H_2 promoting, such as noble metals (e.g., Pt, Pd, Ru, Rh, Cu, Au, Ni), or O_2 promoting, such as transition-metal oxides (e.g., NiO_x, CoO_x MnO_x RuO_2, IrO_2, RhO_2). They are usually loaded onto

the photocatalyst as a dispersion of nanoparticles (typically < 50 nm in size) and their typical role is to: (i) extract photogenerated electrons or holes from the photocatalyst, (ii) generate and/or introduce active sites, and (iii) reduce the activation energy for H_2 and/or O_2 evolution. Consequently, despite the fact that some photocatalysts have been reported to exhibit high activity without the presence of a cocatalyst, the modification with a cocatalyst usually enhances the overall water-splitting efficiency. However, the co-catalysts may also function as catalytic sites for the H_2O formation back-reaction or as e^-/h^+ recombination sites, and therefore, their careful design and optimization are also required to promote overall water-splitting.

Furthermore, in addition to the photocatalyst and co-catalyst engineering, different kinds of reaction systems that can promote separately one of the two half-reactions (the H_2 or O_2 evolution), using appropriate sacrificial reagents, are also generally accepted as a meaningful way to increase the photocatalytic efficiency. [295, 305, 309] In principle, sacrificial reagents are electron donor or acceptor species in the reaction solution that readily react with one type of charge-carrier (electron or hole), while letting the other to react with water molecules, thus facilitating either the H_2 or the O_2 evolution. Sacrificial electron-donors (hole scavengers), which consume the excited VB holes on the surface of the photocatalyst are used to facilitate water reduction by suppressing O_2 evolution, whereas sacrificial electron-acceptors (electron scavengers) are usually used to quench H_2 evolution and promote water oxidation. Generally, hole scavengers must be more readily oxidized than water by excited holes, while the electron scavengers must be more readily reduced than water by excited electrons. For this purpose, the most common sacrificial electron-donors used to scavenge holes are: methanol, ethanol, triethanolamine (TEA), EDTA, or an aqueous solution of Na_2S/Na_2SO_3, whereas metal cations such as Ag^+ and Fe^{3+} or a solution of $Na_2S_2O_8$ are usually utilized as electron scavengers. [305, 310] It is important to note, though, that the ability of a photocatalyst to both reduce and oxidize water separately with the aid of sacrificial electron donors or acceptors, does not guarantee the capability to achieve overall water-splitting without sacrificial reagents. This is because the sacrificial half-reactions are usually downhill processes associated with a decrease in the Gibbs free energy, and thus they are not directly correlated with the (thermodynamically and kinetically) more demanding overall water-splitting mechanism. [309] Nevertheless, from the viewpoint of H_2 production, adding sacrificial electron-donors to accelerate the consumption of VB holes is an effective measure to minimize charge-carrier recombination and enhance the activity of CB electrons, resulting in higher efficiency for H_2 generation. Moreover, due to the absence of O_2 evolution, the reverse reaction to produce H_2O is eliminated, thus increasing the H_2 yield and avoiding the necessity for subsequent separation of the H_2 and O_2 gasses [310], which is also a difficult task for efficient and safe H_2 storage. However, the downside of this strategy is the need to continuously add sacrificial electron-donors to sustain the reaction, since they will be consumed during photocatalysis, resulting

essentially in a system with no net storage of the photon energy. Even so, an attractive solution to this issue is to identify waste materials from industry that can be recovered and used as sacrificial electron donors in photocatalytic systems. One option, for example, is to use aqueous sulfide/sulfite wastes which can well act as hole scavengers to facilitate H_2 production. For this purpose, many sulfurous waste streams can be recovered from petroleum and chemical industries. [289] In addition, other bio-available compounds, such as ethanol, glycerol, sugars and other organic oxygenates, originating from renewable biological substrates or wastes, are also attractive candidates for sacrificial electron-donors that can be utilized in photocatalytic reforming processes to enhance H_2 production. [309] Nevertheless, despite the huge progress made in understanding and improving the reaction mechanisms and conditions in photocatalyzed H_2 production systems, the efficiency is still far from practical applications and it is clear that it depends primarily on material engineering, which should aim at improving the key parameters mentioned before (i.e., light harvesting, charge transfer and separation, band-edge positions, and surface active-sites).

1.5.3.3 Materials for water-splitting – Choice of photocatalyst

From 1972 until the middle of the 1980s, research on semiconductor photocatalysts for water-splitting had largely been devoted to titanates, such as TiO_2 and $SrTiO_3$ materials. [311-314] Since then, several hundreds of semiconductors have been found to be capable of producing H_2 and/or O_2 from water under light irradiation, summarized in many reviews. [237, 305, 307, 315, 316] In general, the various elements composing heterogeneous photocatalyst materials may serve several different purposes such as: (i) forming the band structure, (ii) constructing the crystal structure without direct contribution to the band formation (e.g., alkali, alkaline earth and some lanthanide ions), (iii) forming impurity levels as dopants (e.g., some transition metal cations with partially filled *d* orbitals such as Cr^{3+}, Ni^{2+}, Rh^{3+}, etc.) and (iv) to be used as co-catalysts. [237] An overview of the basic elements and their usual role in semiconductor-based photocatalysts are shown in **Figure 1-23**. On the basis of band structure formation, metal cations with d_0 electronic configuration (such as Ti^{4+}, Zr^{4+}, Nb^{5+}, Ta^{5+} and W^{6+}) or d_{10} electronic configuration (such as Ga^{3+}, In^{3+}, Ge^{4+}, Sn^{4+} and Sb^{5+}) have been usually used to construct CBs, whereas the VBs are mainly originated from the orbitals of non-metal elements, such as O, N, P, S, Se and others, as shown in **Figure 1-23**. [292]

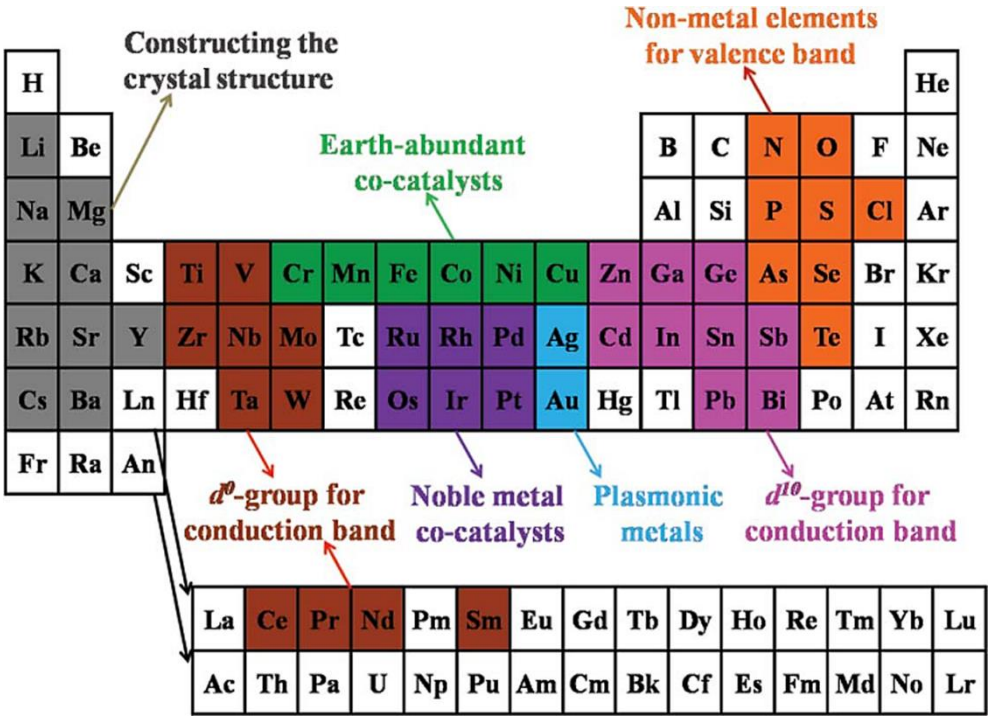

Figure 1-23: Elements and their usual role in semiconductor-based photocatalysts for water-splitting. Reproduced from ref. [292] with permission from The Royal Society of Chemistry. © The Royal Society of Chemistry 2015

Among the various kinds of metal-based photocatalyst materials, particularly transition-metal oxides whose CBs are formed from vacant *d* orbitals (d_0 configuration) or empty hybridized *sp* orbitals (d_{10} configuration) of their metal cations, have been found to be effective for overall water-splitting. [317-324] This is because for many of these oxides, their CB levels are usually positioned at more negative potentials than the hydrogen evolution potential (0 V *vs* NHE, pH 0), while their VB levels are composed of O *2p* orbitals which are located at approximately 3 V (*vs* NHE at pH 0). Thus, both d_0-type and d_{10}-type oxides tend to exhibit a large surplus potential for water oxidation, as shown in **Figure 1-24a**. In this case, however, the more negative CB edge potential than the H^+/H_2 energy level means that their bandgap will inevitably become larger than 3 eV, thus rendering them inactive in the visible-light region. [325] Therefore, as seen in **Figure 1-24a**, most of the metal-oxide photocatalysts capable of overall water-splitting are wide-bandgap semiconductors ($E_g > 3$ eV), which means that are active only under UV irradiation, and hence exhibit an inherently limited energy-conversion efficiency since UV accounts for only 3–4% of the solar energy.

Furthermore, various other metal-oxides, such as Cu_2O, Fe_2O_3, WO_3 and $BiVO_4$, have also been examined owing to their smaller bandgaps and their ability to absorb visible light, but all have shown limited capability for photocatalytic water-splitting and H_2 production. This is because, for example, Cu_2O does not have adequate VB overpotential to drive water oxidation (see **Figure 1-24a**) and it is also known for its poor chemical stability (it forms CuO or Cu because the corresponding redox potentials of Cu_2O lie within the bandgap), whereas the CB levels of Fe_2O_3, WO_3 and $BiVO_4$ are

generally more positive than the water reduction potential (**Figure 1-24a**) and thus cannot generate H_2 under irradiation.

Therefore, over the past decades major efforts have been made to develop new efficient photocatalysts for water-splitting and H_2 production, including doping wide-bandgap semiconductors with metal ions or non-metallic elements or synthesizing modified-oxide or non-oxide materials such as (oxy)nitrides and (oxy)sulfides, in order to expand the response of UV-active photocatalysts to the visible region. [237, 251] In this regard, by adding transition metals with partially filled *d* orbitals (d^n, n = 1–9) to wide-bandgap d_0-type or d_{10}-type oxides, the *d* bands of the transition-metal cations form donor or acceptor energy levels in the bandgap, thus leading to bandgap narrowing. In such doped photocatalysts, however, dopants in the photocatalyst act not only as visible-light absorption inducers but also as recombination sites between photogenerated electrons and holes. [237] Moreover, non-metal dopants such as nitride and sulfide have been reported to increase the activity and also the photostability over that of metal-doped catalysts, by introducing new energy states above the VB and, thus, reducing the effective bandgap and increasing the range of light responsiveness. [326, 327] Nevertheless, with this strategy, the introduced energy states are more likely to form a discrete energy level above the VB (because the doping concentration of the additive is usually low) and this is generally believed to be undesirable for water oxidation, because the photogenerated holes cannot migrate smoothly from the VB to the discrete dopant level.

On the other hand, in contrast to the doping approach, the synthesis of (oxy)nitrides and (oxy)sulfides with d_0 or d_{10} electronic configuration involves the incorporation of nitrogen or sulfur as constituent elements that replace oxygen into the crystal structure of metal oxides. In this case, the CB bottoms of these modified oxides will be similar to those of the corresponding metal oxide — consisted predominantly of the *d* orbitals of the constituent metal cations (with d_0 or d_{10} configuration) — whereas their VBs will consist of N 2p or S 3p orbitals hybridized with O 2p orbitals. Therefore, since the potential of these hybridized orbitals is more negative than that of the O 2p, the new VBs will be higher (more negative) than those of the corresponding metal-oxides, resulting in materials with smaller bandgaps sufficient to absorb visible light. With this band engineering approach, various (oxy)nitride and (oxy)sulfide photocatalysts have been so far synthesized by partial or complete nitridation or sulfidation of metal-oxides and their photocatalytic activity in water-splitting and H_2 or/and O_2 production has been thoroughly studied. [304] However, even though some of these modified-oxide photocatalysts have shown promising results for visible-light water-splitting and H_2 generation, their synthesis in pure form is rather difficult to reproduce and their reported efficiencies are comparatively moderate, possibly due to the presence of a significant number of surface or bulk defects that act as recombination centers for photogenerated electron and holes.

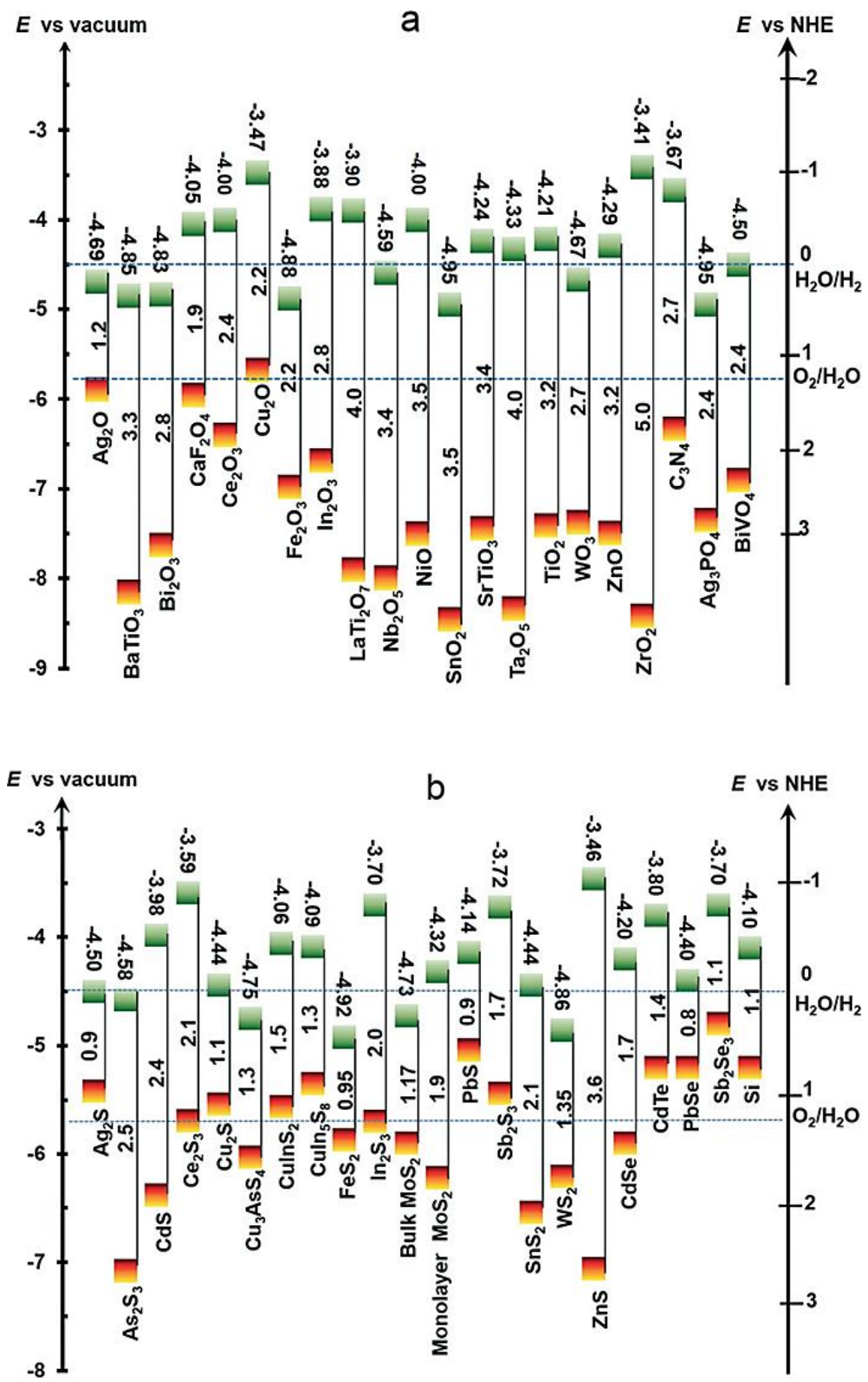

Figure 1-24: Band-edge positions with respect to the vacuum level and the NHE for selected semiconductors at pH=0: (a) various metal-oxides, silver phosphate (Ag_3PO_4) and carbon nitride (C_3N_4); (b) various metal-chalcogenides and silicon (Si). The top squares represent the conduction band edges and the bottom squares the valence band edges. The top numbers show the exact conduction band level *vs* vacuum and the number between squares denotes the bandgap energy in eV. The two dashed lines indicate the water redox reaction potentials in pH=0. Reproduced from ref.[277] with permission from The Royal Society of Chemistry. © The Royal Society of Chemistry 2015.

Besides d_0 and d_{10} metal-oxides, several metal-chalcogenides are also considered very attractive photocatalysts, especially for H_2 production, owing to their relatively high CB position with respect to the water reduction potential. Generally, most of the metal-chalcogenide photocatalysts consist of metal cations with d_{10} configuration (e.g. group IB: Cu, Ag; group IIB: Zn, Cd; group IIIA: Ga, In; group IVA: Ge, Sn) and one or more chalcogen anions (group VIA: S, Se or Te), constructing their CB and VB respectively. Among them, the group II-VI chalcogenides and particularly ZnS, CdS and CdSe are the most popular photocatalysts for water-splitting and H_2 production, due to their interesting optoelectronic and catalytic properties and their favorable band-edge positions, as shown in **Figure 1-24b**. However, despite their appropriate band-edge potentials for water reduction and oxidation, it is well-known that these chalcogenides are not stable in the water oxidation reaction because the S^{2-} and Se^{2-} anions are more susceptible to oxidation than water. This means that the photogenerated holes will preferentially oxidize the catalyst itself rather than water, resulting in the gradual degradation of the photocatalyst structure under long-term exposure to light-irradiation (photo-corrosion). [328-331] Photo-corrosion is actually a common problem for most metal-chalcogenide photocatalysts, and therefore, the use of appropriate sacrificial electron donors (hole scavengers) — that have higher (more negative) oxidation potentials and show faster oxidation kinetics than that of water — is often needed to overcome this issue. Notwithstanding, by using suitable hole scavengers (e.g., lactic acid, ascorbic acid, tertiary-amines, triethanolamine, alcohols, EDTA, Na_2S/Na_2SO_3 pairs and others), the II-VI chalcogenide semiconductors hold great promise as photocatalysts for H_2 generation systems.

For instance, CdSe has a bandgap of about 1.7 eV — very close to the ideal range for visible-light photocatalytic water-splitting as mentioned before — and its CB edge has a suitable potential to catalyze the water reduction reaction (see **Figure 1-24b**). Nevertheless, even with the use of sacrificial reagents and metal Pt co-catalyst, bulk CdSe particles show none or very small photocatalytic activity for H_2 generation, mainly due to slow charge-carrier mobility, high e^-/h^+ recombination rate and low redox overpotential that stem from its narrow bandgap. [332] Yet, the energetics of CdSe can be improved significantly through nanoscaling, taking advantage of the quantum size effect. According to this, Osterloh et. al showed that nanoribbons of CdSe have increased visible-light photocatalytic activity for H_2 production in the presence of Na_2S/Na_2SO_3 pairs as sacrificial reagents. They suggested that quantum confinement caused an increase in the bandgap of CdSe nanoribbons (compared to bulk CdSe) and raised their flat-band to a more negative potential, which is the reason for the enhanced water reduction activity. [333, 334] In addition, Holmes et al. studied the relationship between the degree of quantum size confinement in CdSe NCs and their photocatalytic activity over water splitting. [301] Higher hydrogen production rates were observed in CdSe quantum dots (QDs) with sizes between 2.25 and 3 nm, whereas NCs larger than 3.5 nm showed

zero activity, revealing that quantum size effects in CdSe NCs have a strong influence on their photocatalytic water-splitting activity. Also, their results emphasized the dependency of the charge-transfer kinetics on the thermodynamic driving force of the reaction and the possibility of fine-tuning photocatalytic activity through particle sizing. Nevertheless, despite the promising size-dependent photocatalytic properties of CdSe, selenium is a rare and scarce element in Earth's crust and this inhibits the large-scale production and application of CdSe and other selenide catalysts in H_2 evolution systems. [335, 336]

Due the abundance of sulfur on Earth, metal-sulfides have therefore received most of the attention among the various chalcogenide catalysts. In this context, ZnS has been demonstrated to exhibit a high photocatalytic activity in H_2 production from various electrolyte solutions (S^{2-}, SO_3^{2-}, $S_2O_3^{2-}$, $H_2PO_2^-$), even without the aid of metal co-catalysts (such as Pt). [337] However, with a wide bandgap of about 3.6 eV (see **Figure 1-24b**), ZnS can only absorb UV-light, which is a serious handicap for efficient solar-energy conversion and practical application. On the other hand, CdS is a n-type semiconductor with visible-light response, and thus it is extensively studied in photocatalytic water-splitting for H_2 evolution. [338-347] The large interest in CdS stems from its prominent advantages such as: (i) long charge-carrier diffusion length up to the micrometer scale [348-351], (ii) high electron mobility (more than 350 $cm^2\ V^{-1}\ s^{-1}$) [352], (iii) excellent visible-light response due its narrow bandgap ~2.3–2.4 eV, and (iv) suitable CBM and VBM positions — consisted mainly of the Cd 5*s*5*p* and S 3*p* orbitals, respectively [353] — that straddle the redox potentials for water-splitting; CBM ≈ –0.6 V *vs* NHE and VBM ≈ 1.7–1.8 V *vs* NHE (see **Figure 1-24b**). [341, 354] However, despite these advantages, single-component CdS catalysts generally exhibit low photon-to-hydrogen conversion efficiency and poor stability. These problems arise mainly from the insufficient electron-hole separation capability and low hole-transfer rates of CdS, which lead either to high recombination rates or to the accumulation of photogenerated holes inside the material that cause the anodic-decomposition of CdS, according to **eq. 15**. [355, 356]

$$\mathrm{CdS} + 2\mathrm{h}^+ \rightarrow \mathrm{Cd}^{2+} + \mathrm{S} \qquad E_{\mathrm{decomp}} = +0.32\ \mathrm{V}\ (\mathrm{NHE}, \mathrm{pH}\ 7) \qquad \text{(eq. 15)}$$

Where E_{decomp} = +0.32 V is the anodic decomposition potential of CdS with reference to NHE at pH = 7, which is more negative than the respective water oxidation potential (i.e., +0.82 V *vs* NHE. pH 7) and hence makes photo-corrosion more feasible thermodynamically. [341]

Therefore, the main challenge in developing effective CdS photocatalysts for H_2 production is to eliminate the competitive process of charge-carrier recombination and improve the kinetics of charge-transfer in CdS materials. In this aspect, over the past decades various practices have been adopted to increase the lifetime of photogenerated carriers and improve the photo-conversion efficiency and chemical stability of CdS materials. These include: (i) the use of suitable hole scavengers [341, 356-

358], (ii) doping with metal cations [359-363], (iii) formation of CdS-based solid solutions [364-367], and (iv) coupling CdS with noble-metal-based co-catalysts (e.g., Au, Pt, Pd, Rh, Ru and Ir metals, Pt-, Pd-, Rh-, Ru- and Ir-sulfides, RuO_2, etc.) [339, 368-374], or/and various combinations of noble-metal-free co-catalysts (e.g., TiO_2, Cu_xS, MoS_2, WS_2, Ni, NiO_x, NiS, graphene oxide, carbon nanotubes, g-C_3N_4) [358, 375-395], to form CdS-based heterojunctions. Particularly the synergistic effects from the coupling of CdS with other co-catalysts can largely improve the photochemical activity of CdS and, thus, significantly increase its H_2 production efficiency.

In addition to heterojunction formation, the synthesis of crystalline CdS materials with nanoscale porous structures and high internal surface area is also an important strategy for improving the kinetics of both the mass and charge-transfer processes in CdS catalysts. In general, by combining a large nanoscale porosity with the high activity of a nanostructured semiconductor into the same material, it is possible to design novel catalysts with improved catalytic performance and reliability. As an example, Bao et al. have recently prepared a Pt-loaded nanoporous CdS catalyst with increased surface area (~113 m^2g^{-1}), exhibiting a very high visible-light photocatalytic efficiency for H_2 production from a Na_2S/Na_2SO_3 solution. [396] The enhanced activity was attributed to the efficient charge-carrier separation, fast transport of the photogenerated carriers and the fast photochemical reactions at the enlarged CdS/electrolyte interface, thus demonstrating the advantage of introducing nanoporosity to an active nanostructured photocatalyst. However, despite the high activity, the CdS catalyst in this work was mainly composed of mesoporous nanosheets with sizes up to 60 nm and hollow nanorods with lengths up to 30 nm, hence presenting irregular size and morphology. In relation to this, as described in section 1.1, the design of semiconductor catalysts with ordered 3D mesostructured configurations, comprising a semiconducting framework with a nanocrystal network architecture and an interconnected mesoporous structure with uniform mesopores, is generally considered to be more favorable for achieving improved catalytic performance compared to respective dense materials or porous nanostructures with irregular morphology and porosity. This is because such ordered mesoporous catalysts are expected to benefit from the enhanced diffusion and transport of reactant molecules through the interconnected pores, the large interface area and number of surface active sites accessible to the reactants, and the increased light-harvesting efficiency, which can arise from the enlarged surface-area and multiple scattering of light inside the pores. [117, 397] Moreover, by using small-sized semiconductor particles (dimensions <10 nm) as building-units to construct the framework, the diffusion length of the photoexcited charge-carriers inside the semiconductor will become comparable to the particle size. This means that smaller semiconductor NCs can provide shorter paths for the electrons and holes to reach the semiconductor/electrolyte interface, thereby leading to increased charge transfer rates and resulting in an improved catalytic performance. [155, 296] However, in the case of CdS NCs, a very small particle size (< 3–4 nm) will

limit the visible-light responsiveness of CdS, because of the large increase in the bandgap arising from the quantum size effects. [398, 399] So, in order to achieve a balance between efficient visible-light harvesting and short charge-collection paths, a CdS nanocrystal size of about 4–10 nm should be appropriate. Therefore, developing an effective synthetic method to integrate small uniform-sized CdS NCs into a 3D mesoporous network architecture with interconnected uniform mesopores and catalytically active surface is a key step to the synthesis of advanced functional CdS-based catalysts for highly efficient photocatalytic water-splitting and H_2 production under visible-light iradiation.

1.6 Thesis statement and objectives

As already mentioned in the previous sections, hydrogen fuel produced from abundant and renewable resources, such as water and solar energy, represents a green alternative energy vector capable of replacing fossil fuels and helping us overcome the imminent energy and environmental crisis of our century. To this end, the process of heterogeneous photocatalysis has received immense attention as a potentially sustainable way to convert and store solar-light into chemical energy in the form of hydrogen gas. In this context, the photocatalytic production of H_2 from water can be realized mainly by two process systems, i.e., either by the direct splitting of water into H_2 and O_2, or by using sacrificial reagents as electron-donors (hole scavengers) that prevent the O_2 generation and facilitate the H_2 evolution half-reaction. Between the two, the latter system represents an attractive alternative way for more efficient and safer H_2 production, because it can boost the H_2 production yield, eliminate the difficult task for H_2 and O_2 gas separation, and also offer the possibility for simultaneous abatement of water pollutants if the sacrificial reagents originate from aqueous industrial or biomass wastes. Nevertheless, despite the great progress made so far, the practical application of this technology is still discouraged by the low efficiency of photocatalytic materials. Therefore, developing and exploring new functional photocatalytic materials with improved activity and reliability is a key step in achieving high photocatalytic efficiency for H_2 production, and thus it is an important research target in the fields of materials science, chemistry and engineering. In this direction, designing nanostructured materials with 3D mesoporous nanocrystal-based network morphology, that combine the high reactivity of small semiconductor NCs with the large and accessible surface area of an interconnected mesoporous structure, is a meaningful and compelling strategy to improve the performance of photocatalysts.

So, the general aim of this dissertation is to develop a new class of functional mesoporous photocatalytic materials based on the synthesis of novel 3D mesoporous structures of metal-chalcogenide nanocrystal assemblies (denoted as NCAs) and to study their application in important

photocatalytic processes such as the water reduction for H_2 production. Among the various active photocatalytic materials, the present research focuses on metal-chalcogenides and particularly on the II-VI sulfide semiconductors (ZnS, CdS) due to their attractive size-dependent electronic and photocatalytic properties and low cost. Also, the development of 3D ordered mesoporous catalysts from II-VI sulfide NCs and their application in photocatalysis has not yet been explored. In this respect, the specific research objectives of this Ph.D. thesis are:

- The development and establishment of a new effective and simple templating synthetic method for assembling 3D ordered mesoporous structures from II-VI metal-chalcogenide nanocrystals. This method must allow for the synthesis of tailorable mesoporous architectures from metal-chalcogenide nanocrystal assemblies (NCAs), where the nanocrystal size and composition, the pore size and morphology, as well as the optoelectronic and surface properties, can be easily controlled and modified separately.
- To examine the synthesis of ordered mesoporous metal-sulfide NCAs with different size (e.g., from 4 to 6.5 nm) and composition (e.g. CdS, ZnS) of the nano-building blocks as well as different surfactant-templates in order to explore the flexibility of the proposed synthetic route.
- To characterize all the obtained photocatalysts in terms of structural and physicochemical properties.
- To evaluate the visible-light-driven photocatalytic activity of the newly-developed mesoporous NCAs in processes such as photooxidation reactions of organic compounds and photocatalytic H_2 production from water.
- To fabricate novel mesoporous CdS-based photocatalysts by modifying the surface of CdS NCAs with effective co-catalysts (e.g., Pt nanoparticles, CuS nanocrystals, and $Ni(OH)_2$ species), using simple and straightforward techniques such as photo-deposition or partial cation-exchange. The aim of this part of research is to develop functional CdS-based mesoporous nanocomposites with nano-heterojunctions that shall have advanced charge-carrier dissociation and photocatalytic H_2 production efficiencies under visible-light irradiation.
- To investigate the mechanism of the hydrogen evolution reaction and clarify the role of the co-catalyst components in the catalytic processes.

Chapter 2: Experimental Section

2.1 Synthesis of colloidal CdS and ZnS nanocrystals

Water soluble thiol-capped colloidal CdS and ZnS nanocrystals (NCs) were prepared in a direct and environmentally friendly way, according to a modified wet-chemical synthetic method from the literature. [400, 401] Cadmium chloride ($CdCl_2$) or zinc chloride ($ZnCl_2$) and sodium sulfide ($Na_2S \cdot 9H_2O$) were used as reagents and 3-mercaptopropionic acid (3-MPA) as capping agent. Colloidal CdS NCs with different particle sizes of 4 nm and 6.5 nm in diameter could be prepared by varying the [Cd^{2+}]:[3-MPA]:[S^{-2}] molar ratio. [402] Also, colloidal ZnS NCs with 5 nm in diameter were obtained by changing the metal precursor. The more specific conditions for each synthesis were:

CdS NCs (4 nm in size): For 4 nm-sized CdS NCs, a Cd:3-MPA:S molar composition of 1:2:1 was used. In a typical procedure, 5.5 mmol of $CdCl_2$ and 5.5 mmol of $Na_2S \cdot 9H_2O$ were dissolved separately in 80 mL and 20 mL of deionized water (DI) respectively. After complete dissolution, 11 mmol of 3-MPA were dropped into the $CdCl_2$ solution and the mixture was left under continuous stirring for 15 min at room temperature (RT). Ammonium hydroxide (NH_4OH) was then added to adjust the pH at ~10–11 for 30 min, followed by the addition of the Na_2S aqueous solution. The final mixture was then left under stirring at RT for 1 h, resulting in a clear, greenish yellow colloidal dispersion of 4 nm MPA-capped CdS NCs.

CdS NCs (6.5 nm in size): For 6.5 nm-sized CdS NCs the exact same procedure was followed, but with the difference of using a Cd:3-MPA:S molar composition of 1:1:1 and adjusting the solution pH at ~7. The resultant colloid in this case was a clear, yellow colored sol with 6.5 nm MPA-capped CdS NCs.

ZnS NCs (5 nm in size): ZnS NCs of 5 nm in diameter were obtained by the same synthetic procedure as that of 4 nm CdS NCs, using $ZnCl_2$ as metal precursor and a Zn:3-MPA:S molar ratio of 1:2:1, resulting in a clear and colorless sol of 5 nm MPA-capped ZnS NCs.

In all the cases, stable colloidal dispersions were formed and the 3-MPA-capped chalcogenide NCs were isolated by precipitation with addition of 2-propanol as a non-solvent to destabilize the colloidal sols, followed by centrifugation at 10,000 r.p.m. for 15 min and drying at 40 ^{o}C for about 24 h. The obtained nanocrystalline powders can then be re-dispersed in DI water to form stable and clear colloidal dispersions with concentrations up to 150 mg mL^{-1} by adjusting the pH in the alkaline region (pH ~9–10).

2.2 Synthesis of mesoporous CdS and ZnS NCAs

The general synthetic procedure to prepare ordered mesoporous nanocrystal assemblies (NCAs), either with different particle size (4–6.5 nm) and composition (CdS or ZnS), or using different surfactant-templates, was as follows: Approximately 1.7–2.0 mmol of 3-MPA–capped chalcogenide NCs (either CdS or ZnS) were first suspended in 2.5 mL DI water to produce a stable colloidal dispersion. Next, the chalcogenide colloid was added dropwise to a 2.5 mL aqueous solution containing the surfactant (~10% w/v), and the resultant mixture was kept under stirring for 1 h at room temperature. To this colloidal sol, about 2–3 mL of a 3 wt.% H_2O_2 solution was dropped slowly under continuous stirring until gelation was observed (the clear sol becomes opaque), and then the mixture was left under stirring for an additional 1 h. The gel suspension was then transferred into a 50 mL glass beaker and placed in an oven at 40 °C to slowly evaporate the solvent under static conditions (typically within 3–4 days). To remove the organic-template, the dry-gel product was treated once with ethanol (20 mL) for 2 h under mild stirring and low heating (40 °C), and then three times with DI water (20 mL) for 15 min each. In each treatment the sample was isolated by vacuum filtration and the final template-free mesoporous product was collected after several washings with water and ethanol and drying at 40 °C for about 24 h. With this procedure, first reported in ref., various mesoporous nanocrystal assembly (NCA) materials were synthesized with different particle size, composition, and pore morphology [402], as described below:

NCA-CdS-4: Mesoporous NCAs prepared from the 4 nm MPA-capped CdS NCs, using Brij-58 (i.e., a non-ionic polyoxyethylene-20-cetyl ether [$HO(CH_2CH_2O)_{20}C_{16}H_{33}$] diblock co-polymer designated as POE(20)-*b*-C16 with average M_n ~1124 g mol^{-1}) as structure directing template.

NCA-CdS-6: Mesoporous NCAs prepared from the 6.5 nm MPA-capped CdS NCs, using Brij-58 as BCP template.

NCA-CdS (T): Mesoporous NCAs prepared from the 4 nm MPA-capped CdS NCs using different surfactant templates (content 10% w/v). The symbol "T" corresponds to the commercial name of the various surfactants examined, which are:

- Brij-S100: a non-ionic polyoxyethylene-100-stearyl ether [$HO(CH_2CH_2O)_{100}C_{18}H_{37}$] diblock copolymer designated as POE(100)-*b*-C18 with average M_n ~4670 g mol^{-1}.
- P-123: or Pluronic P-123, a symmetric poly(ethylene-glycol)-*block*-poly(propylene-glycol)-*block*-poly(ethylene-glycol) [$HO(CH_2CH_2O)_{20}(CH_2CH(CH_3)O)_{70}(CH_2CH_2O)_{20}H$] triblock co-polymer, designated as PEG(20)-*b*-PPG(70)-*b*-PEG(20) with average M_n ~5800 g mol^{-1}.
- F-127: or Pluronic F-127, a poly(ethylene-glycol)-*block*-poly(propylene-glycol)-*block*-poly(ethylene-glycol) [$HO(CH_2CH_2O)_{106}(CH_2CH(CH_3)O)_{70}(CH_2CH_2O)_{106}H$] triblock co-

polymer of the Pluronic family, designated as PEG(106)-*b*-PPG(70)-*b*-PEG(106) with average M_n ~12600 g mol^{-1}.

NCA-ZnS-5: Mesoporous NCAs prepared from the 5 nm MPA-capped ZnS NCs, using Brij-58 as diblock copolymer template.

2.2.1 Synthesis of CdS random NC aggregates

Random nanocrystal aggregates (RNAs) of individual CdS NCs were prepared following a similar procedure described above but in absence of template. Briefly, 2 mmol of 3-MPA-capped NCs were dispersed in 5 mL DI water to form a clear colloidal solution. To this solution, about 2 mL of a 3 wt.% H_2O_2 solution were dropped slowly under continuous stirring to form a gel suspension. Then the sample was collected with centrifugation, washed several times with water and ethanol and dried at 40 °C for about 24 h. By using CdS NCs of different particle size, two materials of CdS RNAs were prepared:

RNA-CdS-4: Random aggregates of 4 nm-sized CdS NCs (using 4 nm MPA-capped CdS NCs as starting materials)

RNA-CdS-6: Random aggregates of 6.5 nm-sized CdS NCs (using 6.5 nm MPA-capped CdS NCs as starting materials).

2.3 Synthesis of Pt-decorated CdS NCAs

Mesoporous Pt-decorated CdS NCAs were prepared through a simple and straightforward photochemical reduction and deposition process, where Pt nanoparticles were deposited on the surface of mesoporous CdS NCAs using a three-component reaction approach. [403] For a typical synthesis, 0.1 g of CdS NCAs (NCA-CdS-4) was dispersed by ultrasonication for 15 min in an aqueous solution (20 mL) containing 2.5 mL of triethylamine (TEA ~25-fold excess compared to CdS). [404] After the addition of appropriate aliquots of 1 mg mL^{-1} K_2PtCl_6 aqueous solution (corresponding to various wt.% Pt loadings), the suspension was de-aerated under argon flow for 30 min, and then illuminated for 1 h under visible light with a 300-W Xe lamp (Variac Cermax) equipped with a UV cut-off filter (Asahi Techno Glass, $\lambda \geq 420$ nm). The product was collected by centrifugation, washed with DI water several times, and dried at 40 °C overnight. The mesoporous Pt-loaded CdS composites prepared with this process are referred to as:

***n*% Pt-CdS NCAs:** mesoporous Pt-decorated CdS NCAs, where *n* corresponds to the theoretical (expected from the stoichiometry of reaction) mass percentage (wt.%) of Pt in the composite structure (*n* = 1, 2, 5 and 7 wt.% Pt).

5% Pt-CdS-*b*: mesoporous Pt-decorated CdS NCAs catalyst with 5 wt. % Pt loading, prepared in a similar fashion as the n% Pt-CdS NCAs sample, but using excess K_2PtCl_6 (corresponding to a 10 wt.% Pt content) and a short illumination time (15 min).

For comparison purposes, similar photo-deposition processes were also used to prepare Pt-decorated CdS catalysts with different morphologies than that of the mesoporous NCAs, as described below:

5% Pt-CdS bulk: Pt-decorated bulk CdS microparticles with 5 wt.% Pt content, prepared via the direct reaction of $CdCl_2$ with an equimolar amount of Na_2S in water (at RT) to produce CdS bulk microparticles first, and then photo-deposition of Pt onto the bulk CdS using the same procedure as described above.

5% Pt-CdS NCs: Pt-decorated CdS individual NCs with 5 wt.% Pt content, where Pt nanoparticles were deposited on the surface of 4 nm-sized MPA-capped CdS NCs (50 mg) by in situ photo-reduction (prior to a photocatalytic test) of $PtCl_6^{2-}$ ions (5.4 μmol of K_2PtCl_6) for 1 h under visible light irradiation ($\lambda \geq 420$ nm). In this case, the reaction mixture was an aqueous solution (20 mL) containing 5 M NaOH and 10% v/v ethanol as hole scavenger.

2.4 Synthesis of CuS/CdS NCAs heterostructures

Mesoporous NCA networks of CuS and CdS NCs were prepared with different mol% Cu content by a chemical partial cation-exchange process. [405] For a typical synthesis of 5 mol% CuS/CdS NCAs, 4.22 mL aqueous solution of $CuCl_2$ (1 mg mL^{-1}) was added dropwise to 10 mL aqueous dispersion of CdS NCAs (10 mg mL^{-1}) and the reaction mixture was kept under vigorous stirring for 30 min. The final green-brown product was isolated by filtration, washed several times with water and ethanol, and dried at 40 ºC for 12 h. With this simple process, a series of mesoporous CuS/CdS NCA composites were prepared, by varying the initial Cu^{2+} concentration (using different aliquots of the 1 mg mL^{-1} $CuCl_2$ solution) in the reaction mixture. The resulting materials were referred to as:

***n*% CuS/CdS NCAs:** where *n* corresponds to the theoretical (expected from the stoichiometry of reaction) mol percentage (mol%) of Cu in the composite structure (*n* = 3, 5 and 8 mol% Cu).

For comparison, a CuS/CdS bulk catalyst with 5 mol% Cu content was also prepared, as described below:

5% CuS/CdS bulk: CuS-modified bulk CdS microparticles with 5 mol% Cu content, prepared via the direct reaction of $CdCl_2$ with an equimolar amount of Na_2S in water (at RT) to produce CdS bulk microparticles first, followed by partial cation-exchange with Cu^{2+} to produce a CuS/CdS bulk composite, using the same procedure described above.

2.5 Synthesis of Ni-modified CdS NCAs composites

Ni-modified CdS composites were prepared by a photo-deposition process, carried out in a $NiCl_2$ solution containing triethylamine (TEA) as hole scavenger, where Ni-species (predominantly β-$Ni(OH)_2$ nanoparticles) were deposited on the CdS surface. [406] In a typical reaction to produce Ni-modified CdS NCA composites, mesoporous CdS NCAs (0.1 g) were well-dispersed by ultrasonication for 5 min in 20 mL of TEA aqueous solution (12.5% v/v, which corresponds to a ~25-fold excess compared to CdS). Next, the appropriate aliquots of (1 mg mL^{-1}) $NiCl_2 \cdot 6H_2O$ aqueous solution (corresponding to the desired loadings of Ni) were added to the above suspension, and the mixture was de-aerated by bubbling with Ar gas for 30 min to remove oxygen. After this, the reaction mixture was illuminated for 3 h under continuous stirring using a 365 nm light-emitting diode (50 W UV-LED) as the light source. The product was then separated by centrifugation, washed twice with DI water and ethanol, and kept at 40 °C for about 18 h. By changing the concentration of $NiCl_2$ in the reaction mixture, a series of mesoporous Ni-modified CdS NCAs composites were prepared, denoted as:

***n*% Ni-CdS NCAs:** where *n* corresponds to the theoretical (expected from the stoichiometry of reaction) mass percentage (wt.%) of Ni in the composite Ni-CdS NCAs structure (*n* = 5, 7, 10 and 15 wt.% Ni).

For comparative study, β-$Ni(OH)_2$ microparticles were also prepared by a wet chemical precipitation route, in which sodium hydroxide (NaOH) solution (4 M, 50 mL) was slowly added in a $NiCl_2$ solution (1 M, 50 mL) forming a light-green precipitate. The mixture was then left under continuous stirring at 60 °C for 24 h and the final green β-$Ni(OH)_2$ product was separated by vacuum filtration, washed with DI water and ethanol and then dried at 60 °C overnight. A physical mixture of mesoporous CdS NCAs and β-$Ni(OH)_2$ particles was also produced for comparison purposes, as described below:

10% $Ni(OH)_2$/CdS: the physical mixture of β-$Ni(OH)_2$/CdS NCAs was prepared by simply mixing two separate 50 mL aqueous dispersions (formed by ultrasonication for 15 min), containing proper amounts of the pre-formed β-$Ni(OH)_2$ microparticles (corresponding to an equivalent 10 wt.% Ni)

and mesoporous CdS NCAs. The resulting suspension was stirred for about 24 h at RT and then separated by filtration and heated at 60 ºC overnight.

2.6 Physical Characterization

Thermogravimetric Analysis (TGA): TGA analyses were performed using a Perkin-Elmer Diamond analyzer. Thermal analysis was conducted from 40 to 600 ºC in a nitrogen atmosphere (N_2 flow ~100 mL min^{-1}) with a heating rate of 5 ºC min^{-1}.

Small-Angle X-ray Scattering (SAXS): SAXS measurements were performed on a Rigaku S-MAX 300 high-brilliance system using Cu Kα radiation (λ=1.5406 Å, operating at 80 kV and 40 mA). The sample-to-detector distance and center of the beam were precisely measured using Ag-behenate ($CH_3(CH_2)_{20}COOAg$) as a calibration standard (d_{001} = 58.38 Å). The two-dimensional diffraction images were integrated into a one-dimensional diffraction pattern, as a function of the scattering vector q (**eq. 16**), with the Fit2D program. [407] Scattering data were corrected for dark current and empty tube scattering. The average size of nanoparticles was determined from the scattering data, using the Guinier approximation (**eq. 17**):

$$q = 4\pi \frac{\sin\theta}{\lambda}$$ where 2θ is the scattering angle and λ is the X-ray radiation wavelength **(eq. 16)**

$$I(q) \propto \exp\left(-q^2 R_g^2/3\right)$$ **(eq. 17)**

where $I(q)$ is the intensity as a function of the magnitude q and R_g is the radius of gyration, which is related to the diameter of spherical particles (D) by the following equation [408] :

$$D = 2R_g(5/3)^{1/2}$$ **(eq. 18)**

X-ray Powder Diffraction (XRD): Powder XRD patterns were recorded on a PANalytical X´Pert Pro MPD X-ray diffractometer, operated at 45 kV and 40 mA using Cu Kα radiation (λ=1.5406 Å) in the Bragg– Brentano geometry. The estimated average crystallite size (Ds) of the measured samples was calculated by XRD peak-width analysis and using the Scherrer's equation (**eq. 19**) [409-411] :

$$D_S = 0.9\,\lambda/(B\cos\theta)$$ **(eq. 19)**

where λ is the wavelength of X-rays (λ_{Cu} =1.5418 Å); B is the full-width at half-maximum (FWHM) of the XRD peak centered at 2θ degrees (in rad) and θ is the scattering angle (in degrees).

Scanning Electron Microscopy (SEM): SEM images were obtained using a JEOL JSM-6390 LV scanning electron microscope (SEM) operated at 20 kV. Samples were prepared by carefully mounting fine powders on copper or aluminum SEM specimen stubs using double-sided conductive carbon tape.

Energy-dispersive X-ray Spectroscopy (EDS): EDS spectra were collected using the JEOL JSM-6390LV SEM system equipped with an Oxford INCA PentaFETx3 EDS detector (Oxfordshire, UK). For elemental microprobe analysis, data acquisition was performed at least four times (i.e., at different sample locations) for each sample using an accelerating voltage of 20 kV and a 60 s accumulation time.

Transmission Electron Microscopy (TEM): TEM images were taken with a JEOL JEM-2100 electron microscope, equipped with a LaB_6 filament and operating at an accelerated voltage of 200 kV. Samples were prepared by suspending fine powders in ethanol using sonication, followed by depositing a few drops of solution (drop-casting) onto a holey carbon-coated Cu grid.

X-ray Photoelectron Spectroscopy (XPS): XPS measurements were performed on a Leybold EA-11 analyzer, equipped with an Al Kα X-ray source ($h\nu$=1486.6 eV) using a constant pass energy of 100 eV (FWHM of the Au $4f_{7/2}$ peak was 1.3 eV). The samples were prepared by pressing the powder on a Pb sheet in order to be introduced in an ultrahigh vacuum chamber. The analyzed area was approximately 2×5 mm^2, and the XPS spectra was collected at a 0-degree takeoff angle. In all XP spectra, the C 1*s* peak at 284.8 eV (adventitious carbon) was used for calibration and as a reference binding energy (BE) to charge-correct all the measured BEs.

Nitrogen (N_2) Physisorption: N_2 adsorption and desorption isotherms were measured at -196 ^oC using a Quantachrome NOVA 3200*e* sorption analyzer. Prior to the measurement, all samples were outgassed at 80 °C under vacuum (<10^{-5} Torr) for 12 h. The isotherm types and related pore characteristics were classified according to the IUPAC recommendations [412], which are displayed and summarized at **Figure A-5** in the appendix section. The specific surface areas were calculated by applying the Brumauer-Emmett-Teller (BET) method [413] on the adsorption data in the relative pressure range of P/P_0=0.05–0.24. The total pore volumes were estimated from the amount of adsorbed N_2 at the relative pressure of P/P_0=0.98, and the pore size distributions were derived from the adsorption branch of the isotherms using the nonlocal density function theory (NLDFT) method. [414]

UV-vis/NIR Diffuse Reflectance Spectroscopy (DRS): Diffuse reflectance UV–vis/ near-IR (NIR) spectra were obtained on a Perkin Elmer Lambda 950 optical spectrophotometer, using an integrating sphere, in the wavelength range 200–2500 nm. $BaSO_4$ powder was used as a 100% reflectance standard and as base material on which the powder samples were mounted for each measurement. Diffuse reflectance data were converted to absorption using the Kubelka-Munk function (**eq. 20**):

$$\boldsymbol{\alpha/S = (1-R)^2/(2R)} \qquad \textbf{(eq. 20)}$$

where R is the measured reflectance and α, S are the absorption and scattering coefficients, respectively. [415]

The energy bandgaps (E_g) of the samples were estimated from the onset of absorption and from the $(\alpha h\nu)^2$ *vs* $h\nu$ plots, according to the Tauc relation (**eq. 21**):

$$\boldsymbol{\alpha h\nu \propto \left(h\nu - E_g\right)^r} \qquad \textbf{(eq. 21)}$$

where α is the absorption coefficient, $h\nu$ is the photon energy, E_g is the bandgap and exponent r=1/2 for direct bandgap transitions. [416]

The average size of CdS nanoparticles was calculated based on the optical data, using the Brus equation (**eq. 22**) [417]:

$$\boldsymbol{E_g^{nano} = E_g^{bulk} + \frac{h^2}{8m_0r^2}\left(\frac{1}{m_e^*} + \frac{1}{m_h^*}\right) - \left(\frac{1.8e^2}{4\pi\varepsilon\varepsilon_0 r}\right)} \qquad \textbf{(eq. 22)}$$

where "E_g^{nano}" is the measured bandgap of CdS NCs from the Tauc plot, "E_g^{bulk}" is the energy bandgap of the bulk solid (2.42 eV for CdS), "h" is the Planlk's constant ($6.626\cdot10^{-34}$ J s), "r" is the radius of the nanoparticles, "m_e* (=0.21m_o) and m_h* (=0.8m_o)" are the effective masses of the excited electrons and holes, "m_o" is the real electron mass (9.11 10^{-31} kg), "e" is the elementary charge ($1.602\cdot10^{-19}$ C), "ε_o" is the vacuum permittivity ($8.85\cdot10^{-12}$ C^2 N^{-1} m^{-1}), and "ε" is the relative permittivity of CdS (5.7).

Photoluminescence (PL) Spectroscopy: PL emission spectra were recorded at room temperature on a Jobin-Yvon Horiba FluoroMax-P (SPEX) spectrofluorometer equipped with a 150 W Xenon lamp and operated from 380 to 800 nm. For the PL measurements, the samples were prepared by well-dispersing fine powders in DI water (with the same concentration of 1 mg mL^{-1}) using sonication, followed by placing a small amount (2 mL) in a quartz cuvette and measuring the emission spectra using an excitation wavelength of 360 or 380 nm.

Zeta (ζ) Potential: ζ-potentials were measured with an electrophoretic light scattering method using a micro-electrophoresis cell and a Malvern Zetasizer Nano ZS90 zeta potential analyzer. The samples were prepared by dispersing a small amount of the fine-powders in 0.5 M Na_2SO_4 aqueous solutions (mass content 0.1 mg mL^{-1}) and adjusting the pH to 7 with 0.1 M NaOH or 0.1 M H_2SO_4.

2.7 Electrochemical Measurements

Electrochemical Impedance Spectroscopy (EIS): Electrochemical impedance measurements were performed in a 0.5 M Na_2SO_4 aqueous electrolyte (pH = 7) using an electrochemical workstation equipped with an electrochemical cell and a Metrohm Autolab PGSTAT 302N potentiostat. A three-electrode set-up, with a Pt wire (or a stainless steel SS316, 2 mm diameter) and a silver-silver chloride Ag/AgCl (3 M KCl) as the counter and reference electrodes respectively, was employed to study the samples. The sample working electrodes were fabricated by adding ~10 mg of each sample in 1 mL of DI water, followed by ultrasonication of the mixtures in a water bath to form uniform suspensions. After that, 40 µL of each sample suspension was drop-casted onto fluorine-doped tin oxide (FTO, 9 Ω sq^{-1}) glass substrates, which were masked with an epoxy resin to expose an effective area of 1 cm^2, and heated for 30 min in 60 °C to produce thin films (see **Figure 2-1**). Prior to the sample loading, the FTO glass-slides (1.5 × 2 cm^2) were cleaned thoroughly by sonication once in acetone and next in isopropanol for 15 min, heated at 100 °C on a hot plate for 10 min, and then further treated with UV-ozone plasma for 5 min.

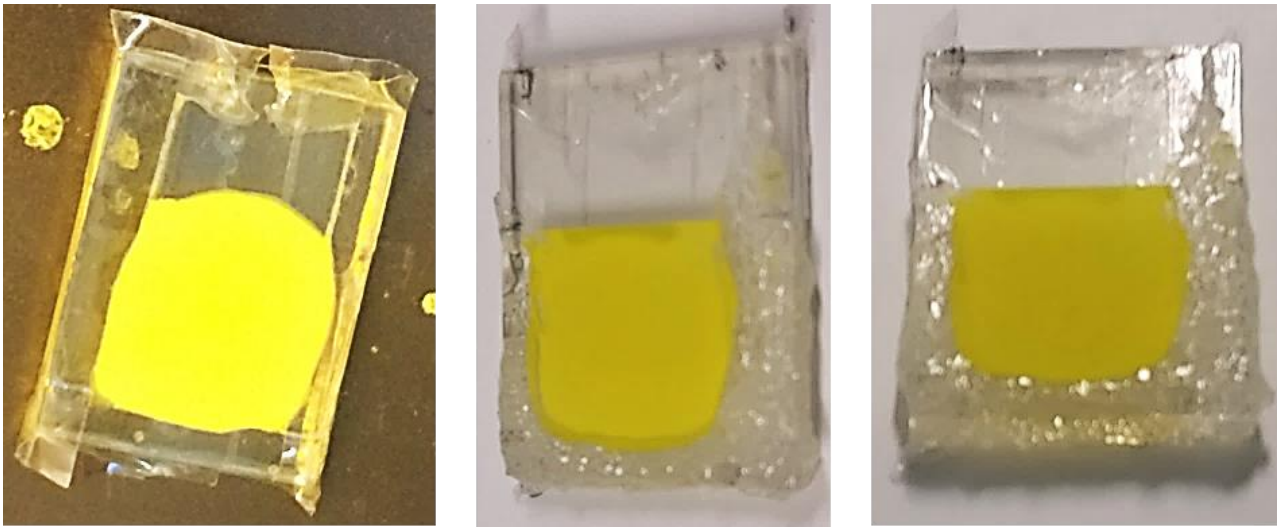

Figure 2-1: Typical examples of thin-film electrodes for EIS measurements, fabricated by drop-casting 40 µL of the sample slurry onto FTO-coated glass substrates.

Mott-Schottky analysis: The Mott-Schottky plots of different samples were generated with impedance-potential technique, performed in the dark at 1 kHz with 10 mV AC voltage amplitude. The differential space-charge capacitance (C_{SC}) of the working electrode-electrolyte interface was measured as a function of the applied potential (V), and Mott-Schottky plots were obtained by plotting ($1/C_{SC}^2$) *vs* V, based on the Mott-Schottky relation (**eq. 23**):

$$\frac{1}{C_{SC}^2} = \frac{2}{\varepsilon\varepsilon_o e N_D}\left(V - V_{FB} - \frac{k_B T}{e}\right) = \frac{2(V - V_{FB})}{\varepsilon\varepsilon_o e N_D} \qquad \textbf{(eq. 23)}$$

where "C_{SC}" is the space-charge capacitance, "V" is the applied potential, "V_{FB}" is the flat-band potential, "N_D" is the donor density of electrode material, "ε_o" is the vacuum permittivity (8.8542×10^{-10} F cm^{-1}), "ε" is the material's relative dielectric constant, "e" is the elementary charge (1.602×10^{-19} C), "k_B" is Boltzmann's constant and "T" is the absolute temperature. Note that, under normal conditions, the term "k_BT/e" is small enough and therefore it is usually negligible. [260] The corresponding V_{FB} values were determined from the intercepts of the extrapolated straight lines with the potential axis ($1/C_{SC}^2 = 0$). The measured potential with reference to the Ag/AgCl electrode ($V_{Ag/AgCl}$) was converted to the normal hydrogen electrode (V_{NHE}) scale using the following formula (**eq. 24**):

$$V_{NHE} = V_{Ag/AgCl} + 0.210\ V \qquad \textbf{(eq. 24)}$$

Also, the donor density (N_D) of the samples was calculated from the slopes of the Mott-Schottky plots, based on **eq. 23**, as follows:

$$N_D = \frac{2(V - V_{FB}) \cdot C_{SC}^2}{\varepsilon\varepsilon_o e} \qquad \textbf{(eq. 25)}$$

where the term $(V\text{-}V_{FB}) \cdot C_{sc}^2$ is the reciprocal of the slope of the Mott-Schottky plot.

Nyquist analysis: For Nyquist plots, the different current output was measured throughout a frequency range of 1 Hz to 1 MHz using a small AC perturbation of 20 mV, under open-circuit potential conditions. All the Nyquist EIS measurements were conducted in the dark and the steady state DC bias was kept at 0 V throughout the experiments. The obtained Nyquist impedance data were modeled with an equivalent electrical circuit using the EC-Lab software package (Bio Logic Science Instruments, version 11.16).

2.8 Photocatalytic Studies

Photooxidation experiments: The photocatalytic oxidation reactions of 1-phenylethanol to acetophenone were carried out as follows: 0.2 mmol of substrate (1-phenylethanol, Sigma-Aldrich) and 0.25 mmol of catalyst were added in 3 mL of benzene (or CH_3CN for experiments with Degussa P25) inside a 5 mL Pyrex glass reactor. Before switching on the lamp, the suspension was stirred for 30 min in the dark to homogeneously disperse the catalyst in the solution and to ensure adsorption-desorption equilibrium. Then the reaction was initiated by irradiation with a Variac Cermax 300W Xe lamp, using a UV cutoff filter (Asahi Techno Glass, $\lambda \geq 420$ nm). During irradiation, the reaction mixture was cooled with water bath (20 ± 2 °C) and bubbled with oxygen at a flow rate of ~1 mL min^{-1}. The products analysis was performed using a Shimadzu GC–MS QP2010 Ultra system equipped with a 60 m Mega-5 MS capillary column. For recycling experiments, the photocatalyst was recovered by centrifugation, dried under vacuum at 60 °C, and used for the next catalytic run.

Photocatalytic H_2 evolution experiments: Photocatalytic water reduction experiments for H_2 evolution were performed in an airtight Pyrex glass reactor, using the 300 W Xe lamp (Variac Cermax, Germany) system with a UV cut-off filter (Asahi Techno Glass, $\lambda \geq 420$ nm). All the experiments were carried out at 20 ±2 °C using an external water-bath cooling system, as shown in **Figure 2-2**. For a typical reaction, 20 mg of catalyst (except otherwise noted) were dispersed with stirring in 20 mL of aqueous electrolyte solution containing a sacrificial hole scavenger. For each experiment, the reaction cell was first de-aerated by purging with Ar gas for at least 30 min to ensure complete air removal, and then irradiated laterally by visible light, as seen in **Figure 2-2**. The evolution of H_2 was analyzed using a Shimadzu GC-2014 gas chromatograph equipped with a thermal conductivity detector (TCD) (using Ar as carrier gas) by injecting 100 µL of gas taken at various time intervals from the headspace of the reaction cell using a gastight syringe.

The photocatalytic H_2 production efficiency of the catalysts was estimated by means of measuring the apparent quantum yield (*QY*). The apparent *QYs* were calculated by analyzing the amount of evolved H_2 at a given illumination wavelength, according to the following equation (**eq. 26**):

$$\boldsymbol{QY}\ (\%) = \frac{\mathbf{2} \times \boldsymbol{N_{H_2}}}{\boldsymbol{N_{hv}}} \times \mathbf{100\%} \qquad \textbf{(eq. 26)}$$

where N_{H2} is the number of evolved H_2 molecules per unit time (i.e., H_2 flux) and N_{hv} is the number of incident photons of a given wavelength per unit time (i.e., photon flux). All *QY* measurements were performed in the optimum reaction conditions of the corresponding photocatalytic experiments

but under monochromatic irradiation of different wavelengths (e.g., λ = 365, 420, 440, 510, 550 and 620 ± 10 nm), by using the Xe lamp and appropriate optical band-pass filters (Asahi Spectra, Japan) or monochromatic LED light sources. For each wavelength, the average intensity of incident photons was measured using a StarLite power-meter equipped with a FL400A-BB-50 fan-cooled thermal sensor (Ophir Optronics Ltd., Jerusalem, Israel).

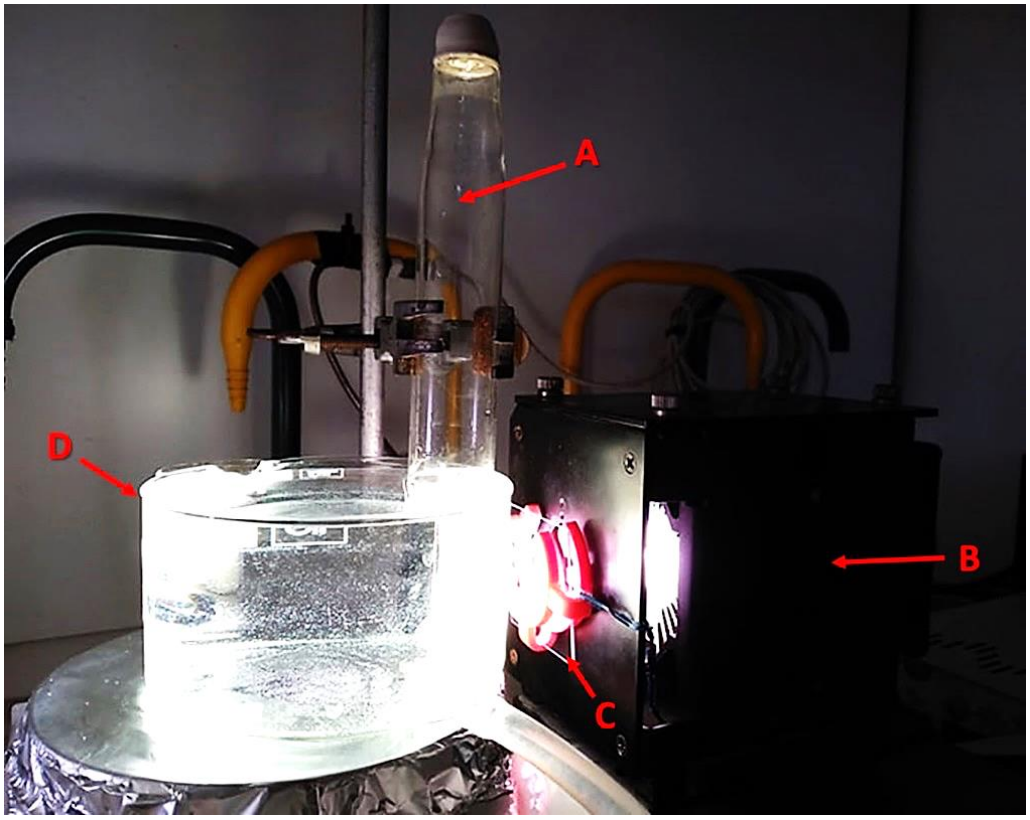

Figure 2-2: Layout example of the photocatalytic H_2 evolution experiments, showing: (A) the airtight Pyrex glass reactor (100 ml), (B) the Variac Cermax 300W Xe lamp, (C) the Asahi Techno Glass UV cutoff filter allowing only the wavelengths with λ ≥ 420 nm to pass through, and (D) the water-bath cooling system with a continuous flow of water to keep a steady reaction temperature at 20 ±2 °C.

Chapter 3: Results and Discussion

3.1 Templated self-assembly of metal-chalcogenide nanocrystals into 3D mesoporous structures

As mentioned in the first chapter, the synthesis of mesoporous assembly architectures from inorganic NCs represents an important challenge in material science and chemical nanotechnology. Such self-assembled materials are of great interest as they can incorporate complementary functionalities, such as nanoporosity and quantum-confined electronic properties of individual NCs, into the same structure. Beyond the distinctive optical, electronic and catalytic properties inherent to the nanocrystal building blocks, the 3D mesoporous networks of inorganic NCs are expected to benefit additionally from the large and accessible pore-surface and facile diffusion of target molecules within the pores. Moreover, self-assembled formulations of nanoparticles may exhibit new collective properties due to interparticle interactions and coupling effects. [116] To develop such nanoparticle-based mesostructures, significant research efforts have been devoted to using organic polymers as structure-directing-agents to direct the assembly of colloidal nanoparticles into mesoscopic architectures.

In this section, the development of a new, simple, and effective templating synthetic strategy is presented, that allows the assembly of II-VI metal-chalcogenide colloidal NCs into ordered 3D mesoporous structures with high internal surface area, uniform pores and optical absorption properties consistent with that of the corresponding starting NCs. For this purpose, the mesostructuring of CdS NCs is primarily examined as a good model example of assembling mesoporous metal-chalcogenide networks because of the facile production of starting CdS nanoparticles and their attractive and well-studied optical, electronic and photocatalytic properties. [162, 166, 418, 419] Thus, by taking advantage of the recent synthetic techniques for elaborating ligand stabilized NCs, water-soluble colloidal CdS NCs with different particle size (i.e., 4 or 6.5 nm) were first prepared and then used as starting building blocks to assemble ordered mesoporous structures with the aid of surfactants. Besides the different particle size, it will be shown that this method can also enable the construction of ordered mesoporous architectures with different composition of the metal sulfide nano-building blocks as well as different porosities.

3.1.1 Synthesis of mesoporous NCA-CdS structures

The synthesis of mesoporous CdS NC assemblies (NCAs) was accomplished via a single-step aqueous chemical process at room-temperature, in which the organization and self-polymerization of colloidal NCs into 3D polymeric networks were simultaneously achieved on the surface of surfactant-micelles, without the need of thermal processing to form a robust NC-linked network. A schematic overview of the overall synthetic route for preparing mesoporous CdS NCAs is illustrated in **Figure 3-1**.[402] In brief, a commercially available polyoxoethylene-*block*-cetyl ether (designated as POE(20)-*b*-C16 or Brij 58) diblock copolymer (BCP) was typically utilized to template an organized cross-linking polymerization EISA process of ligand-stabilized CdS NCs. Among various capping agents for CdS NCs, the 3-mercaptopropionic acid (3-MPA) was selected as an effective ligand because it bears a thiolate group able to bind to the NC's surface and an end-point propionic acid functional group which can provide good dispersion stability of the colloidal nanocrystal solution. More importantly, the propionic acid end-group is anticipated to engage in enthalpic interactions with the polar POE block of the polymer template, which are favorable for promoting the BCP-NC co-assembly towards the formation of ordered mesostructured NC/polymer composites. For the self-polymerization of CdS NCs at the polymer micellar-interface, a mild oxidative sol-gel process was employed. [187, 420-422] By adding a small amount of dilute H_2O_2 solution (~2 mL of 3 wt.% H_2O_2) into the BCP-NC solution, a controlled oxidation of the NC's surface and slow depletion of the surface-bound thiolate ligands was achieved. This mild oxidation process is the key step in the cross-linking polymerization of the colloidal metal sulfide NCs into 3D networks, which occurs by the progressive formation of disulfide (or polysulfide) bonds. [423] As proof of concept, when higher amounts of hydrogen peroxide (>5 mL) were used for the gelation process, the CdS NCs agglomerated and precipitated in an uncontrolled manner, resulting in the formation of untemplated bulky CdS aggregates. [424] Finally, due to the covalent coupling of the CdS NCs and the cross-linked nature of the porous network, the organic template was simply extracted from the hybrid mesostructures (obtained after slow evaporation of the solvent at 40°C) via a post-treatment process in ethanol and water, eventually producing mesoporous structures of CdS NC assemblies. Thus, by using 3-MPA-capped CdS colloidal NCs of ~4 nm or ~6.5 nm particle size, two mesoporous NCA-CdS structures were prepared designated as NCA-CdS-4 and NCA-CdS-6, respectively.

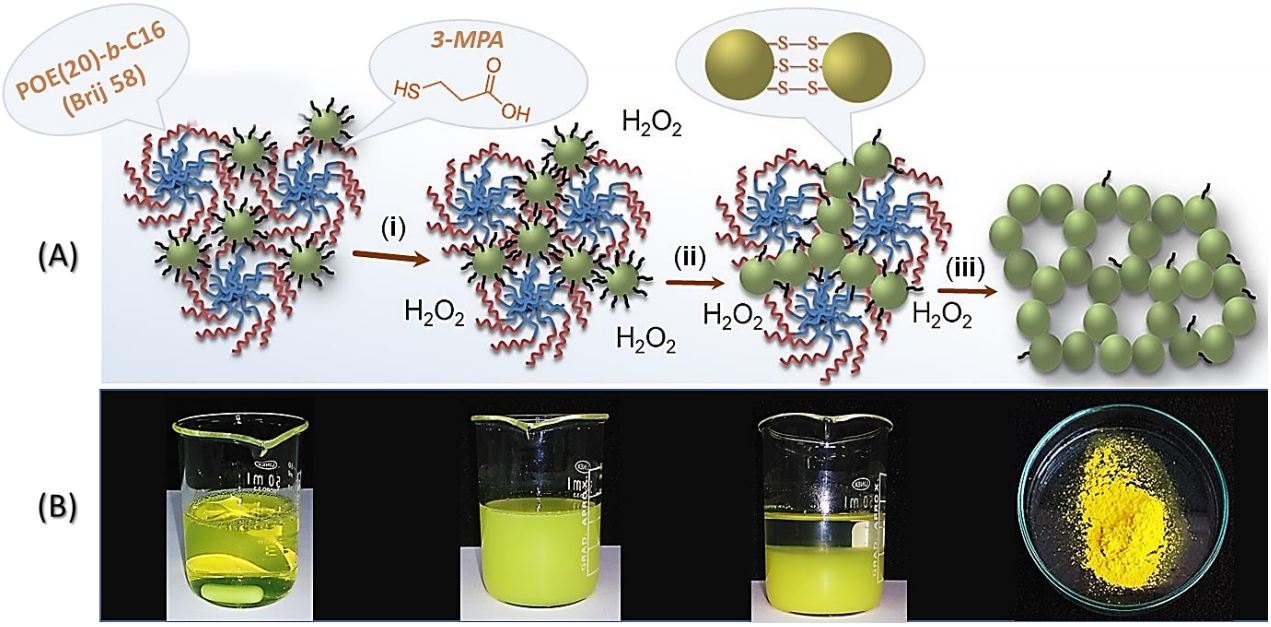

Figure 3-1: (A) Schematic illustration of the evaporation-induced self-assembly (EISA) process, showing a possible reaction route for the formation of mesoporous CdS NCAs (NCA-CdS family): (i) self-assembly and gelation/polymerization of 3-MPA-capped CdS NCs on the surface of BCP micelles (with the aid of 3 wt.% H_2O_2); (ii) progressive surface oxidation and cross-linking of the CdS NCs into a NC-linked network structures by the formation of S–S or polysulfide bonds; and (iii) extraction of the organic template from the hybrid NC/polymer mesostructure to produce a porous replica of the liquid-crystal phase. (B) Typical photographs corresponding to the various stages during the synthesis, showing the visual evolution of the sample from a clear colloidal solution, to a gel suspension after the addition of H_2O_2, and finally to a powder of mesoporous CdS NCAs after template removal. Adapted with permission from ref. [402]. Copyright © 2015, American Chemical Society.

3.1.2 Morphology and structural properties

The mesoporous NCA-CdS products were characterized by thermogravimetric analysis (TGA) to assess the removal of organic molecules from the porous structures. The TGA profiles of the as-prepared materials revealed a minor weight loss until 170 °C due to the liberation of adsorbed moisture, as shown in **Figure 3-2**. The gradual weight loss observed between 170 and 390 °C for NCA-CdS-4 and between 170 and 410 °C for NCA-CdS-6 is accompanied by a process of at least two steps (as indicated by the differential thermogravimetric, DTG, curves) and corresponds to the decomposition of organic molecules remained inside the pores. The TGA analysis for both the NCA-CdS-4 and NCA-CdS-6 samples indicated that, although the ethanol and three water treatment cycles were sufficient to eluate most of the organic molecules, a ~7–8 wt.% of organic residue still remained in the pores. Further efforts to better remove the organic molecules with a prolonged five-cycle ethanol/water washing process still showed a ~7.4% weight loss between 170 and 380 °C due to decomposition of the remaining surfactant molecules (**Figure 3-3**). However, as will be shown later, this remaining organic matter does not impose any significant pore restrictions or affect the surface properties of the as-prepared porous structures. Moreover, it is important to note that the thermal

annealing of samples (under N_2 atmosphere), even though eliminates completely the organic molecules, it leads to the destruction of the NC-based network with consequent loss of porosity.

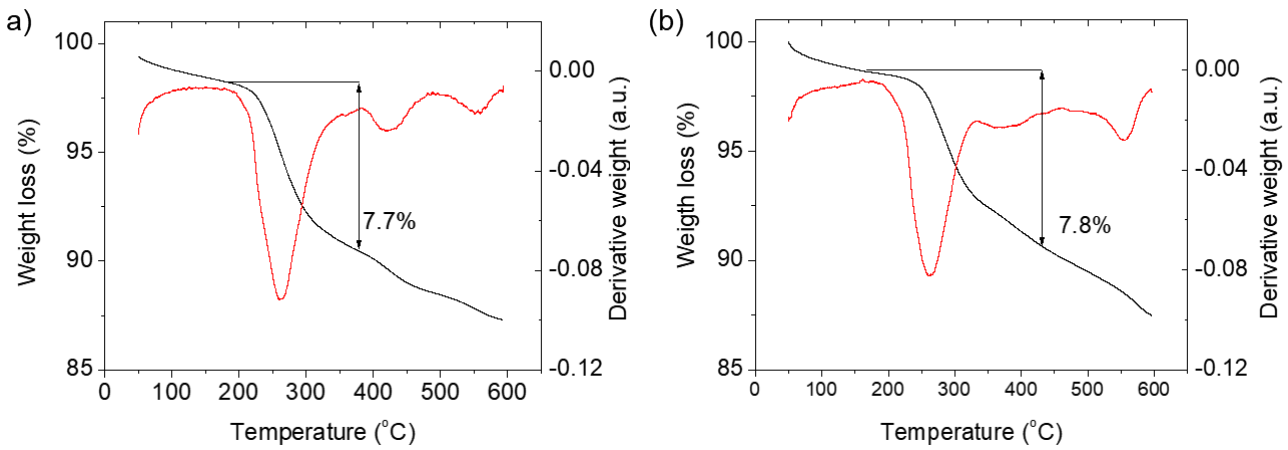

Figure 3-2: TGA profiles (black lines) of the mesoporous (a) NCA-CdS-4 and (b) NCA-CdS-6 materials, obtained after template removal via ethanol treatment and three process cycles with water. The weight loss in these samples, indicated by the corresponding differential thermogravimetric (DTG) curves (red lines), is attributed to the decomposition of organic molecules.

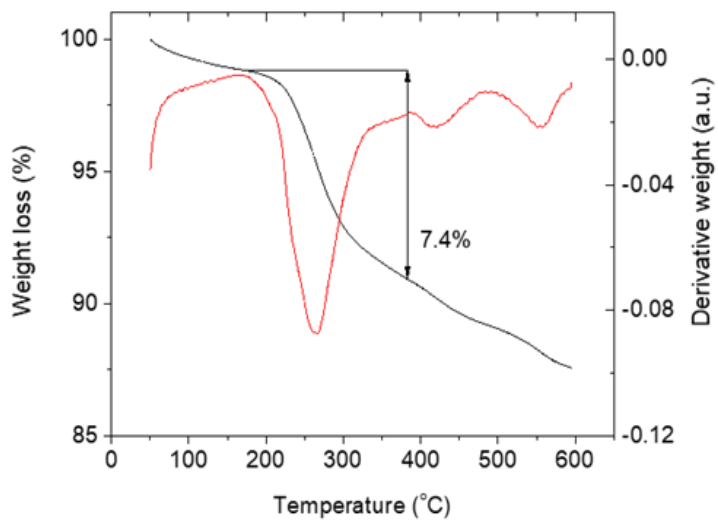

Figure 3-3: TGA profile of mesoporous (black line) NCA-CdS-4 material obtained after a prolonged five-cycle ethanol/water washing process. The weight loss in this sample, indicated by the corresponding differential thermogravimetric (DTG) curve (red line), is attributed to the decomposition of remaining surfactant molecules.

Small-angle X-ray scattering measurements on the mesoporous materials NCA-CdS-4 and NCA-CdS-6 were carried out to verify the mesoscopic ordering. The SAXS patterns in **Figure 3-4a** display a primary diffraction peak at scattering wave vectors (q) of 0.44 nm^{-1} for NCA-CdS-4 and 0.32 nm^{-1} for NCA-CdS-6, which correspond to a d-spacing ($d = 2\pi/q$) of about 14.3 and 19.6 nm, respectively. The presence of these peaks clearly indicates that the as-prepared assembled structures are ordered

(or at least have a low degree of polydispersity) at the mesoscale length. To elucidate the structural ordering of the polymer-templated assemblies, SAXS measurements were conducted for comparison on untemplated porous aggregates of 4 and 6.5 nm-sized CdS NCs. The untemplated materials were prepared following a similar oxidative self-polymerization procedure as described above, but in the absence of surfactant. In this case, the ligand-to-ligand interactions as well as interparticle forces play a dominant role and guide the nanoparticles into close-packed superlattice assemblies. [116, 425] As expected, these materials did not exhibit any distinguishable SAXS scattering peak (**Figure 3-4 b**), and thus can be considered to be random aggregates (RNAs) of individual 4 and 6.5 nm-sized CdS NCs (referred to as RNA-CdS-4 and RNA-CdS-6 respectively).

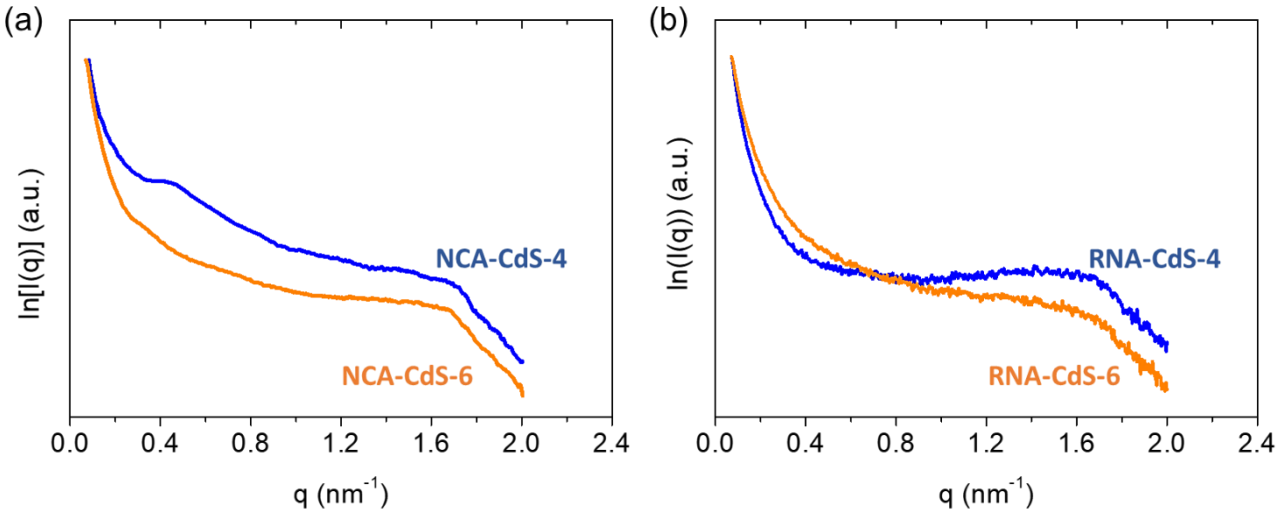

Figure 3-4: Small-angle X-ray scattering patterns of (a) the mesoporous NCA-CdS-4 (blue line) and NCA-CdS-6 samples, and (b) the random aggregates of 4-nm (RNA-CdS-4) and 6.5-nm-sized (RNA-CdS-6) NCs.

Analysis of the X-ray scattering data with Guinier approximation (see **eq. 17** and **18**) showed that the average grain size of the starting CdS nanoparticles did not change during the synthesis procedure. The average particle size of the constituent CdS NCs was estimated to be ~3.9 nm for NCA-CdS-4 and ~6.5 nm for NCA-CdS-6 (**Figure 3-5a**), which is very close to the particle size of the respective starting colloidal NCs, i.e., 3.8 and 6.3 nm for NCA-CdS-4 and NCA-CdS-6, respectively (**Figure 3-5b**).

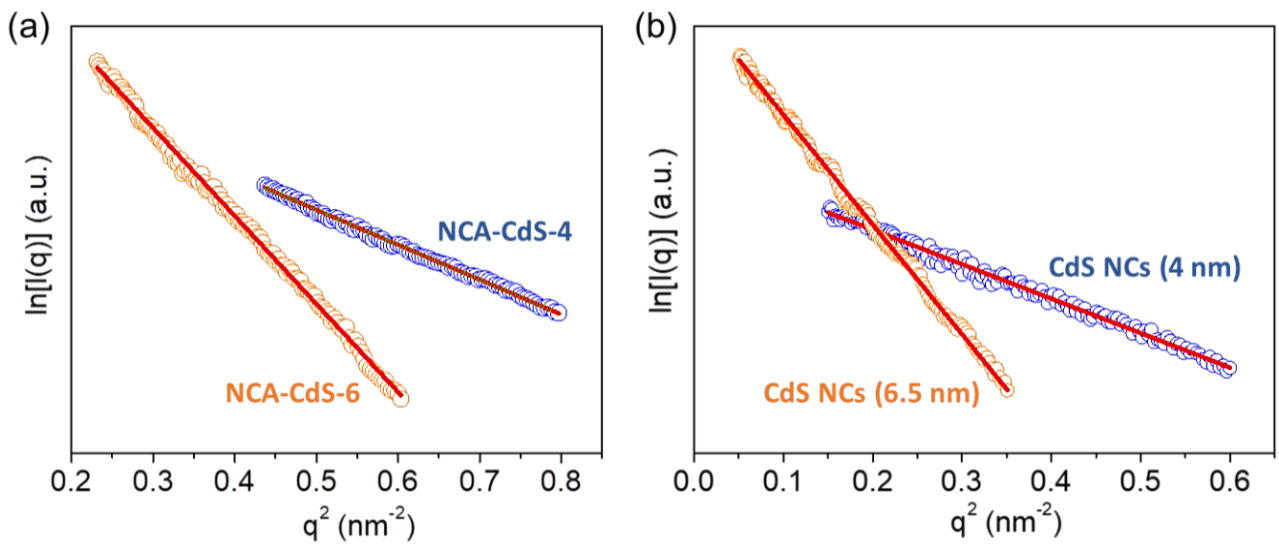

Figure 3-5: Guinier plots derived from scattering data of (a) the mesoporous NCA-CdS materials, giving an average CdS particle size of ~3.9 nm for NCA-CdS-4 and ~6.5 nm for NCA-CdS-6, and (b) the respective colloidal CdS NCs, estimating an average particle size of ~3.8 nm for the CdS NCs (4 nm) and ~6.3 nm for the CdS NCs (6.5 nm). The red lines are fit to the data. The radius of gyration (R_g) is measured from the slope according to eq. 17 and used in eq. 18 to calculate the particle diameter.

Powder X-ray diffraction was employed to probe the crystallinity of the porous networks. As can be seen in **Figure 3-6**, the XRD patterns of the primary CdS NCs and mesoporous structures are almost identical, displaying three diffraction peaks in 2θ scattering angles from 20 to 60° which can be assigned to the (111), (220), and (311) reflections of the CdS zinc-blende structure (JCPDS card no. 42-1411), thus indicating a cubic crystalline phase of CdS NC building blocks that is persist throughout the assembly process. In XRD patterns, the mesoporous materials exhibit a remarkably peak broadening of the Bragg reflections, corresponding to a very small crystal size. A peak-width analysis using the Scherrer's equation (**eq. 19**) gives an average domain size of CdS crystallites of about 2.6 nm for NCA-CdS-4 and 3.2 nm for NCA-CdS-6, which is close to that of the respective starting materials, i.e., ~2.1 nm for NCA-CdS-4 and ~3.0 nm for NCA-CdS-6. These results, along with the SAXS analysis for CdS particle size, suggest that the CdS particles consist of polycrystal domains.

Transmission electron microscopy and selected-area electron diffraction (SAED) were also employed to characterize the morphology and crystal structure of the as-prepared mesoporous assemblies. A typical low-magnification TEM image of the mesoporous NCA-CdS-4 sample is shown in **Figure 3-7a**. The image depicts uniform mesopores that are locally disordered throughout the assembled structure. A high-magnification image of the NCA-CdS-4 material is also shown in **Figure 3-7b**, where the presence of individual NCs that fully connect to form dense wall is visible. Careful analysis of the mesoporous structure gives an average pore diameter of about 6 nm with an average pore-wall thickness of about 7–8 nm. Moreover, the high-resolution TEM image

demonstrates that CdS NCs have a well crystalline structure, showing lattice fringes throughout the nanoparticles that correspond to (101) planes of cubic CdS (inset of **Figure 3-7b**). The crystallinity noted in the XRD patterns was also verified by electron diffraction, where the SAED pattern of NCA-CdS-4 shows broad Debye-Scherrer diffraction rings indexed to the cubic phase of CdS (**Figure 3-7c**).

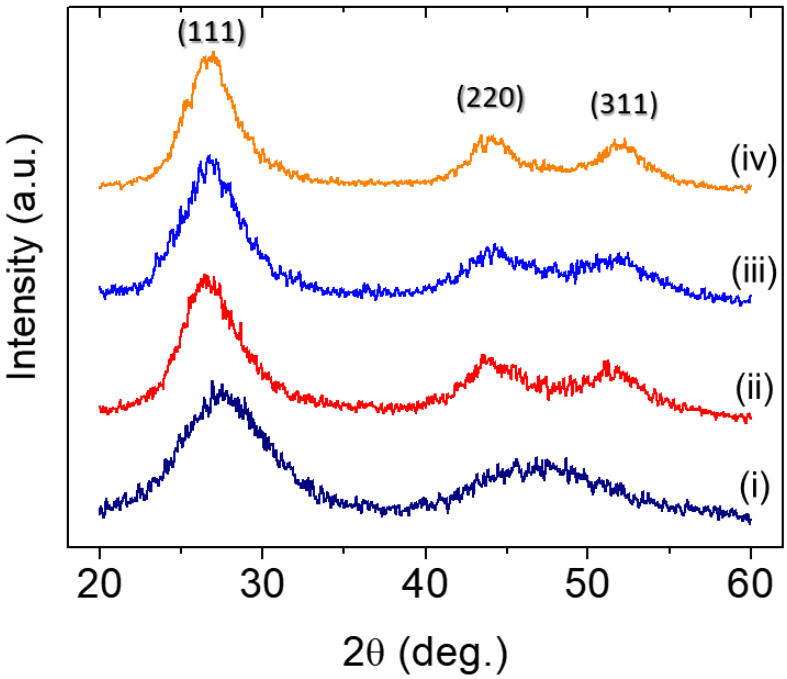

Figure 3-6: Wide-angle X-ray powder diffraction patterns of the mesoporous NCA-CdS materials and the respective CdS colloidal NCs. (i) CdS NCs (4 nm), (ii) CdS NCs (6.5 nm), (iii) NCACdS-4 and (iv) NCACdS-6. All the diffraction peaks were indexed to the (111), (220) and (311) reflections of cubic zinc-blende phase of CdS according to the JCPDS card no. 42-1411.

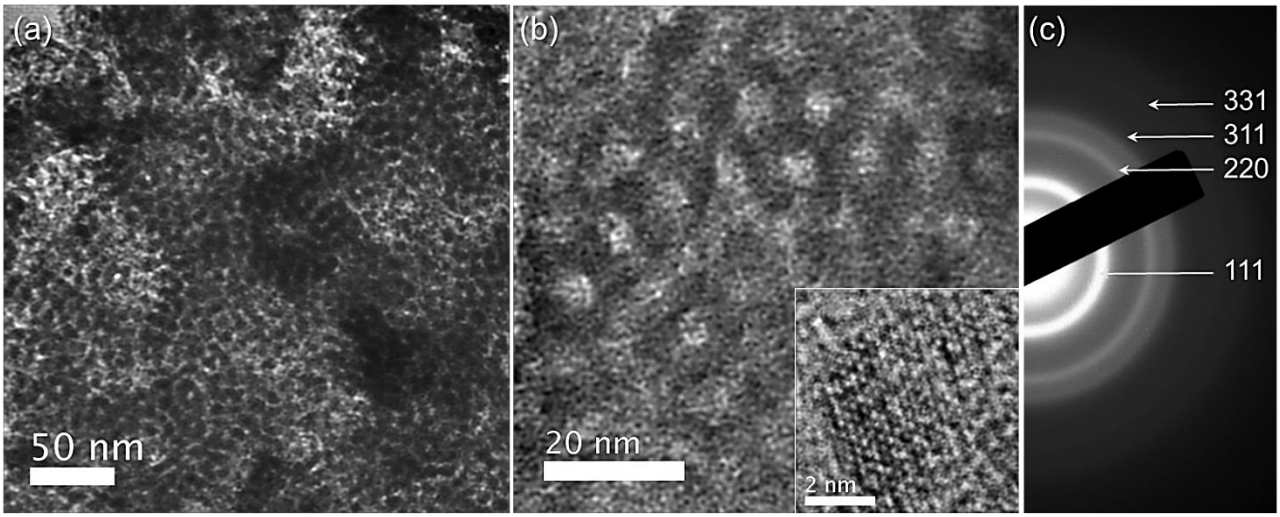

Figure 3-7: (a-b) Typical TEM images of the mesoporous NCA-CdS-4 structure. Inset of panel b: HRTEM image from an individual CdS NC demonstrating high crystallinity with lattice fringes assigned to the (101) planes of cubic CdS, and (c) SAED pattern showing diffraction rings indexed to the cubic scattering profile of CdS.

Nitrogen physisorption measurements indicated that the assembled mesoporous structures possess high porosity with regular mesopores between the connected nanoparticles. In **Figure 3-8**, the N_2 adsorption and desorption isotherms represent typical type IV curves with an H2-type hysteresis loop according to IUPAC classification (see **Figure A-5** in the Appendix section), which are characteristic of mesoporous solids with cylindrical pore channels. [426] The small but resolved adsorption step at mid-relative pressure region (0.4–0.5 P/P_0) is related to the capillary condensation of nitrogen in narrow-sized mesopores. [427] The measured Brunauer-Emmett-Teller (BET) surface area of the mesoporous NCA-CdS-4 sample was found to be 234 $m^2 g^{-1}$ and the total pore volume was estimated at about 0.28 $cm^3 g^{-1}$. Also, a similar surface area (230 $m^2 g^{-1}$) and pore volume (0.30 $cm^3 g^{-1}$) was obtained for the mesoporous networks of 6.5 nm CdS NCs (NCA-CdS-6).

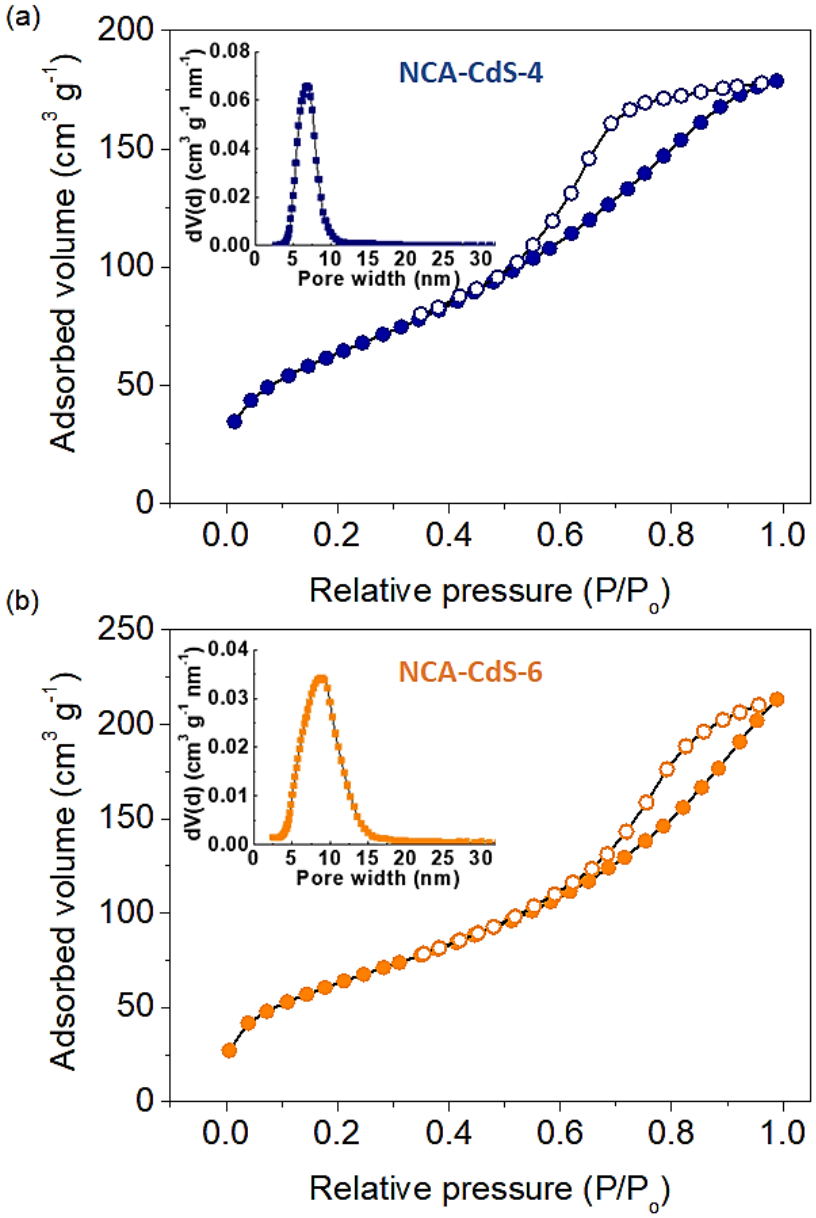

Figure 3-8: Nitrogen adsorption (solid symbols) and desorption (open symbols) isotherms at -196 °C of the (a) NCA-CdS-4 and (b) NCA-CdS-6 mesoporous materials. Insets show the corresponding NLDFT pore size distributions calculated from the adsorption branch of isotherms.

The pore-size distributions, assessed from the adsorption data using the nonlocal density functional theory (NLDFT) method, were found to be quite narrow with a peak maximum of ~6.8 nm for NCA-CdS-4 (inset of **Figure 3-8a**), which is consistent with the interparticle edge-to-edge distance observed from TEM (ca. 6 nm), and ~8.8 nm for NCA-CdS-6 (inset of **Figure 3-8b**). Given the respective CdS particle size derived from SAXS data, these results indicate that an average of two NCs compose the thickness of the pore-walls in these materials, which is also in line with TEM observation. For comparison, the adsorption-desorption isotherm obtained from the random aggregates (i.e. the RNA-CdS-4 sample) in **Figure 3-9**, indicates a combination of type-I and type-II curves with an H4-hysteresis loop (also see **Figure A-5** in the Appendix section), which according to IUPAC classification is attributed to nanoporous solids with narrow slit-like pores. [427] The BET surface area of this material was measured to be 126 m^2g^{-1}, while NLDFT pore-size distribution analysis points to the formation of nanoparticle aggregates with ~2.6 nm-sized interstitial voids. Therefore, these marked differences in the surface area and pore width between the random aggregates and the templated material are indicative of the different pore morphologies. Also, these results signify the role of the polymer-template in the formation of the NCA mesoporous structures.

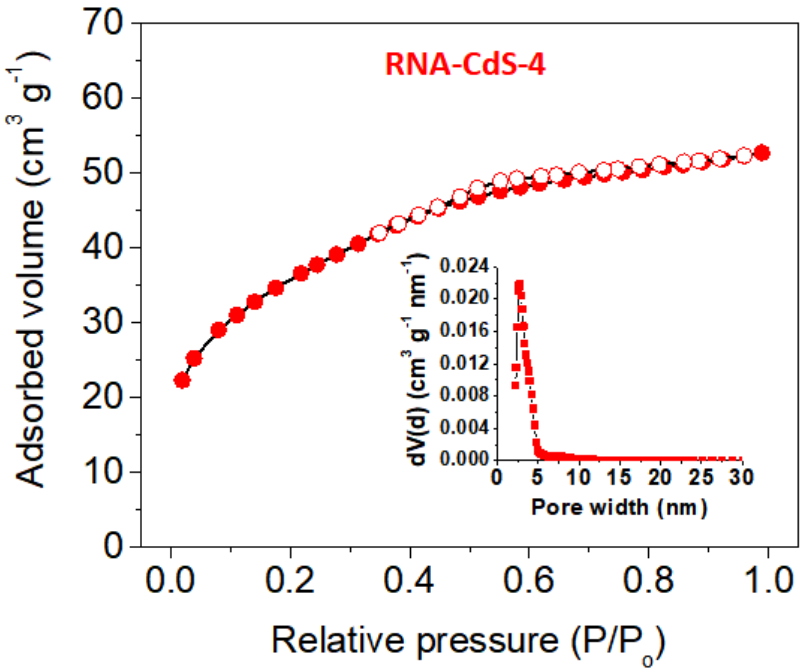

Figure 3-9: Nitrogen adsorption and desorption isotherm at -196 °C of the RNA-CdS-4 material. Analysis of the adsorption data with the BET method gives a surface area of 126 m^2g^{-1} and total pore volume of 0.08 $cm^3 g^{-1}$. Inset shows the NLDFT pore size distribution calculated from the adsorption branch of the isotherm, indicating a pore size of ~2.6 nm attributed to slit-shaped interstitial voids between the randomly aggregated nanoparticles.

Furthermore, to explore the surfactant-templating versatility and the effect of organic templates on the porous structure, NCA-CdS mesostructures (with 4 nm CdS NCs) were prepared with different templates and then characterized by N_2 physisorption. The adsorption-desorption isotherm of the NCA-CdS (Brij S-100) material (**Figure 3-10a**), obtained after templating with a polyoxyethylene-100-stearyl ether (designated as POE(100)-*b*-C18 or Brij S-100, M_n ~4670 g mol^{-1}) diblock copolymer, shows a type IV curve with an H2-type hysteresis loop that corresponds to a mesoporous morphology with cylindrical pore channels, similar to that of the Brij 58-templated NCA-CdS-4 material. The NLDFT analysis gives a narrow pore-size distribution with an average pore width of ~7.8 nm (inset of **Figure 3-10a)**, indicating that the use of Brij S-100 leads to the formation of larger mesopores compared to Brij 58. This enlargement in the pore width can be interpreted by the larger hydrophilic POE block of Brij S-100 polymer compared to that of Brij 58 (i.e., POE(100) *vs* POE(20), respectively). Also, a similar isotherm type and narrow pore-size distribution with a pore width of about 7.0 nm were obtained for the sample NCA-CdS (P-123) (**Figure 3-10b)** prepared using a poly(ethylene glycol)-*block*-poly(propylene glycol)-*block*-poly(ethylene glycol) triblock copolymer (designated as PEG(20)-*b*-PPG(70)-*b*-PEG(20) or Pluronic P-123, M_n ~5800 g mol^{-1}). The similar pore width of the NCA-CdS (P-123) material with that of the NCA-CdS-4 (prepared with Bri 58) can be also explained from the commensurate sizes of the hydrophilic blocks of the Brij 58 and Pluronic P-123 polymers, further suggesting that the hydrophilic block of the BCP templates plays a dominant role in forming the pore size in these NCA mesostructures. Consistent with this, the NCA-CdS (F-127) material, which is produced using a triblock co-polymer of the Pluronic family (designated as PEG(106)-*b*-PPG(70)-*b*-PEG(106) or Pluronic F-127, M_n ~12600 g mol^{-1}) with a higher hydrophilic-to-hydrophobic ratio, exhibited larger mesopores with an average size of about 9.4 nm, as shown in **Figure 3-10c**.

All together, these results demonstrate the flexibility of the present synthetic strategy in preparing porous architectures of CdS NCAs, where the pore size and morphology can be easily tuned by employing different structure-directing agents. The textural properties of all the prepared materials are summarized in **Table 3-1**.

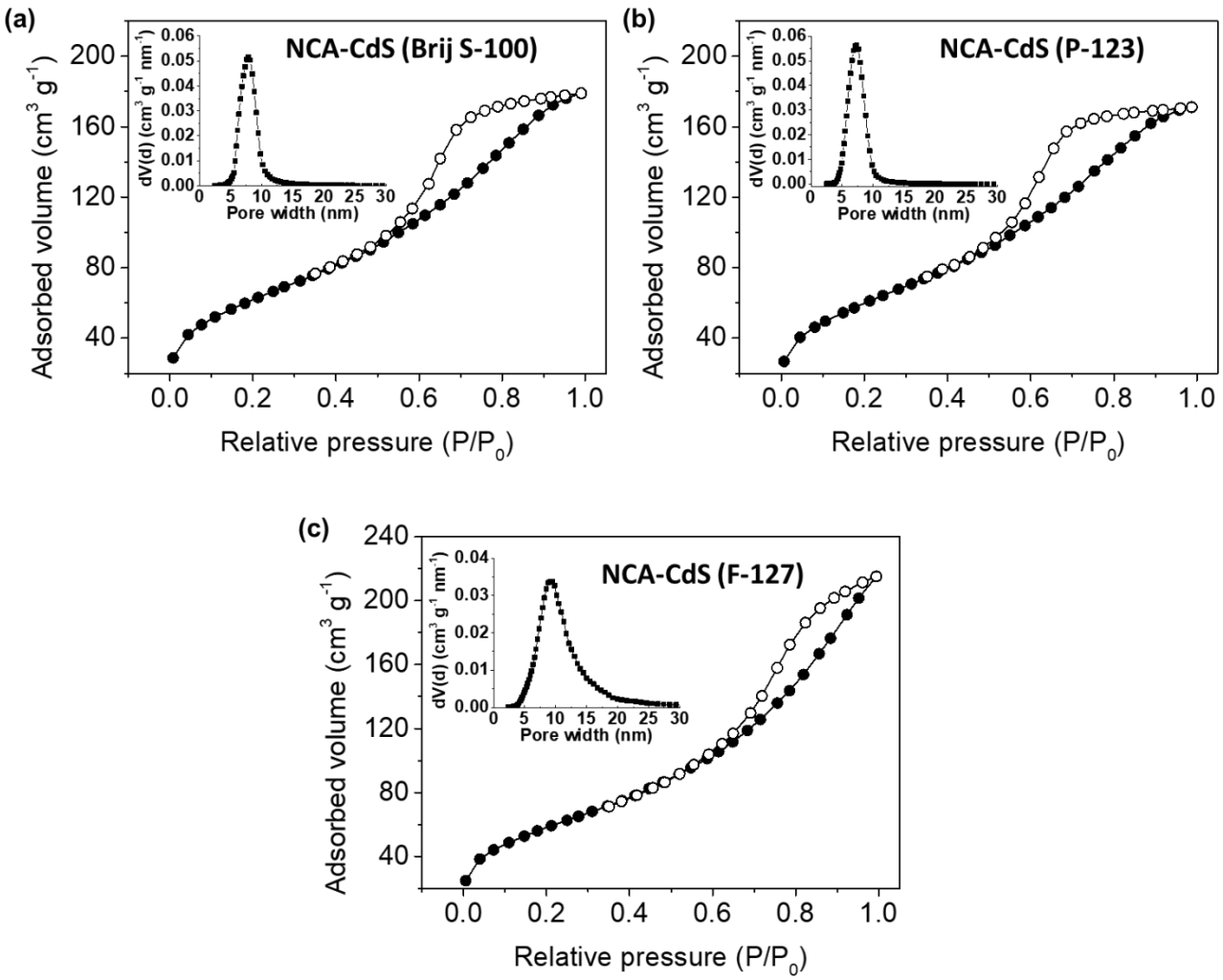

Figure 3-10: N_2 adsorption and desorption isotherms at –196 °C and the corresponding NLDFT pore size distributions (insets) for the NCA-CdS porous structures prepared with the 4-nm-sized CdS NCs using different templates (10% w/v concentration). (a) NCA-CdS (Brij S-100) prepared with the POE(100)-*b*-C18 diblock copolymer, (b) NCA-CdS (P-123) prepared with the PEG(20)–PPG(70)–PEG(20) triblock copolymer and (c) NCA-CdS (F-127) prepared with the PEG(106)–PPG(70)–PEG(106) triblock copolymer.

Table 3-1: Textural properties of the materials prepared with different templates, and CdS and ZnS particle sizes.

Sample	Template	Surface area (m^2 g^{-1})	Pore volume (cm^3 g^{-1})	Pore width (nm)
NCA-CdS-4	POE(20)-*b*-C16	234	0.28	6.8
NCA-CdS-6	POE(20)-*b*-C16	230	0.30	8.8
RNA-CdS-4	—	126	0.08	2.6
NCA-CdS (Brij S-100)	POE(100)-*b*-C18	228	0.28	7.8
NCA-CdS (P-123)	PEG(20)–PPG(70)–PEG(20)	222	0.26	7.2
NCA-CdS (F-127)	PEG(106)–PPG(70)–PEG(106)	214	0.33	9.4
NCA-ZnS-5	POE(20)-*b*-C16	334	0.33	5.8

The mesoporous ensembles were found to exhibit a well-defined electronic structure, as interpreted by ultraviolet–visible/near-IR diffuse reflectance spectroscopy (UV–vis/NIR DRS). The optical absorption spectra of mesoporous materials produced with different CdS building blocks (**Figure 3-11**) show sharp absorption onsets associated with electronic transitions in the energy range from 2.50 eV (495 nm) for NCA-CdS-6 to 2.63 eV (471 nm) for NCA-CdS-4. This variation in the energy gap with the diameter of the CdS NCs is associated with quantum size effects of the constituent nanoparticles, supporting the notion that the quantum-confined electronic properties of the colloidal CdS NCs are persisted in the assembled structures. Note that the bandgap energy of a fine semiconductor, blue shifts as the particle size decreases. [428, 429] The resultant mesoporous assemblies showed a slightly narrower energy gap (by 30–40 meV) compared with the energy gap of the respective CdS building blocks (i.e., 2.53 eV and 2.67 eV for the 6.5 and 4-nm-sized CdS NCs, respectively), manifesting a greater delocalization of the excitons, possibly due to interparticle coupling effects. [353, 430, 431]

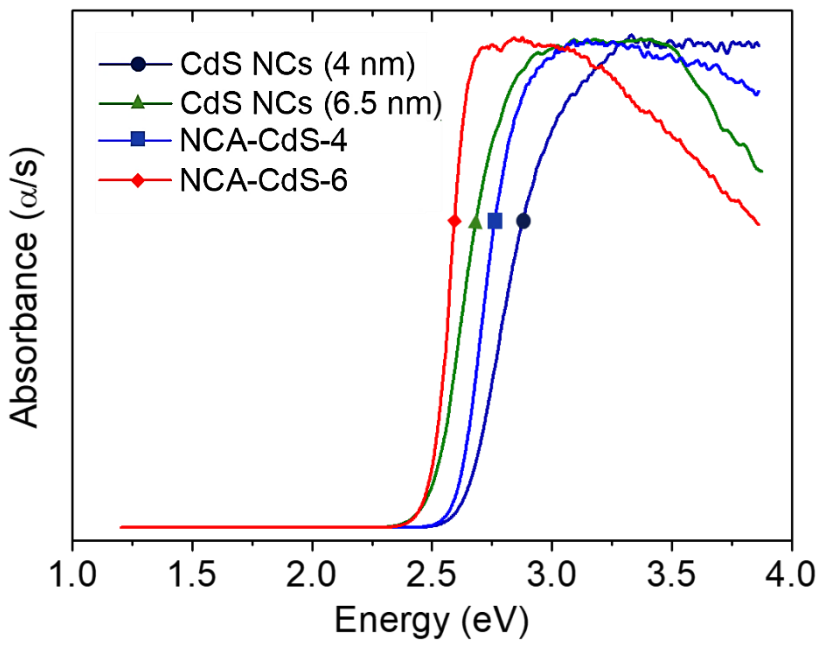

Figure 3-11: Optical absorption spectra of the 4 and 6.5 nm-sized CdS NCs and the corresponding mesoporous NCA-CdS-4 and NCA-CdS-6 materials, derived from UV–vis/NIR DRS measurements. Diffuse reflectance data were converted to absorption (α/S) using the Kubelka-Munk function.

The emission properties of the 3-MPA-capped CdS NCs and the resultant mesoporous structures were investigated using photoluminescence (PL) spectroscopy. As seen in **Figure 3-12**, the mesoporous networks show an emission in the 450–700 nm range (~1.7–2.8 eV) at room temperature, when excited with photons of high energy (380 nm). The peak maximum of the PL spectra (~2.3 eV) is located at wavelengths near the band-edge absorption of CdS, suggesting an interband luminescence process (i.e., between the quantized energy states of conduction and valence band),

although minor contribution of surface and deep-level states to the emission process due to residual thiolate ligands cannot be excluded. [432] The photoemission energy of the assembled mesoporous samples is very close to that of the respective individual NCs, suggesting that the assembly process does not significantly alter the PL response of the nanoscale CdS building blocks. The slight blue shift observed in the PL spectra of assembled structures compared to the PL signal of individual CdS NCs (by ~30–50 meV) could be attributed to a lower density of interband states, due to the removal of thiolate ligands from the NCs' surface. Moreover, a slight change in the quantum size effect, arising from some etching of the nanoparticles' surface during the mild oxidation process, could also be a possible explanation. [433]

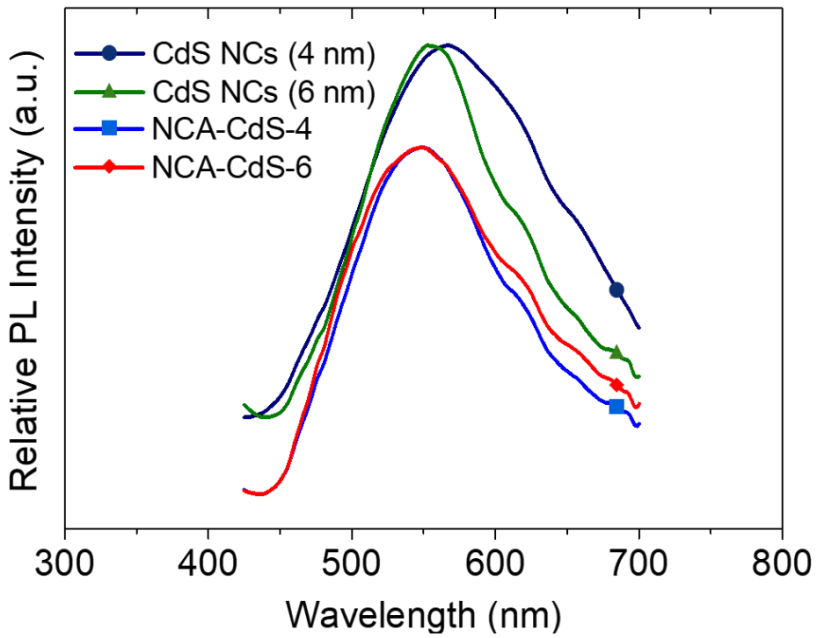

Figure 3-12: Room-temperature PL emission spectra of the 4 and 6.5 nm-sized MPA-capped CdS NCs and the corresponding mesoporous NCA-CdS-4 and NCA-CdS-6 materials. The PL spectra are normalized to their maximum intensity.

Besides different particle size and organic templates, the present synthetic method could be applicable to the synthesis of mesoporous assemblies from other metal-chalcogenide NCs, such as II-VI semiconducting nanoparticles. To test this expectation, the preparation of a porous ZnS-based assembled structure (denoted as NCA-ZnS-5) was also examined, by using colloidal MPA-capped ZnS NCs (with 5 nm diameter) as starting building blocks and Brij 58 as template. As follows from SAXS, XRD and TEM analysis (**Figures 3-13** and **3-14**), the NCA-ZnS-5 material exhibits a similar structural morphology with that of the NCA-CdS-4 sample, comprising a relatively ordered structure (SAXS peak at q=0.47 nm^{-1}) of connected 5-nm-sized ZnS nanoparticles (assessed from Guinier and TEM analysis) of zinc-blende cubic crystal phase (indicated by HRTEM, XRD and SAED patterns) with highly porosity (as inferred from low-magnification TEM in **Figure 3-14**).

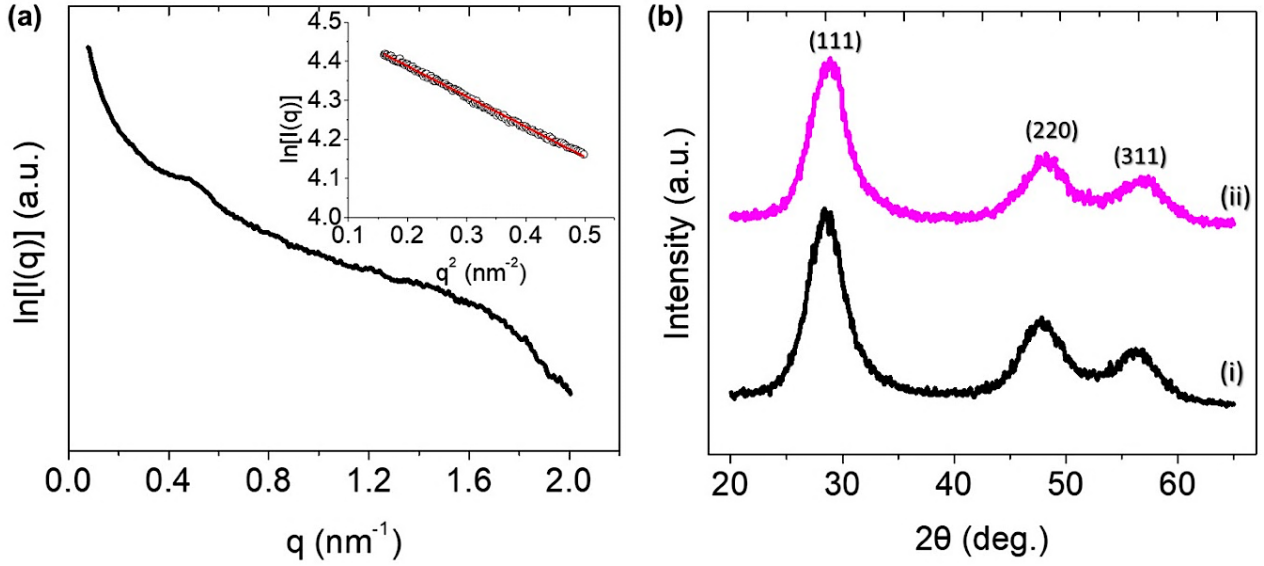

Figure 3-13: (a) Small-angle X-ray scattering of mesoporous NCA-ZnS-5 sample. Inset: the corresponding Guinier plot indicating an average particle size of constituting NCs ~5 nm. (b) XRD patterns of (i) the 3-MPA capped ZnS NCs (5 nm in size) and (ii) the corresponding mesoporous NCA-ZNS-5 structure. The diffraction peaks were indexed to the (111), (220) and (311) reflections of cubic zinc-blende phase of ZnS according to the JCPDS card no. 77-2100.

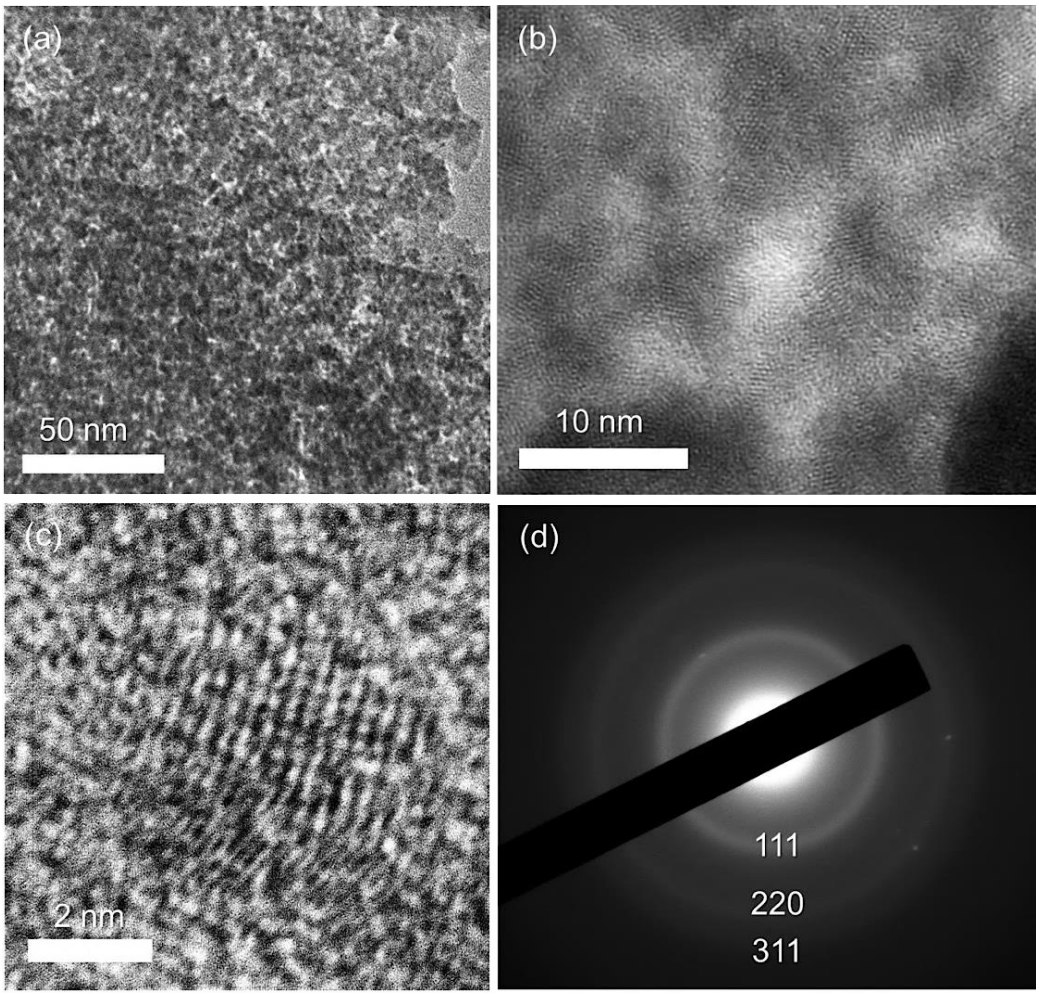

Figure 3-14: (a and b) TEM images, (c) high-resolution TEM and (d) SAED pattern for mesoporous NCA-ZnS-5 material.

Nitrogen physisorption measurements (**Figure 3-15a**) revealed that the NCA-ZnS-5 sample possesses a mesoporous network with large BET surface area and pore volume, and a narrow pore size distribution (see **Table 3-1**). Also, similar to the CdS NC assemblies, the optical absorption properties of the NCA-ZnS-5 material are an intrinsic characteristic of the assembled nanocrystal network and depend on its ZnS NC constituents, exhibiting almost identical bandgap energies (i.e., ~3.88 eV for 3-MPA-capped ZnS NCs and ~3.87 eV for the corresponding mesoporous NCA-ZnS-5 material) as shown in **Figure 3-15b**.

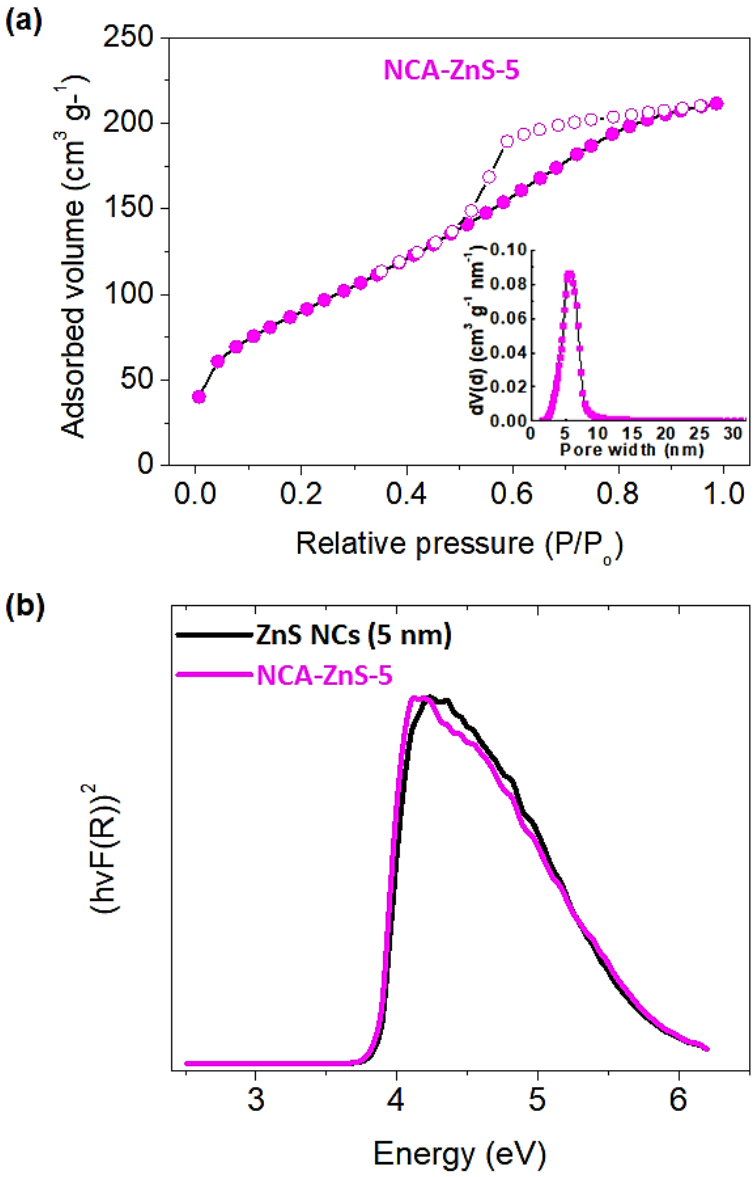

Figure 3-15: (a) Nitrogen adsorption-desorption isotherms at -196 °C of mesoporous NCA-ZnS-5 material. Analysis of the adsorption data with the BET method gives surface area of 334 m^2 g^{-1} and total pore volume of 0.33 cm^3 g^{-1}. Inset shows the NLDFT pore size distribution calculated from the adsorption branch of isotherms, indicating a pore size of ~ 5.8 nm. (b) Tauc plot derived from diffuse reflectance UV-Vis/NIR data according to the Tauc relation (eq. 21) for 5-nm-sized ZnS NCs (black line) and the corresponding mesoporous NCA-ZnS-5 sample (magenta). The onsets of the sharp linear increase are associated with electronic transitions in the energy range of ~ 3.88 eV for ZnS NCs (5 nm) and ~ 3.87 eV for mesoporous NCA-ZnS-5 material.

3.1.3 Probing photocatalytic activity of NCA-CdS mesostructure

More importantly, owing to the large internal surface area, 3D open pore structure with uniform mesopores and visible-light response, the present mesoporous CdS NC assemblies are anticipated to excel in photocatalytic reactions. For this purpose, the photocatalytic activity of mesoporous NCA-CdS-4 material was evaluated using the visible-light ($\lambda \geq 420$ nm) aerobic photo-oxidation of 1-phenylethanol to acetophenone as a probe reaction. For comparison, the photocatalytic activity of the random CdS NC aggregates (RNA-CdS-4) as well as of the commercial TiO_2 Degussa (P25) catalyst (20–30 nm particle size with ca. 50 m^2 g^{-1} BET surface area), which is a well-known photoactive material (i.e., Degussa P25 was selected as a benchmark catalyst), was also examined. The evolution of the photo-oxidation conversion of 1-phenylethanol to acetophenone presented in **Figure 3-16** shows that the mesoporous NCA-CdS-4 exhibits high reactivity, with a respective conversion factor of ~98% in 1 h. Indeed, the visible-light photocatalytic activity of NCA-CdS-4 greatly exceeds that of the RNA-CdS-4 material (~60%) and the Degussa P25 nanoparticles (~34%); notwithstanding that the photoreaction over TiO_2 nanoparticles was examined under UV light ($\lambda > 320$ nm).

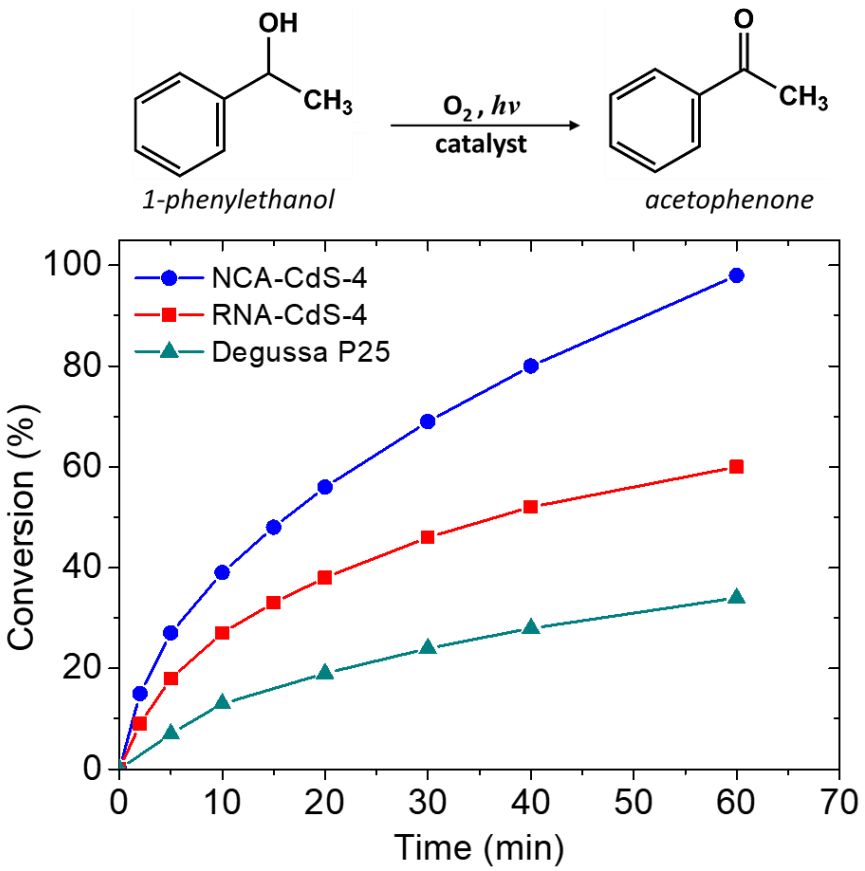

Figure 3-16: Conversion of 1-phenylethanol to acetophenone as a function of irradiation time for the mesoporous NCA-CdS-4 as well as the random aggregates of 4 nm-sized CdS NCs (RNA-CdS-4) and TiO_2 Degussa (P25) nanoparticles. Reaction conditions: 3 mL benzene containing 0.2 mmol 1-phenylethanol and 0.25 mmol catalyst, O_2 bubbling (rate ~1 mL/min), steady temperature at 20 °C, visible-light irradiation ($\lambda \geq 420$ nm). The photo-oxidation over TiO_2 nanoparticles was performed in 3 mL of CH_3CN, under UV-light irradiation ($\lambda > 320$ nm).

Analysis of the catalytic data using the pseudo-first-order reaction model $\ln(C_t/C_o) = kt$ reveals that the reaction proceeds at a faster rate over mesoporous NCA-CdS-4 (kinetic constant, k = 0.053 min^{-1}) than the random aggregates RNA-CdS-4 (k = 0.032 min^{-1}) and Degussa P25 nanoparticles (k = 0.014 min^{-1}), as shown in **Figure 3-17**. Assuming that the oxygen concentration remains constant during the reaction, the oxidation of alcohol can be considered a pseudo-first order process, in which the reaction rate is proportional to the concentration of substrate.

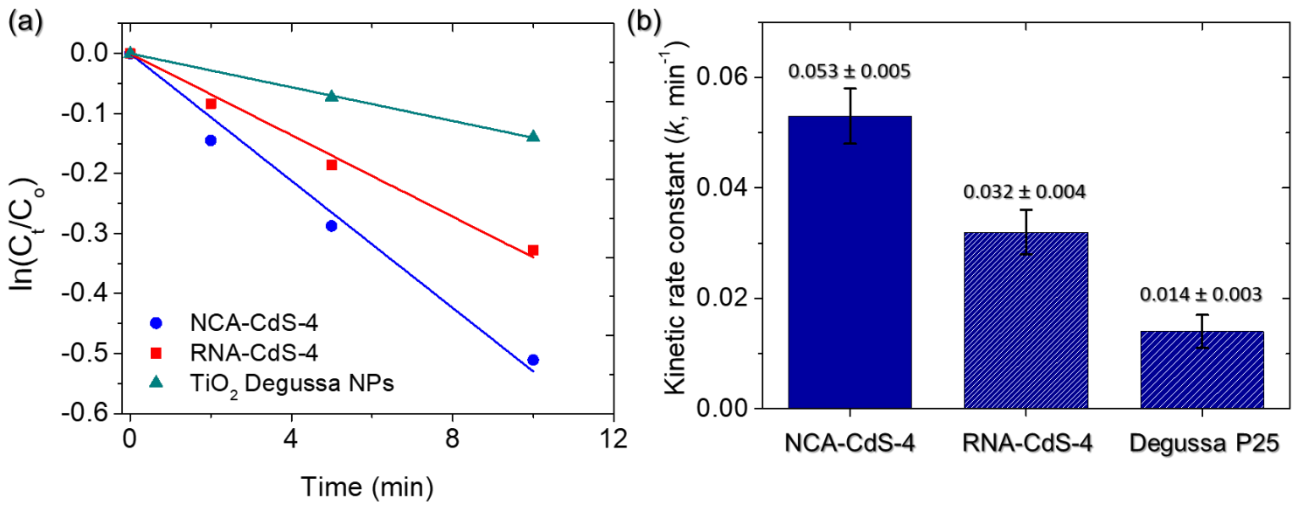

Figure 3-17: (a) Kinetic profiles of 1-phenylethanol photo-oxidation over the NCA-CdS-4, RNA-CdS-4 and Degussa P25 catalysts. C_o and C_t are the initial and final (after time t) molar concentrations of 1-phenylethanol, respectively. The lines are fit to the data. (b) Corresponding column plot of the kinetic rate constants (k).

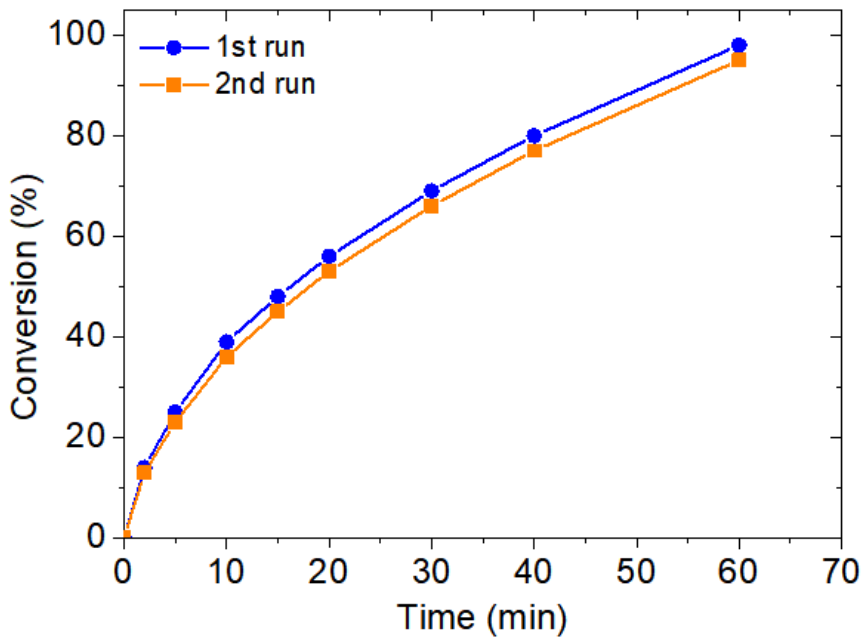

Figure 3-18: Recycling study of the mesoporous NCA-CdS-4 photocatalyst. Reaction conditions: 0.2 mmol 1-phenylethanol, 0.25 mmol catalyst, ~1 mL min^{-1} O_2, 3 mL benzene, 20 °C, visible-light irradiation (λ > 420 nm).

All these results consistently show that, despite the organic molecules remaining in the pores (ca. 7–8 wt.% as indicated from TGA analysis), the pore surface of NCA-CdS-4 is photocatalytically active and accessible to the target molecules, contributing to the high catalytic activity. It should be stressed that the activity of the mesoporous NCA-CdS-4 is among the highest reported activities for CdS-based catalytic systems, including porous aggregates of sheet-like CdS [434], mesoporous polyoxometalate-Ag_2S-CdS heterostructures [435] and CdS/graphene nano-composites [436]. The increased photocatalytic performance observed for NCA-CdS-4 can be ascribed to the small grain size of CdS NCs, which minimize the distance that photogenerated electrons and holes need to reach the solid/liquid interface, and to the 3D open pore structure which facilitates fast molecular transport, and possibly efficient light-harvesting via multiple scattering within the assembled nanoparticles. [397] Moreover, the NC-linked mesoporous networks constructed by this surfactant-templating process were also found to be quite stable under the present catalytic conditions. Catalyst recycling experiment showed that the high activity and selectivity are still retained after two consequent runs, giving a conversion percentage of 1-phenylethanol to acetophenone more than 95% in 1 h, as shown in **Figure 3-18**.

Therefore, the proposed synthetic approach of linking metal chalcogenide nanoparticles together to construct ordered mesoporous architectures, opens up great opportunities for designing and fabricating new multifunctional materials. Such novel porous materials from semiconducting NCs hold great promise for potential technological applications including photocatalysis, energy conversion and production of renewable solar fuels such as hydrogen.

3.2 Mesoporous Pt-decorated CdS NCAs Composites

As mentioned earlier, hydrogen is considered an alternative and environmentally-friendly energy carrier that has attracted broad attention in recent years as a potential solution to the global energy problem and environmental pollution. For this reason, semiconductor photocatalysis has become an intriguing approach for the economical and eco-friendly production of hydrogen from water, by using solar energy. A key element of this approach is the development of efficient photocatalysts that exhibit high visible-light activity, long-term stability and low cost. In this direction, metal-sulfides hold great promise for photocatalytic water reduction and H_2 generation, owing to their generally lower bandgap (relative to most metal-oxides) and remarkable size-dependent optical and electronic properties. Among the various investigated metal sulfide-based materials (e.g., MoS_2, $EMoS_x$ (E = Fe, Co), $Cu_xZn_{1-x}S$, etc.) [344, 437-440], CdS-based catalysts are the most extensively used in photocatalytic H_2 production from water [341, 371, 379, 390, 396, 441-443] due to the visible-light photoresponse (E_g ~2.3-2.4 eV), high electron mobility (~350 $cm^2 V^{-1} s^{-1}$) and favorable conduction

band-edge potential of CdS, which is well above the thermodynamic threshold for water reduction (–0.41 V *vs* NHE, pH = 7). However, the hydrogen evolution activity of single-component CdS catalysts is often plagued by the slow transfer of surface-reaching holes to electrolytes and poor electron-hole separation yield, which lead also to anodic photocorrosion and gradual degradation of the catalysts. Therefore, one of the main challenges in designing effective CdS-based photocatalysts is to eliminate the competitive process of charge-carrier recombination and improve the kinetics of charge-transfer processes. In this respect, one of the most effective methods to increase the lifetime of photogenerated carriers in CdS materials is the surface-modification with metal nanoparticles, especially noble metals such as Au, Pt, Pd, Rh and Ru, as co-catalysts (see section 1.5.3.3). These metal nanoparticles are considered to act as effective electron acceptors, facilitating the electron injection from semiconductor to metal and thus increasing the charge separation efficiency. [444, 445] In addition, noble metal nanoparticles, can decrease the kinetic barrier for interfacial electron transfer across the semiconductor/electrolyte interface, thus promoting hydrogen evolution catalysis. To this end, metal Pt having a high work function (Φ ~ 5.6 eV) [446] and a lower metal-hydrogen bond strength (see **Figure A-6** in the Appendix section) has been recognized as one of the most effective co-catalysts in photocatalytic hydrogen evolution reaction. [373, 447] On the other hand, to improve hole-transport properties and enhance the hydrogen evolution kinetics, a suitable hole-scavenger that can be oxidized during the photocatalytic process is essential in this system. It has been suggested that usage of sacrificial reagents such as S^{2-}/SO_3^{2-} not only promote hydrogen evolution by consuming the photogenerated holes, but also prevent sulfur-containing catalysts (such as CdS) from anodic corrosion. [337, 341, 448] Also, recent studies have shown that hole removal is a rate-limiting step and the driving force for hole-scavenging is strongly related to the production rate of hydrogen in CdS-based systems. [356, 357] On this basis, Simon et al. recently demonstrated an efficient fast transport mechanism for photoexcited holes, by employing a $^{\bullet}OH/^{-}OH$ redox couple, functioning as a shuttle to efficiently mediate the hole transfer from the CdS surface to the hole scavenger (ethanol), resulting in enhanced H_2-evolution rates. [358]

This section describes the design and fabrication of novel mesoporous composites of Pt-decorated CdS NCAs with variable size of Pt nanoparticles, and the investigation their photocatalytic H_2-production activity under visible-light irradiation. The reactivity of mesoporous CdS NCAs using different hole-scavengers as well as the effect of Pt nanoparticle-size on the H_2-generation activity, are also explored.

3.2.1 Synthesis of mesoporous Pt-CdS NCAs

Following the aqueous synthetic route as described previously — involving an EISA process with oxidative coupling of thiol-capped CdS NCs in the presence of an amphiphilic polyoxoethylene-*b*-cetyl ether (Brij-58) BCP-template [402] — ordered 3D mesostructures of CdS nanocrystal assemblies (NCAs) were first prepared (using 4 nm-sized NCs as starting materials), and then the materials obtained after template removal were decorated with Pt nanoparticles of variable size (ranging from 1.8 to 3.3 nm). [404] The deposition of Pt onto the CdS NCAs surface was realized by a straightforward photochemical reduction method under visible-light irradiation ($\lambda \geq 420$ nm), using appropriate amounts of K_2PtCl_6 (corresponding to various wt.% Pt loadings) and triethylamine (TEA) as hole scavenger (~25-fold excess compared to CdS). Besides effective hole scavenging, the presence of TEA creates an alkaline reaction solution (pH ~10) in which Pt^{4+} species can be easily reduced to metallic Pt^0 by the photoexcited electrons on the CdS surface. It has been suggested that the promotional effect of alkaline conditions on Pt reduction is attributable to enhanced hydrolysis of $PtCl_6^{2-}$ to species containing fewer Cl^- ions, such as $Pt(OH)_5Cl^{2-}$ and $Pt(OH)_6^{2-}$, which are more susceptible to reduction. [373] A schematic overview of the Pt photo-deposition process on the surface of mesoporous CdS NCAs is illustrated in **Figure 3-19**. By this procedure, a series of Pt-decorated mesoporous CdS NCAs composites were prepared with various Pt loadings, denoted as n% Pt-CdS (where n = 1, 2, 5 and 7 wt.%).

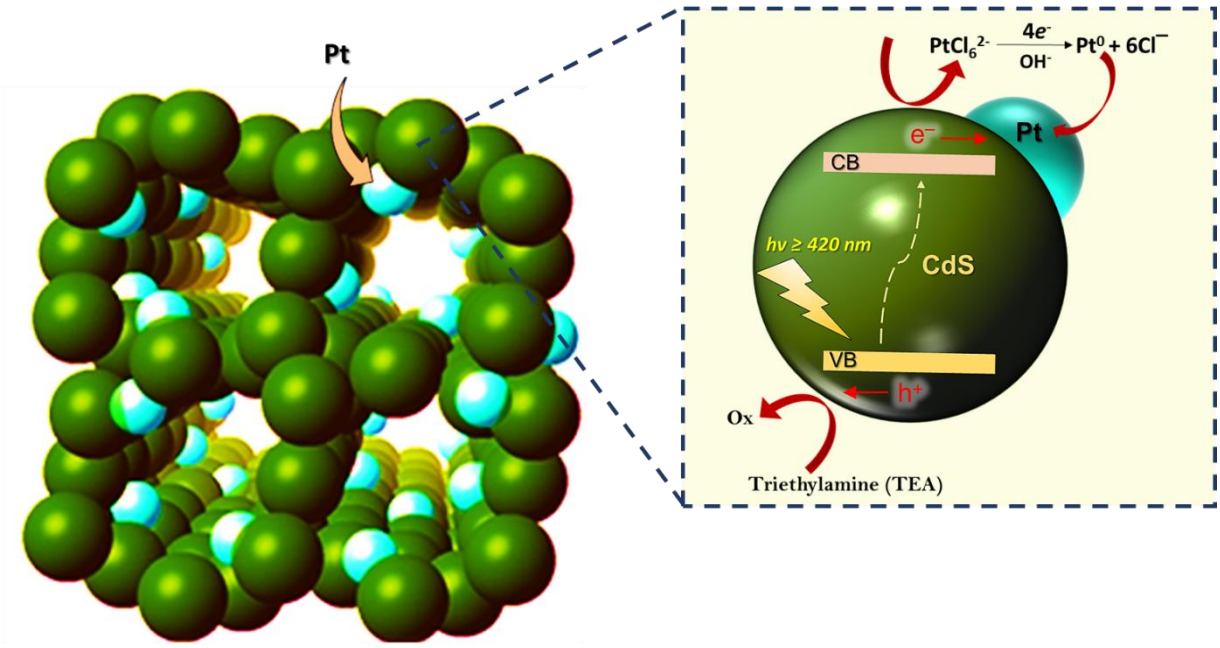

Figure 3-19: Schematic illustration of the photo-deposition process of Pt nanoparticles on the surface of mesoporous CdS NCAs.

3.2.2 Structural characterization of photocatalysts

The chemical composition of the as-obtained Pt-decorated CdS NCAs was determined by energy dispersive X-ray spectroscopy. The EDS spectra of the samples showed strong Cd and S signals with a molar ratio of Cd/S very close to the expected 1:1 stoichiometry. Also, EDS analysis confirmed the presence of platinum at different Pt/Cd ratios (**Figure 3-20)**, which correspond to Pt loadings from ~1 to ~7 wt% as shown in **Table 3-2**. Note that the Pt content, as obtained by EDS, is very close to those expected from the stoichiometry of reactions (within ~0.2 wt.% deviation), suggesting the complete deposition of Pt onto the CdS NCAs surface.

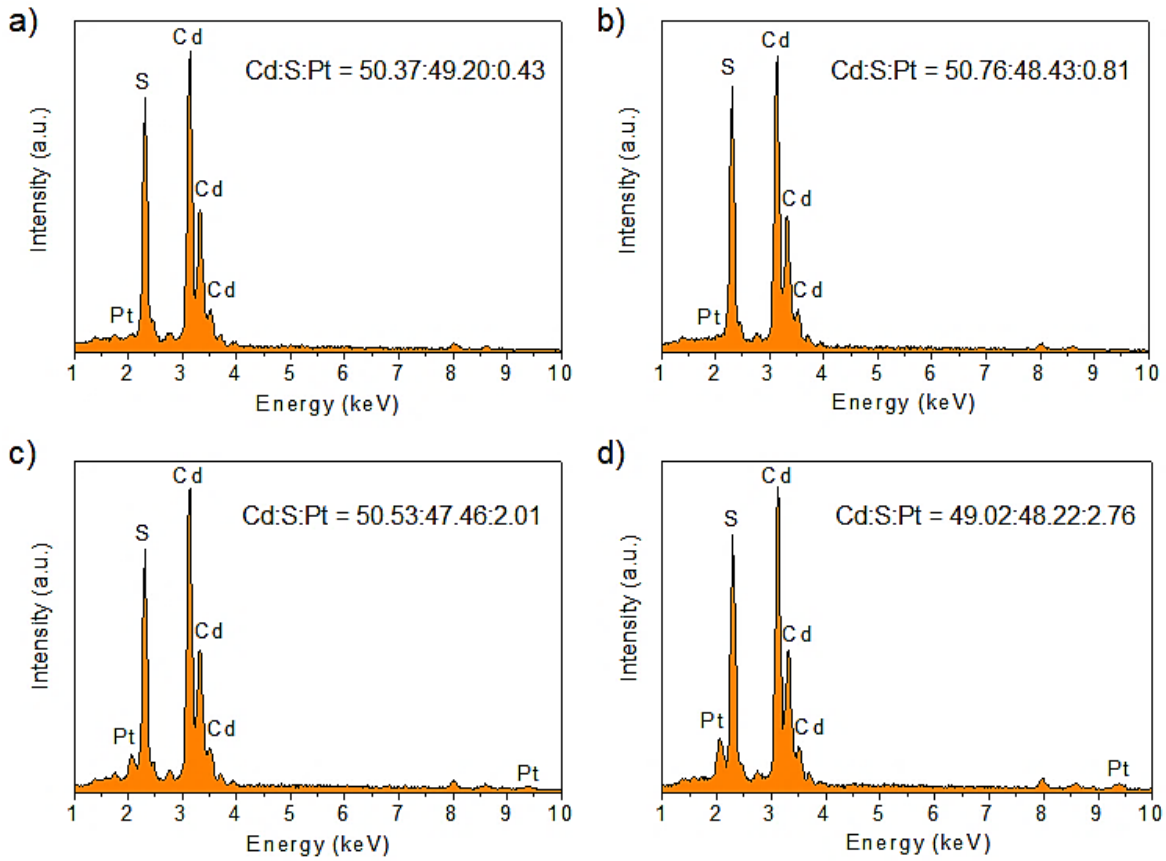

Figure 3-20: Typical EDS spectra of the mesoporous Pt-decorated CdS NCAs: a) 1% Pt-CdS, b) 2% Pt-CdS, c) 5% Pt-CdS and d) 7% Pt-CdS.

Scanning and transmission electron microscopy along with selected-area electron diffraction were utilized to characterize the morphology and crystal structure of the as-prepared materials. The SEM images of the 5% Pt-CdS NCAs sample, which is the most active catalyst in this study, indicate an irregular 3D porous morphology composed of a network of very small particles with sizes less than 7 nm (**Figure 3-21**).

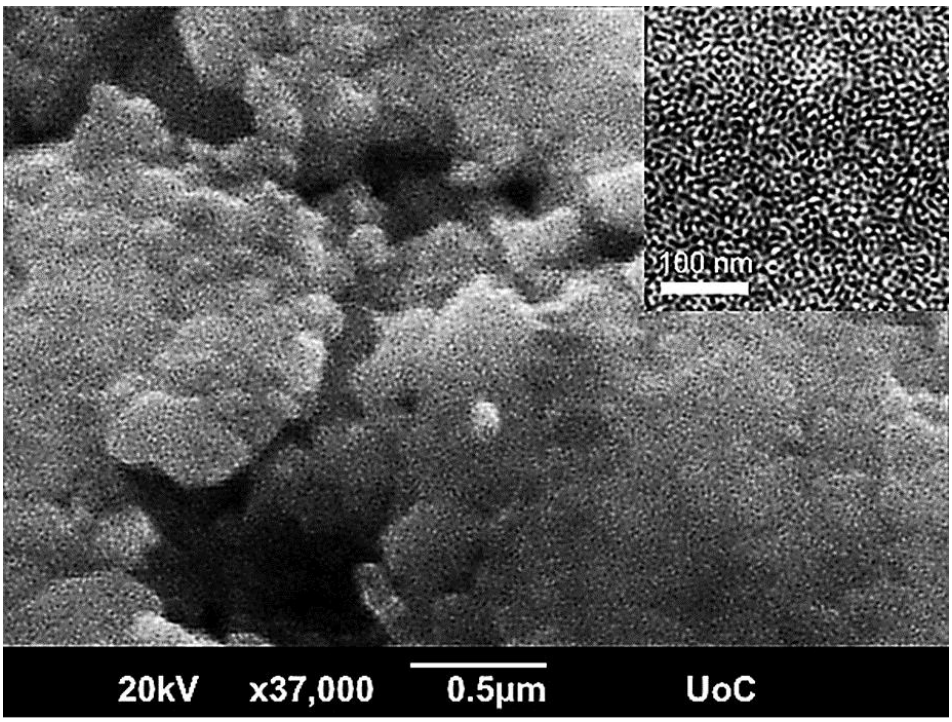

Figure 3-21: Typical SEM images of the 5% Pt-CdS NCAs catalyst.

The microstructure of the 5% Pt-CdS NCAs catalyst was further investigated by TEM and a representative image is shown in **Figure 3-22a**. The image shows a highly porous network consisting of connected CdS nanoparticles with diameter ~4–5 nm, which is consistent with the particle size of the starting CdS NC building blocks (ca. 4.6 nm). This indicates minimal coarsening of CdS NCs during the oxidative polymerization process. Note that the size of the starting thiol-capped colloidal CdS NCs was determined from their bandgap, obtained by UV-Vis absorption spectrum (see **Figure 3-22d**), and using the Brus equation (**eq. 22**). A closer TEM observation also reveals small Pt nanoparticles (appearing as darker spots) that are randomly distributed over the CdS NCAs mesostructure. By means of this technique, the average diameter (d_p) of the Pt nanoparticles was estimated to be ~2.6 nm (see inset of **Figure 3-22a**).

Moreover, the high-resolution TEM image in **Figure 3-22b** confirms the good crystallinity of the 5% Pt-CdS sample, showing lattice spacings of 2.3 and 3.4 Å that correspond to the *d* spacing of the (111) lattice planes of face-centered cubic (fcc) Pt and zinc-blende CdS, respectively. Besides, the SAED pattern in **Figure 3-22c** displays a series of diffuse Debye-Scherrer rings, which can be assigned to the cubic phase (zinc-blende) of CdS, further confirming the well-defined nanocrystalline structure of CdS.

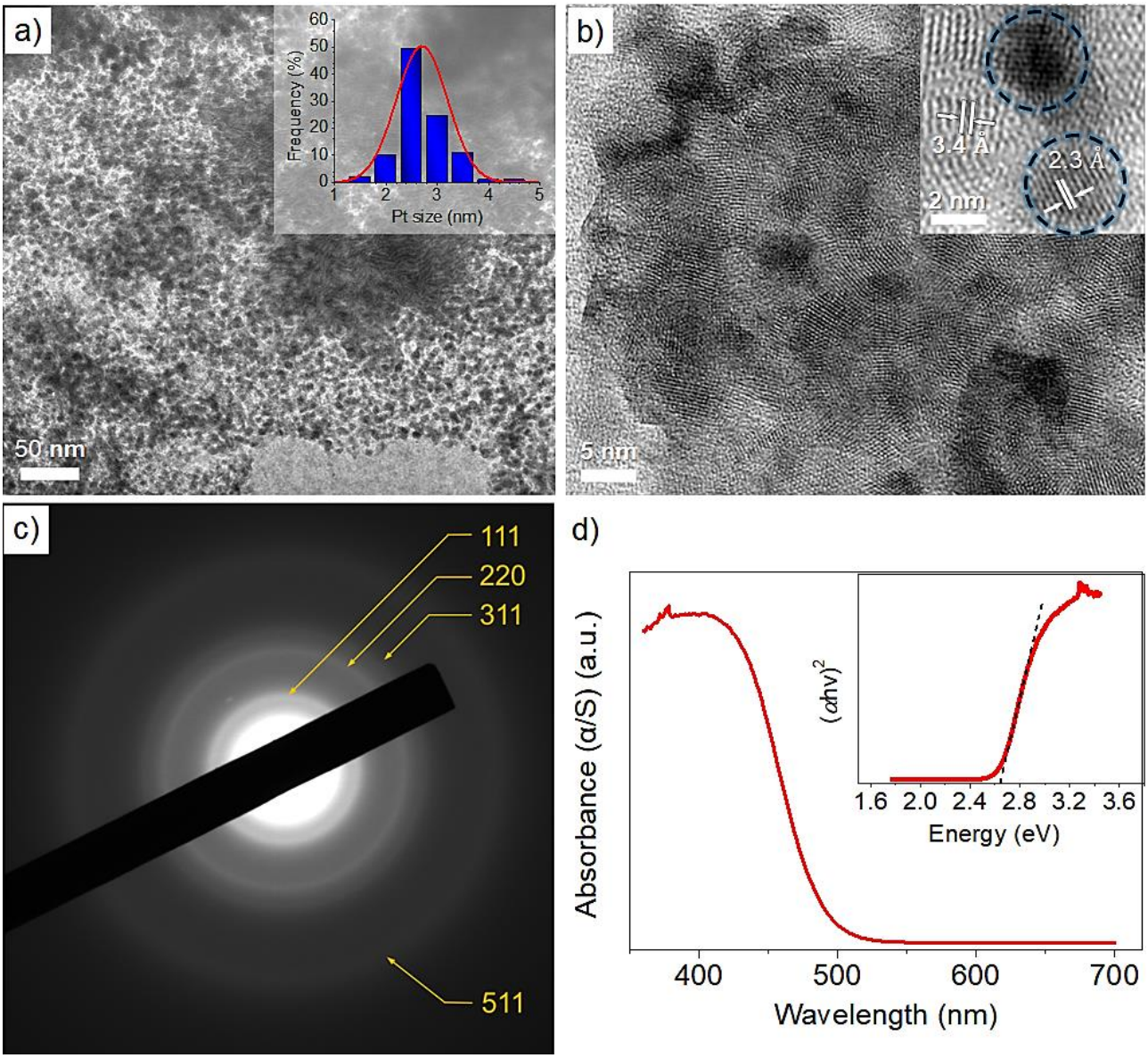

Figure 3-22: (a)Typical TEM image and Pt particle size distribution plot (inset), (b) HRTEM images showing the corresponding (111) crystal planes of cubic CdS and fcc Pt lattices (indicated by the circle frames), and c) SAED pattern of the mesoporous 5% Pt-CdS NCAs sample. d) Optical absorption spectrum of thiol-capped CdS NCs indicating a sharp absorption edge at 468 nm (2.65 eV). The average size of the starting CdS nanoparticles (ca. 4.6 nm) was calculated based on the estimated bandgap from the optical data and using the Brus equation (eq. 22).

Furthermore, the size histograms obtained after TEM analyses (based on a count of more than 50 individual Pt nanoparticles) on the respective Pt-CdS NCAs catalysts containing 1, 2, and 7 wt.% Pt, showed that the average diameter of the metal Pt nanoparticles was 1.8, 2.1, and 3.3 nm, respectively (**Figure 3-23**). Taken together, the TEM data for all the Pt-decorated samples reveal that the particle size of Pt on CdS NCAs consistently increased with increasing Pt content (see **Table 3-2**), as expected.

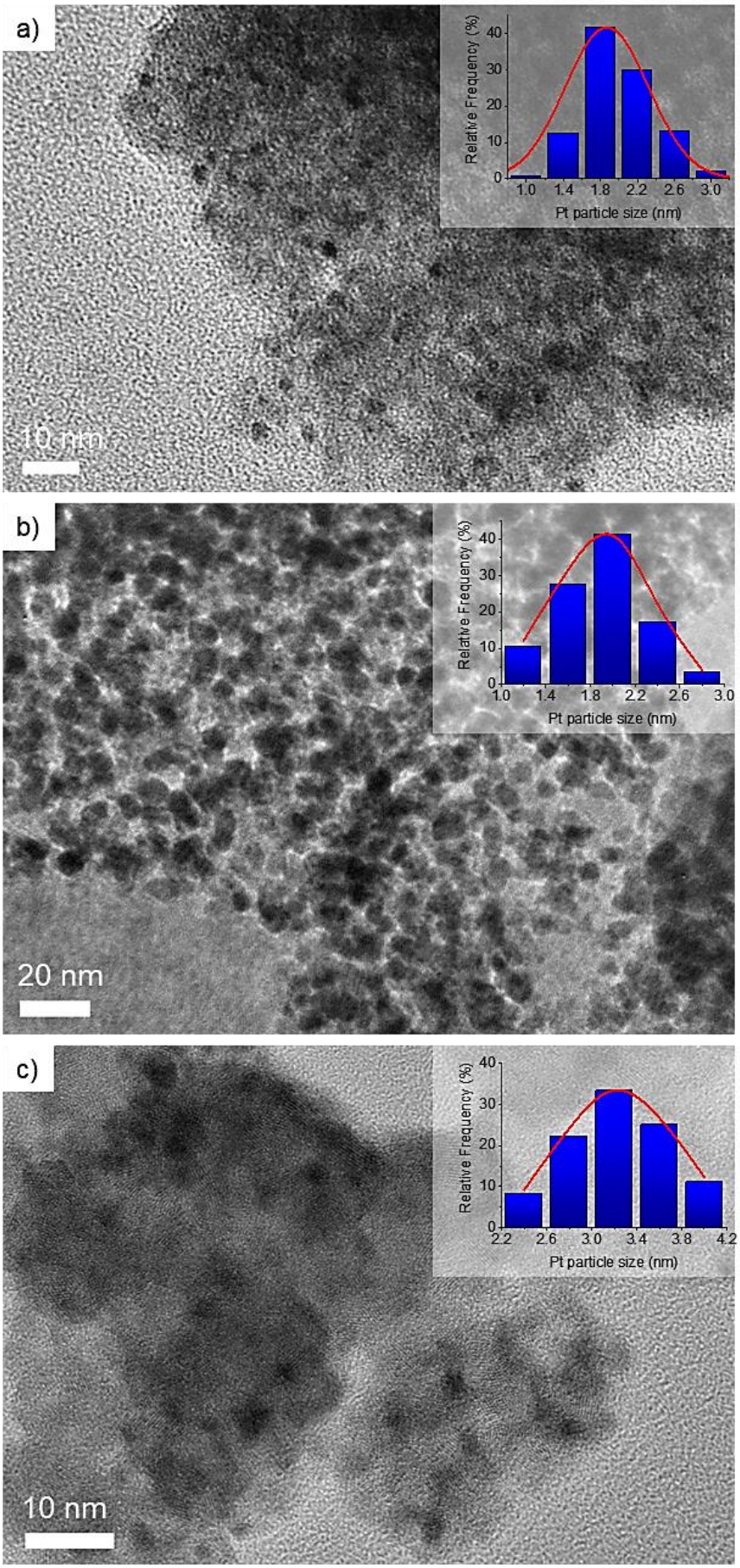

Figure 3-23: Typical TEM images and (insets) the corresponding particle size distribution histograms of the Pt nanoparticles for mesoporous (a) 1% Pt-CdS, (b) 2% Pt-CdS and (c) 7% Pt-CdS materials.

The crystallinity of the as-prepared materials was also verified by X-ray diffraction. The XRD patterns of the mesoporous Pt-CdS NCAs show three intense diffraction peaks at 2θ scattering angles of 20–60°, which, according to the SAED diffraction pattern can be indexed as the (111), (220), and (311) planes of the cubic CdS (JCPDS card no. 42–1411), see **Figure 3-24**. Of note, the remarkable peak broadening of the XRD reflections suggests a very small grain composition, which is in agreement with TEM observations. A peak-width analysis using the Scherrer's equation (**eq. 19**) gives an average domain size of CdS crystallites at ~2.1–2.4 nm. Convincing evidence of the presence of crystalline Pt was obtained in the XRD pattern of high Pt-loaded sample (7% Pt-CdS), which shows two weak features at ~40° and ~46° that can be assigned to the (111) and (200) planes of the fcc Pt structure. The lack of diffraction peaks due to metallic platinum in the catalysts with lower Pt loadings (<7 wt.%) is attributed to the small grain size and high dispersion of Pt nanoparticles on the CdS NCAs surface.

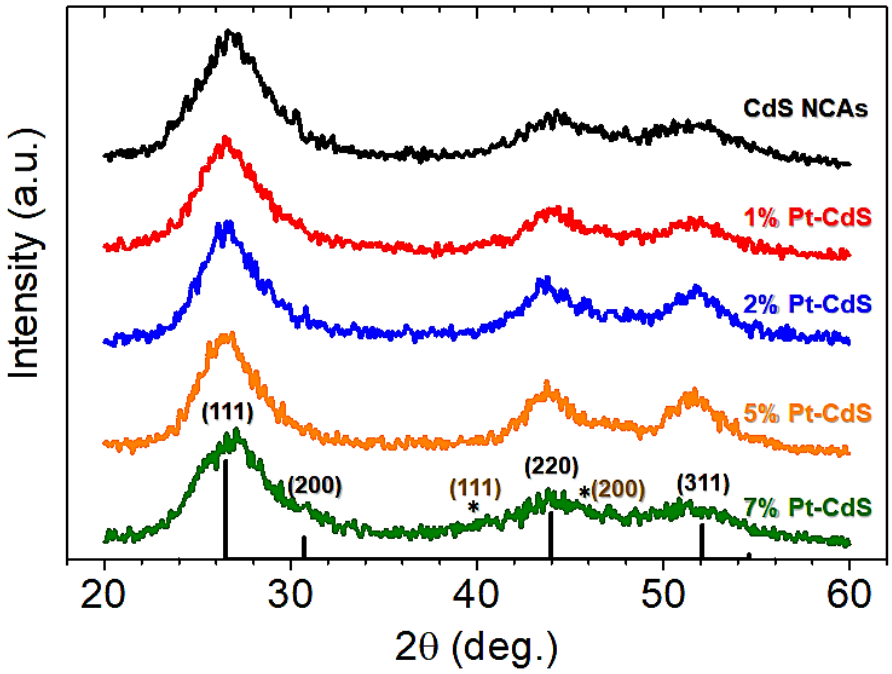

Figure 3-24: XRD patterns of mesoporous CdS and Pt-CdS NCAs materials. The standard diffraction lines of zinc blende CdS (vertical solid lines) according to the JCPDS card no. 42–1411 are also given. The symbol (*) denotes the diffraction features corresponding to metal Pt.

The porosity of the as-prepared materials was evaluated by nitrogen physisorption measurements at −196 °C. **Figure 3-25a** compares the N_2 adsorption and desorption isotherms and the corresponding pore size distribution plots of the pristine mesoporous CdS and 5% Pt-CdS NCAs samples. The corresponding plots for the other Pt-decorated CdS NCAs samples are also shown in **Figure 3-25b-d**. All the samples exhibit typical type IV isotherms with a pronounced H2-type hysteresis loop, which according to IUPAC classification (see A.1 and A.2 in the Appendix), which are characteristic of mesoporous materials with interconnected structure. [412] The small but resolved adsorption step

at mid-relative pressure range (P/P_o = 0.4–0.5) is related to the capillary condensation of nitrogen in narrow-sized mesopores. [427] On the basis of the Brunauer-Emmett-Teller (BET) model, the Pt-decorated CdS NCAs were found to have large specific surface areas (~225–260 $m^2 g^{-1}$), which are slightly lower than the measured surface area (274 $m^2 g^{-1}$) of the pristine CdS sample (see **Table 3-2**).

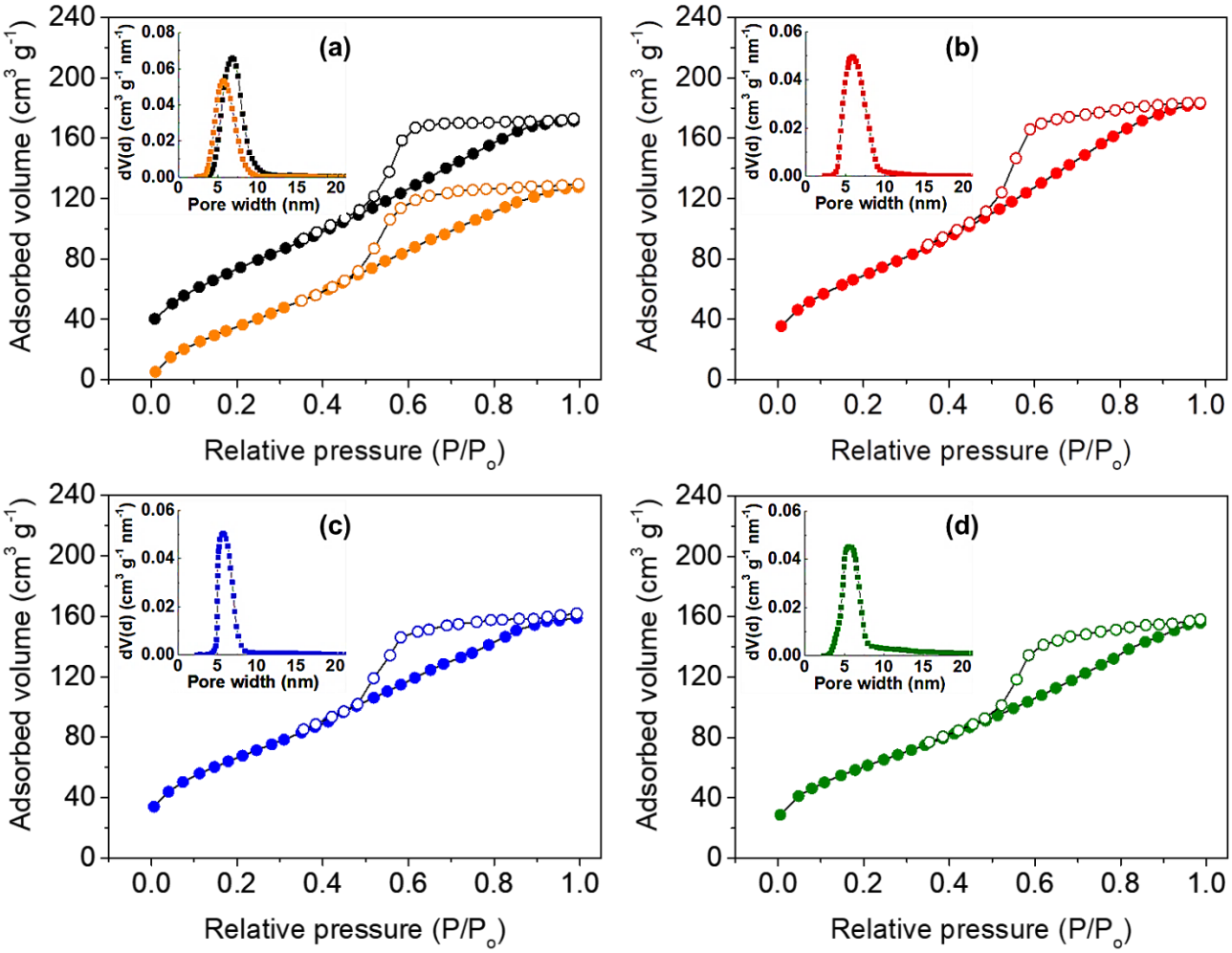

Figure 3-25: (a) N_2 adsorption and desorption isotherms at -196 °C for the pristine mesoporous CdS (black) and 5% Pt-CdS (orange) NCAs materials. The N_2 isotherms of 5% Pt-CdS NCAs are offset by 30 $cm^3 g^{-1}$ for clarity. Inset: the corresponding NLDFT pore size distributions derived from the adsorption branch of isotherms. (b-d) The respective N_2 isotherms and NLDFT pore size distributions (insets) for the 1% Pt-CdS (red), 2% Pt-CdS (blue) and 7% Pt-CdS (green) NCAs.

The pore width in these materials was assessed from the adsorption branch of isotherms using the NLDFT method. [414] The fit results indicate quite narrow distributions of pore sizes with a peak maximum of ~6.6 nm for pristine CdS and around 5.7–6.1 nm for Pt-CdS NCAs, as shown in the insets in **Figure 3-25**. Associated with the TEM results, the continuous decrease in surface area and pore size for Pt-loaded materials is consistent with deposition of the Pt nanoparticles inside the pores of CdS NCAs. Regardless, the pore structure of the Pt-decorated materials still remains largely open

and accessible. The textural parameters of the pristine mesoporous CdS and the respective Pt-CdS NCAs samples are summarized in **Table 3-2**.

Table 3-2: Analytical data and textural properties of the mesoporous CdS and Pt-decorated CdS NCAs.

Sample	Pt loading[a)] (wt.%)	Pt size[b)] (nm)	Surface area (m^2 g^{-1})	Pore volume (cm^3 g^{-1})	Pore size (nm)	Energy gap (eV)
CdS NCAs	0	0	274	0.28	6.6	2.63
1% Pt-CdS	1.14	1.8±0.4	260	0.26	6.1	2.51
2% Pt-CdS	2.12	2.1±0.4	246	0.23	5.9	2.48
5% Pt-CdS	5.08	2.6±0.5	230	0.21	5.9	2.43
7% Pt-CdS	7.07	3.3±0.6	225	0.21	5.7	2.39

[a)] Based on EDS analysis. [b)] Average Pt particle size (d_p) on the basis of TEM analysis.

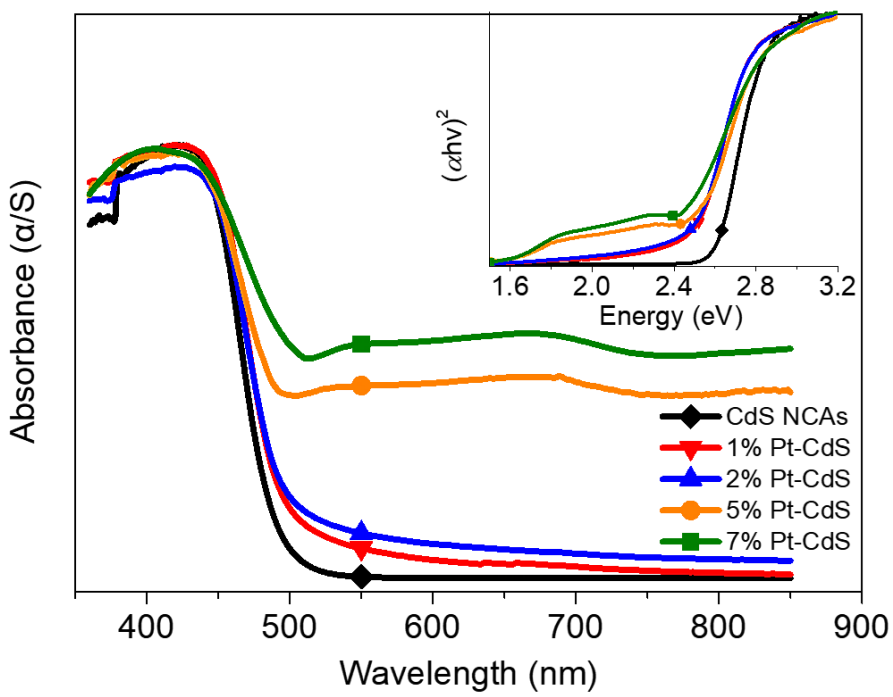

Figure 3-26: UV–vis/ NIR absorption spectra of mesoporous CdS and Pt-decorated CdS NCAs. Inset: the corresponding Tauc plots [$(\alpha h\nu)^2$ *vs* photon energy ($h\nu$), where α is the absorption coefficient, h is Planck's constant and ν is the light frequency].

The electronic structure of the pristine and Pt-decorated CdS NCAs was investigated with UV–vis/NIR diffuse reflectance spectroscopy. The optical absorption spectrum of CdS NCAs, transformed from the diffuse reflection data according to the Kubelka–Munk function (**eq. 20**), displays a sharp absorption onset at around 471 nm (2.63 eV), assigned to the interband transition of CdS NCs (**Figure 3-26**). The relevant blue shift in the energy gap compared to the bulk CdS (~2.4 eV) is ascribable to the quantum size effects of the constituent CdS NCs due to their very small size.

As for Pt-CdS NCAs, with increasing Pt loading, a distinct red shift in optical absorption spectra and an enhanced absorption tail in the 550–760 nm region can be clearly seen. In particular, the energy bandgap of Pt-CdS NCAs materials varies systematically from 2.50 to 2.39 eV as the loading content of Pt increases from 1 to 7 wt% (see **Table 3-2** and **Figure 3-26, inset**). This behavior is probably related to the strong exciton–plasmon interactions between quantum-confined electronic states in CdS NCs and dielectric-confined electromagnetic modes in Pt nanoparticles. [449] The broad absorption tail at wavelengths longer than 550 nm is possibly attributed to a dumping effect in the localized surface plasmon resonance (LSPR) of Pt nanoparticles. [273, 450, 451]

3.2.3 Photocatalytic water reduction study

The photocatalytic water reduction experiments were carried out in an airtight reaction cell filled with argon to evaluate the activity of Pt-decorated CdS NCAs towards H_2 production. The evolved H_2 was sampled with a syringe and analyzed using a gas chromatograph (GC) equipped with a thermal conduction detector. The catalyst amount was first optimized by measuring the H_2 evolution for different concentrations of CdS NCAs in an aqueous solution containing Na_2S (0.35 M) and Na_2SO_3 (0.25 M). As shown in **Figure 3-27**, with increasing catalyst concentration the H_2-evolution rate increased until reaching a maximum at 1.0 g L^{-1}. The hydrogen evolution improvement with increasing the catalyst amount can be attributed to the increase in light absorption by the catalyst nanoparticles. On the other hand, additional increase in the CdS NCAs concentration (2 g L^{-1}) slightly decreased the production rate of H_2, probably due to a light-scattering effect from the excessive particles in the reaction solution.

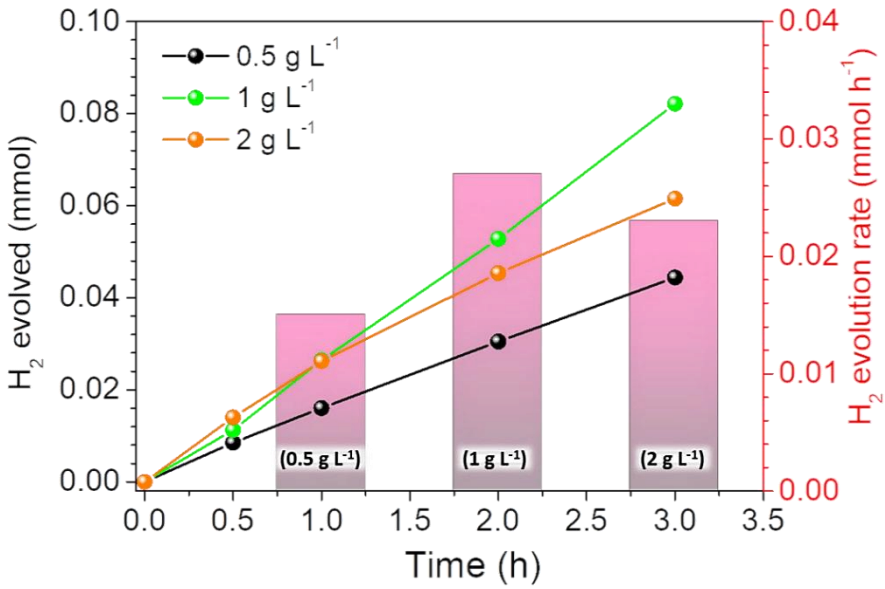

Figure 3-27: Photocatalytic H_2 production (lines) and average H_2 evolution rates over 3-h irradiation period (columns) under visible light ($\lambda \geq 420$ nm), for various concentrations of mesoporous CdS NCAs catalyst. Reaction conditions: 20 mL of 0.35 M Na_2S and 0.25 M Na_2SO_3 aqueous solution at 20 °C.

Next, the reactivity of surface-reaching holes towards various sacrificial electron donors — such as triethylamine (TEA), ethanol, Na_2S/Na_2SO_3, and ethanol/NaOH — and its effect in the water reduction activity of CdS NCAs, was also explored. Among the various hole scavengers, ethanol (10% v/v) in a 5 M NaOH solution (pH ≈ 14.7) was found to be the most efficient, leading to a marked enhancement in H_2 evolution rate (**Figure 3-28**). In agreement with previous work [358], this enhancement relies on the higher mobility of the molecular redox couple $^{\bullet}OH/^{-}OH$ and its great ability to react with both semiconductor and sacrificial agent (i.e., ethanol). Namely, in highly alkaline solutions (pH > 14), the photocatalytic oxidation process entails fast diffusion of hydroxyl anions (^{-}OH) to the semiconductor surface, where they are rapidly oxidized by the VB holes into hydroxyl radicals ($^{\bullet}OH$). These $^{\bullet}OH$ radicals can then diffuse away and oxidize ethanol to acetaldehyde (and/or acetic acid) at a higher rate than direct oxidation of ethanol by the photogenerated holes. Therefore, a kinetically hindered hole-transfer reaction is replaced with two faster reactions, thus preventing the competitive electron–hole recombination and accelerating the water reduction process. [358] However, in neutral solution (pH = 7), the redox potential of $^{\bullet}OH/^{-}OH$ pair lies in the range of 2.0–2.1 V *vs* NHE, that is, more positive than the VBM potential of CdS (ca. 1.8–1.9 V *vs* NHE). This means that the VB holes of CdS are thermodynamically unable to oxidize ^{-}OH. [452] Nevertheless, as a common feature of many chalcogenide semiconductors, the band-edge potentials of CdS do not follow the Nernstian relation with pH (−59 mV per pH unit) but shift by about −33 mV per unit pH increase. [340, 358] As a result, a crossover between the VBM of CdS and redox potential of $^{\bullet}OH/^{-}OH$ pair is expected to occur at high pH values (pH ≈ 14–15), thus allowing the formation of $^{\bullet}OH$ (see **Figure A-7** in the Appendix).

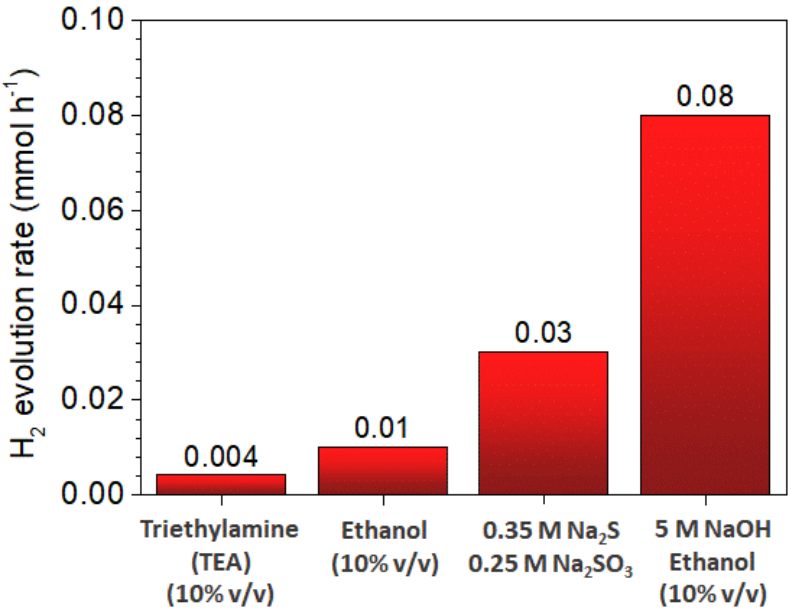

Figure 3-28: Effects of different hole scavengers on the H_2 evolution rate of CdS NCAs catalyst under visible light irradiation (λ ≥ 420 nm). *Reaction conditions:* 20 mg catalyst, 20 mL water/sacrificial reagent solution, 20 °C, 3 h reaction time.

In the following, the effect of Pt surface-deposition on the H_2-production activity of CdS NCAs was investigated. All photocatalytic reactions were performed under visible-light irradiation ($\lambda \geq 420$ nm) using a fixed catalyst concentration (1 g L^{-1}), with ethanol (10% v/v) as a hole scavenger in alkaline (5 M NaOH) solution. The time-courses of photocatalytic H_2-evolution for the Pt-CdS NCAs catalysts with different Pt loadings are compared in **Figure 3-29a**. It can be seen that the photocatalytic activity of the samples increases with increasing Pt content and reaches an optimum at 5 wt.%.

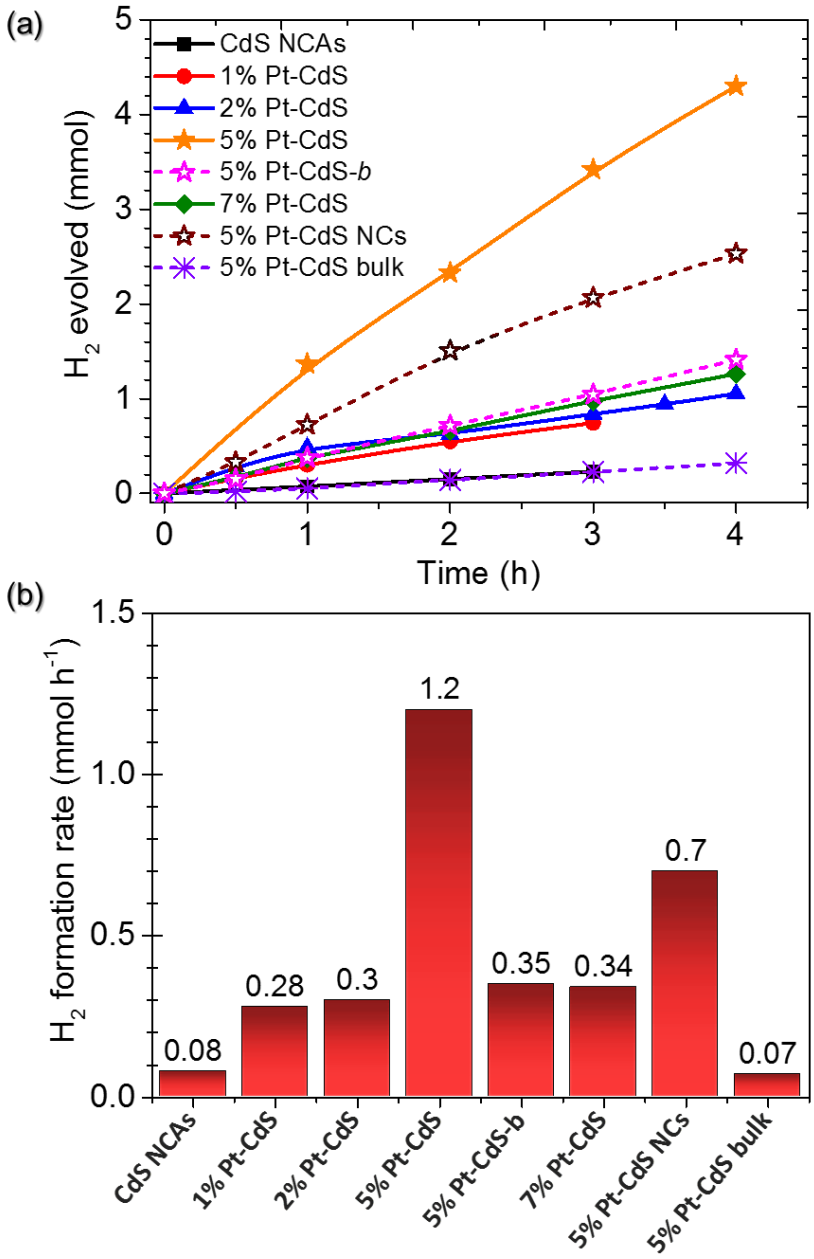

Figure 3-29: (a) Time courses of photocatalytic H_2 production (lines), and (b) the corresponding average H_2-evolution rates (columns), for the mesoporous CdS NCAs and Pt-decorated CdS catalysts. The respective results for the mesoporous Pt-loaded CdS sample (5% Pt-CdS-*b*) with smaller Pt nanoparticles (~1.9 nm), as well as the Pt-decorated colloidal CdS NCs (5% Pt-CdS NCs) and the Pt-loaded bulk CdS (5% Pt-CdS bulk), are also shown for comparison. All photocatalytic reactions were performed as follows: 20 mg of catalyst dispersed in a 20 mL aqueous solution containing 5 M NaOH and 10% (v/v) ethanol; 300-W Xe light radiation with a long-pass cut-off filter allowing $\lambda \geq 420$ nm.

Of particular note, the 5% Pt-CdS NCAs catalyst can achieve an average H_2-evolution rate of 1.2 mmol h^{-1} (**Figure 3-29b**) under the examined reaction conditions (or ~60 mmol h^{-1} g^{-1} mass activity), exhibiting an unprecedented 70% apparent quantum yield (QY) at 420 nm (calculated according to **eq. 26**, with an average light intensity of 7 mW cm^{-2}, corresponding to a number of incident photons of about 1.48×10^{16} s^{-1}). Interestingly, this is the highest recorded H_2-evolution quantum efficiency for Pt-loaded CdS photocatalytic systems without the combined use of oxidation co-catalysts. [292] For instance, Bao et al. have reported a nanoporous Pt-loaded (13 wt. %) CdS catalyst exhibiting a QY of ~60% at 420 nm [396], while Li et al. have demonstrated a very high QY (~93% at 420 nm) for a dual co-catalyst Pt-PdS/CdS system but with a QY of only 50% for the respective Pt/CdS catalyst (i.e., without the use of PdS as oxidation co-catalyst) [371]. Moreover, a ternary CdSe@CdS-Pt photocatalytic system has also been reported recently, exhibiting a record QY of near-unity (i.e., ~100% at 455 nm). [453] This photocatalyst, however, was consisted of single Pt-tipped CdS nanorods with CdSe-seeds embedded asymmetrically within the rod structure, which acted as hole collector co-catalysts. By comparison, the apparent QY obtained from a double Pt-decorated CdS nanorod was about 59%, which is significantly lower than that of the present mesoporous 5% Pt-CdS catalyst. Also, previous studies on similar unseeded (i.e., without CdSe) Pt-tipped CdS nanorod systems have shown very low quantum efficiencies for H_2 production. [356, 357, 454]

In order to reassess the catalyst amount in the 5 M NaOH/ethanol (10% v/v) reaction solution, further control experiments over the concentration of mesoporous 5% Pt-CdS NCAs showed that the H_2-evolution rate reaches again a maximum at 1 g L^{-1} (**Figure 3-30**), indicating that is the optimum catalyst concentration under the catalytic conditions.

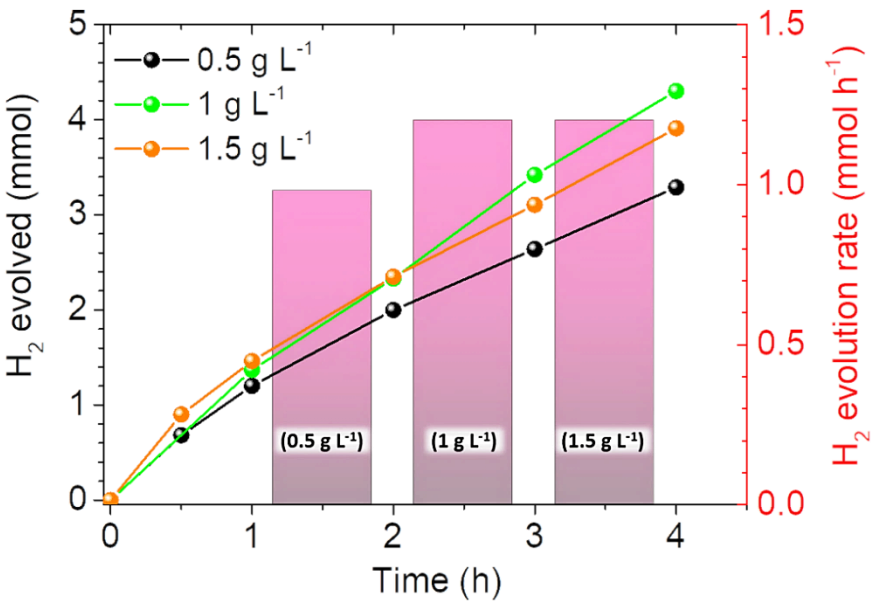

Figure 3-30: Photocatalytic H_2 production (lines) and average H_2 evolution rates over 4-h irradiation period (columns) under visible light (λ≥420 nm) for various concentrations of 5% Pt-CdS catalyst. Reaction conditions: 20 mL of 5M NaOH aqueous solution containing 10% (v/v) ethanol at 20 °C.

In addition to Pt loading, morphological effects are also contributing to the high photocatalytic activity of mesoporous Pt-CdS catalysts. To verify this, the hydrogen evolution activity of mesoporous 5% Pt-CdS NCAs was compared with that of 5 wt.% Pt-loaded bulk CdS microparticles and 3-MPA-capped CdS colloidal NCs. For this study, Pt deposition on CdS microparticles (surface area ~79 $m^2 g^{-1}$) was performed using a similar photochemical reduction process as that of the Pt-CdS NCAs. For the Pt-CdS NCs, Pt nanoparticles were deposited on the surface of 3-MPA-capped colloidal CdS NCs (size ~4–5 nm) by in situ photo-reduction of $PtCl_6^{2-}$ ions for 1 h prior to the photocatalytic test. EDS and TEM analysis showed that both Pt-CdS bulk and Pt-CdS NCs samples contain about 5 wt.% of Pt with an average diameter of ~3–4 nm (**Figure 3-31**).

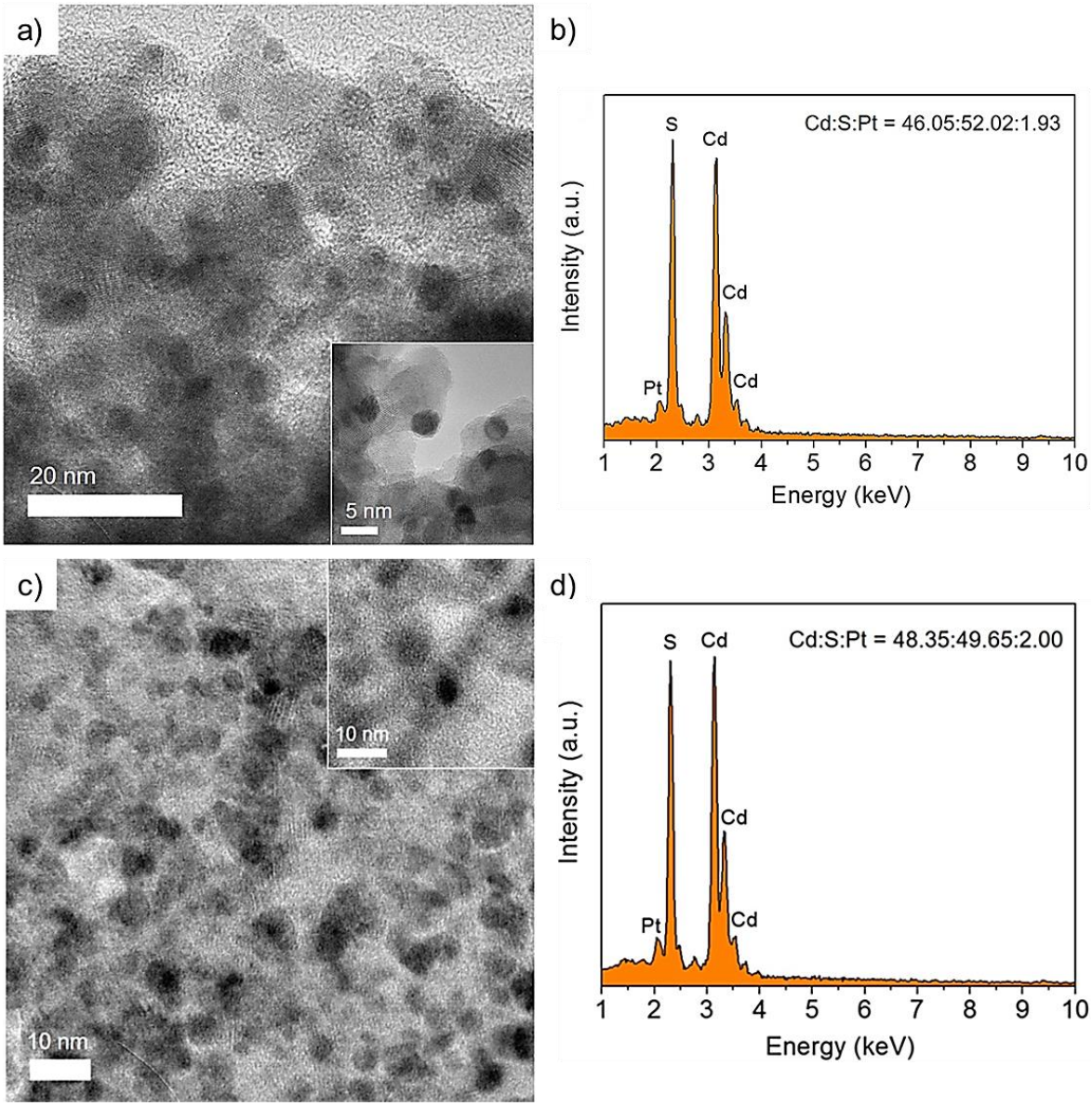

Figure 3-31: (a and c) Typical TEM images of the 5% Pt-CdS bulk and colloidal 5% Pt-CdS NCs respectively, revealing that small Pt nanoparticles with diameter of ca. 3–4 nm are deposited on the surface of CdS particles. (b and d) The respective EDS spectra for the 5% Pt-CdS bulk and 5% Pt-CdS NCs. EDS analysis indicates that the loading amount of Pt is ~5.35 wt. % for the bulk CdS and ~5.28 wt. % for the thiol-capped CdS NCs.

In all cases, 20 mg of each catalyst was dispersed in 20 mL of 5 M NaOH alkaline solution containing 10% (v/v) ethanol as sacrificial reagent and irradiated under the same conditions; the catalytic results are presented in **Figure 3-29** and **Table 3-3**. The results show that the mesoporous 5% Pt-CdS NCAs sample is more active than its bulk counterpart and isolated NCs by approximately a factor of 17 and 2, respectively. This highlights the advantage of the interconnected porous structure and large accessible surface of the mesoporous nanostructures, which provide efficient transportation of electrolytes between the nanoparticles, thus leading to improved reaction kinetics.

Furthermore, the mesoporous 5% Pt-CdS NCAs also demonstrated sufficient stability under the examined conditions. The stability of the catalyst was assessed by performing three consecutive 5-h photocatalytic tests. After each test, the catalyst was isolated from the reaction mixture by centrifugation, washed several times with deionized water, and re-dispersed in a fresh reaction solution, so as to replenish with hydroxyl ions and hole scavenger molecules (ethanol). Before each photocatalytic cycle, the reaction cell was de-aerated by purging with Ar gas for 30 min to remove O_2 from the reaction mixture (according to GC analysis). As shown in **Figure 3-32**, the H_2-evolution efficiency remains stable (within 5% deviation) at least for three catalytic cycles (i.e., over a 15-h total irradiation period) without any sign of decay. During the 15-h of irradiation, a total sum of 15.9 mmol (~356 mL STP) of H_2 was produced, corresponding to an average H_2-production rate of about 1.1 mmol h^{-1}.

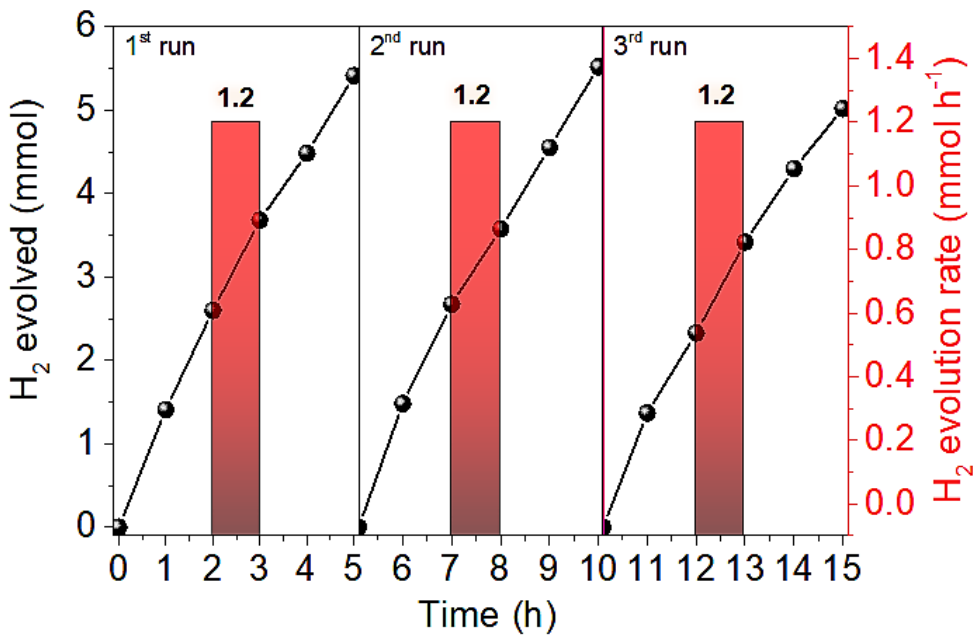

Figure 3-32: H_2-production (lines) and H_2-evolution rates (columns) during the photocatalytic stability study over the mesoporous 5% Pt-CdS NCAs catalyst. The displayed H_2-evolution rates for each cycle were averaged over the 5-h illumination period. All photocatalytic reactions were performed as follows: 20 mg of catalyst dispersed in 20 mL aqueous solution containing 5 M NaOH and 10% (v/v) ethanol; 300-W Xe light radiation with a long-pass cut-off filter allowing $\lambda \geq 420$ nm.

Assuming that all Pt atoms are involved in catalysis, the turnover frequency (TOF) of the catalyst (**eq. 27**) during the 15-h reaction was calculated to be ~0.12 s^{-1}, which is one of the highest among reported values for hydrogen evolution catalysts.

$$\mathbf{TOF} = \frac{\mathbf{2 \times (mole\ of\ evolved\ H_2)}}{\mathbf{(time\ unit) \times (mole\ of\ Pt)}} \qquad \textbf{(eq. 27)}$$

For example, previous studies on MoS_2 and CoP electrocatalysts have shown TOF values of 0.02 s^{-1} and 0.046 s^{-1} respectively, whereas a highly active MoS_2/CdS photocatalyst has demonstrated a TOF of 0.05 s^{-1}. [379, 455, 456]

Moreover, under the examined conditions the Pt nanoparticles remained stabilized on the surface of mesoporous CdS NCAs, with no evidence of detachment. Characterizations by EDS, XRD, and TEM reveal that the composition, crystallinity and morphology of the 5% Pt-CdS NCAs sample are well preserved after the catalytic reactions (**Figure 3-33**).

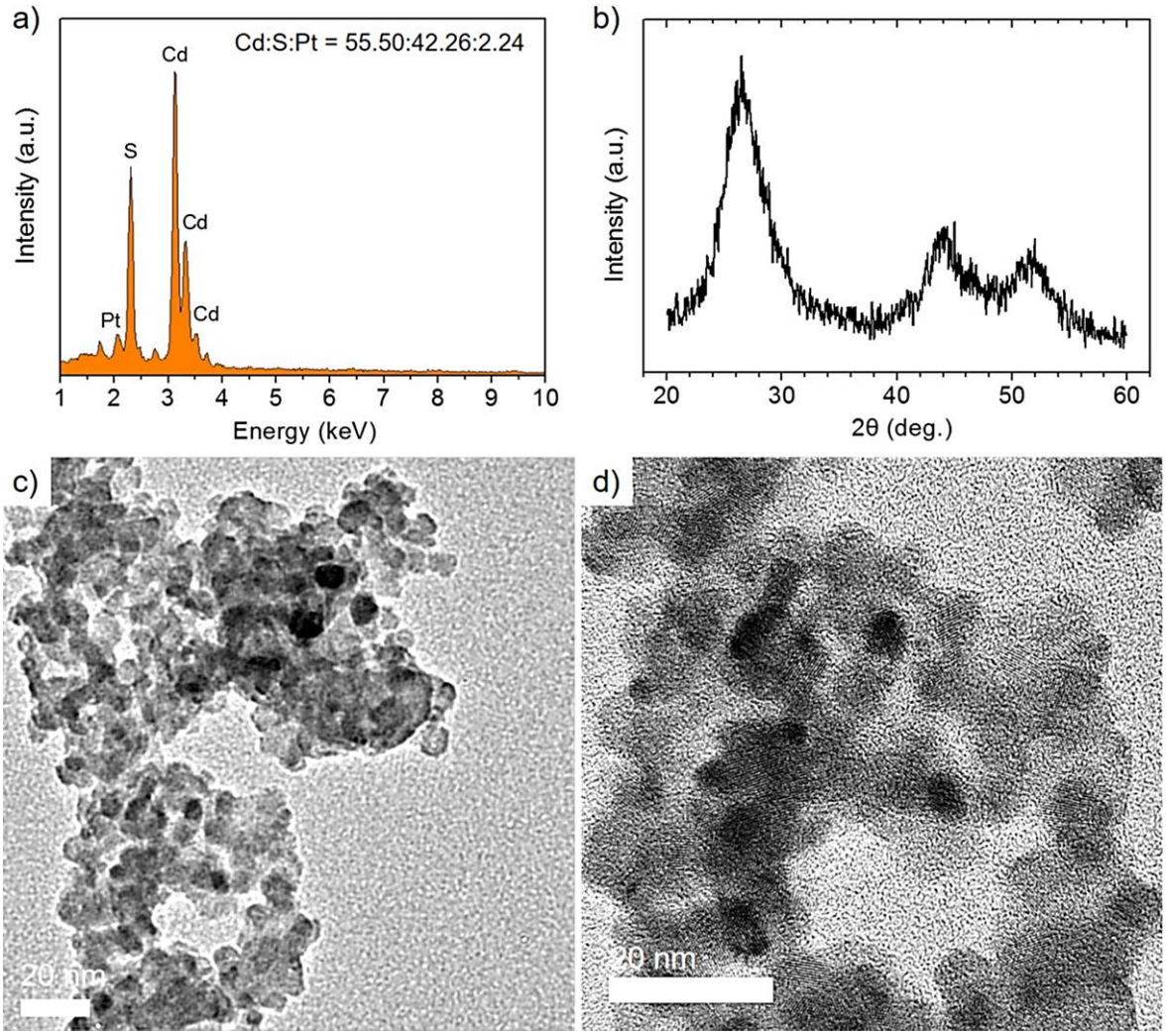

Figure 3-33: Typical (a) EDS spectrum, (b) XRD pattern and (c, d) TEM images for the three times reused 5% Pt-CdS catalyst (obtained after 15-h photocatalytic reaction). The EDS results indicate a Pt loading of ~5.17 wt. %, the XRD data reveal that the constituting CdS nanoparticles retain the cubic-zinc-blende structure, while the TEM images show a porous structure consisting of an interconnected network of CdS and Pt nanoparticles with diameters ca. 4–5 nm and 3 nm, respectively.

Also, N_2 physisorption measurements of the regenerated sample showed a BET surface area of 142 m^2 g^{-1}, which is lower than that of the fresh catalyst (ca. 230 m^2 g^{-1}), and a pore volume of 0.30 cm^3 g^{-1}. In addition, pore size analysis points to the formation of a slightly wider pore-size distribution with a peak maximum at about 6.3 nm (**Figure 3-34**). Because this activity was obtained by using CdS structures loaded only with a Pt-reduction co-catalyst, some minor photocorrosion of the CdS lattice, and thus a rearrangement of CdS nanoparticles in the porous framework are possible explanations for the lower surface area observed after prolonged catalysis. However, further improvement of their long-term performance and stability are anticipated, for instance, if heterojunctions with suitable oxidation co-catalysts are introduced along with Pt.

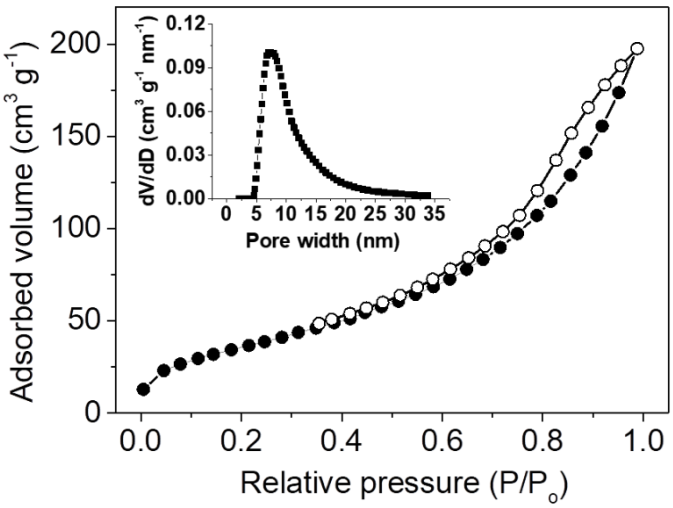

Figure 3-34: N_2 adsorption (filled cycles) and desorption (open cycles) isotherms at -196 °C for the three times reused 5% Pt-CdS catalyst (obtained after 15-h photocatalytic reaction). BET analysis gives a surface area of ~142 m^2 g^{-1} and a pore volume of ~0.30 cm^3 g^{-1}. Inset: The corresponding NLDFT pore size distribution calculated from the adsorption branch of isotherms, indicating an average pore size of ~6.3 nm.

3.2.4 Effect of Pt nanoparticles on the photocatalytic activity

In order to elucidate the effect of Pt nanoparticles on the H_2-production activity of mesoporous Pt-CdS NCAs, photocatalytic measurements were conducted under monochromatic irradiation with λ = 550 nm (using a bandpass filter, Asahi Spectra, Japan). In this study, no H_2 evolution was detected over the mesoporous 5% Pt-CdS, even after 4 h of irradiation (results not shown). This clearly suggests that even though deposition of Pt nanoparticles on the CdS surface can extend the light absorption into the NIR region (as revealed by the optical absorption measurements), the reaction mainly proceeds through the photoexcitation of CdS NCs. Therefore, it can be concluded that the

activity enhancement for the Pt-CdS NCAs catalysts is related to the efficient charge-carrier separation at the Pt/CdS junction.

Subsequently, two issues need to be addressed concerning the catalytic activity of Pt-CdS NCAs, that is, the loading amount and particle size of Pt. For this reason, further control experiments were performed using a 5 wt.% Pt-loaded CdS NCAs catalyst but with a different size of Pt nanoparticles, prepared via a similar photo-deposition method. As shown in **Figure 3-35**, the obtained catalyst (denoted as 5% Pt-CdS-*b*) possessed a similar composition as the 5% Pt-CdS NCAs sample, but featured smaller Pt nanoparticles (ca. 1.9 nm in size).

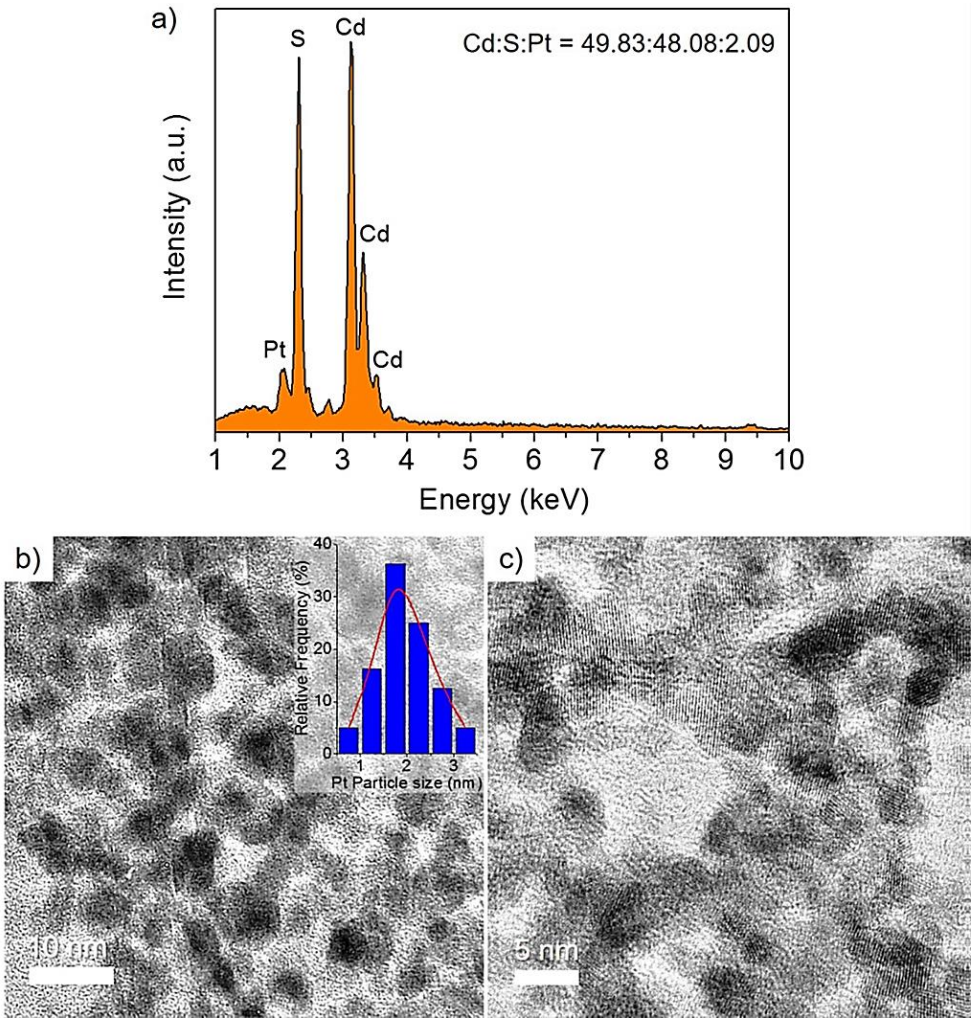

Figure 3-35: Typical (a) EDS spectrum and (b, c) TEM images of the mesoporous 5% Pt-CdS-*b* sample. The EDS analysis indicates a Pt content of about ~5.34 wt.%. Inset of panel b: Particle size distribution histogram of Pt nanoparticles, showing an average particle size of 1.9 ± 0.6 nm.

Interestingly, under identical conditions this catalyst showed a lower activity compared to the 5% Pt-CdS NCAs, giving an average H_2-evolution rate of 0.35 mmol h^{-1} (see **Figure 3-29** and **Table 3-3**). On the basis of the above results, it can be concluded that the particle size of Pt has a more prominent impact on the catalytic activity of Pt-CdS NCAs materials. The photocatalytic H_2 evolution

activity results for all the studied catalysts are summarized in **Table 3-3**. Also, to further highlight the impact of Pt particle-size in the photocatalytic reduction of water, the size of Pt nanoparticles in the mesoporous CdS NCAs catalysts can be correlated with the corresponding H_2-evolution rates. As shown in **Figure 3-36**, the rate of H_2 evolution on Pt-CdS NCAs increases proportionally with the Pt nanoparticle-size, reaching a maximum at 2.6 nm, and then decreases substantially when the Pt particle size exceeds 3 nm.

Table 3-3: Photocatalytic H_2 production and average H_2-evolution rates of mesoporous CdS and Pt-decorated CdS NCAs. The corresponding catalytic results for the 5 wt.% Pt-loaded CdS NCs (5% Pt-CdS NCs) and CdS bulk material (5% Pt-CdS bulk), as well as the mesoporous 5% Pt-CdS-*b* sample with 1.9 nm average diameter Pt nanoparticles, are also given for comparison.

Catalyst	Evolved H_2[a)] [mmol]	Average H_2-evolution rate[a)] [mmol h^{-1}]
CdS NCAs	0.23	0.08[b)]
1% Pt-CdS	0.74	0.28[b)]
2% Pt-CdS	0.84	0.30
5% Pt-CdS	3.42	1.21
5% Pt-CdS-*b*	1.04	0.35
7% Pt-CdS	0.98	0.34
5% Pt-CdS NCs	2.07	0.70
5% Pt-CdS bulk	0.23	0.07

[a)] Reaction conditions: 20 mg catalyst, 20 mL of alkaline (5 M NaOH) solution containing ethanol (10% v/v) as hole scavenger, visible-light irradiation (λ ≥ 420 nm using a cut-off filter), 4 h irradiation time, 20 °C; [b)] Average H_2-evolution rate over 3-h irradiation period.

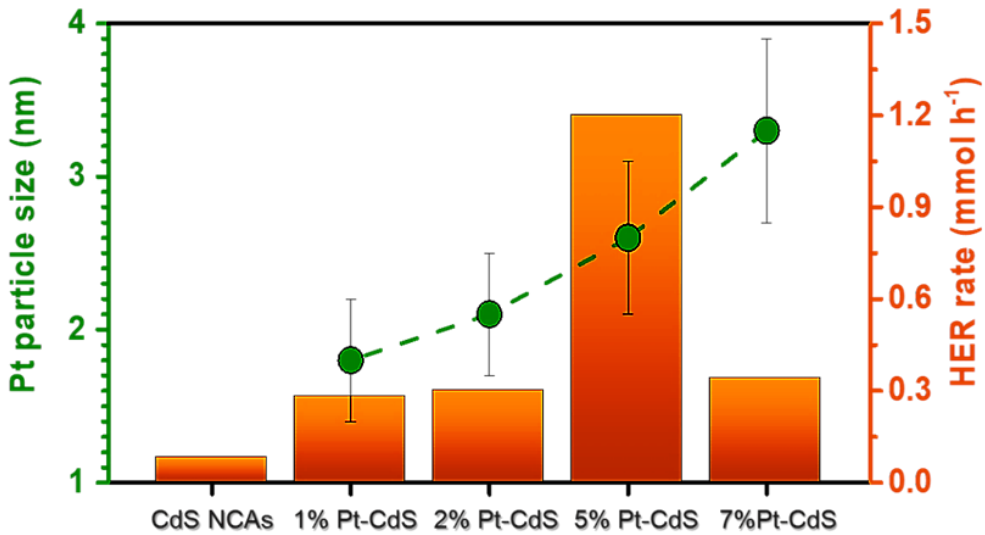

Figure 3-36: Correlation between the H_2-evolution rates (bars) and average size of Pt nanoparticles (dashed line) for the mesoporous CdS NCAs and the Pt-decorated CdS materials. The vertical lines represent the standard error. The H_2-evolution rates were measured under visible-light irradiation (λ ≥ 420 nm) in a 5 M NaOH solution containing ethanol (10% v/v) as hole scavenger and 1 g L^{-1} catalyst concentration.

So, for the apparent correlation with the H_2-production performance, there must be an effect of Pt particle-size on the electrochemical properties of Pt-CdS NCAs materials. As will be discussed below, this effect probably results from a balance between an increase in charge distribution due to the transfer of electrons from CdS NCs to Pt and a decrease in the available metal-support contact area. Thus, to give a clear picture of the band alignment between Pt and CdS NCs and to understand the role of Pt on the photocatalytic activity, the flat-band potentials (V_{FB}) of mesoporous CdS and Pt-decorated NCAs were measured using electrochemical impedance spectroscopy and Mott-Schottky analysis (**Figure 3-37**).

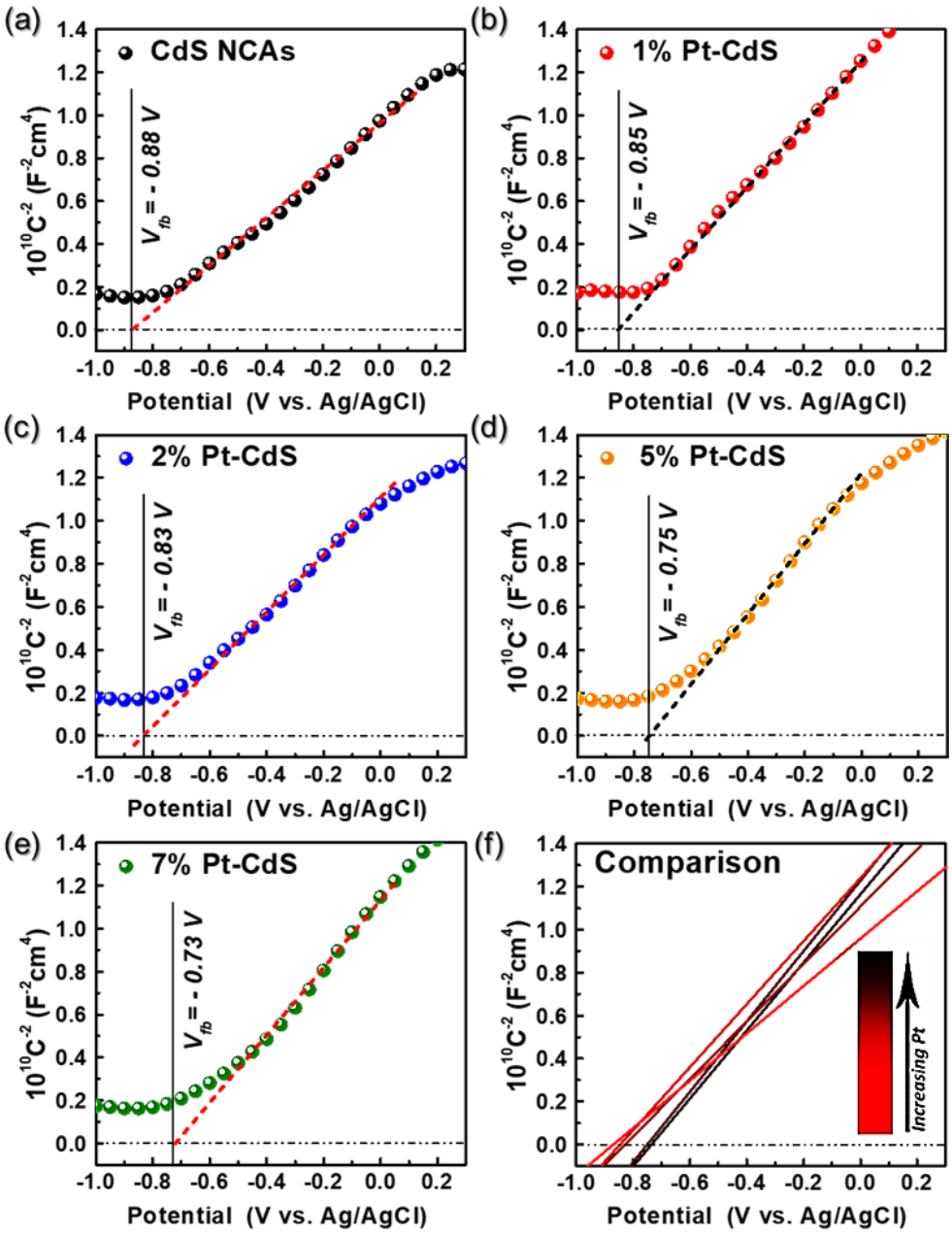

Figure 3-37: (a-e) Mott-Schottky plots for the mesoporous CdS and Pt-loaded CdS NCAs samples. (f) Comparison of the corresponding linear fits of the Mott-Schottky plots (the lines darken with increasing Pt loading), indicating that the slope increases with increasing the Pt content in CdS NCAs.

Figure 3-37 shows the obtained Mott–Schottky plots ($1/C^2$ *vs* applied voltage) and the respective fits of the linear portion of the plots for the mesoporous CdS and Pt-decorated CdS NCAs (measured as thin-film electrodes on FTO-coated glasses). The corresponding flat-band potentials (V_{FB}), obtained from the intercepts of the extrapolated straight lines at $1/C^2 = 0$ (according to **eq. 23**) are listed in **Table 3-4**. From the Mott–Schottky plots, it can be clearly seen that all samples exhibit positive slopes, which is indicative of the n-type behavior of CdS (i.e., electrons are the majority charge-carriers). Based on the measured V_{FB} potentials and optical bandgaps (determined from UV-Vis/NIR absorption spectra) and assuming that the flat band lies very close to the CB-edge for heavily doped n-type CdS [457], a reasonable energy band diagram can be constructed for each catalyst, as shown in **Figure 3-38.**

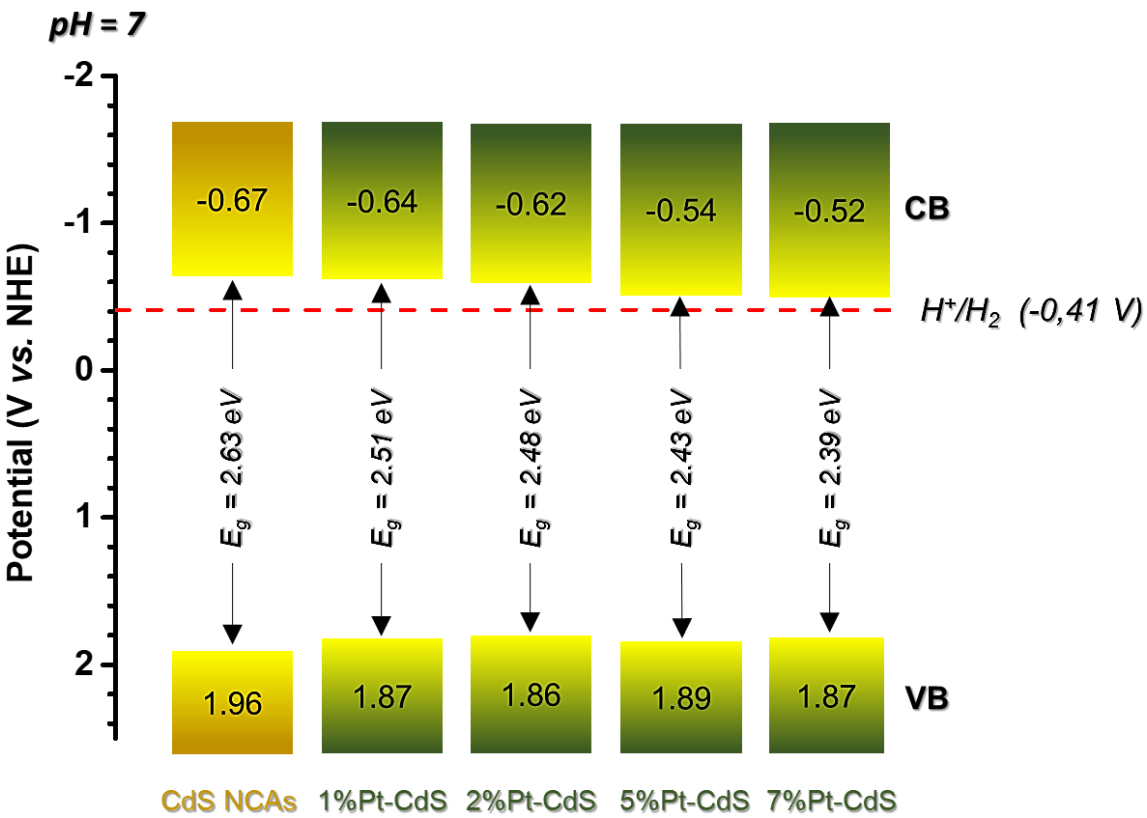

Figure 3-38: Energy band diagram schemes of the mesoporous CdS and Pt-decorated CdS NCAs. The conduction band (CB) edges were estimated from the flat-band potentials obtained from Mott-Schottky plots, and the valence band (VB) edges by adding the bandgap of each sample (determined from the UV-Vis/NIR absorption spectra) to the respective flat-band potential. All the potentials were converted from the Ag/AgCl electrode scale to the normal hydrogen electrode (NHE) scale using eq. 24.

From these band-edge diagrams and the Mott–Schottky plots, several important conclusions can be inferred: (i) the deposition of Pt nanoclusters lower the electron donor density of CdS, as indicated from the increased slopes in the Mott–Schottky plots of the Pt-decorated CdS materials compared to the slope of the pristine CdS NCAs, and (ii) the flat-band potential of CdS NCAs shifts to a more positive (anodic) direction, that is, from –0.67 V to –0.52 V (*vs* NHE) as the Pt loading increases

from 0 to 7 wt.%. Given that the electron affinity (χ_S) of n-type CdS is approximately 4.8 eV (in vacuum scale) [458] and the respective work function (Φ_M) of Pt is 5.65 eV [459], a Schottky contact should be established at the interface of Pt/CdS. When such contact is made, electrons can lower their energy by flowing from the semiconductor's CB into the metal. Therefore, the resulting potential drop across the Pt/CdS junction may cause a deformation of the band structure that continues until the chemical potential of CdS reaches equilibrium with the Fermi level of Pt. Thus, it is not surprising that the flat-band potential of CdS NCAs shifts towards more positive values after the deposition of Pt nanoparticles. However, taking into consideration the size-dependent shift in the work function of small-sized Pt nanoparticles, as noted in the literature [460, 461], an opposite shift in the V_{FB} of Pt-decorated samples (i.e., cathodic shift) would be expected with increasing the Pt particle size; since the work function of Pt decreases with increasing the particle diameter according to (**eq. 28**):

$$\boldsymbol{\Phi_M = \Phi_{bulk} + \frac{1}{d_p}} \qquad \textbf{(eq. 28)}$$

where, Φ_M is the work function of small spherical Pt metal nanoparticles, Φ_{bulk} is the work function of bulk Pt (5.65 eV) and d_p is the nanoparticle diameter.

From **eq. 28**, the Φ_{nano} values for 1.8, 2.1, 2.6, and 3.3 nm-sized Pt particles were calculated to be 6.25, 6.16, 6.07 and 5.98 eV, respectively (see **Table 3-4**). In this respect, one likely reason for the gradual anodic shift observed in V_{FB} with increasing d_p from 1.8 to 3.3 nm may be the lower Schottky barrier created at the Pt/CdS junction, as the Pt work function is decreased. The Schottky barrier height (SBH), which is defined as the difference between the work function of metal (Φ_M) and the electron affinity of the semiconductor (χ_S) (**eq. 29**), will determine the ease with which charge-carriers can cross the metal/semiconductor junction. [263, 462]

$$\boldsymbol{SBH = \Phi_M - \chi_S} \qquad \textbf{(eq. 29)}$$

This means that a decrease in the work function of Pt nanoparticles would lower the height of Schottky barrier, thus promoting efficient electron transfer across the junction [461] (from the photoactivated CdS to Pt), resulting in higher photocatalytic H_2-production activity. The calculated SBH values for the mesoporous Pt-decorated CdS NCAs samples are listed in **Table 3-4**, where the systematic narrowing of the Schottky barrier height with increasing the Pt nanoparticle size is clearly indicated.

To better assay the effect of Pt particle size on the electronic structure of CdS, the carrier concentrations (N_D) of the catalysts were also calculated from the slopes of Mott–Schottky plots, according to **eq. 25**. As shown in **Table 3-4**, this analysis yielded N_D values of 1.45×10^{17} cm^{-3} for pristine CdS and 1.05×10^{17}, 1.16×10^{17}, 9.46×10^{16}, and 9.95×10^{16} cm^{-3} for the Pt-CdS NCAs loaded with Pt nanoparticles of 1.8, 2.1, 2.6, and 3.3 nm size, respectively. This descending trend in carrier

concentration is in reasonable agreement with the estimated Schottky barrier heights (SBH) of Pt-CdS NCAs, further suggesting that a more efficient charge-transfer may take place as the Pt particle-size is increased. However, although the deposition of Pt particles with larger diameter (3.3 nm) can create Pt/CdS Schottky contacts with lower barrier height, this seems to be rather detrimental to the charge-transport properties, as implied from the relatively higher donor density of the 7% Pt-CdS catalyst compared to that of 5% Pt-CdS. This observation suggests that, in addition to the energetic issues, the electron-transfer efficiency of Pt-CdS NCAs could be affected also by the number of surface Pt atoms at the interface with CdS support. Therefore, the density of Pt edge-sites (*N*s) on the surface of Pt-CdS NCAs catalysts was calculated, based on the contact length between CdS and the perimeter Pt atoms for each Pt nanoparticle and the specific surface area of the CdS support, according to the following relation (**eq. 30**):

$$\boldsymbol{N_S = \frac{L_C}{d_{atom,Pt} \cdot S_{CdS}}} \qquad \textbf{(eq. 30)}$$

where, $d_{atom,Pt}$ is the atomic diameter of Pt (=0.35 nm), S_{CdS} is the surface area of the CdS host material (274 m^2 g^{-1}), and L_C is the total length of the contact between CdS and the perimeter atoms of Pt nanoparticles, derived from **eq. 31** below:

$$\boldsymbol{L_C = 2\pi r \cdot \frac{m_{Pt}}{V_{Pt} \cdot \rho_{Pt}}} \qquad \textbf{(eq. 31)}$$

where, m_{Pt} is the loading amount of Pt, V_{Pt} is the volume of each Pt nanoparticle ($V=(4/3)\pi r^3$) assuming spherical shape with average radius *r*, and ρ_{Pt} is the mass density of Pt (21.45 g cm^{-3}).

The results, which are summarized in **Table 3-4**, show that *N*s increases when the Pt loading rises from 1 to 5 wt.%, due to the moderate increase in the particle size. On the contrary, higher Pt loadings (7 wt.%) result to large nanoparticles that apparently afford a decreased number of Pt edge-atoms at the contact interface, as indicated from the lower *N*s value of 7% Pt-CdS (~1.89×10^{-2} Pt sites per gram per nm^2 of support catalyst) relative to that of the 5% Pt-CdS catalyst (~2.20×10^{-2} sites g^{-1} nm^{-2}). This finding reveals that for catalysts with large Pt nanoparticles, the decrease in Schottky barrier height can be superimposed by the decrease in the contact area between Pt and CdS (assuming that all Pt/CdS junctions have similar interfacial interactions). Therefore, in addition to the energetic aspect, the contact area is an important factor to be considered during the optimization of the Pt-CdS junction, as it can deteriorate the smooth interparticle electron-transfer process even under energetically favorable conditions. This can be easily affirmed by comparing the electron donor densities and photocatalytic activities obtained from catalysts with 5 and 7 wt.% Pt loadings.

Table 3-4: Electrochemical properties and analytical data for the mesoporous CdS and Pt-CdS NCAs catalysts. The calculated density of Pt edge sites at the interface between Pt nanoparticles and CdS is also shown.

Sample	Flat Band pH=7 (V_{FB}) (V vs NHE)	Pt Work Function (Φ_M) (eV)	Schottky Barrier Height[a)] (SBH) (eV)	Donor Concentration[b)] (N_D) (cm^{-3})	Density of Edge Sites[c)] (Ns) (Pt sites g^{-1} nm^{-2})
CdS NCAs	-0.67	-	-	1.45×10^{17}	-
1% Pt-CdS	-0.64	6.25	1.45	1.05×10^{17}	1.03×10^{-2}
2% Pt-CdS	-0.62	6.16	1.36	1.16×10^{17}	1.40×10^{-2}
5% Pt-CdS	-0.54	6.07	1.27	9.46×10^{16}	2.20×10^{-2}
7% Pt-CdS	-0.52	5.98	1.18	9.95×10^{16}	1.89×10^{-2}

[a)] Calculated with eq. 29 using χ_s=4.8 eV for CdS and the obtained Φ_M values for Pt nanoparticles from eq. 28; [b)] N_D values were obtained with the help of eq. 25 using the slopes of the Mott-Schottky plots and the relative dielectric constant of CdS (ε = 8.9); [c)] N_S values were calculated according to eq. 30 and 31 assuming spherical Pt nanoparticles and circular contact area between Pt particles and CdS support.

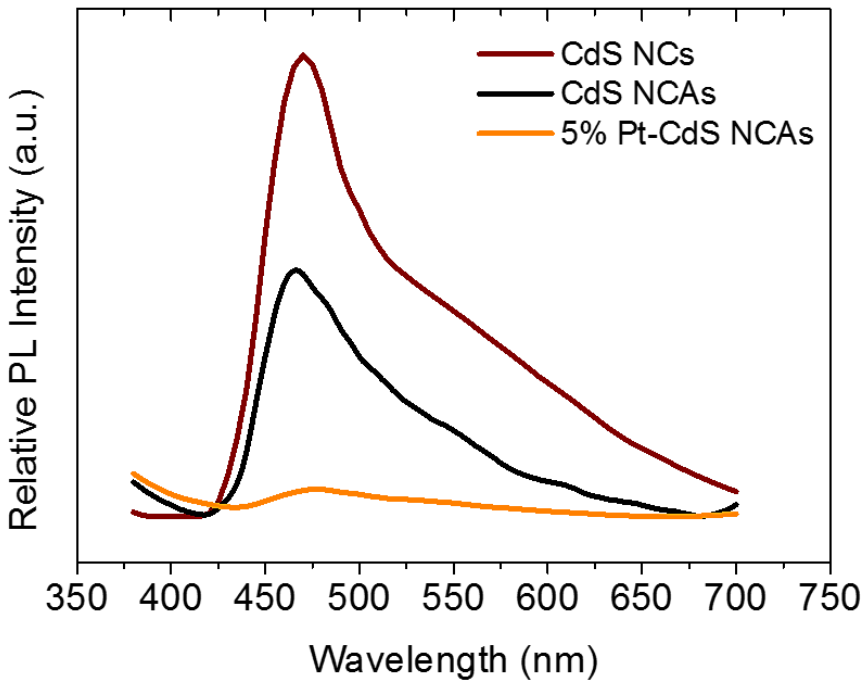

Figure 3-39: Room-temperature PL emission spectra of the mesoporous CdS NCAs and 5% Pt-CdS catalysts and starting 3-MPA–capped CdS NCs. All measurements were performed in water (1 mg mL^{-1} sample concentration) using an excitation wavelength of 360 nm.

In addition, photoluminescence (PL) spectra showed a remarkable decrease in the band-edge emission at 470 nm for 5% Pt-CdS NCAs, and to a lower extent for pristine material compared to the 3-MPA-capped CdS NCs (see **Figure 3-39**). This suggests that the majority of the photogenerated electrons at the CdS NCs are delocalized throughout the assembled network, reducing the recombination probability of charge carriers. The presence of Pt nanoparticles on the surface of CdS can further suppress the recombination of electron–hole pairs through the efficient charge-separation at the Pt/CdS nanojunctions. This is evident from the dramatic quenching of the excitonic emission of the mesoporous 5% Pt-CdS NCAs sample.

Therefore, these findings suggest that the role of Pt nanoparticles on the prepared catalysts of this work is to promote a charge distribution in the band-edge states of CdS NCs by shifting the V_{FB} potential to more positive values and to extend the lifetime of charge-carriers. This effect definitely plays a vital role in photocatalytic processes at the Pt/CdS junctions, in which the internal electrostatic field drives the transfer of photo-excited electrons from the CB of CdS NCs into Pt nanoparticles, where hydrogen evolution take place, while in the meantime the holes left on the VB of CdS migrate to the surface and oxidize $^{-}$OH into $^{\bullet}$OH radicals. A schematic illustration of the photocatalytic H_2-generation process over mesoporous Pt-CdS NCAs is shown in **Figure 3-40.**

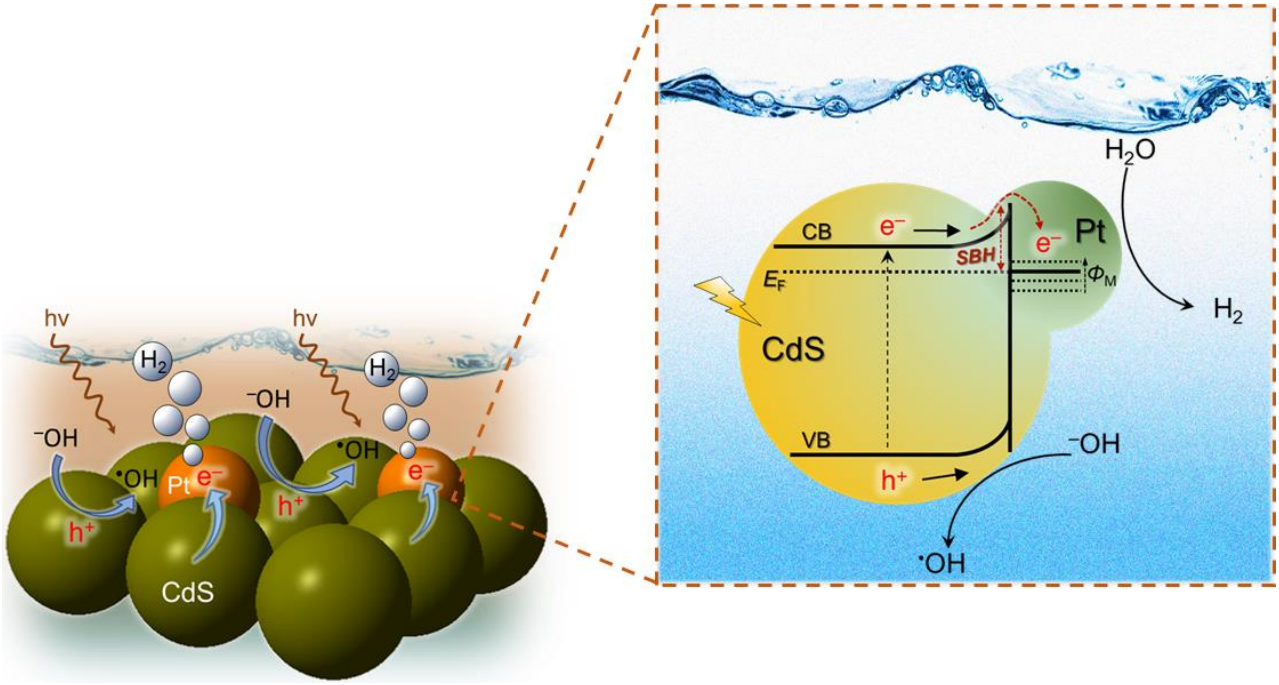

Figure 3-40: Schematic illustration of the photocatalytic H_2-production mechanism at the Pt/CdS interface under visible-light irradiation and in the presence of a $^{\bullet}$OH/$^{-}$OH redox mediator (VB: valence band; CB: conduction band; E_F: Fermi level; Φ_M: metal nanoparticle work function; and *SBH*: Schottky barrier height). Adapted with permission from ref. [404]. © 2016 WILEY-VCH Verlag GmbH & Co. KGaA, Weinheim.

Overall, the enhanced catalytic activity is attributed to the decrease in the work function of Pt nanoparticles by increasing the particle size and to the increased number of surface Pt edge-sites at the contact interface of CdS with Pt nanoparticles. These result in the decrease of the Schottky barrier height (SBH) created at the Pt/CdS junctions and the promotion of smooth electron transfer from photoactivated CdS to Pt. Moreover, the 3D open-pore structure and large accessible surface area also have a profound effect on the hydrogen evolution efficiency, by providing effective transportation of electrolyte-molecules between the nanoparticles, thereby improving the reaction kinetics. Consequently, the mesoporous Pt-CdS NCAs containing 5 wt.% Pt with ~2.5 nm average nanoparticle size exhibits a very high photocatalytic activity with an apparent QY of 70% at $\lambda = 420 \pm 10$ nm. Thus, these results demonstrate the potential of the mesoporous Pt-CdS NCAs catalysts to serve as efficient and stable photocathodes for water reduction and H_2-production under visible light.

3.3 Mesoporous heterostructures of p-CuS/n-CdS NCAs

Despite the advantageous properties of CdS, as described earlier, the development of effective CdS-based photocatalysts with low cost and enhanced photon-to-hydrogen conversion efficiency is a compelling challenge. An effective way to overcome the limitations of charge recombination and anodic photocorrosion in CdS materials is the coupling of CdS with other co-catalysts, which can increase its electron–hole separation yield through the efficient charge-carrier dissociation at the interface of the formed heterojunctions. To this end, a variety of CdS-based composite nanostructures, such as MoS_2/CdS [379], WS_2/CdS [381], NiS/CdS_7 [390], Pt/CdS [396, 404] and CNT/CdS [463], have been developed and studied, showing promising results. However, even though these hybrid catalysts can achieve a significant increase in photocatalytic H_2-production activity compared to pure CdS, most of them either offer low solid/electrolyte interface area or contain precious and rare metals (e.g., Pt), thereby limiting their practical application. Very recently, CuS/CdS nanoparticle aggregates has been suggested as a cost-effective and sustainable catalyst for the hydrogen evolution reaction. These studies indicated that CuS particles may expand the light absorption range and prolong the lifetime of the photogenerated charge-carriers in CdS. [377, 378] Nevertheless, the role of CuS in photochemical activity of CdS is still poorly understood. Also, these aggregated nanoparticle materials adopt close-packed structures with low surface area-to-volume ratio, which generally restricts their catalytic performance. Therefore, it is highly desirable to develop composite CuS/CdS nanostructures with high porosity and surface area, because enhanced catalytic performance might be obtained due to their unique morphology.

In this section, the synthesis of new 3D mesoporous heterostructures consisting of interconnected CuS and CdS NCs is presented and their photocatalytic activity in water reduction reaction under

visible-light is studied. Also, the photoelectrochemical behavior of the prepared mesoporous CuS/CdS NCAs and the role of CuS on the enhanced photocatalytic performance of the heterostructures is investigated.

3.3.1 Synthesis of mesoporous CuS/CdS NCAs

Porous networks of connected CuS and CdS NCs were produced via the new polymer-templating oxidative self-polymerization process to assemble first thiol-capped CdS NCs into mesoporous NCAs structures. Next, a cation-exchange treatment was performed to partially replace Cd^{2+} with Cu^{2+} on the surface of CdS NCAs. [405] During the partial cation-exchange process, the large disparity in the products solubility — i.e., the K_{sp} values between CdS (8×10^{-27}) and CuS (6.3×10^{-36}) — is the driving force for the spontaneous topotactic transformation of CdS into CuS (**eq. 32**), giving rise to the formation of CuS/CdS binary nanoheterostructures. [464]

$$\mathrm{CdS} + \mathrm{Cu}^{2+} \rightarrow \mathrm{CuS} + \mathrm{Cd}^{2+} \qquad \textbf{(eq. 32)}$$

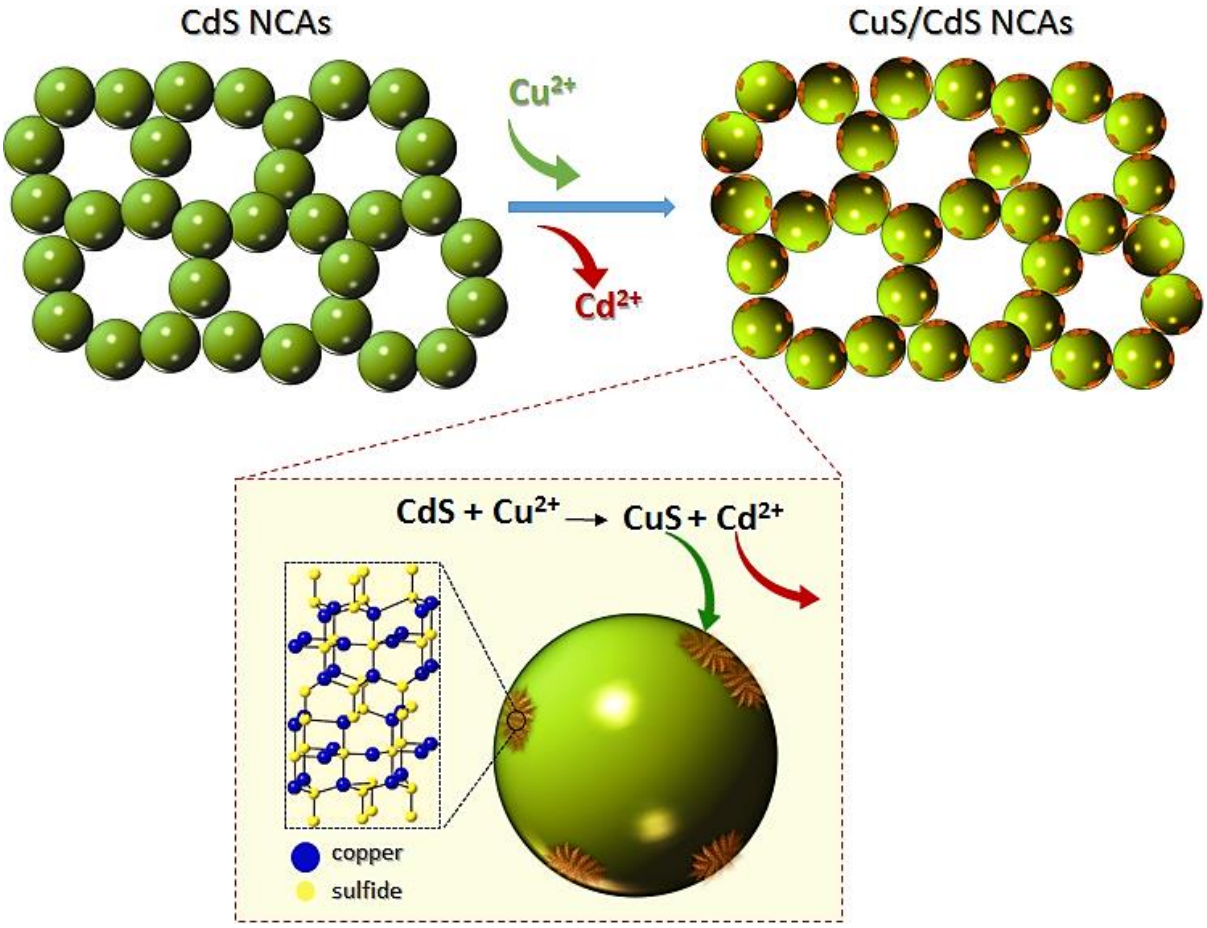

Figure 3-41: Schematic illustration of the partial cation-exchange process to prepare mesoporous nanoheterostructures of CuS/CdS NCAs.

A schematic representation of the synthetic process to prepare mesoporous nano-heterostructures of CuS/CdS NCAs is illustrated in **Figure 3-41.** By this procedure, a series of heterojunction composite assemblies of CdS and CuS NCs with different content of Cu (denoted as n% CuS/CdS NCAs, where n= 3, 5 and 8 mol %) was obtained by varying the initial Cu^{2+} concentration in the reaction mixture. In general, the partial transformation of CdS NCs into CuS/CdS composites is believed to occur through the following steps: (i) deposition of insoluble CuS nanoclusters on the surface of CdS NCs, by preferential exchange with surface Cd^{2+} cations and nucleation reactions with S^{2-} ions at the surface, (ii) mutual diffusion of Cu^{2+} (inward diffusion) and S^{2-} and Cd^{2+} ions (outward diffusion, that is, dissolution of CdS from the interior to the exterior), and (iii) interfacial bonding by the reaction between the Cu^{2+} and S^{2-} ions at the inner surface of the formed CuS NCs in contact with CdS. [465] Significantly, the growth of CuS within the CdS NCs leads to an intimate contact between the two components, in a way that could not be achieved by a simple physical mixture of CdS and CuS particles. [377, 438, 465] This is particularly important for photocatalysis since, as will be discussed later, the interfacial transfer of photoexcited electrons and holes in the p-CuS/n-CdS heterojunction region can suppress charge recombination and thus increase the photocatalytic activity towards H_2 production.

3.3.2 Structural characterization of photocatalysts

The chemical composition of the as-prepared CuS/CdS NCAs was determined by EDS. EDS analysis of the mesoporous single CdS NCAs showed strong Cd and S signals with a molar ratio of Cd/S very close to the expected 1:1 stoichiometry (**Figure 3-42a**). The presence of Cu atoms in the composite heterostructures was confirmed by the EDS spectra obtained from different areas of samples, showing the presence of copper at different Cu/Cd atomic ratios, which correspond to a Cu loading from ~3 to ~8 mol % (see **Figure 3-42 b-d** and **Table 3-5**). The estimated copper content, as obtained by EDS microanalysis, is consistent with the expected composition from the stoichiometry of reactions, suggesting the complete incorporation of Cu ions into the CdS lattice.

The crystallinity of all the samples was verified by powder X-ray diffraction. The XRD patterns of pristine CdS NCAs and CuS/CdS heterostructures in **Figure 3-43** display three intense diffraction peaks in 2θ scattering angles from 20 to 60º, which can be assigned to the (111), (220), and (311) reflections of the CdS zinc-blende structure (JCPDS card no. 42-1411). In addition, the remarkable peak-broadening of the X-ray reflections points to the formation of crystalline materials with a very small grain composition. A peak-width analysis using the Scherrer equation (**eq. 19**) gives an average CdS crystallite size of ~2.6 nm. However, XRD analysis does not provide convincing evidence for the presence of CuS, even in the XRD pattern of CuS/CdS NCAs sample with 8 mol% Cu. This can

be attributed to the small grain size and high dispersion of CuS nanocrystallites in the mesoporous CdS structure.

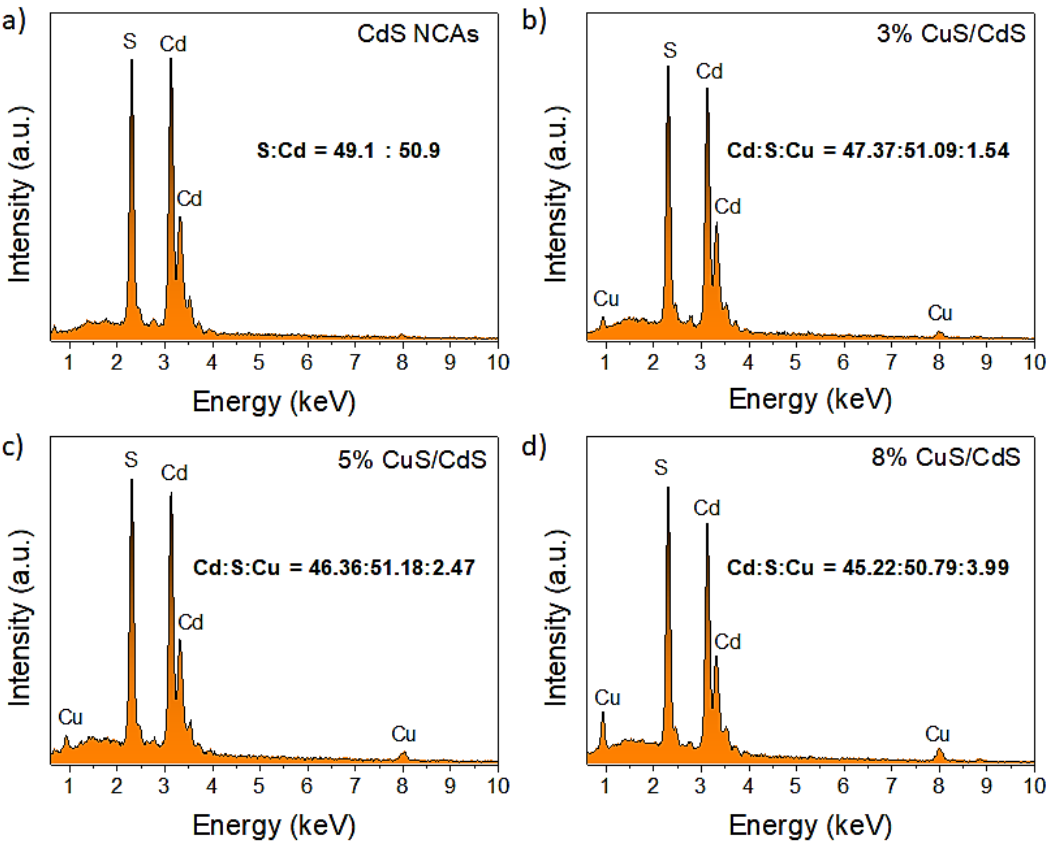

Figure 3-42: Typical EDS spectra of the mesoporous (a) CdS NCAs and (b-d) as-prepared CuS/CdS NCAs heterostructures with 3, 5, and 8 mol% Cu^{2+} loading.

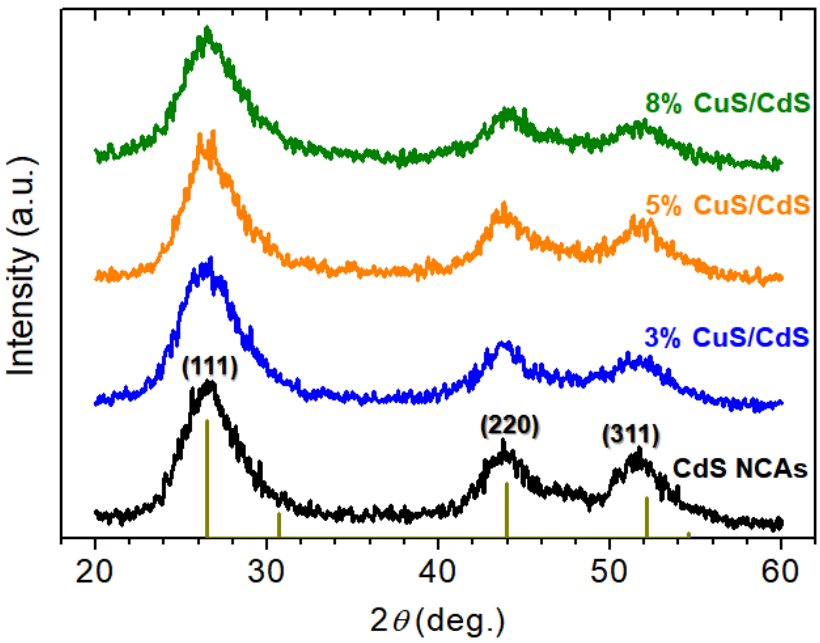

Figure 3-43: Powder XRD patterns for the mesoporous CdS and CuS/CdS NCAs. The standard diffraction lines of zinc-blende CdS (JCPDS card no. 42-1411) are also given.

Moreover, the valence state of Cd and Cu atoms in the composite materials was investigated with X-ray photoelectron spectroscopy (XPS). A typical high-resolution Cd 3d XPS spectrum for the 5% CuS/CdS NCAs catalyst, which is the most active catalyst of the CuS/CdS NCAs series, shown in **Figure 3-44a**. This spectrum reveals a peak-doublet at binding energies (BE) of 404.6 and 411.4 eV corresponding to Cd^{2+} $3d_{5/2}$ and $3d_{3/2}$ core-levels in CdS, respectively. [466] In addition, **Figure 3-44b** displays the XPS spectrum of Cu 2p for the 5% CuS/CdS NCAs, showing the BE of Cu $2p_{3/2}$ and Cu $2p_{1/2}$ core-level signals at 932.6 and 952.4 eV respectively, which are typical values for Cu^{2+} in CuS compounds. [467, 468] The symmetric shape of the Cu 2p peaks suggests that the copper species in the catalyst exist as a single-phase of CuS. Meanwhile, a weak satellite feature at BE ~943.2 eV further confirms the paramagnetic nature of Cu^{2+}. [469]

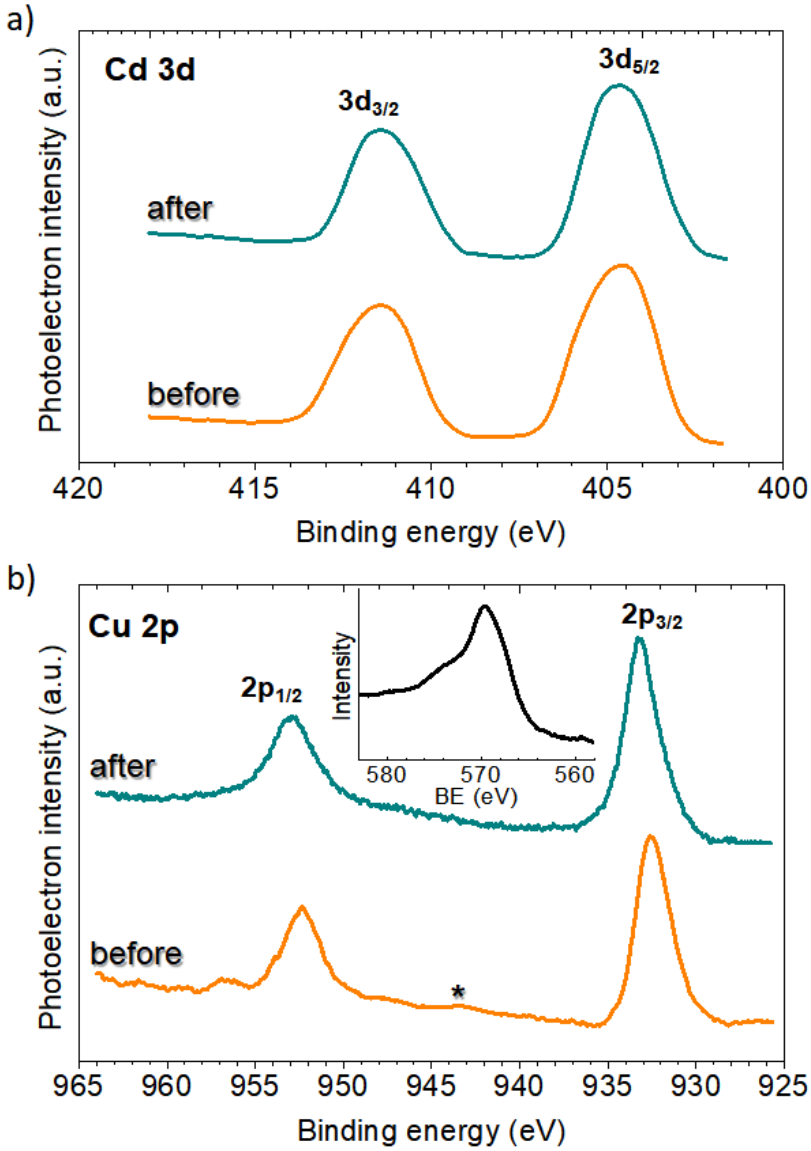

Figure 3-44: High-resolution XPS of (a) the Cd 3d and (b) the Cu 2p core-level photoelectron spectra for the mesoporous 5% CuS/CdS NCAs sample, before (orange lines) and after 20-h photocatalytic reaction (green lines). The symbol (*) in panel b shows the satellite peak at ~943.2 eV, characteristic of the Cu^{2+} ions. Inset of panel b: The Auger Cu LMM spectrum of the material retrieved after photocatalytic reaction, indicating the presence of Cu_2S species (peak at 569.6 eV).

Typical transmission electron microscopy images of the 5% CuS/CdS NCAs catalyst are shown in **Figure 3-45**. The images reveal a disordered porous network consisting of connected nanoparticles with a grain size of about 5–6 nm, and pores that are formed between the assembled nanoparticles. To further probe the crystal structure of the mesoporous network, selected-area electron diffraction and high-resolution TEM were also utilized. The SAED pattern shown in the inset of **Figure 3-45a** displays a series of diffuse Debye-Scherrer rings that can be indexed to the zinc-blende structure of CdS, in agreement with XRD results. The HRTEM image in **Figure 3-45b**, however, reveals the composite structure of the 5% CuS/CdS NCAs material. It shows distinct lattice fringes with 3.4, 3.0 and 2.0 Å interplanar spacings that correspond to the (111) facets of cubic CdS and, according to the fast Fourier transformation (FFT) pattern (inset of **Figure 3-45b**), and to the (012) and (008) facets (along the [100] direction) of the hexagonal P63/mmc lattice of CuS, respectively. Taken together with the XRD and XPS analysis, these results are consistent with the formation of mesoporous catalysts comprising of connected covellite (CuS) and cubic CdS NCs.

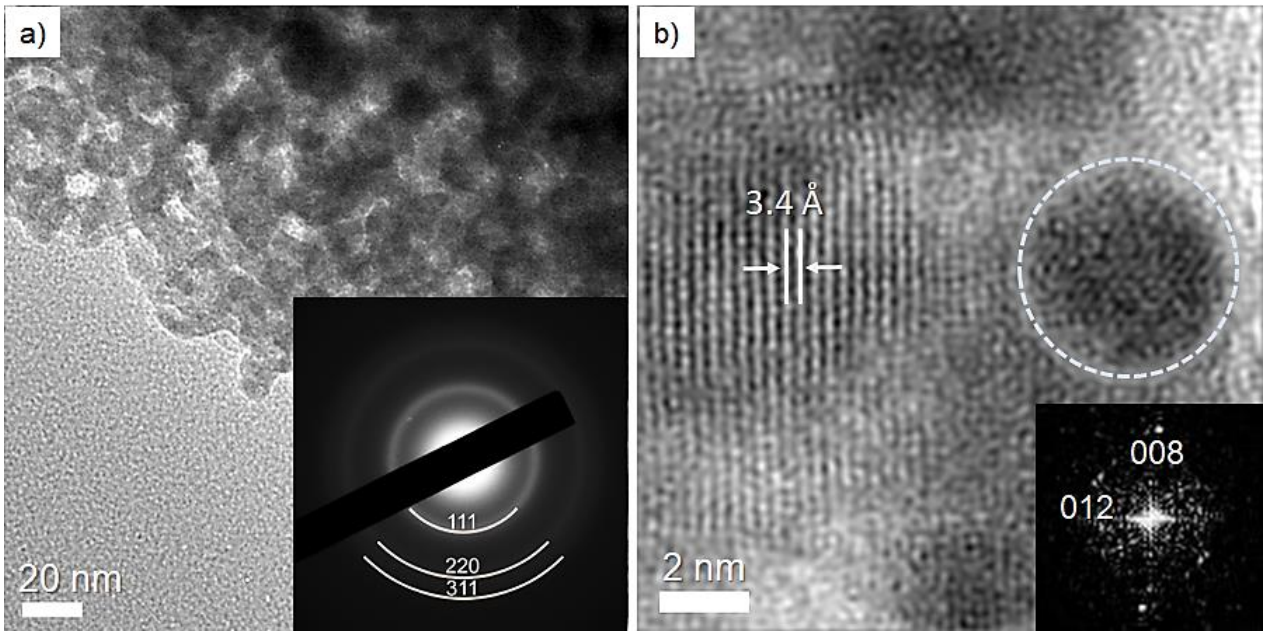

Figure 3-45: (a) Typical TEM image showing a disordered porous structure of interconnected nanoparticles (inset: SAED pattern taken from a small area of the nanoparticle network), and (b) HRTEM image, for the mesoporous 5% CuS/CdS NCAs sample. Inset of panel b: FFT pattern recorded on the portion indicated by the white circle, showing the (008) and (012) lattice planes of hexagonal (*P*63/*mmc*) CuS.

The porosity of the as-prepared materials was evaluated by performing nitrogen physisorption measurements at –196 °C. The N_2 adsorption and desorption isotherms and the corresponding pore size distributions of mesoporous CdS NCAs and the CuS/CdS NCAs heterostructures with various Cu content, are displayed in **Figure 3-46**. All the samples exhibited typical type IV isotherms with a pronounced H2-type hysteresis loop, which according to IUPAC classification (see A.1 and A.2 in

the Appendix) are characteristic of mesoporous materials with interconnected structure.[412] The small but resolved adsorption step at relative pressure range (P/P_o) of 0.4–0.6 is related to the capillary condensation of nitrogen in narrow-sized mesopores. [427]

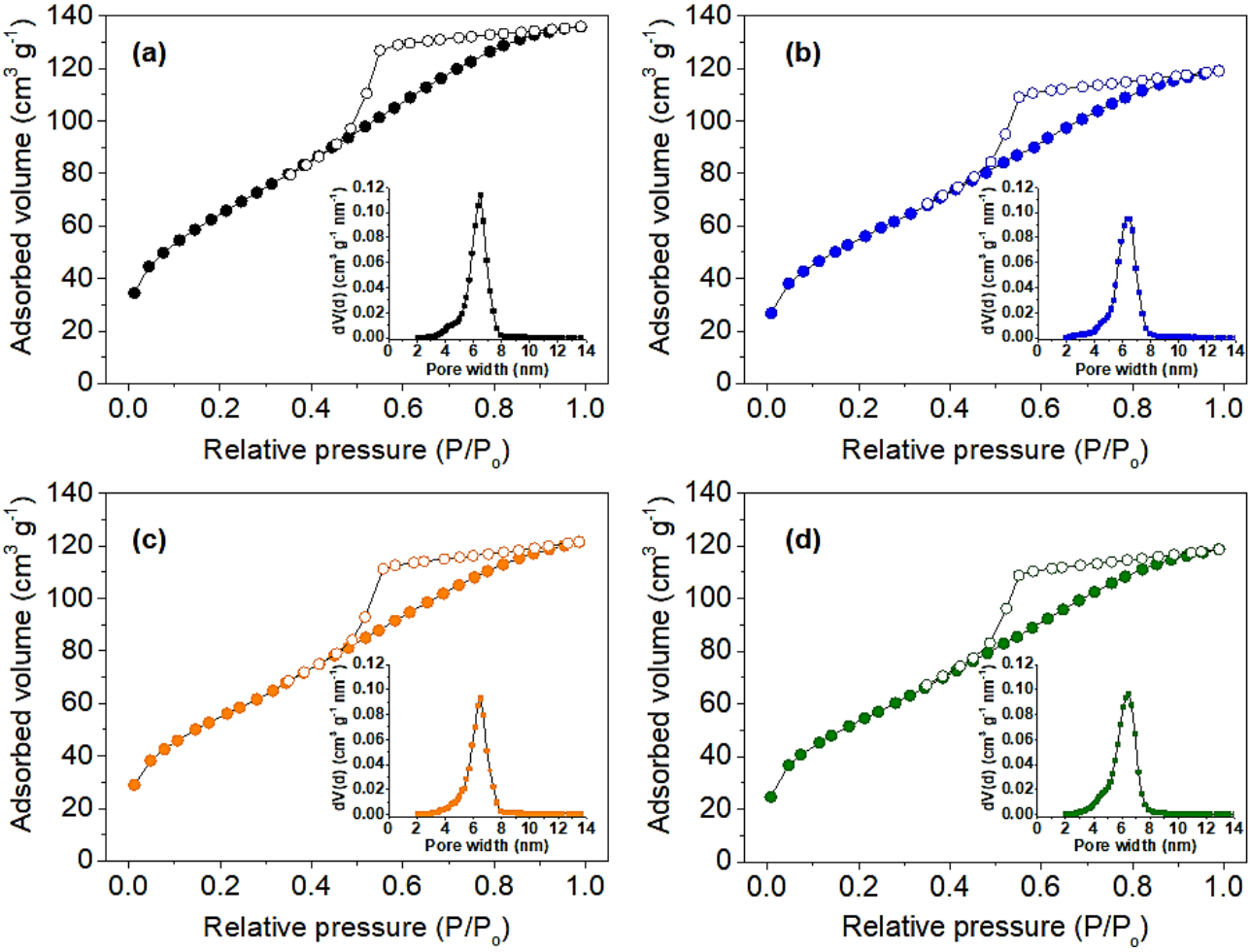

Figure 3-46: N_2 adsorption (filled cycles) and desorption (open cycles) isotherms at -196 °C and (inset) the corresponding NLDFT pore size distributions calculated from the adsorption branch of isotherms, for the mesoporous (a) pristine CdS NCAs (black) and the (b) 3% CuS/CdS (blue), (c) 5% CuS/CdS (orange), and (d) 8% CuS/CdS (green) NCAs composites.

The mesoporous CuS/CdS NCAs composites exhibited Brunauer–Emmett–Teller (BET) surface area of 198–203 m^2 g^{-1} and total pore volume of 0.18–0.19 cm^3 g^{-1}, which are slightly lower than those of the pristine CdS NCAs sample (238 m^2 g^{-1} and 0.21 cm^3 g^{-1}, respectively), as shown in **Table 3-5**. The decrease in surface area and pore volume for the CuS-loaded materials is presumably due to a partial etching of the CdS NC surface during the cation-exchange process, leading to a rearrangement of CdS nanoparticles in the porous framework. Moreover, the pore width in these materials was assessed from the adsorption branch of isotherms using the non-local density functional theory (NLDFT) model. [414] The results for CdS NCAs and the respective CuS/CdS composites reveal a quite narrow pore-size distribution (see insets in **Figure 3-46**), with an average size of ~6.4–6.5 nm (**Table 3-5**).

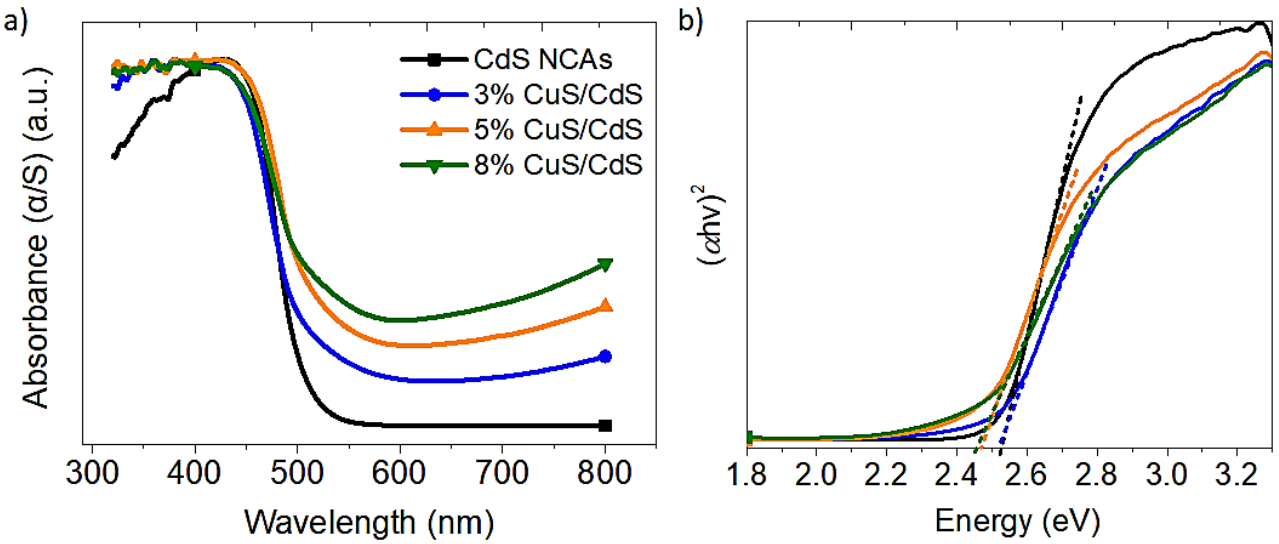

Figure 3-47: a) Optical absorption spectra of mesoporous CdS NCAs and the CuS/CdS composites with various Cu content, and b) the corresponding Tauc plots based on eq. 21, i.e., the curves of $(\alpha hv)^2$ versus photon energy (hv), where α, h and v are the absorption coefficient, Planck's constant and light frequency, respectively.

The electronic structure of the pristine and Cu-containing CdS NCAs was investigated with diffuse reflectance UV–vis/NIR. The DRS spectra of all the measured samples were converted to absorption using the Kubelka-Munk function (**eq. 20**). The spectrum of mesoporous pure CdS NCAs shows a sharp optical absorption onset at around 488 nm (~2.54 eV), corresponding to the intrinsic interband electron transition in CdS (**Figure 3-47a**). The large blue shift in the energy gap of CdS NCAs compared to that of a typical bulk CdS (i.e., 2.42 eV) is reflective of quantum size-effects in CdS NCs due to their very small diameter (ca. 5–6 nm). Using the measured optical bandgap and Brus equation (**eq. 22**), the size of the constituent CdS NCs was estimated to be ~5.7 nm, which is consistent with TEM observations. The energy bandgaps of the mesoporous CuS/CdS NCAs, which are calculated from the corresponding Tauc plots based on **eq.21** for a direct gap semiconductor (**Figure 3-47b**), vary systematically with increasing the Cu content from 2.52 eV for 3% CuS/CdS NCAs to 2.47 eV for the 8 mol% Cu-loaded sample; all the measured textural and electronic properties of the as-prepared catalysts are summarized in **Table 3-5**. This behavior is related to the strong electron interactions between quantum-confined electronic states in CdS and CuS NCs, indicating that CuS domains are in intimate contact with the CdS structure. In addition, careful analysis of the absorption shoulder seen in the range of 510–580 nm (as the Cu content increases), gives an absorption onset at 564 nm (~2.2 eV) that can be assigned to the bandgap transition of CuS. [470] Also, the absorption tails observed in the spectra of the Cu-loaded samples at wavelengths longer than 600 nm are associated with the d-d electronic transitions of Cu^{2+}. [471] As expected, this

absorption increases with increasing the Cu content in the CuS/CdS composites, extending their light-absorption in the NIR region.

Table 3-5: Textural properties and analytical data for the as-prepared mesoporous CdS and CuS/CdS NCAs catalysts.

Sample	Cu loading[a)] (mol%)	Surface area (m^2 g^{-1})	Pore volume (cm^3 g^{-1})	Pore size (nm)	Energy gap (eV)
CdS NCAs	0	238	0.21	6.5	2.54
3% CuS/CdS	3.14	203	0.19	6.4	2.52
5% CuS/CdS	5.06	201	0.19	6.4	2.48
8% CuS/CdS	8.11	198	0.18	6.4	2.47

[a)] Based on EDS analysis

3.3.3 Photocatalytic water reduction study

All the photocatalytic water-reduction experiments for hydrogen evolution were carried out under visible-light ($\lambda \geq 420$ nm) irradiation, using an aqueous solution containing Na_2SO_3/Na_2S (0.25M/0.35M, respectively) as sacrificial reagents. As mentioned earlier, the usage of sacrificial electron donors such as S^{2-}/SO_3^{2-} is necessary for sulfur-containing catalysts (such as CdS) to promote hydrogen-evolution and prevent them from anodic photocorrosion by preferentially consuming the photogenerated holes. [337, 341, 448]

As shown in **Figure 3-48**, the pure mesoporous CdS NCAs show a rather low H_2-production activity, with an average H_2-evolution rate of 0.03 mmol h^{-1}, due to the fast recombination of photoexcited electron–hole pairs. In contrast, the CuS/CdS heterostructures showed a considerable increase in H_2-production activity, clearly indicating that the incorporated CuS compound in the CdS structure plays an important role in enhancing the photocatalytic efficiency. In particular, the catalytic activity of mesoporous CuS/CdS NCAs increases with increasing Cu content and reaches an optimum at 5 mol%, achieving a H_2-evolution rate of 0.16 mmol h^{-1} (see **Figure 3-48b)**, which is about 5.3 times higher than that of pure CdS NCAs. However, further increase in Cu loading to 8 mol% leads to a small reduction of the photocatalytic activity, as inferred by the lower H_2-evolution rate of the 8% CuS/CdS sample (0.12 mmol h^{-1}). This is probably related to one or a combination of the following causes: (i) high Cu content presumably leads to excessive incorporation of CuS clusters that decrease the active surface area of CdS, (ii) excessive formation of CuS NCs on the surface of CdS may also reduce the light-harvesting ability of CdS nanoparticles and (iii) CuS at high content may act as charge-carrier recombination centers, deteriorating the photocatalytic performance.

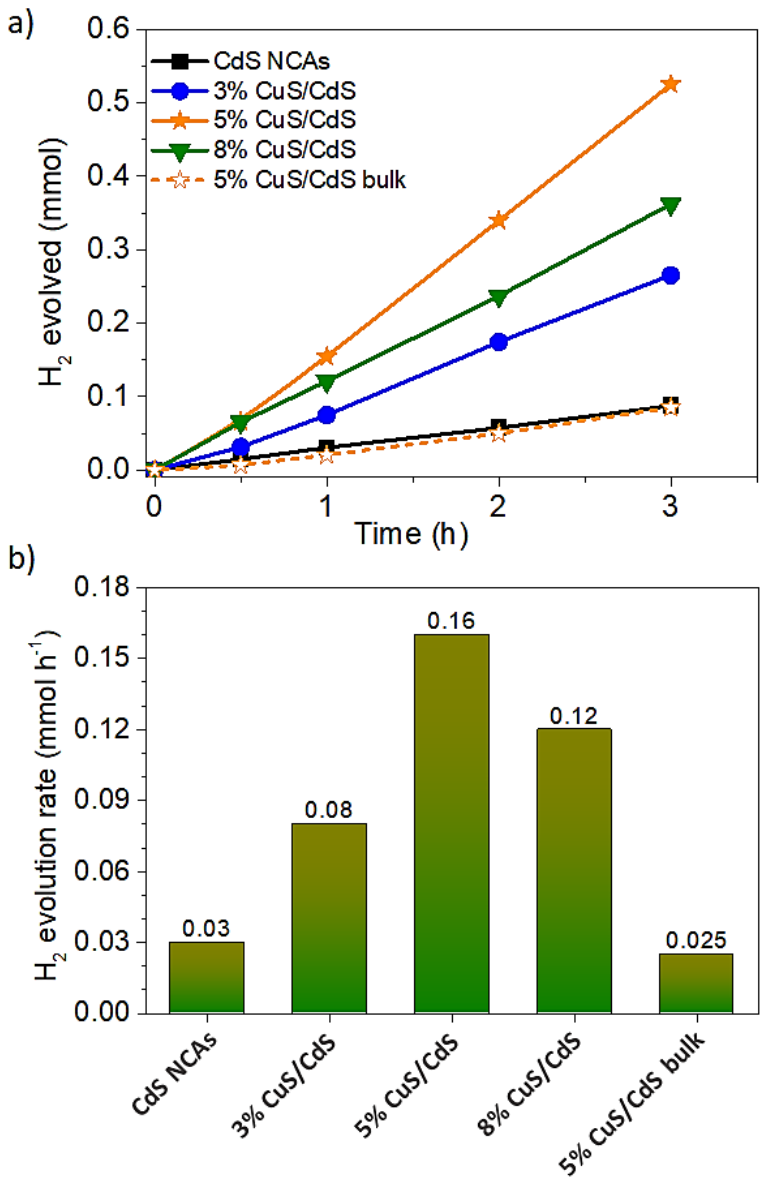

Figure 3-48:a) Time courses for photocatalytic H_2-production and (b) the corresponding H_2-evolution rates, for the mesoporous CdS and CuS/CdS NCAs catalysts. The H_2-evolution *vs* time for the 5 mol% Cu-loaded CdS bulk material (5% CuS/CdS bulk) is also given. The photocatalytic reactions were performed as follows: 20 mg of catalyst were dispersed in 20 mL aqueous solution containing 0.35 M Na_2S and 0.25 M Na_2SO_3; steady reaction temperature at 20 °C; 300-W Xenon light irradiation with a long-pass cut-off filter allowing $\lambda \geq 420$ nm.

Notably, the mesoporous 5% CuS/CdS NCAs catalyst showed significantly higher activity than its bulk counterpart, composed of CuS-loaded CdS microparticles. In particular, when a CdS bulk solid containing 5.1 mol% Cu (as obtained by EDS analysis, **Figure 3-49a**) was used as catalyst (denoted as 5% CuS/CdS bulk), it exhibited a H_2-evolution rate of 0.025 mmol h^{-1} under similar conditions (see **Figure 3-48b)**, which is remarkably lower than that of mesoporous 5% CuS/CdS NCAs. This may be attributed to the low surface area of the 5% CuS/CdS bulk material (BET surface ~45 m^2 g^{-1}, **Figure 3-49b**). Therefore, the enhancement in photocatalytic activity of mesoporous CuS/CdS NCAs is related not only to the formation of CuS/CdS nanoheterojunctions, but also to the

interconnected pore-structure and the enlarged catalyst/electrolyte interface area, which facilitate mass transport between the nanoparticles and provide more active-sites accessible to reactants.

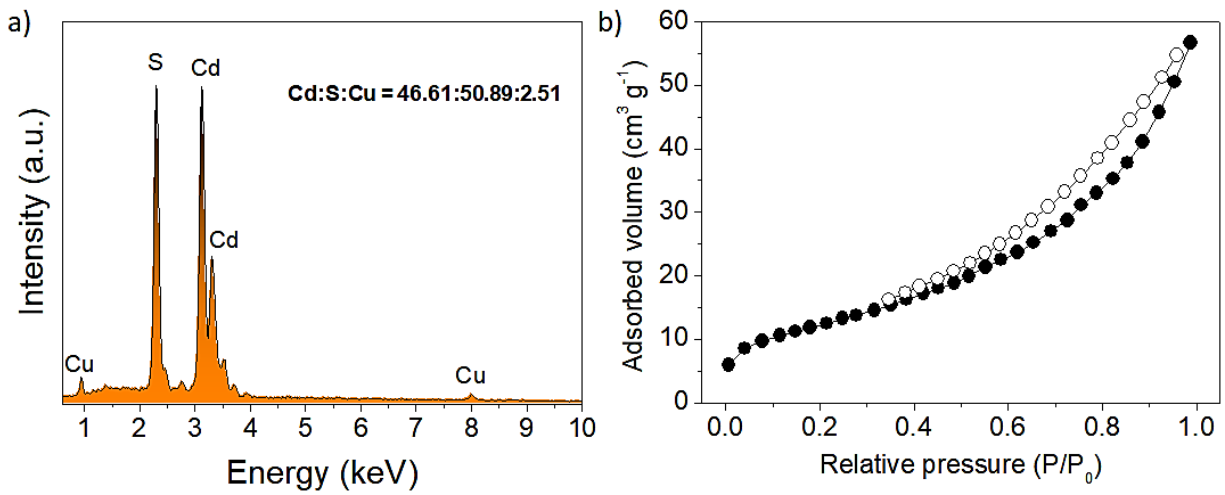

Figure 3-49: (a) Typical EDS spectrum of the Cu-loaded CdS bulk solid (5% CuS/CdS bulk), corresponding to a Cu content of ~5.1 mol%, and (b) N_2 adsorption-desorption isotherms at -196 °C for the 5% CuS/CdS bulk material. Analysis of the adsorption data indicates a BET surface area of ~45 m^2 g^{-1} and a total pore volume of 0.08 cm^3 g^{-1}.

Afterwards, the reaction conditions were optimized by measuring the H_2-evolution for different concentrations of the mesoporous 5% CuS/CdS NCAs catalyst, and the results are displayed in **Figure 3-50**. It can be seen that, with increasing catalyst concentration, the H_2-evolution rate increased to reach a maximum at ~2 g L^{-1}. This H_2-production increase with the catalyst concentration can be interpreted to an enhancement in light absorption by the catalyst's nanoparticles. On the other hand, excess amount of catalyst loading in the reaction (i.e., 2.5 g L^{-1}) resulted in a slightly lower H_2-production activity (0.24 mmol h^{-1}), probably due to the light scattering effect from the particles.

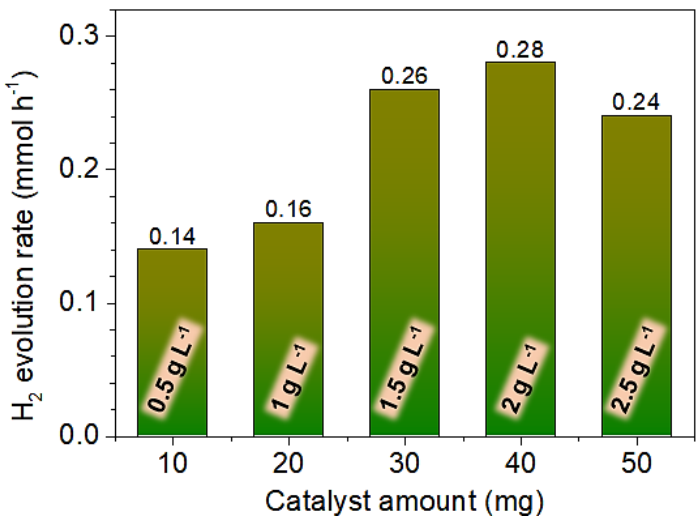

Figure 3-50: Photocatalytic H_2-evolution rates over different amounts (concentrations) of the mesoporous 5% CuS/CdS catalyst. Reaction conditions: 20 mL aqueous solution containing 0.35 M Na_2S and 0.25 M Na_2SO_3; steady reaction temperature at 20 °C; 300-W Xenon light irradiation with a long-pass cut-off filter allowing $\lambda \geq 420$ nm.

Of particular note, the mesoporous 5% CuS/CdS catalyst at 2 g L^{-1} concentration achieves an average H_2-evolution rate as high as 0.28 mmol h^{-1} (or ~7 mmol h^{-1} g^{-1} mass activity). Under these conditions, an apparent quantum yield (QY) of 12.6 % (at λ = 420 ±10 nm) was obtained, according to **eq. 26** and assuming all incident photons (N_{hv} = 9.3×10^{16} s^{-1}) were absorbed by the catalyst's nanoparticles. This efficiency is among the highest reported values for noble-metal-free metal sulfide photocatalysts, as compared to the respective photocatalytic H_2-production activities of other metal-sulfide nanostructures shown in **Table 3-6**.

Table 3-6: Comparison of H_2-production activities for different metal-sulfide-based photocatalysts without noble-metal co-catalysts, studied under similar experimental conditions.

Photocatalyst	**Reaction conditions: catalyst mass, sacrificial**	**Light source**	**H_2-production (QY at 420 nm)**	**Ref.**
MoS_2/CdS composites	0.1 g catalyst, lactic acid (10 vol%)	300-W Xe lamp (λ>420 nm)	0.53 mmol h^{-1}	[379]
WS_2/CdS particles	0.1 g catalyst, lactic acid (10 vol%)	300-W Xe lamp (λ>420 nm)	0.42 mmol h^{-1} (QY ~5%)	[381]
NiS/CdS composites	0.3 g catalyst, lactic acid (30 vol%)	300-W Xe lamp (λ>420 nm)	2.18 mmol h^{-1} (QY ~51.3%)	[390]
CuS/CdS NCAs (present catalyst)	**0.04 g catalyst, 0.25 M Na_2SO_3/0.35 M Na_2S**	**300-W Xe lamp (λ>420 nm)**	**0.28 mmol h^{-1} (QY ~12.6%)**	**[405]**
CuS/ZnS nanosheets	0.2 g catalyst, 0.25M Na_2SO_3/0.35 M Na_2S	350-W Xe lamp (λ>420 nm)	0.21 mmol h^{-1} (QY ~20%)	[438]
CdS/CNTs nanocomposites	0.035 g catalyst, 0.25 M Na_2SO_3/0.35 M Na_2S	300-W Xe lamp (λ>420 nm)	0.17 mmol h^{-1} (QY ~2.1%)	[463]
Co_3O_4/CdS nanocomposites	50 mg catalyst, lactic acid (10 vol%)	350-W Xe lamp (λ>420 nm)	0.15 mmol h^{-1} (QY ~9.7%)	[472]
Cu_2S/CdS nanoparticles	0.2 g catalyst, 0.25M Na_2SO_3/0.35 M Na_2S	300-W Xe lamp (λ>420 nm)	0.4 mmol h^{-1} (QY ~9.5%)	[473]
$Cd_{0.8}Zn_{0.2}S$ particles	0.2 g catalyst, 0.25M Na_2SO_3/0.35 M Na_2S	350-W Xe lamp (λ>430 nm)	0.18 mmol h^{-1} (QY ~10.2%)	[474]
CdS/$Zn_{0.2}Cd_{0.8}S$ nanocomposites	0.2 g catalyst, 0.04 M Na_2SO_3/0.1 M Na_2S	350-W Xe lamp (λ>400 nm)	0.11 mmol h^{-1} (QY ~6.3%)	[475]
$Cd_{0.1}Cu_{0.01}Zn_{0.89}S$ particles	0.3 g catalyst, 0.3 M Na_2SO_3/0.2 M Na_2S	350-W Xe lamp (λ>430 nm)	0.35 mmol h^{-1} (QY ~9.6%)	[476]
$(Zn_{0.95}Cu_{0.05})_{0.67}Cd_{0.33}S$ nanocrystals	0.3 g catalyst, 0.35 M Na_2SO_3/0.25 M Na_2S	300-W Xe lamp (λ>420 nm)	0.51 mmol h^{-1} (QY ~15.7%)	[477]
ZnS-In_2S_3-CuS nanospheres	0.3 g catalyst, 1.2 M Na_2SO_3/0.1 M Na_2S	300-W Xe lamp (λ>400 nm)	3.6 mmol h^{-1} (QY ~22.6%)	[478]
CdS-ZnS-In_2S_3 microspheres	0.015 g catalyst, 1.4 M Na_2SO_3/0.1 M Na_2S	300-W Xe lamp (λ>400 nm)	0.12 mmol h^{-1} (QY ~40.9%)	[479]
ZnS-In_2S_3-Ag_2S nanostructures	0.015 g catalyst, 0.35 M Na_2SO_3/0.25 M Na_2S	300-W Xe lamp (λ>400 nm)	0.05 mmol h^{-1} (QY ~19.8%)	[480]

Furthermore, the assembled mesoporous CuS/CdS NC network was also found to be stable under the examined conditions. The stability of the mesoporous 5% CuS/CdS catalyst was assessed by performing four consecutive 5-h photocatalytic tests. After each test, the catalyst was isolated from the reaction mixture by centrifugation, washed with a polysulfide solution and DI water to remove adsorbed sulfur species, and re-dispersed in a fresh reaction solution. Before each photocatalytic reaction, the reaction cell was de-aerated by purging with argon until no O_2 was detected (by GC analysis). As shown in **Figure 3-51**, the catalyst exhibits a quite stable H_2-evolution rate (within 5% deviation) over a total 20-h illumination period. A small decrease in the H_2-evolution rate during the third and fourth cycle of reuse may hint some minor photocorrosion of the CdS lattice or accumulation of adsorbed disulfide species on the CdS surface that act as optical filter reducing the light absorption of CdS [341] — although the partial loss of catalyst mass during the isolation-reuse process is a probable explanation for the slightly lower activity.

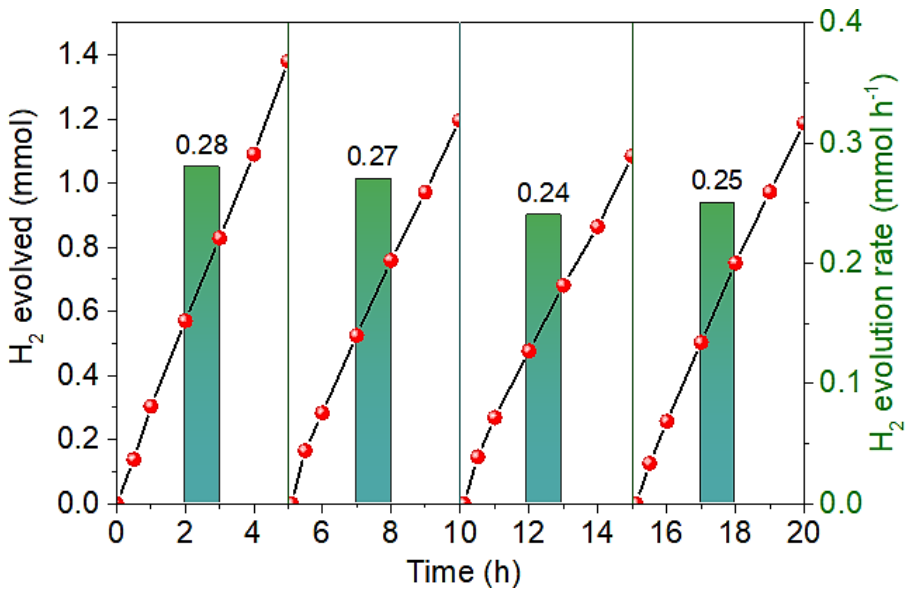

Figure 3-51: Recycling study for the mesoporous 5% CuS/CdS NCAs catalyst. The H_2-evolution rates (columns) were averaged over 5 h of illumination. Reaction conditions: 40 mg of catalyst dispersed in 20 mL aqueous solution containing 0.35 M Na_2S and 0.25 M Na_2SO_3; steady reaction temperature at 20 °C; 300-W Xenon light irradiation with a long-pass cut-off filter allowing $\lambda \geq 420$ nm.

In addition, X-ray microanalysis and nitrogen physisorption measurements were employed to examine the chemical and structural stability of the reused catalyst. EDS results showed a ~5.09 mol% of Cu content (**Figure 3-52a**), while N_2 physisorption analysis indicated a BET surface area of 180 $m^2\ g^{-1}$, pore volume of 0.20 $cm^3\ g^{-1}$ and pore size of 6.2 nm (**Figure 3-52b**), which are similar to those of the fresh sample. However, after catalysis the XPS spectrum of the mesoporous 5% CuS/CdS sample (green line in **Figure 3-44b**), shows that a fraction of Cu^{2+} ions are reduced to Cu^{+}, judging from the shift of the Cu $2p_{3/2}$ and Cu $2p_{1/2}$ signals to higher binding energies (at 933.2 and 952.9 eV, respectively). [481, 482] Moreover, the accompanying Auger Cu LMM spectrum (see inset

in **Figure 3-44b)** reveals a peak at 569.6 eV, indicating also the presence of Cu_2S species in this sample. [473, 483] Thus, it is apparent that CuS was partially reduced to Cu_2S during the visible-light irradiation. On the contrary, the XPS spectrum of the regenerated 5% CuS/CdS sample showed Cd $3d_{5/2}$ and $3d_{3/2}$ core-level signals with binding energies at 404.7 and 411.5 eV, respectively (green line in **Figure 3-44a**), which are almost identical to those of the fresh catalyst, thus indicating that CdS NCs are chemically stable under the examined reaction conditions.

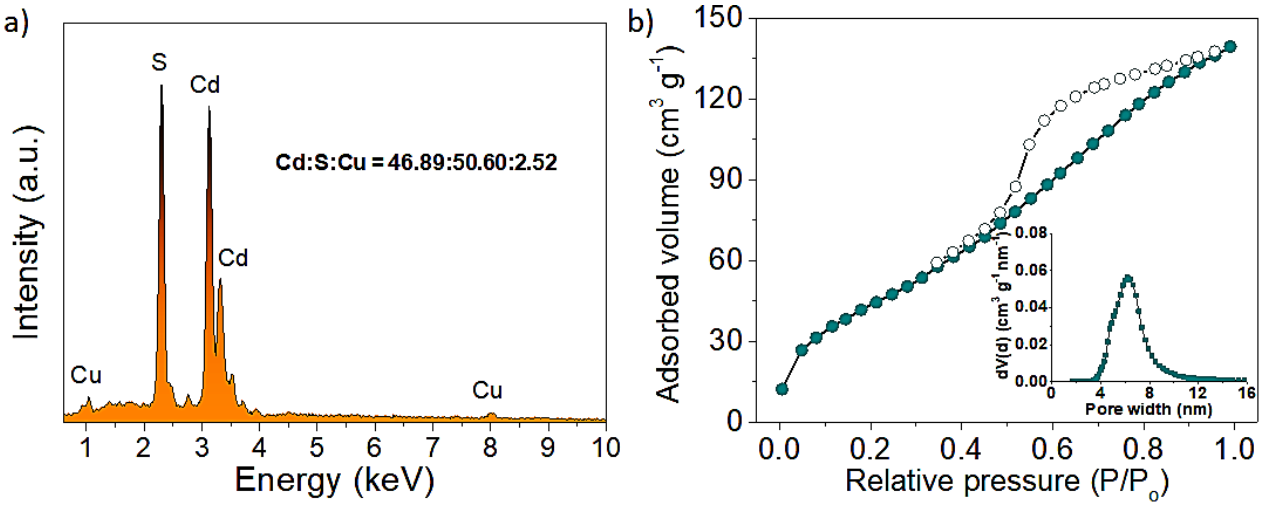

Figure 3-52: (a) Typical EDS spectrum corresponding to a Cu content of ~5.09 mol%, and (b) N_2 adsorption-desorption isotherms at -196 °C and the corresponding NLDFT pore size distribution (inset), for the mesoporous 5% CuS/CdS NCAs catalyst retrieved after 20 hours of photocatalytic reaction.

3.3.4 Role of CuS in photocatalytic activity

To gain a better understanding of the role of CuS in the H_2-production activity of CuS/CdS NCAs, a controlled photocatalytic H_2-evolution reaction was carried-out under monochromatic irradiation with λ = 550 ±10 nm (using a band-pass filter, Asahi Spectra, Japan). In this experiment, the mesoporous 5% CuS/CdS catalyst exhibited very low H_2-production activity (ca. 4.65 μmol h^{-1}) that corresponds to an apparent QY of about 0.94% (N_{hv}=1.65×10^{17} s^{-1}). Considering that CdS absorbs photons with wavelengths shorter than 500 nm, this activity can be attributed solely to the photoexcitation of CuS. Of note, single-component mesoporous CuS assemblies, which were obtained by complete cation-exchange of CdS NCAs using a 10-fold molar excess of Cu^{2+} (relative to CdS), showed a negligible visible-light H_2-production activity, even after 4 h of illumination (results not shown). The lack of activity can be attributed to the low reducing potential of the conduction band (CB) electrons (–0.33 V *vs* NHE, pH = 7) with respect to water-reduction and to the inefficient charge-carrier separation in CuS. Thus, the above results clearly demonstrate that CuS itself cannot generate significant amount of H_2, although it can extend the light absorption of the composite heterostructures to the visible-NIR region (as inferred by UV– vis/NIR spectroscopy).

Therefore, it can be concluded that the improved photoactivity of the composite catalysts was mainly due to the efficient charge-carrier dissociation at the CuS/CdS interface, which lowers the charge-recombination loss. Study of electronic relaxation in the as-prepared CuS/CdS heterostructures by photoluminescence spectroscopy indicates that this is indeed the case. **Figure 3-53** compares the PL spectra of the mesoporous pure CdS NCAs and the corresponding CuS/CdS heterostructures with different Cu-loadings. The results reveal that addition of Cu into the CdS structure leads to a gradual quenching of the band-edge excitonic emission at 470 nm, which may indicate that the majority of the photoexcited carriers are delocalized in the formed CuS–CdS nano-heterostructures. Hence, the incorporation of CuS phase seems to impede the radiative recombination of charge-carriers through an effective separation of electron-hole pairs across the CuS/CdS nanojunctions.

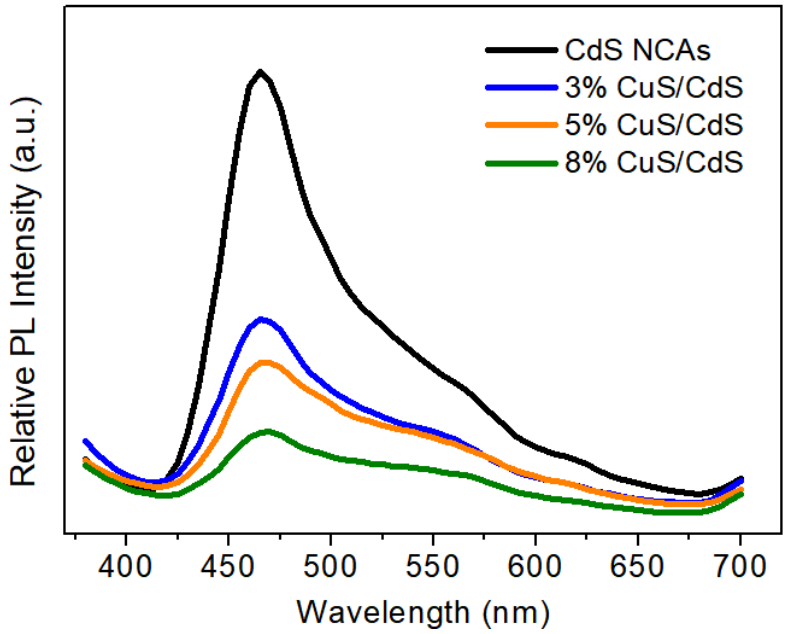

Figure 3-53: Room-temperature PL emission spectra for the mesoporous CdS NCAs and the respective CuS/CdS heterostructures with various Cu-content. All measurements were performed in water (1 mg mL^{-1} sample concentration) using an excitation wavelength of 360 nm.

The effect of CuS loading on the electronic band structure, and thus on the electrochemical properties of CuS/CdS composites, was further investigated by electrochemical impedance spectroscopy. **Figure 3-54** displays the Mott-Schottky plots ($1/C^2$ *vs* applied potential) and the corresponding fits of the linear portion of the plots for the mesoporous CdS NCAs and CuS/CdS composites containing 3, 5 and 8 mol% Cu (measured as thin-film electrodes on FTO-coated glasses). The obtained flat-band potentials (V_{FB}), measured from the intercepts of the extrapolated linear fits with the potential axis ($1/C^2 = 0$, according to **eq. 23**), show that V_{FB} shifts gradually to a more negative (cathodic) direction, that is, from –0.40 V to –0.53 V (*NHE*, pH = 7), as the Cu content increases from 0 to 8 mol%. Moreover, the electron donor density (N_D) of CdS (calculated from the

slopes of Mott-Schottky plots, according to **eq. 25)** seems to decrease initially with the addition of 3 mol% Cu (i.e., from 3.93×10^{16} cm^{-3} for pure CdS to 3.28×10^{16} cm^{-3} for 3% CuS/CdS NCAs), and then progressively increases with increasing the Cu content to 5 mol% (3.71×10^{16} cm^{-3}) and 8 mol% (4.55×10^{16} cm^{-3}), as evidenced by the change in slope of the Mott-Schottky plots. Of note, all the obtained Mott-Schottky plots showed positive slopes in the applied potential range from –0.7 V to –0.4 V (Ag/AgCl, pH=7), which is indicative of the n-type behavior for CdS, as expected. All the measured electrochemical properties of CuS/CdS NCAs are summarized in **Table 3-7**.

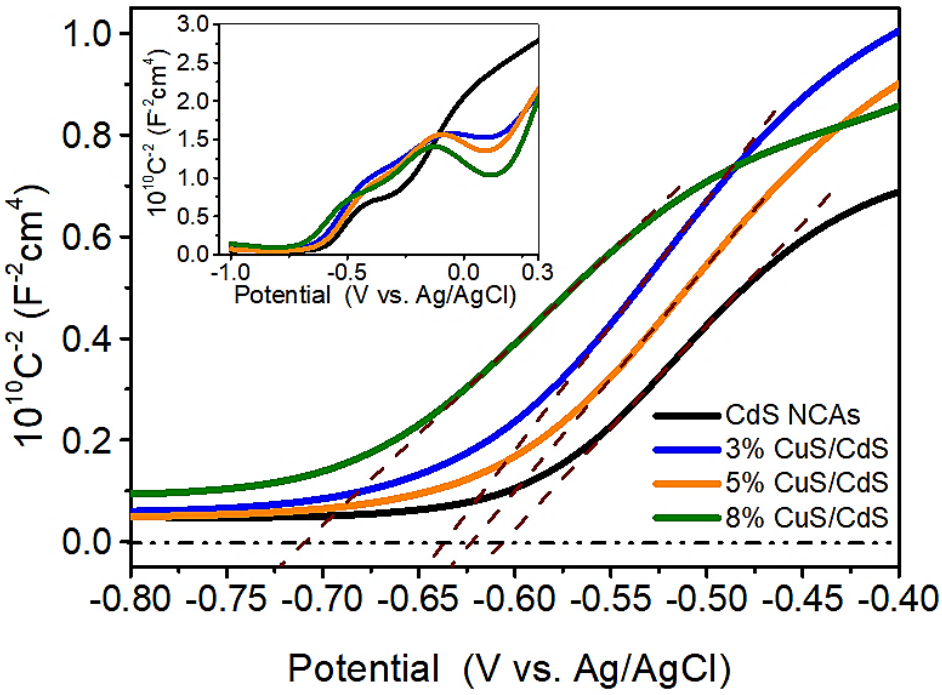

Figure 3-54: Mott-Schottky plots (dashed lines are fit to the data) of the mesoporous CdS NCAs and CuS/CdS composites with different Cu content. Inset: the respective plots for a wider range of applied potentials.

Table 3-7: Analytical data obtained from Mott-Schottky plots for the mesoporous pristine CdS and different Cu-loaded CdS NCAs.

Sample	Flat Band[a)] [V_{FB}] (V *vs* NHE)	Slope ($F^{-2}cm^4V^{-1}$)	Donor concentration[b)] [N_D] (cm^{-3})
CdS NCAs	-0.40	4.034×10^{10}	3.93×10^{16}
3% CuS/CdS	-0.43	4.825×10^{10}	3.28×10^{16}
5% CuS/CdS	-0.44	4.267×10^{10}	3.71×10^{16}
8% CuS/CdS	-0.53	3.466×10^{10}	4.55×10^{16}

[a)] The flat-band potentials were converted from the Ag/AgCl electrode scale to the normal hydrogen electrode (NHE) scale using eq. 24.; [b)] The N_D values were obtained with the help of eq. 25 using the slopes of the Mott-Schottky plots and the relative dielectric constant of CdS (ε = 8.9)

The observed cathodic shift in the flat-band positions and increase in donor (electron) density of CdS upon CuS addition may be explained by a possible unpinning of its Fermi level via passivation of surface-states on CdS NCs from CuS deposition. Such a behavior is suggested by the increased positive Mott-Schottky slopes of the Cu-loaded samples compared to the slope of pure CdS NCAs (see inset of **Figure 3-54**) and also by considering the formation of p–n heterojunctions between CdS and CuS NCs. CuS is a p-type semiconductor [470, 484-486]. This means that, when CdS and CuS NCs are placed in contact with each other, given that the Fermi level of n-type CdS (ca. 4.5–4.9 eV) is more negative than the Fermi level of p-type CuS (ca. 5.1–5.3 eV) [487], a built-in potential ($\Delta\Phi_{SC}$) of approximately 0.4–0.8 V will be formed at the interface of CuS/CdS junction. That results to an internal electric field which drives electrons from the CB of CdS to CuS until the system reaches equilibrium. Reasonable energy diagrams of the band alignment between CuS and CdS NCs before contact and after equilibrium conditions are illustrated in **Figure 3-55**. In **Figure 3-55a**, the conduction band (CB) and valence band (VB) levels of CdS and CuS (before contact) were estimated using the well-known Mulliken electronegativity theory [354, 488], according to the following equations:

$$\boldsymbol{E_{CB} = \chi_{abs} - 0.5 \cdot E_g} \qquad \textbf{(eq. 33)}$$

$$\boldsymbol{E_{VB} = \chi_{abs} + 0.5 \cdot E_g} \qquad \textbf{(eq. 34)}$$

where, E_{CB} and E_{VB} are the conduction and valence band-edge energy levels (in eV *vs* vacuum) respectively, E_g is the band gap of the semiconductor and χ_{abs} denotes the absolute electronegativity of the semiconductor. The reported χ_{abs} values for CdS and CuS are 5.18 eV and 5.27 eV, while the *Eg* values (measured by UV– vis/NIR spectroscopy) are 2.54 eV and 2.2 eV, respectively. Thus, the E_{VB} and E_{CB} of CdS NCs were estimated to be 6.45 eV and 3.9 eV *(vs* vacuum), respectively, while the corresponding band-edge levels of CuS NCs were found to be 6.37 eV for E_{VB} and 4.17 eV for E_{CB} (*vs* vacuum). At equilibrium condition, the redistribution of charge-carriers will generate a depletion layer (positively-charged region) in CdS and a negatively-charged region (accumulation layer) in the CuS side of the p-CuS/n-CdS junction. Indeed, the formation of a depletion region in CdS NCs also explains the observed initial decrease in the donor density of CdS when a small amount (3 mol%) of Cu is incorporated (see **Table 3-7**). By increasing the CuS loading, as a result of the internal electric field and accumulation of electrons in CuS, its CB will gradually shift and eventually rise above the CB level of CdS (**Figure 3-55b**). This assumption is also supported by the cathodic shift in V_{FB} and the increase in N_D values with increasing the Cu-content in the CuS/CdS NCAs composites.

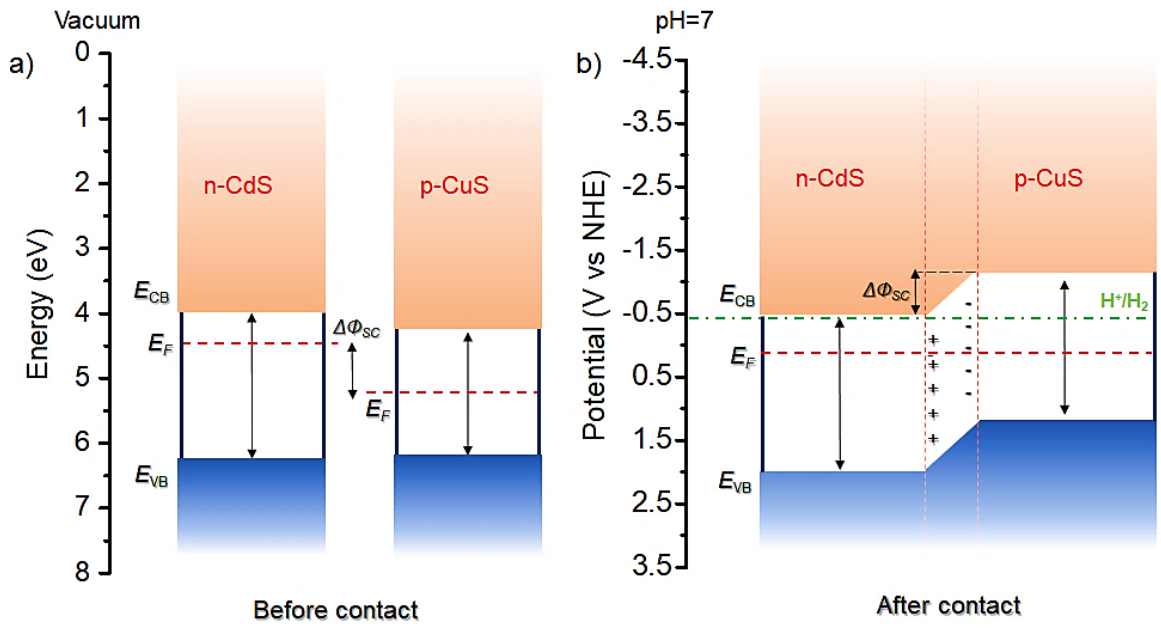

Figure 3-55: (a) Energy band diagrams of the n-type CdS and p-type CuS semiconductors, before contact. The conduction band (E_{CB}) and valence band (E_{VB}) energy levels of CdS and CuS semiconductors were estimated from eq. 33 and eq. 34, respectively, according to the Mulliken electronegativity theory. (b) Band alignment scheme of the formed p–n junction upon contact equilibrium between CdS and CuS NCs. The shown band-edge potential positions are based on the UV–vis/NIR and EIS results for the mesoporous 5% CuS/CdS sample, considering also a build-in potential ($\Delta\Phi_{SC}$) of ~0.8 eV.

Overall, the nanoscale p–n CuS/CdS heterojunctions facilitate the efficient distribution of charge-carriers, through the cathodic shift of the V_{FB} and the appropriate alignment in the band-edge positions of the composites. These effects, along with the large surface area provided by the 3D porous structure of the assembled NCs, definitely have a great impact on the enhanced photocatalytic activity of the mesoporous CuS/CdS heterostructures. Based on the obtained results, a possible mechanism for the photocatalytic H_2-production on mesoporous CuS/CdS NCAs is proposed and illustrated in **Figure 3-56**. Under visible-light irradiation, both CdS and CuS get excited and generate electron-hole pairs. The favorable thermodynamic conditions of the band structure and the internal electrostatic field drive the transfer of photoexcited electrons from the CB of CuS to the CB of CdS, giving rise to an accumulation of electrons in CdS where H_2-evolution take place. In addition, during the course of irradiation, a fraction of photoexcited electrons from the VB of CdS (E_{VB} = 2 V *vs* NHE, pH = 7, as determined according to E_{FB} from EIS and E_g from optical absorption measurements, see **Tables 3-5** and **3-7**) may be also transferred to the CuS NCs (interfacial charge transfer, IFCT), causing their partial reduction to Cu_2S (E^o = –0.91 V *vs* NHE, pH=7). The excitation energy for this direct electronic transition is estimated to be approximately 2.9 eV (ca. 430 nm), and thus it is a viable option under the examined irradiation conditions (i.e., $\lambda \geq$ 420nm). [438] This is also corroborated by the presence of Cu_2S in the reused 5% CuS/CdS NCAs catalyst, as evidenced by XPS spectroscopy (see **Figure 3-44**).

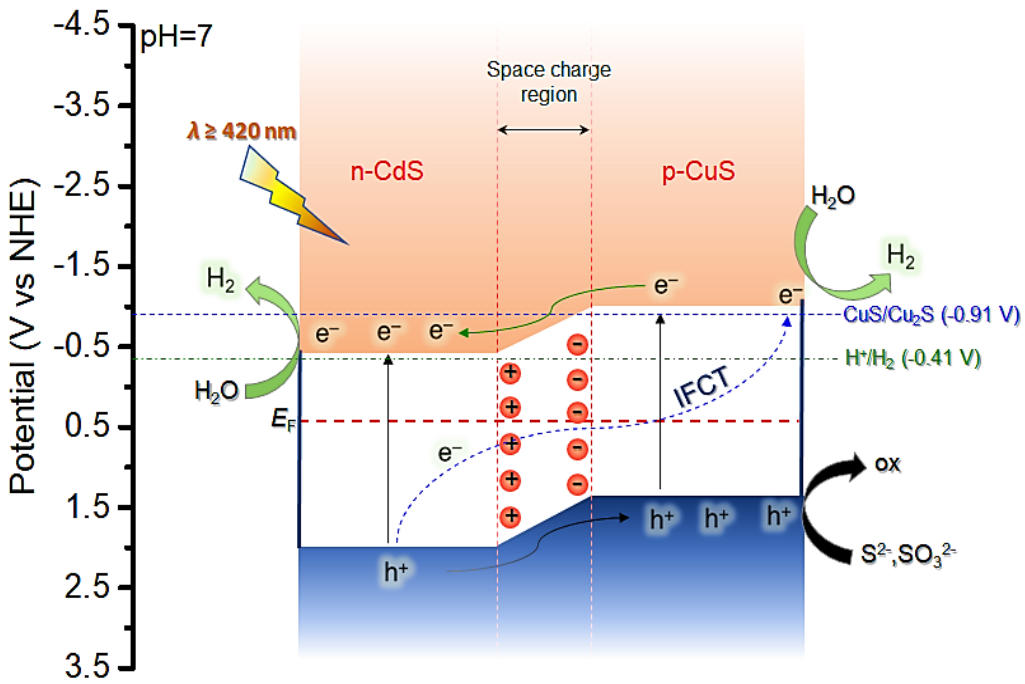

Figure 3-56: Schematic illustration of the photocatalytic H_2-production mechanism at the p-CuS/n-CdS heterostructure, under visible-light irradiation and in the presence of S^{2-}/SO_3^{2-} sacrificial reagents. The shown band-edge potential positions are based on the UV–vis/NIR and EIS results for the mesoporous 5% CuS/CdS sample. The respective redox potentials of the H^+/H_2 and CuS/Cu_2S pairs at pH=7 are also shown. IFCT corresponds to the photo-induced interfacial charge transfer of electrons from the VB of CdS to the level of the CuS/Cu_2S redox couple, where water-reduction into H_2 also occurs according to eq. 35 and eq. 36 reactions. Adapted from ref. [405] by permission of The Royal Society of Chemistry.

These in-situ formed CuS/Cu_2S nanocrystals are proposed to serve as functional co-catalysts, further enhancing the separation and lifetime of photogenerated charge-carriers (through IFCT from the VB of CdS to the CuS/Cu_2S), and contributing as well to H_2-production according to the following reactions [438, 489]:

$$2CuS + 2e^- \rightarrow Cu_2S + S^{2-} \quad \textbf{(eq. 35)}$$

$$Cu_2S + 2H^+ + S^{2-} \rightarrow 2CuS + H_2 \quad \textbf{(eq. 36)}$$

Meanwhile, since the VB of CuS NCs lies in a higher (more positive) potential than that of CdS (see **Figure 3-55b**), the photoexcited holes can migrate to CuS where they oxidize the sacrificial S^{2-}/SO_3^{2-} reagents to $S_2O_3^{2-}/SO_4^{2-}$. [310] As a consequence, an efficient charge carrier separation is successfully achieved through the nanoscale p–n junctions of CuS and CdS NCs, thus leading to an enhanced photocatalytic H_2-production activity. As a confirmation of this assumption, the PL results have indicated the improved separation of photoexcited electrons and holes within the composite CuS/CdS structure. Therefore, these results suggest the great possibility for the implementation of this new mesoporous p-CuS/n-CdS NCAs heterojunctional photocatalyst as a sustainable and low-cost alternative in solar energy-conversion applications.

3.4 *Mesoporous* β-$Ni(OH)_2$-modified CdS NCAs

The previous sections of this chapter demonstrated that, through the combination of nanostructuring and the use of co-catalysts, the photocatalytic H_2-evolution activity of CdS can be remarkably improved. We found that, although CuS NCs could serve as sustainable co-catalysts enhancing the visible-light photocatalytic activity of CdS [405], their overall contribution to the H_2-production efficiency still cannot match that of noble-metal co-catalysts such as Pt [396, 404]. Hence, the development of cost-effective and highly active noble-metal-free CdS-based photocatalysts is of great importance in the search for efficient materials for sustainable H_2-generation technologies. To this end, recent investigations have shown that inexpensive and more abundant Ni-based materials, such as nickel oxides/hydroxides and sulfides, can function as efficient photo- and electrochemical catalysts for hydrogen evolution. Thus, various CdS-based heterostructures, such as NiO_x-loaded CdS particles [387], 3D NiO-CdS heterostructures [490], Ni-modified CdS particles [383], nanorods [358, 382], nanosheets [384] and nanoparticles [491, 492], NiS-loaded CdS nanorods [493], nanowires [494] and microparticles [390], CdS/RGO composites [495], and $Ni(OH)_2$-modified CdS [385] and CdS/g-C_3N_4 composites [394], have already been fabricated and examined as H_2-evolution catalysts. The results of these studies indicated that the Ni-containing CdS heterostructures can achieve improved photocatalytic performance, owing to the high interfacial separation and transfer of the photoexcited charge-carries. As such, the photon-to-hydrogen conversion efficiency of these catalysts ranges from 2.8% up to 74.1% under 400 – 450 nm light irradiation, which is comparable to that of precious-metal-loaded CdS catalysts. [383, 385, 387, 390, 394, 490, 493, 496] Notwithstanding the remarkable progress, the underlying role of deposited nickel species in enhancing the photocatalytic performance for H_2-evolution is still poorly understood. Moreover, the development of mesoporous 3D hetero-nanostructures from Ni-modified ultra-small CdS nanoparticles with inherently large surface-area and interconnected open-pore structure has not been reported yet.

In this section, we present the fabrication of new functional mesoporous CdS-based heterostructures, comprising of interconnected β-$Ni(OH)_2$-modified CdS nanocrystal assemblies (NCAs) with high surface area and 3D porous network, and we demonstrate their high performance in visible-light photocatalytic H_2-production from aqueous alkaline solution. Furthermore, the effect of β-$Ni(OH)_2$ particles on the H_2-production activity of these newly developed catalysts is investigated, and some insights into the photocatalytic reaction mechanism are also given.

3.4.1 Synthesis of mesoporous Ni-CdS NCAs

Mesoporous networks of Ni-modified CdS NC assemblies (NCAs) were prepared by the oxidative coupling of thiol-capped CdS NCs in the presence of a block copolymer (Brij 58) as structure-directing template [402], followed by a straightforward photochemical reduction-deposition of nickel cocatalyst, using triethylamine (TEA) as sacrificial electron donor. With this procedure, a series of heterojunction Ni-CdS composite frameworks with different Ni loadings (i.e., 5, 7, 10 and 15 wt.% Ni) were prepared by varying the Ni^{2+} precursor concentration (from 4.5 to 15 mM) in the reaction solution [406]. The catalysts, hereafter, are referred to as n% Ni-CdS, where n is the mass percentage of Ni atoms in the composite structure. As will be indicated later, during the photo-deposition process, small metallic Ni^0 nanoclusters are initially deposited on the CdS NCAs surface via photochemical reduction of the Ni^{2+} ions (**eq. 37**), and then a large part of them is oxidized to the β-$Ni(OH)_2$ phase by reacting with excess OH^- in the solution (**eq. 38**) [497, 498] (in particular, triethylamine with pKa ~10.8 forms alkaline solution). A schematic representation of the photochemical deposition of Ni^0/β-$Ni(OH)_2$ nanostructures on the CdS NCAs surface is illustrated in **Figure 3-57**.

$$Ni^{2+} + 2e^- \rightarrow Ni^0 \qquad \textbf{(eq. 37)}$$

$$Ni^0 + 2OH^- \rightarrow \beta\text{-}Ni(OH)_2 + 2e^- \qquad \textbf{(eq. 38)}$$

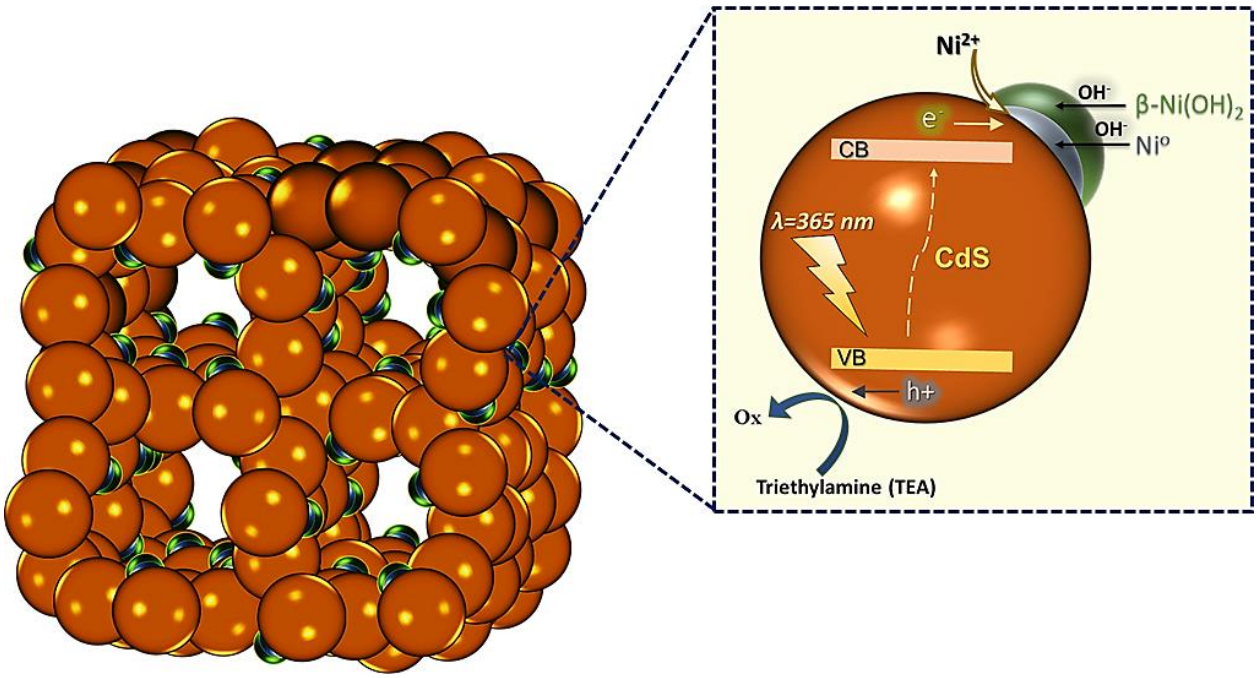

Figure 3-57: Schematic illustration of the photo-deposition process of Ni^0/β-$Ni(OH)_2$ nanoparticles on the surface of mesoporous CdS NCAs.

3.4.2 Morphology and structural characterization

The elemental composition of the Ni-modified samples was determined by energy dispersive X-ray spectroscopy. The EDS spectra showed strong Cd and S signals with an atomic ratio of Cd/S very close to the expected 1:1 stoichiometry of the CdS compound (**Figure 3-58**). Also, EDS analysis confirmed the presence of Ni at different Ni/Cd ratios, which correspond to Ni loadings from ~5 to ~15 wt. %, see **Table 3-8**. Notably, the obtained Ni-content was found to be very close to that expected from the stoichiometry of reactions (within ~0.5 wt.% deviation), suggesting the complete deposition of Ni-species onto the CdS support.

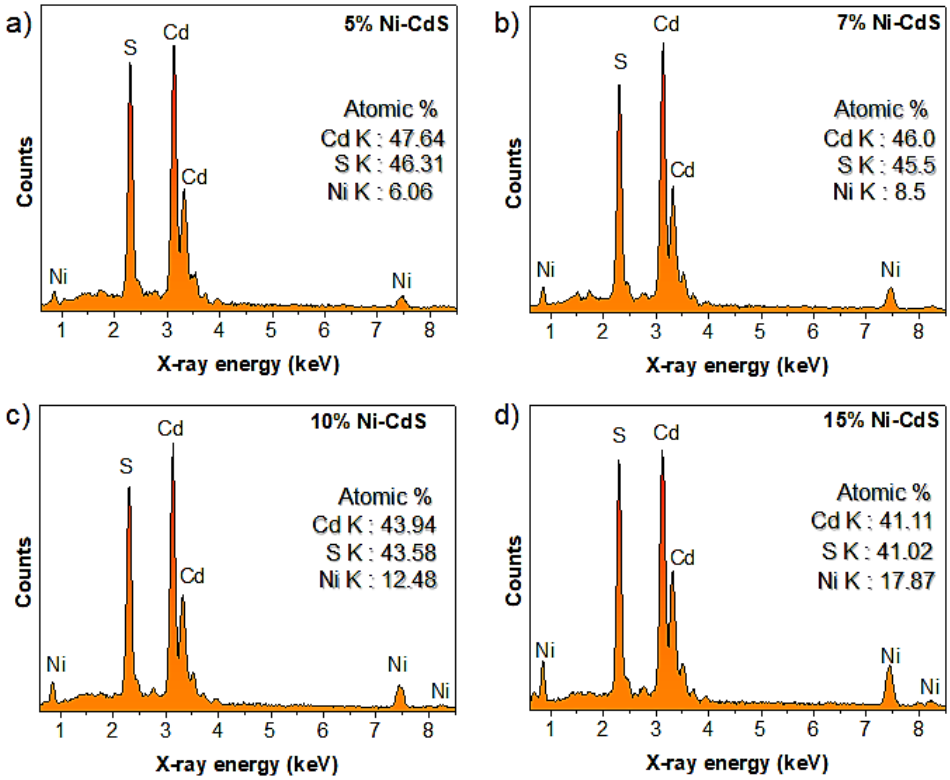

Figure 3-58: Typical EDS spectra of the mesoporous Ni-modified CdS NCAs, a) 5% Ni-CdS, b) 7% Ni-CdS, c) 10% Ni-CdS, and d) 15% Ni-CdS, with 5, 7, 10 and 15 wt. % Ni content, respectively.

The crystallinity of the as-prepared mesoporous catalysts was characterized by powder X-ray diffraction. As shown in **Figure 3-59**, all samples exhibit three distinct diffraction peaks at 2θ scattering angles of 20º–60º, which are attributed to the zinc-blende structure of CdS (JCPDS no. 42-1411). The broadness of the XRD reflections infers the presence of very small crystal-grain sizes, and a peak-width analysis of the XRD patterns using the Scherrer equation (**eq. 19**) indicates that the CdS NC-framework comprises nanocrystallites with an average size of 2–2.3 nm. However, no obvious diffraction peaks for Ni-species were observed, even in the XRD pattern of the 15 wt.% Ni-loaded sample, possibly due to the high-dispersion and small size of their crystal grains.

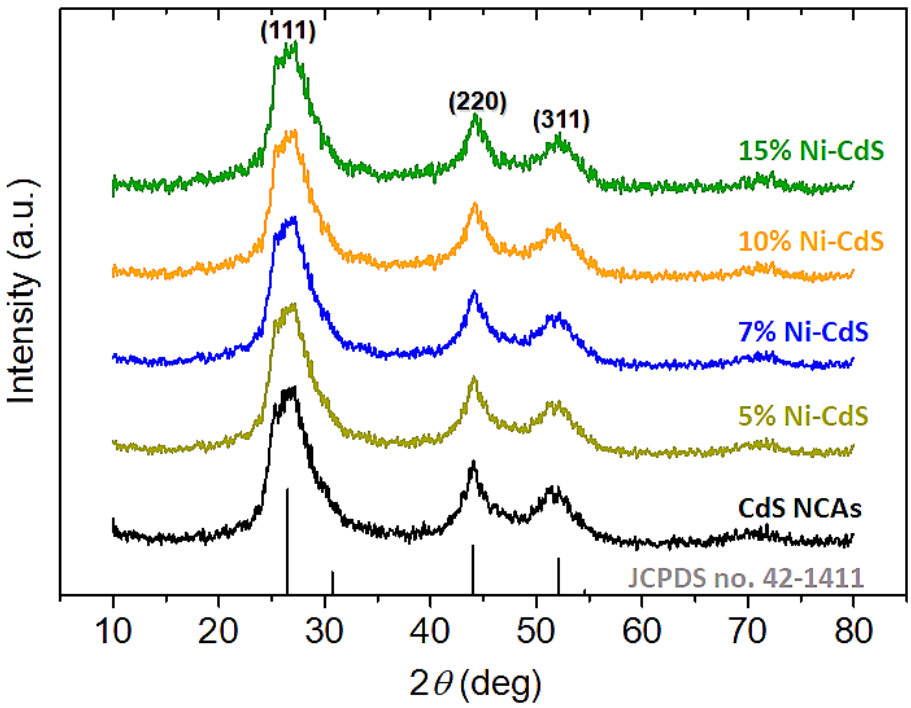

Figure 3-59: Powder XRD patterns for the mesoporous CdS and Ni-modified CdS NCAs catalysts. The standard diffraction lines of zinc-blende CdS (JCPDS card no. 42-1411) are also given.

Therefore, to elucidate the crystal phase of the Ni-deposited species, a photo-deposited 20 wt.% Ni-CdS NCAs sample was also prepared and its crystallinity investigated with XRD. This sample showed four new weak features at 2θ angles of about 19°, 33°, 38° and 59° (see **Figure 3-60**), which can be assigned respectively to the (001), (100), (101) and (110) diffraction peaks of hexagonal *β*-$Ni(OH)_2$ (space group *P*-3*m*1(164)), according to the JCPDS card no. 14-0117.

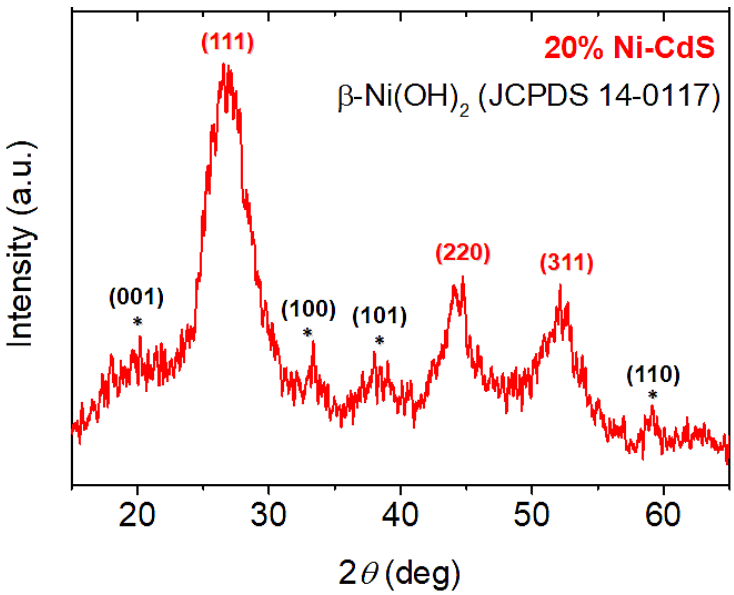

Figure 3-60: XRD pattern of the mesoporous Ni-CdS NCAs sample photo-deposited with 20 wt.% Ni (20% Ni-CdS). The peaks noted with the symbol (*) correspond to the hexagonal phase of *β*-$Ni(OH)_2$ according to the JCPDS no. 14-0117.

Representative transmission electron microscopy images for the mesoporous Ni-CdS NCAs with 10 wt.% Ni (10% Ni-CdS), which is the most active catalyst among the as-prepared Ni-CdS composites, are shown in **Figure 3-61**. The images in **Figures 3-61a and b** show an open-pore structure composed of interconnected CdS nanoparticles with diameters ~4–5 nm. Furthermore, from the high-resolution TEM investigation in **Figure 3-61c**, some small nanocrystals with a size of ~3–4 nm can be discerned on the surface of CdS. A careful examination by fast Fourier transformation analysis (inset of **Figure 3-61c**) revealed that these nanocrystals adopt a hexagonal structure, showing well-resolved (100) and (011) lattice planes of β-Ni(OH)$_2$ with 2.7 and 2.3 Å spacing, respectively.

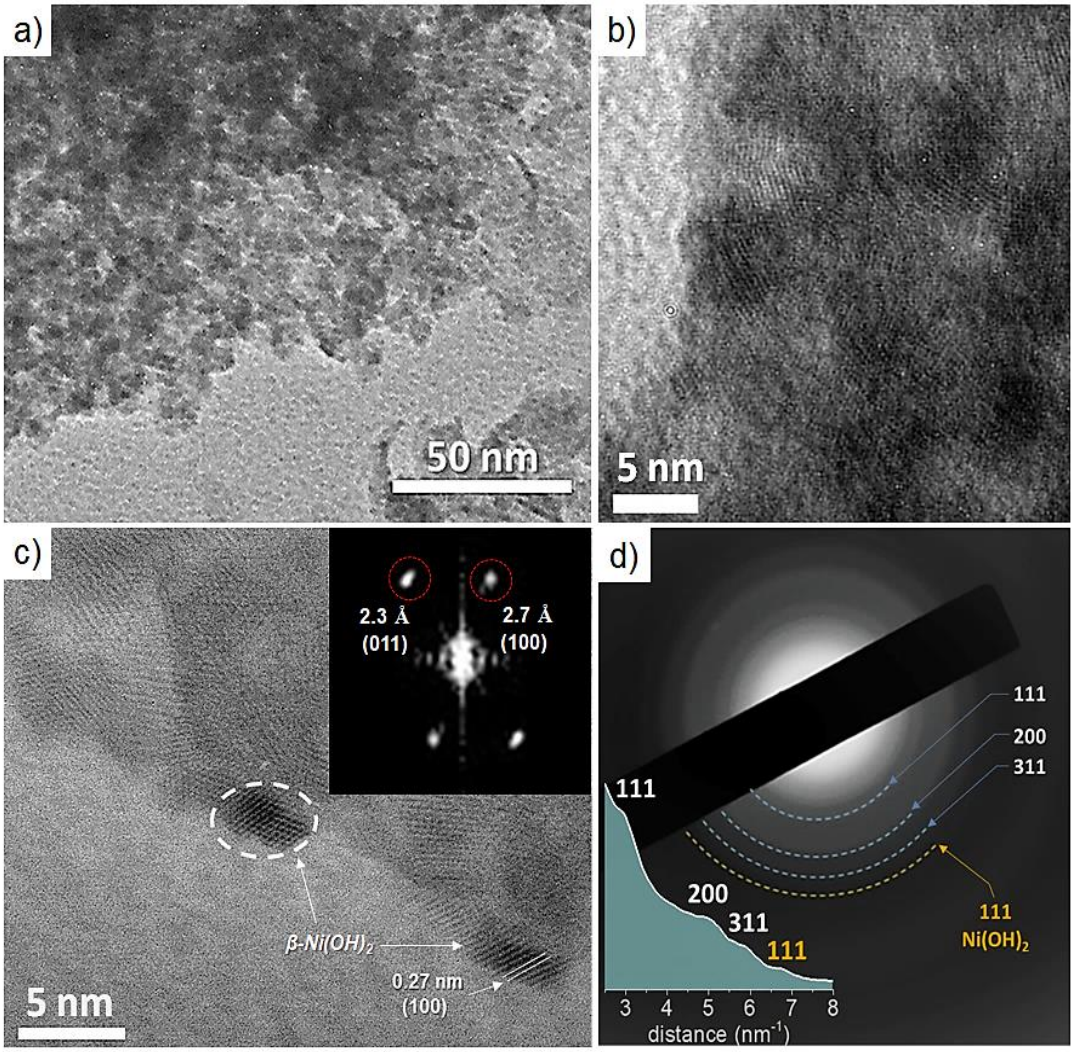

Figure 3-61: (a, b) Typical TEM images at different magnifications of the mesoporous 10% Ni-CdS NCAs catalyst, displaying the porous morphology of the assembled NCs. (c) HRTEM image showing β-Ni(OH)$_2$ nanoparticles in intimate contact with CdS. Inset, the corresponding FFT pattern of the circled area, indicating the (100) and (011) lattice planes (along the [0$\bar{1}$1] zone axis) of the hexagonal β-Ni(OH)$_2$. (d) SAED pattern (inset: the corresponding profile of the SAED intensity) taken from a small area of the mesoporous 10% Ni-CdS NCAs structure.

Besides, the selected-area electron diffraction pattern taken from a small area of the mesoporous structure (**Figure 3-61d**) displays a series of broad Debye-Scherrer diffraction rings, coinciding with

the (111), (220) and (311) planes of zinc-blende CdS structure, and an additional diffraction ring (with d-spacing of ~1.5 Å) that can be assigned to the (111) plane of hexagonal β-$Ni(OH)_2$, in agreement with the XRD and HRTEM results. Hence, all the above results firmly confirm the deposition of β-$Ni(OH)_2$ nanoparticles on the CdS surface and, more importantly, with intimate contact which is beneficial for the interfacial charge-transfer within the heterostructured catalyst.

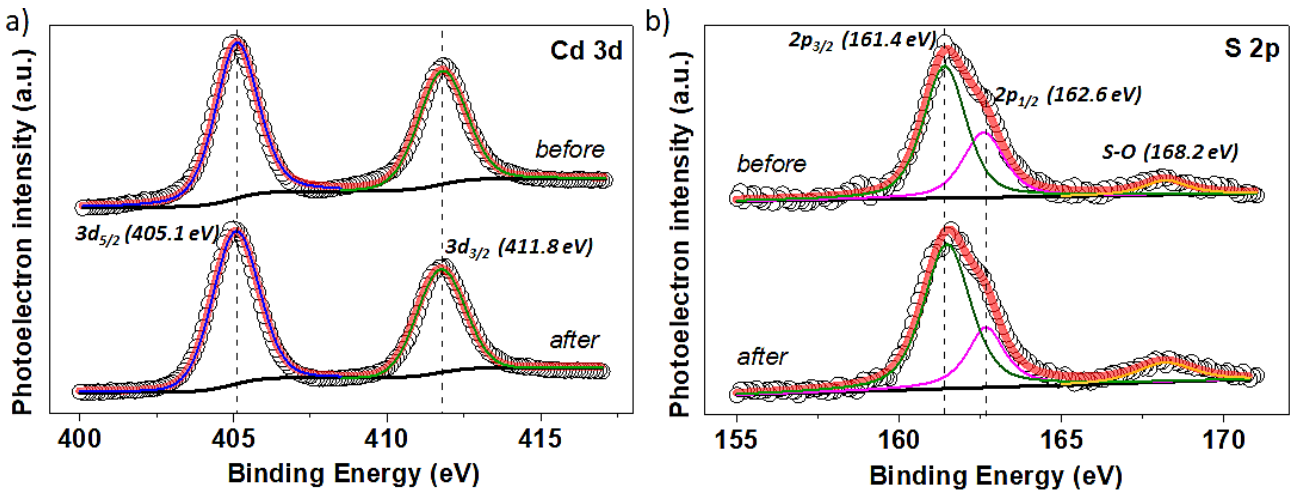

Figure 3-62: High-resolution XPS (a) Cd 3d and (b) S 2p core-level spectra for the 10% Ni-CdS NCAs catalyst before and after 20 h of photocatalytic reaction.

To investigate the chemical state of elements constituting the mesoporous structure, X-ray photoelectron spectroscopy analyses were performed. **Figure 3-62** presents typical Cd 3d and S 2p core-level spectra obtained from the mesoporous 10% Ni-CdS NCAs sample. The Cd 3d XPS spectrum (**Figure 3-62a**) shows two symmetrical peaks at 405.1 and 411.8 eV binding energies, which are assigned to the Cd $3d_{5/2}$ and Cd $3d_{3/2}$ spin-orbit components of Cd^{2+} in CdS. [499] As shown after fitting in **Figure 3-62b,** the XPS S 2p core-level doublet peaks at 161.4 and 162.6 eV correspond to the S $2p_{3/2}$ and S $2p_{1/2}$ levels in CdS, respectively. Also, the spin-orbit splitting of these peaks (i.e., 1.2 eV) and their ~2:1 area ratio, match well the respective values reported for S^{2-} ions in CdS. [500, 501] The lack of further S $2p_{3/2}$ and S $2p_{1/2}$ peak splitting suggests that there are no S lattice atoms bonding with Ni, since the S $2p_{3/2}$ and S $2p_{1/2}$ XPS peaks of NiS are close to 161.9 eV and 162.8 eV, respectively, thereby indicating that there is no contribution of a NiS phase in the composite Ni-CdS heterostructures. [361, 390] This means that Ni atoms are not incorporated into the CdS lattice, but rather studded on the surface of CdS. This observation also agrees with the theoretical prediction based on the product solubility constants (K_{sp}) of NiS (3×10^{-19}) and CdS (8×10^{-27}), in which the substitutional replacement of the Cd(II) ions in CdS with Ni(II) ($Ni^{2+} + CdS \rightarrow Cd^{2+} + NiS$) is less efficient. [464] Moreover, the weak S 2p peak observed at higher

binding energy (ca. 168.2 eV) is probably due to the formation of some oxide (S–O) species on the surface of CdS, possibly after the synthesis process and exposure to air. [502, 503]

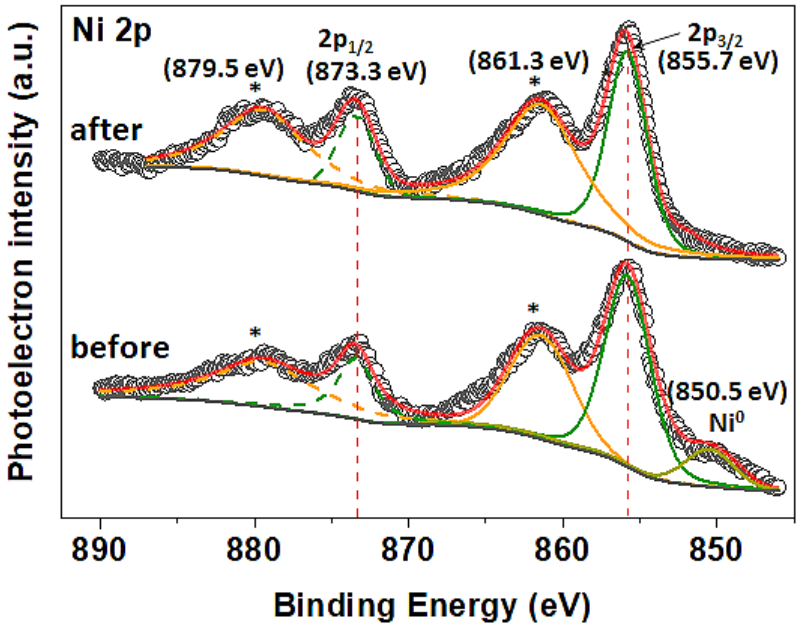

Figure 3-63: Ni 2p XPS spectra for mesoporous 10% Ni-CdS NCAs before and after catalytic reaction for 20 h. The spectra were fitted by taking the Shirley background. Embedded peaks for the metallic Ni, Ni^{2+} ions, and satellite peaks of the Ni $2p_{3/2}$ and $2p_{1/2}$ spin-orbits are represented as yellow, green, and orange curves, respectively. The red lines are the fits of the XPS peak analysis to the experimental data.

As for the XPS Ni 2p core-level region in **Figure 3-63**, deconvolution of the spectrum shape reveals two intense peaks at 855.7 and 873.3 eV assigned to the Ni $2p_{3/2}$ and Ni $2p_{1/2}$ spin-orbits of Ni^{2+} (as in $Ni(OH)_2$), and a small feature at 850.5 eV which can be ascribed to metallic Ni. [504, 505] Also, the broad XPS peaks appearing at binding energies of 861.3 and 879.5 eV (FWHM ~5.5–6.5 eV) are attributed to the respective Ni $2p_{3/2}$ and Ni $2p_{1/2}$ shake-up satellite peaks of Ni^{2+} in $Ni(OH)_2$. [506-508] Therefore, combined with XRD and TEM analysis, these results indicate the prevalence of the β-$Ni(OH)_2$ phase with a small amount of metallic Ni (possibly embedded in the β-$Ni(OH)_2$ layers and/or at the β-$Ni(OH)_2$/CdS interfaces). Further analysis of the XPS Ni $2p_{3/2}$ peaks gives a relative atomic percentage of 12% for Ni metal (see **Table 3-10***)*. From the above results, it can be deduced that metallic Ni nanoclusters were probably deposited first on the surface of CdS via the photochemical reduction of Ni^{2+} ions by the photo-exited electrons (**eq. 37**), and then partially oxidized to the hydroxide phase due to the alkaline reaction solution formed by the presence of TEA, according to **eq. 38**. Moreover, a quantitative analysis from the XPS data (i.e., intensity of XPS peak for each constituent element normalized by the corresponding relative atomic sensitivity factor) indicates a Ni/CdS atomic ratio close to 0.42 (see **Table 3-10**). Note that, although this value is much higher than that expected for a CdS material containing 10 wt.% Ni (i.e. ~0.29), implying some degree

of compositional heterogeneity in the sample, this discrepancy may be mainly due to the distribution of Ni-species on the CdS surface rather than within the CdS structure.

The porosity of the all the prepared materials was determined with N_2 physisorption measurements at –196 °C. **Figure 3-64** presents the N_2 adsorption and desorption isotherms and the corresponding pore-size distribution plots for the mesoporous pure CdS NCAs and the Ni-modified CdS NCAs with 5, 7, 10 and 15 wt.% Ni loadings. All isotherms are associated with a typical type IV curve featuring a H2-type hysteresis loop, being characteristic of porous solids with interconnected mesopores according to IUPAC classification (see A.1 and A.2 in the Appendix). [412] In addition, the isotherms show a weak but noticeable adsorption step at relative pressure (P/P_o) from 0.4 to 0.6 that is attributed to the capillary condensation of nitrogen in uniform narrow-sized mesopores. [427]

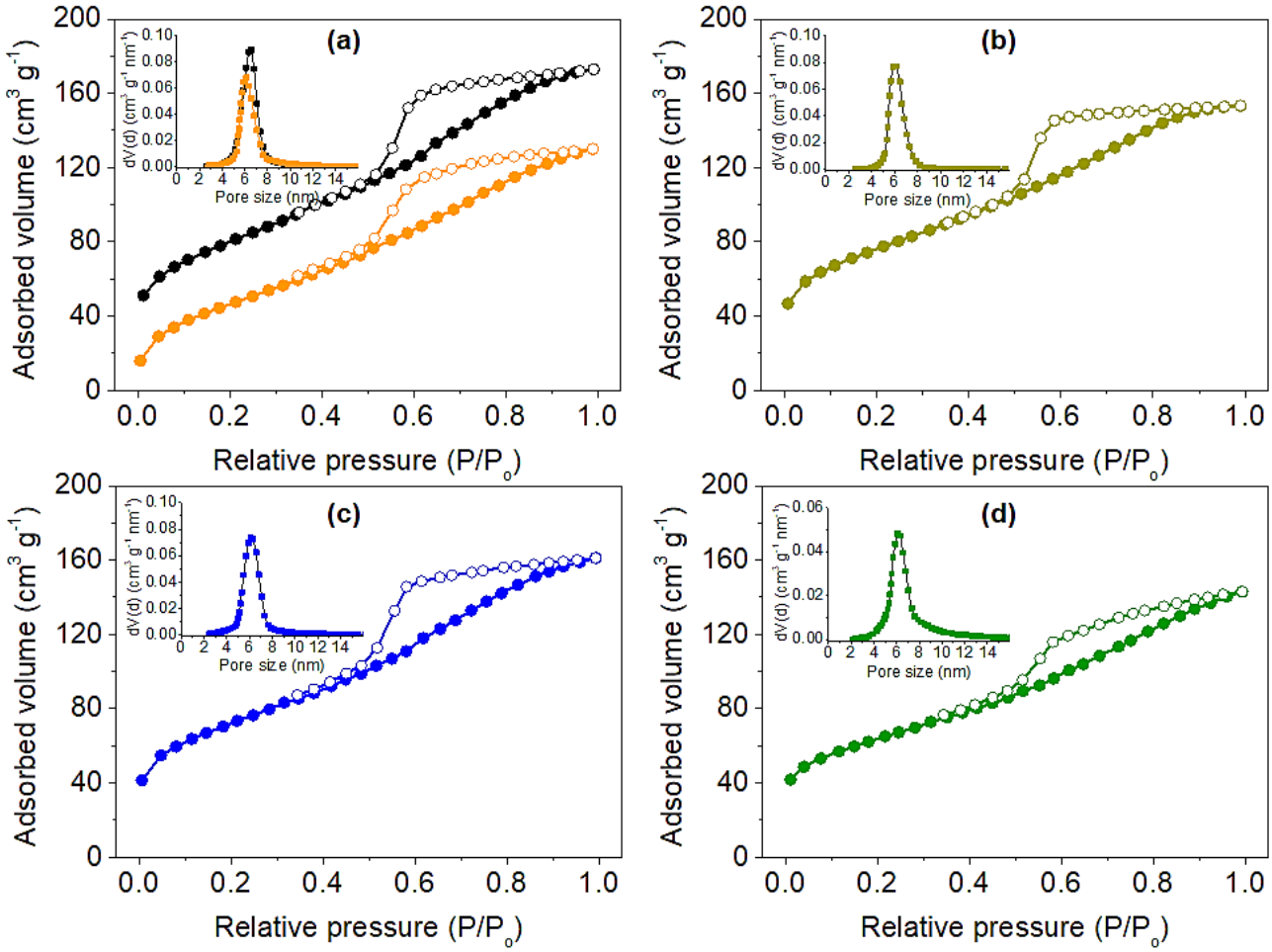

Figure 3-64: N_2 adsorption and desorption isotherms at −196 °C of the mesoporous (a) pure CdS NCAs (black) and 10% Ni-CdS (orange) samples, and for the (b) 5% Ni-CdS, (c) 7% Ni-CdS and (d) 15% Ni-CdS composites. The plot of 10% Ni-CdS (orange) is offset by 20 cm^3 g^{-1} for clarity. Insets: the corresponding NLDFT pore size distributions calculated from the adsorption branch of isotherms.

The Brunauer–Emmett–Teller (BET) surface areas and total pore volumes of the mesoporous Ni-CdS heterostructures were estimated to be 164–207 m^2 g^{-1} and 0.19–0.21 cm^3 g^{-1}, respectively, which are somewhat lower than those of the pristine CdS NCAs sample (223 m^2 g^{-1}, 0.24 cm^3 g^{-1}), as shown in **Table 3-8**. Moreover, the pore-size in these materials was estimated from the adsorption branch of isotherms using the non-local density functional theory method. [414] The NLDFT analysis indicated quite narrow size distributions of pores with a pore size at 6.6 nm for pure CdS NCAs and approximately 6–6.1 nm for the Ni-modified samples (see insets of **Figure 3-64** and **Table 3-8**). The observed gradual reduction in surface area, pore-volume, and pore-size with increasing the Ni-content in the Ni-modified materials, possibly reflects the progressive deposition of Ni-species inside the pores of CdS NCAs.

Furthermore, the UV–vis/NIR diffuse reflectance spectroscopy indicated that the as-prepared Ni-modified materials have a well-defined electronic structure similar to that of pristine CdS. As shown in **Figure 3-65a**, the spectrum of CdS NCAs exhibit a sharp optical absorption onset at around 458 nm (~2.71 eV), which is attributed to the excitonic absorption band of CdS. The large blue shift in the energy gap compared to that of a typical bulk CdS (2.4 eV) can be associated with the quantum-confinement effect in CdS nanoparticles due to their very small size (~4.2 nm, as estimated by the Brus relation according to **eq. 22**). The optical bandgaps (E_g) for all the prepared catalysts were determined from their respective Tauc plots based on **eq.21** for direct gap semiconductors (as shown in **Figure 3-65b**), and the results are presented in **Table 3-8**. Compared with pure CdS, the obtained E_g values of the Ni-modified catalysts exhibit a minimal blue shift (by ~10–20 meV), indicating that the bandgap of CdS does not change appreciably after modification with Ni. This leads also to the hypothesis that the Ni atoms are not incorporated into the CdS lattice, but exist instead on the surface of the host CdS material, supporting the HRTEM and XPS results. In relation to this, Ni-doping is known to induce a red-shift in the absorption onset of CdS due to the formation of new mid-gap energy states [509, 510], which is not evident here. Moreover, as shown in the inset of **Figure 3-65b**, the Ni-containing materials display also two absorption bands in the visible/NIR range (peaks at 670 nm and 1200 nm), which can be ascribed to the d–d interband transitions of Ni(II) in β-$Ni(OH)_2$. [511] Indeed, not unexpectedly, the intensity of these peaks progressively increases as the loading amount of Ni increases from 0 to 15 wt.%. Also, for comparison, pure β-$Ni(OH)_2$ particles were prepared and examined with UV-vis/NIR spectroscopy. As shown in **Figure 3-66**, the UV-vis/NIR absorption spectrum of pure β-$Ni(OH)_2$ exhibits an intense absorption band in the 350–440 nm range, which can be also ascribed to an interband d-d electronic transition of Ni(II) in $Ni(OH)_2$. [511, 512] The energy level of this transition (~2.8–3.5 eV), however, lies in the same range as the optical absorption of CdS NCAs (onset at 2.71 eV). This suggests that the surface modification of CdS with β-$Ni(OH)_2$ is not expected to cause any noticeable change in the apparent bandgap of CdS NCs, which

is also confirmed by the UV-Vis/NIR measurements of the Ni-modified samples. All the measured textural and electronic properties of the as-prepared catalysts are summarized in **Table 3-8.**

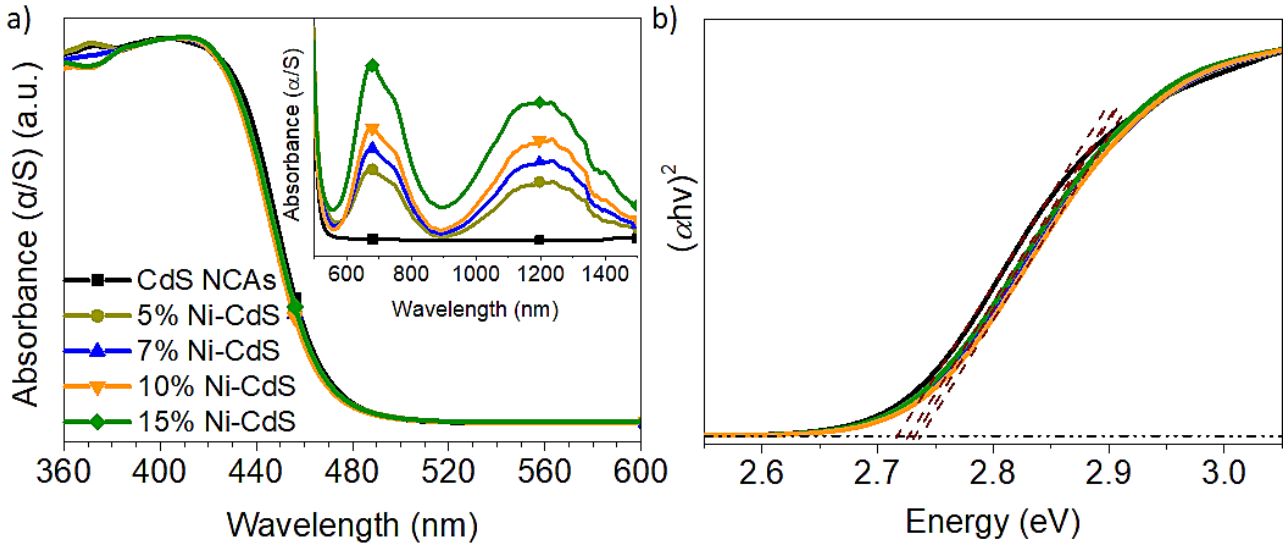

Figure 3-65: a) UV-Vis/NIR absorption spectra (inset: the respective spectra in the wavelength region of 600 − 1500 nm) and b) the corresponding Tauc plots (i.e., the curves of (αhv)^2 versus photon energy (hv), where α, h and v are the absorption coefficient, Planck's constant and light frequency, respectively), for the mesoporous CdS NCAs and the Ni-modified CdS samples with 5, 7, 10, and 15 wt.% Ni content.

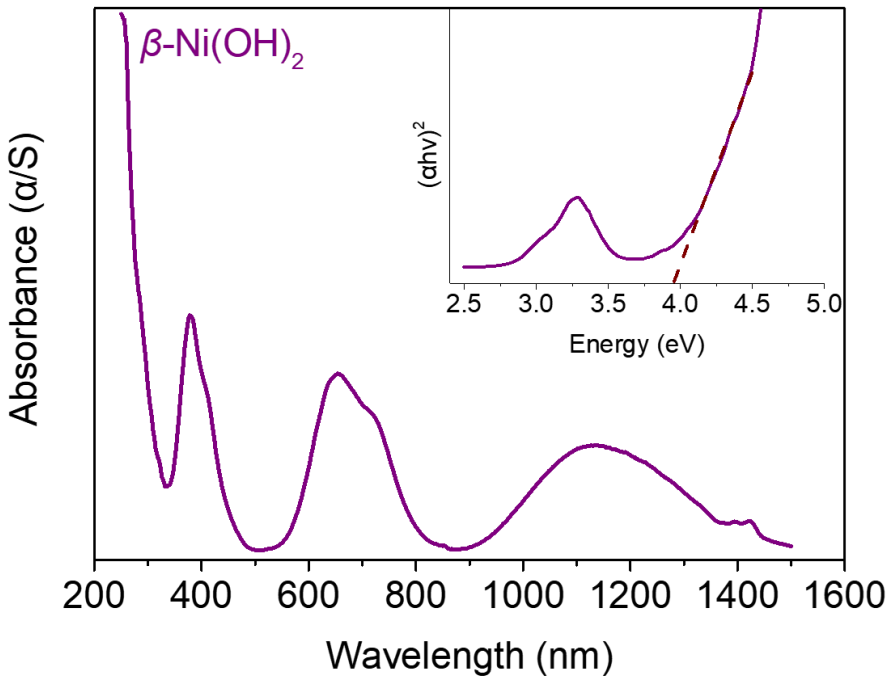

Figure 3-66: Optical absorption spectrum of the as-prepared pure β-Ni(OH)$_2$ microparticles, showing the characteristic d-d interband transitions at 380, 670 and 1150 nm, and the steep absorption bellow 320 nm corresponding to the band-gap transition. Inset: the corresponding Tauc plot for direct gap semiconductor, showing an energy band gap of 3.9 eV.

Table 3-8: Textural properties and analytical data for the mesoporous CdS NCAs and the as-prepared Ni-CdS NCAs catalysts.

Sample	Ni content† (wt.%)	BET Surface ($m^2 g^{-1}$)	Pore Volume ($cm^3 g^{-1}$)	Pore Size (nm)	Energy Gap‡ (eV)
CdS NCAs	-	223	0.24	6.6	2.71
5% Ni-CdS	4.91	207	0.21	6.1	2.72
7% Ni-CdS	6.98	196	0.21	6.1	2.72
10% Ni-CdS	10.35	179	0.20	6.1	2.73
15% Ni-CdS	15.01	164	0.19	6.0	2.72

† Based on EDS analysis, ‡ Energy bandgaps as obtained from the Tauc plots based on eq. 21.

3.4.3 Photocatalytic water reduction study

The photocatalytic water-reduction activity for H_2 evolution of the as-produced mesoporous catalysts was evaluated under visible-light irradiation ($\lambda \geq 420$ nm) at 20 °C. All the photocatalytic experiments were carried out in an airtight Pyrex cell using ethanol (10% v/v) in a NaOH solution (5 M) as a sacrificial reagent. As outlined earlier, the $^{\bullet}OH/OH^{-}$ redox couple can effectively suppress the charge-carrier recombination by reacting more favorably than water and ethanol with the surface-reaching holes. [358] More specifically, in highly alkaline solutions (pH > 14), the H_2-evolution process entails fast diffusion of OH^{-} anions to the CdS surface, where they are rapidly oxidized by the VB holes into $^{\bullet}OH$ radicals. [452] Therefore, a kinetically hindered oxidation reaction is replaced with another faster (one-electron) oxidation reaction, preventing the competitive electron–hole recombination at the surface of the catalyst and accelerating the overall water-reduction process.

Figure 3-67 displays the time courses and average rates of photocatalytic H_2-evolution over the mesoporous CdS NCAs and the Ni-modified CdS catalysts with different Ni loadings. The Ni-free CdS NCAs exhibited a moderate H_2-evolution rate of 0.08 mmol h^{-1} (see **Figure 3-67b**) due to the fast recombination of photoexcited electron-hole pairs. In contrast, the Ni-modified materials showed a remarkable improvement in the photocatalytic H_2-production performance (**Figure 3-67a)**, clearly indicating that deposition of β-$Ni(OH)_2$ onto CdS has a strong effect on the photoelectrochemical performance of the Ni-modified heterostructures. The results showed that the photoactivity for H_2-production was greatly increased with the loading amount of Ni and the highest rate, that is, 0.93 mmol h^{-1} was obtained at 10 wt.% Ni-content (**Figure 3-67b**). This activity is about 12-times higher than that of single-component CdS NCAs. Further increment in the Ni loading (15 wt.%), however, results to a decrease in the photocatalytic H_2-production performance, as indicated by the lower

activity (0.53 mmol h^{-1}) of the 15% Ni-CdS composite. As will be discussed below, the lower activity of the high Ni-loaded sample may be attributed to the sluggish charge-transfer kinetics and loss of photogenerated carriers by recombination at the interface between β-$Ni(OH)_2$ nanoparticles and CdS host catalyst, possible due to the poor interparticle contact and interfacial defects.

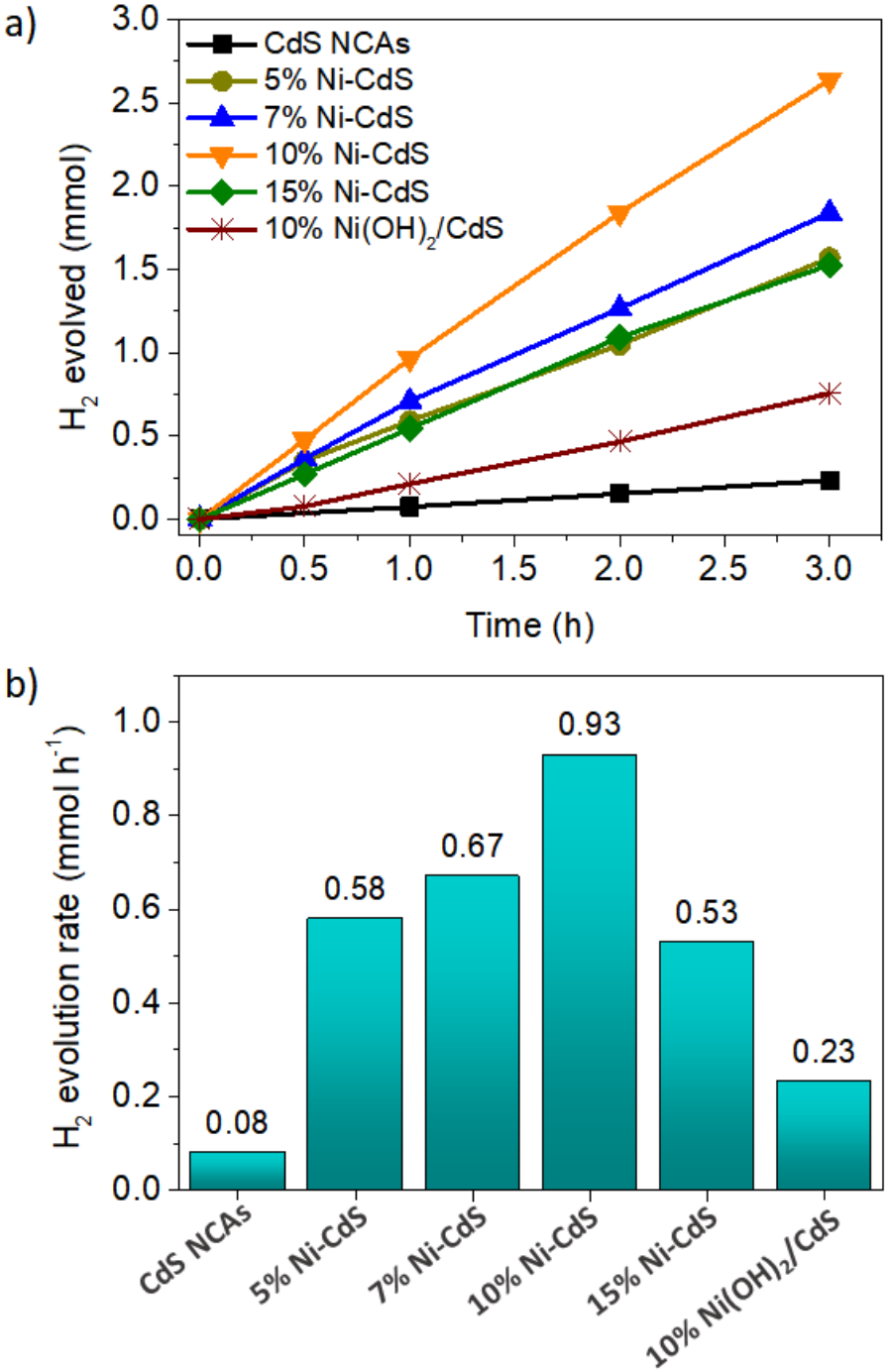

Figure 3-67: a) Time courses of photocatalytic H_2-production and b) the respective average H_2-evolution rates (over 3-h irradiation period) for the mesoporous CdS NCAs and the Ni-modified CdS catalysts with 5, 7, 10, and 15 wt.% Ni content. The H_2-evolution results for the physical mixture of β-$Ni(OH)_2$ particles and CdS NCAs with 10 wt.% Ni-equivalent (10% $Ni(OH)_2$/CdS) is also given. Catalytic reaction conditions: 20 mg of catalyst in a 5 M NaOH aqueous solution (20 mL, pH 14.7) containing ethanol (10% v/v) as sacrificial electron donor; steady reaction temperature at 20 °C; 300 W Xe light irradiation with a UV cut-off filter ($\lambda \geq 420$ nm).

Next, a series of photocatalytic H_2-evolution tests were performed in order to optimize the amount of the 10% Ni-CdS catalyst. As seen in **Figure 3-68a**, the evolution rate of H_2 increases with increasing catalyst amount and reaches a maximum at 40 mg (i.e., 2 mg mL^{-1} catalyst concentration). This increment in H_2 production can be interpreted by the increased utilization of incident light by the catalyst's particles. As for the higher catalyst loading (50 mg, or 2.5 mg mL^{-1} concentration), the reduced H_2-evolution rate (1.1 mmol h^{-1}) is related to the light scattering from the excessive particles in the reaction suspension. Moreover, comparative experiments using methanol as sacrificial reagent in a 5 M NaOH solution (pH 14.7), as well as ethanol in pH 10 and neutral (pH 7) solutions, indicated that these hole scavengers are less effective in promoting H_2-evolution; the corresponding H_2-production rates were found to be ~0.7, ~0.2 and ~0.2 mmol h^{-1}, respectively (see **Figure 3-68b**). The lower activity for the 5M-NaOH/methanol system is attributed to the slower rate of methanol oxidation by the hydroxyl radicals — particularly, the rate constant of hydrogen abstraction by $^{\bullet}OH$ radicals from methanol is 0.64×10^{12} cm^3 mol^{-1} s^{-1} versus 2.25×10^{12} cm^3 mol^{-1} s^{-1} from ethanol [513] — whereas for the ethanolic solutions at pH 7 and 10, the low efficiency is due to the direct oxidation of ethanol by the photogenerated holes, instead of the faster reaction with $^{\bullet}OH$ radicals formed at high pH (>14).

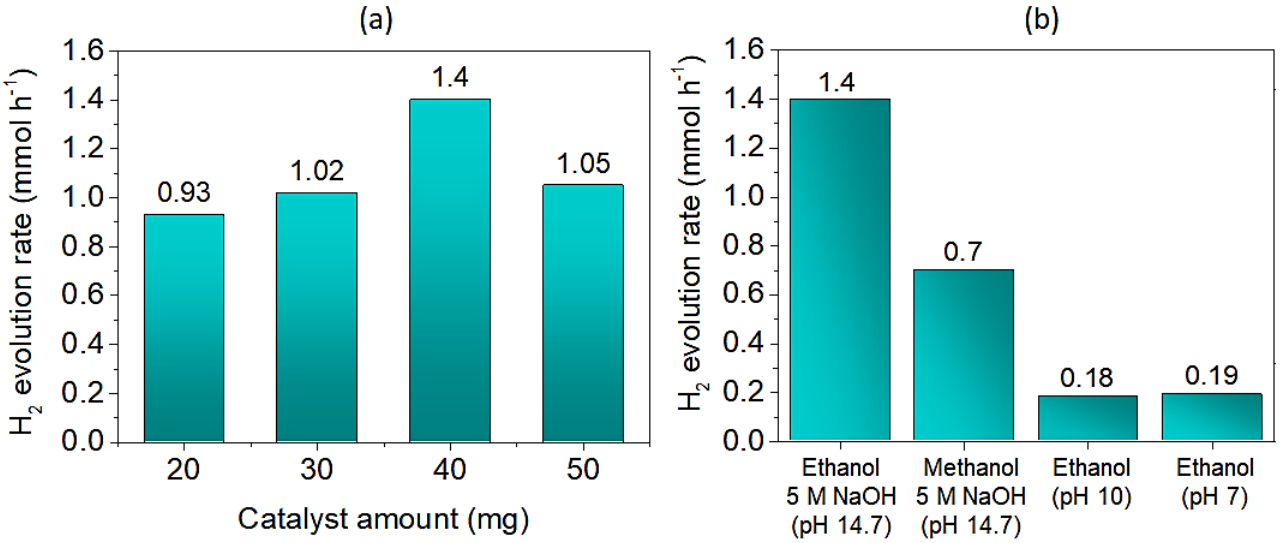

Figure 3-68: a) Photocatalytic H_2-production activities for different amounts (concentrations) of the mesoporous 10% Ni-CdS catalyst in a 5M NaOH solution containing ethanol (10% v/v) as sacrificial reagent. b) Photocatalytic H_2-evolution rates over the 10% Ni-CdS catalyst (40 mg) using different sacrificial reagents, i.e., ethanol (10% v/v) in neutral aqueous solution (pH 7) and in aqueous NaOH solutions of pH 10 and 14.7 (5M NaOH), as well as methanol (10% v/v) in a 5 M NaOH (pH 14.7) aqueous solution. All photocatalytic reactions were performed in a 20 mL aqueous solution containing the sacrificial reagent, under steady reaction temperature (20 °C) and visible-light irradiation by a 300-W Xe light source with a UV cut-off filter (λ ≥ 420 nm).

Notably, the mesoporous 10% Ni-CdS catalyst under optimum conditions shows an impressive performance for water reduction, reaching a H_2-production rate of 1.4 mmol h^{-1} (~35 mmol g_{cat}^{-1} h^{-1}) and achieving an apparent quantum yield (QY) of 72% at 420 nm; measured according to **eq.26** using monochromatic light irradiation and assuming all incident photons (N_{hv}=9.46×10^{16} s^{-1}) were absorbed by the catalyst's particles. As far as one can tell, this is one of the highest recorded efficiencies for photocatalytic systems containing a nickel-based co-catalyst [389, 514, 515] and among the best reported values for CdS-based photocatalysts [396, 404]. **Table 3-9** shows a comparison of the photocatalytic H_2-production activities of different CdS-based photocatalysts.

Table 3-9: Comparison of the photocatalytic H_2-production activities and quantum yields of different Ni-modified and Pt-loaded CdS-based photocatalysts.

Photocatalyst	Co-catalyst	Light source	Reaction solution	Catalyst amount (g)	H_2 evolution		Ref.
					Activity ($\mu mol \cdot h^{-1} \cdot g^{-1}$)	QY (%)	
CdS nanorods	Ni	Laser diode (λ = 447 nm)	5 M NaOH Ethanol (10 vol%) (V=3 mL)	-	63000	53 (447 nm)	[358]
CdS nanorods	Ni	300 W Xe (λ > 420 nm)	1 M $(NH_4)_2SO_3$ (V=50 mL)	0.1	25848	27 (420 nm)	[382]
CdS particles	Ni	300 W Xe (λ > 400 nm)	Lactic acid (50 vol%) (V=50 mL)	0.1	30048	-	[383]
CdS nanosheets	Ni	Laser diode (λ = 405 nm)	Ethanol (90 vol%) (V=5 mL)	-	~350000	25 (405 nm)	[384]
CdS nanoparticles	Ni	300 W Xe (λ > 420 nm)	2-propanol (100 vol%) (V=5 mL)	0.006	46600	48 (447 nm)	[491]
CdS 3D nanowires	NiO	500 W H (Uv-Vis)	Na_2SO_3/Na_2S (0.25 M/0.35 M) (V=50 mL)	0.2	745	6	[386]
CdS particles	NiO_x	300 W Xe (λ > 400 nm)	Methanol (30 vol%) (V=100 mL)	0.1	5908	9 (400 nm)	[387]
CdS nanorods	NiS	300 W Xe (λ > 420 nm)	Na_2SO_3/Na_2S (0.25 M/0.35 M) (V=80 mL)	0.05	1131	6 (420 nm)	[388]
CdS nanowires	NiS	300 W Xe (λ≥420 nm)	Lactic acid (20 vol%) (V=100 mL)	0.005	158720	74 (420 nm)	[389]
CdS particles	NiS	300 W Xe (λ>420 nm)	Lactic acid (30 vol%) (V=100 mL)	0.3	7266.7	51 (420 nm)	[390]

RGO-CdS composites	Ni_xS	500 W Hg (λ>400nm)	Ethanol (50 vol%) (V=10 ml)	0.0005	17500	3 (410 nm)	[393]
$Cd_{0.5}Zn_{0.5}S$ composites	NiS_x [a)]	300 W Xe (λ>430 nm)	Na_2SO_3/Na_2S (0.25 M/0.35 M) (V=180 mL)	0.1	44600	94 (425 nm)	[516]
CdS nanorods	$Ni(OH)_2$	300 W Xe (λ≥420 nm)	TEOA [b)] (25 vol%) (V=80 mL)	0.05	5085	28 (420 nm)	[385]
CdS/g-C_3N_4 nanorods	$Ni(OH)_2$	300 W Xe (λ>420 nm)	Na_2SO_3/Na_2S (0.35 M/0.25 M) (V=80 mL)	0.001	115180	17 (450 nm)	[394]
CdS NCAs	**β-$Ni(OH)_2$**	**300 W Xe (λ≥ 420 nm)**	**5 M NaOH Ethanol (10 vol%) (V=20 mL)**	**0.04**	**35000**	**72 (420 nm)**	**[406]**
CdS nanoparticles	Pt-PdS	300-W Xe (λ>420 nm)	Na_2SO_3/Na_2S (0.5 M/0.5 M) (V=200 mL)	0.3	29233	93 (420 nm)	[371]
CdS nanostructures	Pt	300 W Xe (λ>420 nm)	Na_2SO_3/Na_2S (0.25 M/0.35 M) (V=200 mL)	0.15	27333	60 (420 nm)	[396]
CdS NCAs	Pt	300 W Xe (λ>420 nm)	5 M NaOH Ethanol (10 vol%) (V=20 mL)	0.02	60000	70 (420 nm)	[404]
CdSe@CdS nanorods	Pt	LED (λ=455 nm)	KOH (pH 15) 2-propanol (10 vol%) (V=10 mL)	0.002	142000	99 (455 nm)	[453]

[a)] Mixture of $Cd_{0.5}Zn_{0.5}S$ twinned photocatalyst and an unanchored NiS_x co-catalyst. [b)] TEOA: Triethanolamine.

Further irradiation control experiments over the mesoporous 10% Ni-CdS NCAs catalyst showed that the apparent quantum yields at 365, 440, 510 and 620 nm incident light wavelengths are 77%, 55%, 2% and 0.2%, respectively. Notably, as presented in **Figure 3-69**, the overall trend in the apparent QY correlates well with the optical absorbance of the catalyst, suggesting that the H_2-production activity of the Ni-CdS NCAs composites is initiated from the interband carrier photoexcitation in the host CdS photocatalyst. In agreement with this, as expected due to the large bandgap of β-$Ni(OH)_2$ (ca. 3.9 eV, see inset of **Figure 3-66**), no hydrogen evolution was observed when β-$Ni(OH)_2$ microparticles were employed as the catalyst (data not shown), indicating that β-$Ni(OH)_2$ alone is catalytically inactive for H_2-production under visible-light irradiation. In addition, compared to the mesoporous 10% Ni-CdS NCAs, a much lower rate of H_2-evolution (0.23 mmol h^{-1}) was obtained when a physical mixture of CdS NCAs and β-$Ni(OH)_2$ particles (with equivalent 10 wt.% Ni loading) was employed as catalyst (labeled as 10% $Ni(OH)_2$/CdS) under identical conditions, see **Figure 3-67**. From the above results, it can be deduced that the close interconnection (as

evidenced from HRTEM) and, therefore, the strong electrical coupling between β-$Ni(OH)_2$ and CdS nanomaterials plays a crucial role in the reaction mechanism, by facilitating the interfacial charge-transfer and spatial separation of photoinduced electron-hole pairs across the heterojunction. Overall these attributes contribute to the improvement of the visible-light photocatalytic performance of the heterostructured materials.

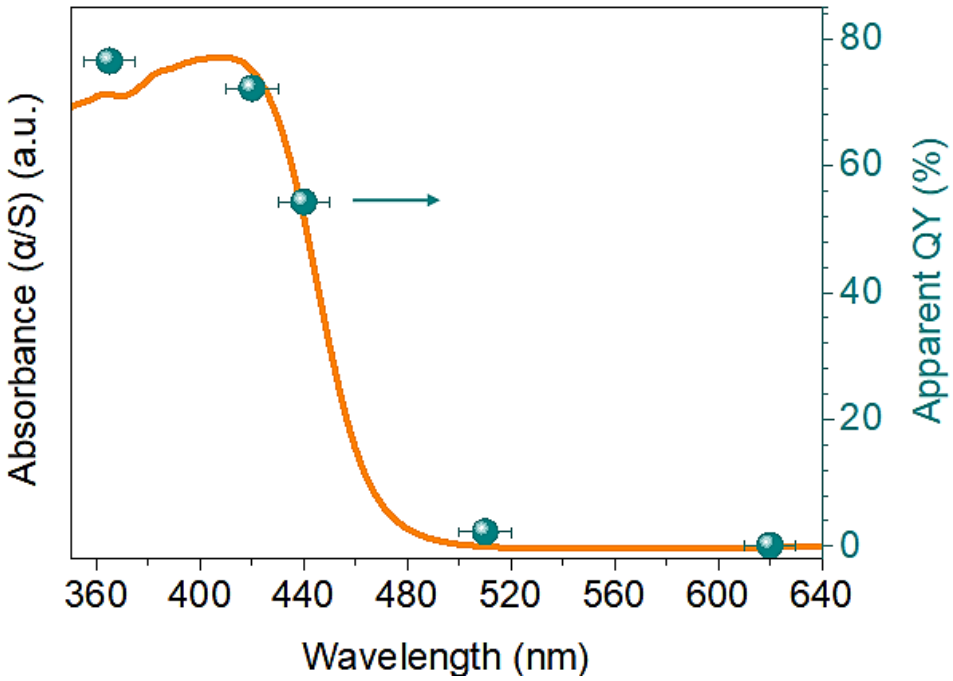

Figure 3-69: UV-vis diffuse reflectance spectrum of the mesoporous 10% Ni-CdS NCAs catalyst and the apparent QYs of H_2-evolution under different incident-light irradiation wavelengths. The error bars refer to the wavelength range of the incident light. Reaction conditions: 40 mg of catalyst, 20 mL aqueous solution containing 5 M NaOH and 10% (v/v) ethanol, under LED light irradiation. The power density of the incident light was 2.55, 14.3, 14.8, 18.8 and 23.4 mW cm^{-2} for the 365, 420, 440, 510 and 620 nm wavelengths, respectively.

The mesoporous 10% Ni-CdS heterostructure also showed sufficient stability after prolonged photocatalysis. The reusability of the catalyst was investigated by conducting four consecutive 5-h photocatalytic runs. Before reuse, the catalyst was separated from the reaction solution by centrifugation, washed several times with water, and re-dispersed in a fresh 5 M NaOH-ethanolic solution. Before catalysis, the reaction cell was de-aerated by Ar gas for at least 30 min, until no oxygen was detected (by GC analysis). As seen in **Figure 3-70**, after four successive photocatalytic runs, the H_2-evolution rate still reached 1.2 mmol h^{-1}, which corresponds to 86% of its initial activity, demonstrating very good stability. The total H_2 amount evolved after a 20-h visible light irradiation period was 23.6 mmol (or ~566 mL, at 20 ºC) that corresponds to an average H_2-evolution rate of about 1.2 mmol h^{-1}. In addition, EDS and N_2 physisorption measurements were employed to assess any changes in composition and morphology of the recovered catalyst after 20-h reaction. The EDS spectra (**Figure 3-71a** and **Table 3-10**) indicated a Cd:S ratio of 1:1 and a Ni content of ~10.6 wt.%,

while analysis of the obtained N_2 adsorption and desorption isotherms revealed a surface area of 148 $m^2\ g^{-1}$, pore volume of 0.17 $cm^3\ g^{-1}$ and pore size of 6 nm (**Figure 3-71b**), which are very close to those of the fresh material.

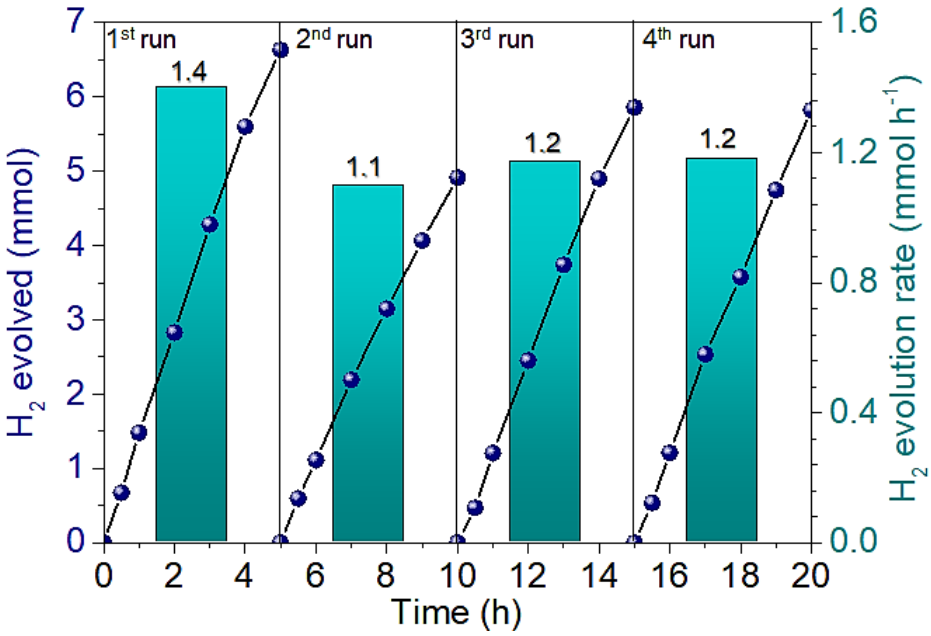

Figure 3-70: Catalytic recycling tests over the mesoporous 10% Ni-CdS NCAs catalyst. The bars denote the rate of H_2-evolution averaged over 5-h reaction time. All catalytic tests were conducted using 40 mg of catalyst in a 5 M NaOH aqueous solution (20 mL, pH 14.7) containing ethanol (10% v/v) as hole scavenger, and under visible light irradiation using a 300 W Xe light source equipped with a UV cut-off filter ($\lambda \geq 420$ nm).

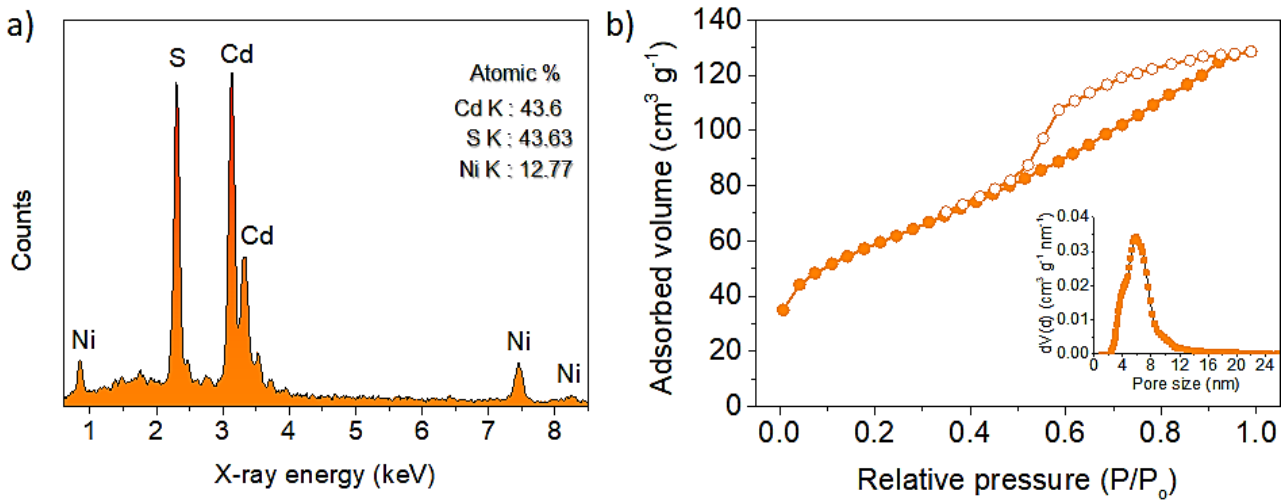

Figure 3-71: a) Typical EDS spectrum and b) N_2 adsorption-desorption isotherms at –196 °C (inset: the corresponding NLDFT pore size distribution) for the mesoporous 10% Ni-CdS NCAs catalyst retrieved after 20-h of photocatalytic reaction.

Furthermore, the recovered sample was also studied using XPS. The XPS spectra of the Cd 3d and S 2p regions (see **Figure 3-62**) showed no obvious changes in the chemical states of Cd^{2+} and

S^{2-}, respectively, demonstrating the good chemical stability of CdS in the heterostructured catalyst. However, after 20-h photocatalytic reaction, the Ni 2p spectrum (see **Figure 3-63**) shows a noticeable difference in the chemical state of the Ni-species, where the respective Ni $2p_{3/2}$ and Ni $2p_{1/2}$ core-level peaks at 855.7 and 873.3 eV remained unchanged but the peak at 850.5 eV appears to fully disappear, suggesting the complete transformation of Ni(0) to Ni(II). This assumption is supported by XPS elemental analysis on the reused sample, which revealed a Ni/CdS atomic ratio close to 0.43 (see **Table 3-10**), very similar to that of the fresh catalyst (ca. 0.42), indicating that the disappearance of metallic Ni is due to its photochemical transformation to N(II) species and not by its detachment from the CdS surface; these findings are also in line with the EDS results (see **Figure 3-71a**). As will be discussed below, a possible explanation for the photochemical conversion of metallic Ni is due to the fact that the photoexcited holes may transfer from CdS to the Ni species, by which a portion of these holes oxidize Ni metal to Ni(II). The Ni(II) ions can then readily react with hydroxide ions (OH_{aq}^-) due to the surrounding alkaline environment (5 M NaOH) to yield β-$Ni(OH)_2$. This observation is also consistent with previous studies, which indicated that Ni/NiO_x core-shell nanoparticles supported on $SrTiO_3$ can be converted to β-$Ni(OH)_2$ under photochemical reduction of water. It was suggested that a disproportionation reaction of NiOOH species (formed by the photooxidation of NiO_x) with metallic Ni leads to the formation of β-$Ni(OH)_2$. [517]

Table 3-10: Nickel characteristics and relative percentages of the mesoporous 10% Ni/CdS catalyst before (fresh sample) and after 20-h photocatalytic reaction.

Sample (10% Ni-CdS)	**Ni loading** [a)] **(wt %)**	**Ni^0 metallic** [b)] **(%)**	**Ni^{2+} as $Ni(OH)_2$** [b)] **(%)**	**Atomic ratio Ni/CdS** [b)]
Before catalysis	10.4	12	88	0.42
After catalysis	10.6	-	100	0.43

[a)] **Based on EDS analysis.** [b)] **Based on XPS analysis.**

Clearly, all the above results indicate that the prepared 10% Ni-CdS NCAs sample is a highly efficient and stable photocatalyst. It should be stressed that the initially formed Ni(0) species have a negligible effect on the photocatalytic activity of the Ni-CdS NCAs heterostructures. To prove this notion, a fifth consecutive 5-h photocatalytic run was performed using a fresh NaOH-ethanol aqueous solution. The results showed that the reused 10% Ni-CdS NCAs sample (retrieved after a 20-h photoreaction) still achieves a high level of H_2-production, showing almost the same H_2-evolution rate of 1.17 mmol h^{-1} (**Figure 3-72**), indicating that the high activity and stability of the Ni-modified heterostructures is mainly due to the formed β-$Ni(OH)_2$/CdS heterojunctions.

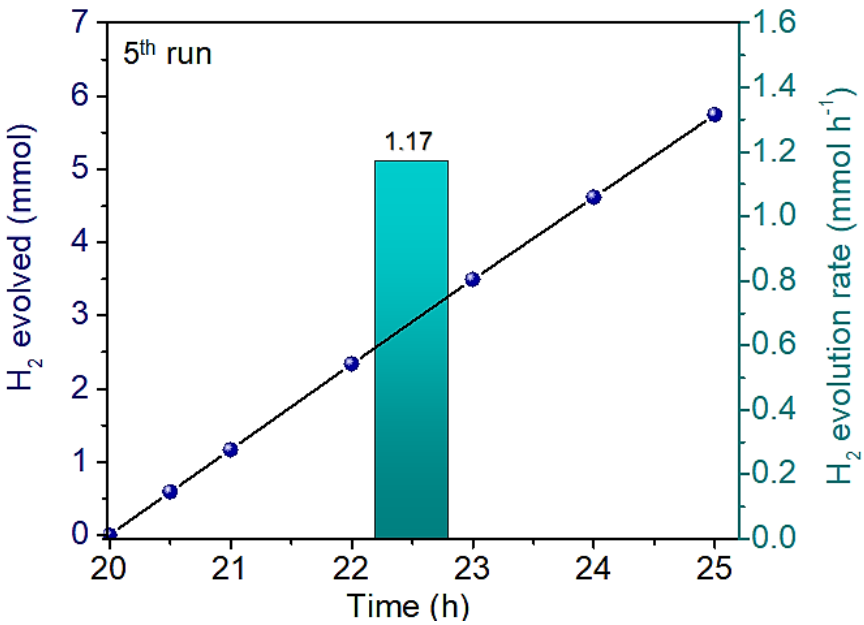

Figure 3-72: Time course of photocatalytic H_2-production (line) and average H_2-evolution rate (bar) for the four-times reused 10% Ni-CdS NCAs catalyst (retrieved after 20-h photoreaction).

3.4.4 Effect of β-Ni(OH)$_2$ on the photocatalytic activity

To investigate the charge-transfer and separation efficiency of the mesoporous CdS NCAs and the Ni-modified CdS heterostructures, their photoluminescence (PL) was measured using a 360 nm excitation wavelength, as shown in **Figure 3-73**. The PL emission spectrum of mesoporous CdS NCAs exhibits an intense peak at 470 nm, which is ascribed to the band-edge transitions of the CdS nanocrystal framework. In contrast, deposition of Ni species onto the CdS surface led to a continuous quenching of the PL intensity, which is attributed to the suppressed charge-carrier recombination, arising from the efficient dissociation of photogenerated electron-hole pairs over the heterostructured framework. Here it is assumed that the contribution of non-radiative exciton relaxation through defect states is negligible. The downward trend of the PL intensity for the investigated samples is CdS NCAs < 5% Ni-CdS < 7% Ni-CdS < 15% Ni-CdS < 10% Ni-CdS. These results indicate that a Ni-loading of 10 wt.% is able to provide a higher charge-separation efficiency across the β-Ni(OH)$_2$/CdS interface, giving rise to a more favorable charge-transfer process. As for the somewhat lower charge-separation observed in the 15 wt.% Ni-loaded sample, as depicted in **Figure 3-73**, it could be related to surface defects created at the interface between β-Ni(OH)$_2$ and CdS particles, which may function as recombination sites of photogenerated carriers. Of note, all the mesoporous CdS and Ni-CdS NCAs materials exhibited a lower PL intensity than that of the precursor colloidal CdS NCs, which is attributed to the efficient delocalization of excitons over the cross-linked NC-assembled structure.

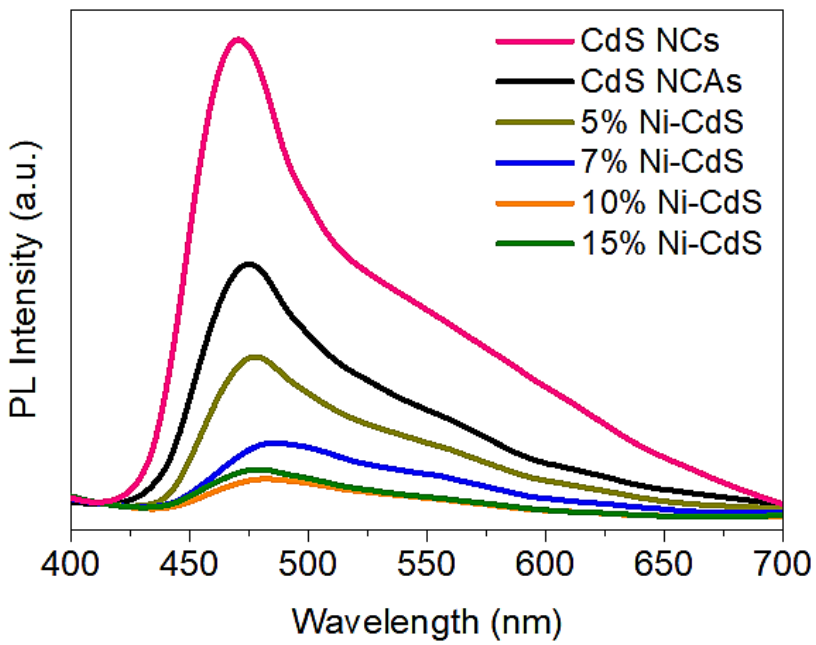

Figure 3-73: Room-temperature PL emission spectra of the mesoporous CdS NCAs and the Ni-modified CdS composites, as well as of the precursor (thiol-capped) colloidal CdS NCs. PL experiments were carried out in water (sample concentration 1 mg mL^{-1}) using a 360 nm excitation wavelength.

In addition, electrochemical impedance spectroscopy measurements were also carried out to get a better understanding of the role of β-Ni(OH)$_2$ in the reaction pathway and the enhanced photocatalytic activity of the Ni-CdS NCAs heterostructures. **Figure 3-74** depicts the Nyquist impedance plots (plot of the real impedance (Z′) *vs* the negative imaginary impedance (-Z″) or negative reactance) of pure CdS and the Ni-CdS NCAs with 10 and 15 wt. % Ni loadings. All samples were measured as thin-film electrodes, fabricated by drop-casting on glass substrates coated with fluorine-doped tin oxide (FTO) layer and the EIS measurements were performed at an open-circuit potential in a frequency range from 1 to 1×10^6 Hz. The measured EIS data were modeled with an equivalent electrical circuit $R_s(Q_f/(R_dL_{ad}(Q_{dl}/R_{ct})))$ (see inset of **Figure 3-74)** using the EC-Lab software package (Bio Logic Science Instruments, version 11.16), and the results are listed in **Table 3-11**. According to the used equivalent circuit, R_s represents the electrolyte resistance, R_{ct} and Q_{dl} are the charge-transfer resistance and the double layer capacitance (C_{dl}), respectively, and R_d and Q_f elements account for the defect resistance (associated with the pores, cracks and grain boundaries in the solid film) and material's solid-film capacitance (C_f), respectively. Note that such a circuit model is a good approximation for studying solid electrodes with different degrees of surface roughness and physical non-uniformity. [518, 519] In addition, an inductor (L_{ad}) to the proposed circuit model, which account for the pseudo-inductive behaviour in the high frequency domain, was also necessary for fitting the experimental results. As previously discussed in the literature, such a high-frequency pseudo-inductive behaviour is a rather common feature in electrochemical active materials containing

heterogeneity or energy disorder (e.g., conducting metal-oxides and nanostructured semiconductors), caused either by disordered charge-carrier relaxation and/or disordered movement of adsorbed redox species at the surface of the electrode (pores, cracks, grain boundaries, etc.). [520-523]

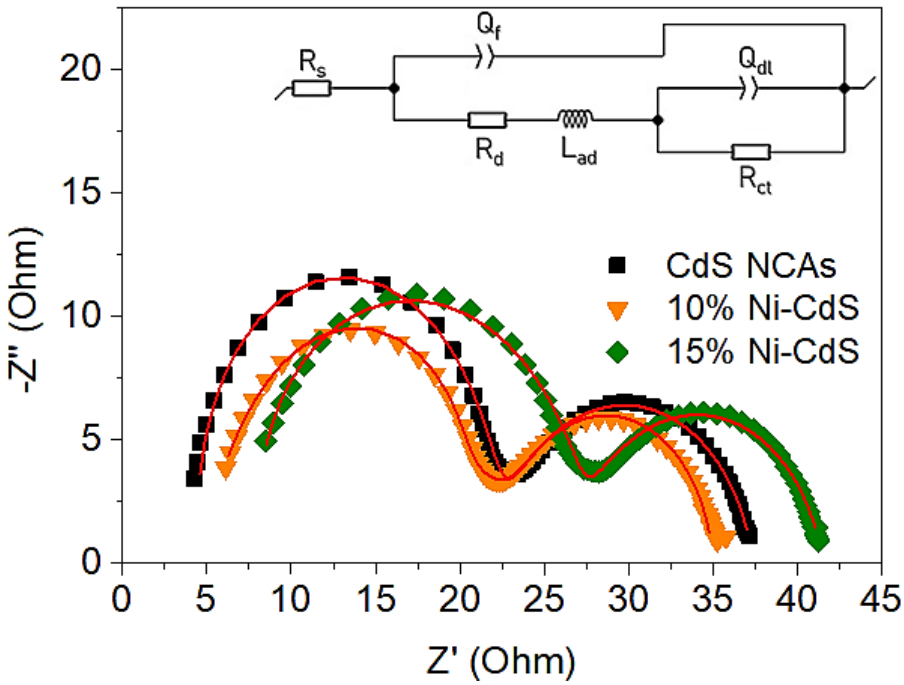

Figure 3-74: EIS Nyquist plots (inset: equivalent circuit model used to simulate the impedance measurements as a function of frequency) for mesoporous CdS NCAs and the Ni-CdS composites with 10 and 15 wt.% Ni loadings. The red lines are fits to the experimental data.

Thus, the estimated charge-transfer resistance (R_{ct}) for the 10% Ni-CdS sample was found to be 13.1 Ω, which is lower than that of the 15% Ni-CdS (14.5 Ω) and pure CdS NCAs (15.3 Ω) materials, indicating a faster transport of photogenerated carriers in the 10 wt.% Ni-loaded catalyst. Also, the total polarization resistance ($R_{tot} = R_d + R_{ct}$) for each electrode follows the order: CdS NCAs (~33.3 Ω) > 15% Ni-CdS (~33.0 Ω) > 10% Ni-CdS (~28.6 Ω). In general, a lower charge-transfer resistance is anticipated to enhance the photoactivity of the catalyst by inducing high electron-transfer conductivity through the framework and prolonging the lifetime of photogenerated charge-carriers. Obviously, the catalyst loaded with 10 wt.% Ni (primarily as β-$Ni(OH)_2$, as demonstrated by the TEM and XPS results) provides the most efficient separation and transfer of photoinduced charge-carriers, which correlates well with its outstanding photocatalytic H_2-evolution activity. This is also consistent with the lower recombination rate of band-edge excitons in the mesoporous 10% Ni-CdS hetero-structure, as revealed by the PL results (see **Figure 3-73**).

Table 3-11: EIS equivalent circuit fitted parameters for the mesoporous CdS NCAs and the Ni-CdS catalysts with 10 and 15 wt.% Ni loadings).

Sample	R_s (Ω)	R_d (Ω)	C_f (F)	L_{ad} (H)	R_{ct} (Ω)	C_{dl} (F)	x^2 †
CdS NCAs	4.23	18.04	60.54×10^{-9}	6.63×10^{-6}	15.29	15.34×10^{-6}	0.029
10% Ni-CdS	6.13	15.49	50.13×10^{-9}	3.81×10^{-7}	13.09	14.18×10^{-6}	0.019
15% Ni-CdS	8.49	18.48	40.57×10^{-9}	3.88×10^{-8}	14.54	15.71×10^{-6}	0.028

† **chi-squared test of the model fitting.**

Furthermore, to attain a clearer picture of the electronic band structure and charge-transfer mechanism of the as-prepared mesoporous Ni-CdS heterostructures, EIS Mott-Schottky measurements were also performed at an AC frequency of 1 kHz in 0.5 M Na_2SO_4 electrolyte (pH = 7). The Mott-Schottky plots and the corresponding fits of the linear portion of the inverse square space-charge capacitance ($1/C_{sc}^2$) as a function of applied potential (V) (according to **eq.23**) for pure CdS NCAs and the Ni-modified CdS samples (with 5, 10 and 15 wt.% Ni-loadings) are shown in **Figure 3-75**. It is apparent that the mesoporous CdS NCAs shows a positive linear slope, indicating n-type conductivity, that is, electrons are the majority carriers. For the Ni-CdS NCAs heterostructures, however, a bell-shaped behavior in the Mott-Schottky plots was observed. This strongly suggests the formation of a p–n junction at the β-$Ni(OH)_2$/CdS interface, which could further affect the separation and recombination dynamics of the photoinduced charge-carriers. The corresponding flat-band (V_{FB}) potentials estimated from the intercept of the extrapolated straight lines with the potential axis ($1/C_{sc}^2 = 0$) are listed in **Table 3-12**. The Mott-Schottky results indicated that, with increasing Ni content from 0 to 15 wt.%, the V_{FB} potential of CdS gradually shifts to a cathodic (negative) direction, that is, from –0.71 V to –0.86 V *vs* NHE. Moreover, the deposition of β-$Ni(OH)_2$ on the surface of CdS NCAs increases slightly the donor density (N_D) of CdS from 3.0×10^{17} to 4.0×10^{17} cm^{-3}, as inferred from the decreased positive slopes in the Mott-Schottky plots of the Ni-modified samples. However, a different trend in the N_D value of the 10% Ni-CdS sample can be observed, which is very close to that of pure CdS NCAs (see results in **Table 3-12**). These results can be explained possibly due to the lower charge-transfer efficiency of the 5 and 15 wt.% Ni-loaded materials, which could result in the accumulation of electrons at the junction interface with increasing the applied potential, whereas the increased transfer efficiency of the 10% Ni-CdS catalyst (as inferred by Nyquist measurements) denotes a smoother flow of carriers across the β-$Ni(OH)_2$/CdS junction to the electrolyte, resulting to a more effective charge-separation and depletion of electrons at the contact interface. As for the observed up-shift in the V_{FB} positions of the Ni-CdS composites,

this can be understood as a result of the CdS surface passivation by the β-Ni(OH)$_2$ particles, thereby suppressing the band-edge pinning. In fact, as previously described in chapter 1, charged surface states and adsorbed surface charges can indeed induce a potential shift within the Helmholtz layer (V_H), that can be altered by surface passivation (under the same electrolyte conditions). [272, 524] This shift of V_H by surface passivation can, in turn, affect the V_{FB} according to **eq. 6** (i.e., $V_{FB} = V_H + \Phi_S - 4.5$, where Φ_S is the work function of the semiconductor and -4.5 eV is the *NHE* redox level with respect to vacuum), leading to a shift towards more negative or positive potentials (cathodic or anodic shift respectively) depending on the net surface charge. To elucidate this possibility, the ζ-potential of the catalysts was measured in a 0.5 M Na_2SO_4 solution at pH 7 condition (similarly to the EIS measurements). The obtained ζ-potentials for the 10% Ni-CdS, 15% Ni-CdS and CdS NCAs catalysts were found to be –15.6, –15.4 and –11.0 mV, respectively. Clearly, particles in these suspensions were all negatively charged. Nevertheless, compared to pristine CdS NCAs, the higher negative net charge of the Ni-modified materials (i.e., the 10% Ni-CdS and 15% Ni-CdS catalysts) is in line with the premise of a negative shift in V_H [245], and thus the cathodic shift of the V_{FB} level, upon surface-modification with β-Ni(OH)$_2$.

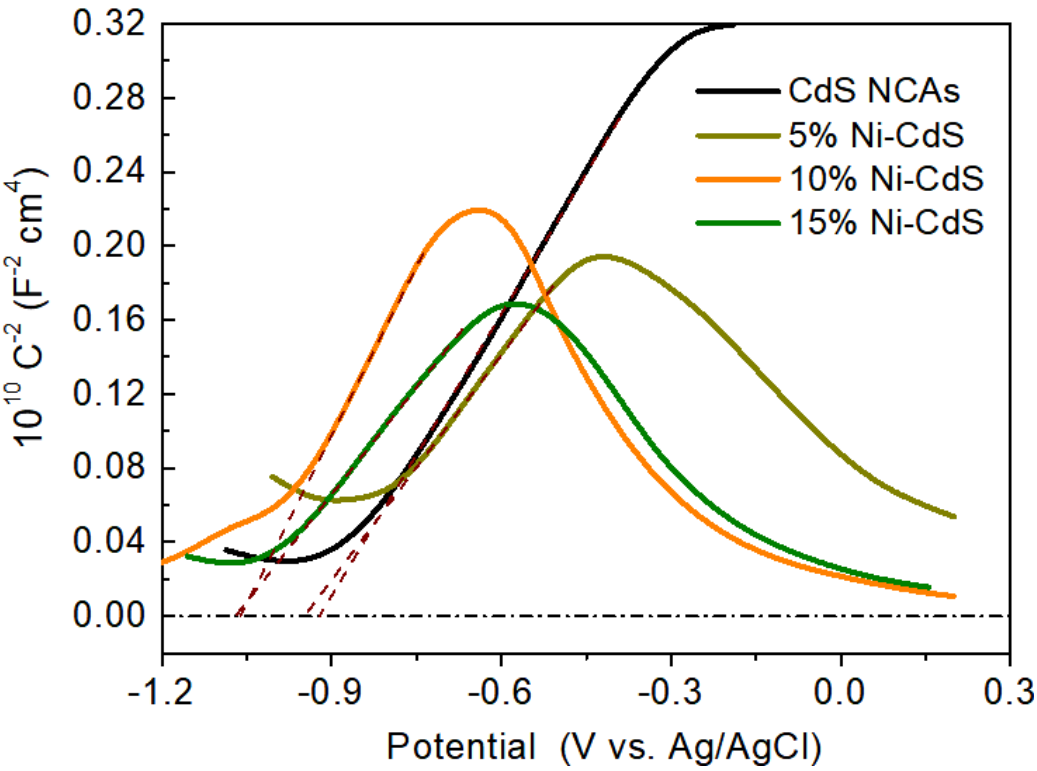

Figure 3-75: Mott−Schottky plots of the $1/C_{SC}^2$ as a function of applied potential (V) (according to eq. 23) with reference to the of Ag/AgCl (3 M KCl) electrode potential, for the mesoporous CdS NCAs and the Ni-modified CdS NCAs materials with 5, 10 and 15 wt.% Ni-loadings.

Table 3-12: Analytical data obtained from Mott-Schottky plots for the mesoporous pristine CdS NCAs and the Ni-modified CdS catalysts with 5, 10, and 15 wt.% Ni-loadings.

Catalyst	Flat Band (V_{FB})	Valence Band† (E_V)	Slope	Donor density‡ (N_d)
	(V vs NHE, pH=7)		(F^{-2} cm^4 V^{-1})	(cm^{-3})
CdS NCAs	–0.71	2.00	5.192×10^9	3.0×10^{17}
5% Ni-CdS	–0.74	1.98	4.066×10^9	3.9×10^{17}
10% Ni-CdS	–0.84	1.89	4.932×10^9	3.2×10^{17}
15% Ni-CdS	–0.86	1.86	3.955×10^9	4.0×10^{17}

† The VB level of the catalysts was estimated by adding the bandgap (E_g) of each sample to its V_{FB} value.
‡ The N_D values were obtained according to eq. 25 using the slopes of the Mott-Schottky plots and the relative dielectric constant of CdS (ε = 8.9).

Based on the measured V_{FB} values and optical bandgaps (as obtained from UV–vis/NIR absorption data), the energy band diagrams for each catalyst can be constructed, as illustrated in **Figure 3-76**. Here it is assumed that the V_{FB} level serves as a good approximation of the CB-edge position, which is quite reasonable for heavily doped n-type semiconductors, such as CdS.[457] In relation to this, it is typical for the CB edge of many n-type semiconductors to be about 0.1–0.3 V higher (more negative) than the flat-band potential. [525, 526]

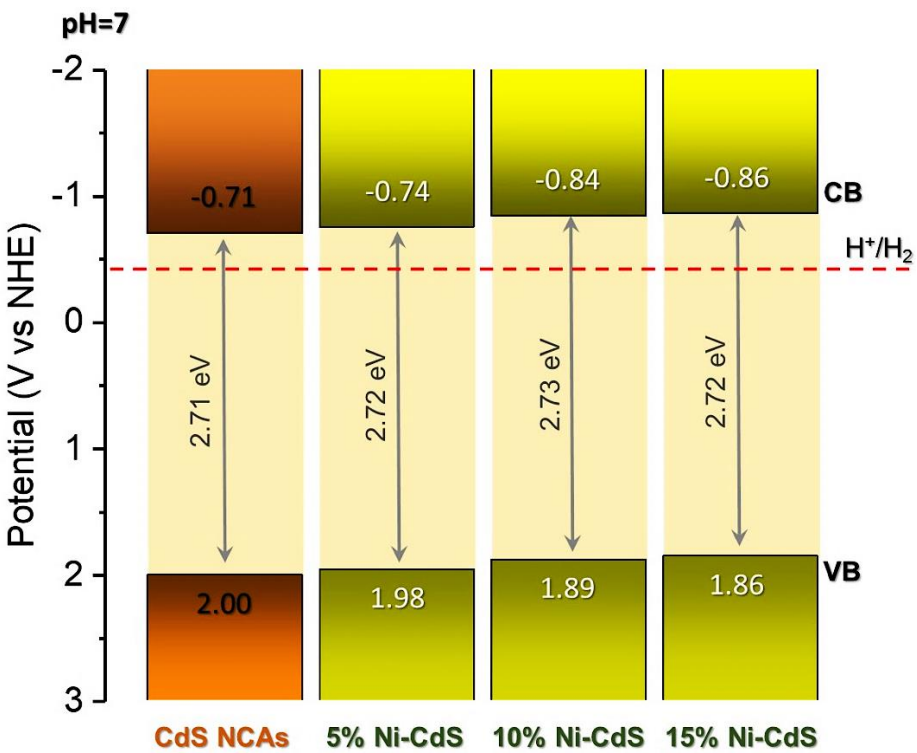

Figure 3-76: Energy band diagram schemes of the mesoporous CdS NCAs and the Ni-CdS heterostructures with 5, 10, and 15 wt.% Ni-loadings. The conduction band (CB) edges were estimated from the flat-band potentials obtained from Mott-Schottky plots, and the valence band (VB) edges by adding the bandgap of each material to the respective flat-band potential. All the potentials were converted from the Ag/AgCl electrode scale to the normal hydrogen electrode (NHE) scale using eq. 24.

Therefore, it can be deduced that the intrinsic electric field created at the p–n β-Ni(OH)$_2$/CdS junctions, as corroborated by the aforementioned EIS results, dictates the charge-transfer processes through the negative shift of V_{FB} and suitable band-edge alignment at the nanoscale β-Ni(OH)$_2$/CdS contacts. Notably, Ni-hydroxide is known to be a p-type semiconductor with a Fermi level at ~5.4–5.6 eV *vs* vacuum [527, 528], which is more positive than the Fermi level of CdS (ca. 4.5 eV *vs* vacuum). [487] This means that when β-Ni(OH)$_2$ particles are anchored onto the CdS surface, an internal electric field is formed at the β-Ni(OH)$_2$/CdS junction interface that promotes the transfer of electrons from CdS to β-Ni(OH)$_2$ until their Fermi levels reach equilibrium. At this condition, the electron flow creates a space-charge region, i.e., a positively charged area in the CdS side and a negatively charged area in the β-Ni(OH)$_2$ side, leading to the upward bending of the CB edge of CdS near the contact interface with β-Ni(OH)$_2$ (**Figure 3-77**). For the β-Ni(OH)$_2$-modified CdS heterostructures, the potential barrier-height (Φ_{SC}) formed, defined by the energy difference of the Fermi level of β-Ni(OH)$_2$ and the Fermi level of CdS, was found at ~0.9–1.1 eV.

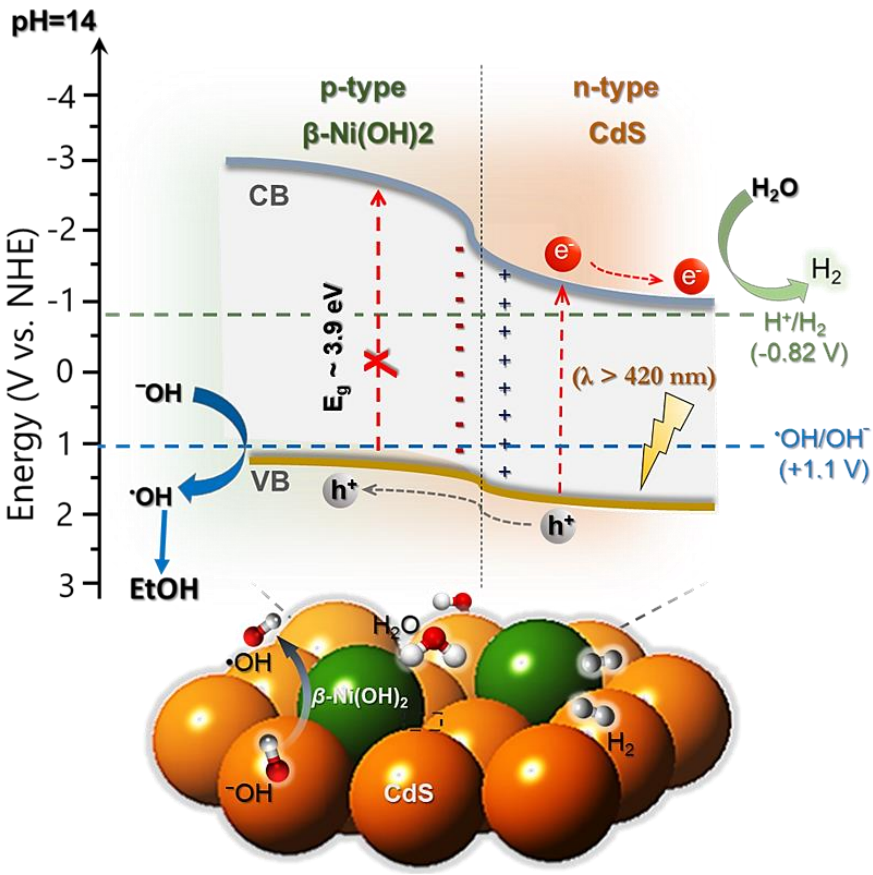

Figure 3-77: Schematic representation of the energy diagram of the β-Ni(OH)$_2$/CdS heterojunction (at pH 14) and proposed mechanism of visible-light photocatalytic H$_2$-production by the mesoporous Ni-CdS heterostructured catalysts. Modified with permission from ref. [406]. Copyright © 2018, American Chemical Society.

All these effects definitely have an impact on the photocatalytic performance of the mesoporous Ni-CdS heterostructured catalysts. Specifically, as illustrated in **Figure 3-77**, upon visible light illumination the CdS nanoparticles get excited and generate electron-hole pairs, whereas β-$Ni(OH)_2$ itself cannot absorb light at this wavelength range ($\lambda \geq 420$ nm) owing to its large band gap (ca. 3.9 eV). Because of the intimate contact, the internal electric field, and the favorable Type-II band-alignment formed between the p–n β-$Ni(OH)_2$/CdS junctions (particularly, CdS holds more positive VB and CB edges compared to β-$Ni(OH)_2$), the photoinduced holes generated in the VB of CdS can migrate to the β-$Ni(OH)_2$ nanoparticles, thus leading to an accumulation of photogenerated electrons in the CB of CdS where the photocatalytic water-reduction reaction occurs. It is also worth pointing out that, due to the high internal surface area of the 3D open-pore structure, the mesoporous CdS NC assemblies can provide increased number of accessible reaction centers capable of reducing water to H_2. In this regard, it has been established that, in alkaline medium, the H_2-evolution reaction proceeds through the initial water-discharge step (Volmer reaction: $H_2O + e^- + M \rightarrow M–H_{ads} + OH^-$) on a positively-charged metal site (M), followed by either the electrochemical Heyrovsky desorption step ($H_2O + e^- + M–H_{ads} \rightarrow M + H_2 + OH^-$) or the Tafel recombination step ($2M–H_{ads} \rightarrow 2M + H_2$).[440, 529] On the other hand, the photoinduced holes gathered in β-$Ni(OH)_2$ can be effectively consumed, by oxidizing the sacrificial reagent (ethanol) through the $^{\bullet}OH/OH^-$ redox shuttle mechanism, as previously described.

Furthermore, Mott-Schottky analysis on the pure β-$Ni(OH)_2$ particles showed that their V_{FB} level lies at about 1.31 V *vs* NHE (at pH = 7), confirming their p-type behavior (**Figure 3-78**). However, a common feature of p-type NiO_x films is that their VB lies about 0.4 eV lower (more positive) than the Fermi-level. [530, 531] Therefore, the VB of β-$Ni(OH)_2$ is expected to be approximately 1.7 V and 1.4–1.5 V *vs* NHE before contact and after equilibrium with CdS, respectively, which is comparable to the redox potential of surface adsorbed $^{\bullet}OH/OH_{aq}^-$ pairs (1.36–1.49 V *vs* NHE, pH = 7) [532]. Here, according to the Anderson's affinity rule [533], the valence band offset (ΔE_v) between CdS and β-$Ni(OH)_2$ was found to be ~0.2–0.3 eV, calculated by **eq. 39**:

$$\boldsymbol{\Delta E_V = (E_{g1} + \chi_1) - (E_{g2} + \chi_2)} \qquad \textbf{(eq. 39)}$$

where E_{g1} and E_{g2} are the band gap energies and χ_1 (3.8 eV) and χ_2 (2.3–2.4 eV) are the electron affinities of the CdS and β-$Ni(OH)_2$ semiconductors, respectively.

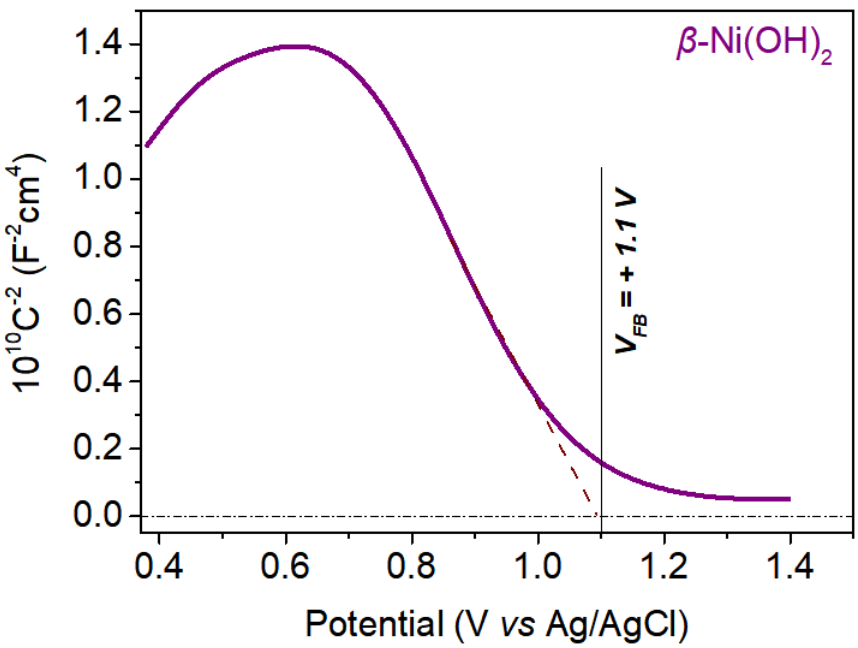

Figure 3-78: Mott-Schottky plot of the inverse square space-charge capacitance ($1/C_{SC}^2$) as a function of applied potential (*V*) relative to the Ag/AgCl (3 M KCl) electrode potential, for the as-prepared pure *β*-Ni(OH)$_2$ particles. The negative slope of the corresponding linear fit indicates a p-type conductivity for *β*-Ni(OH)$_2$.

However, given that the band edge positions of CdS usually shift with pH by ca. –33 mV/pH unit [355, 358], at pH 14 the VB of CdS will shift to 1.77 V *vs* NHE and, in turn, the VB potential of *β*-Ni(OH)$_2$ will also shift to approximately 1.2–1.3 V *vs* NHE. On the contrary, the $^{\bullet}OH/OH_{aq}^{-}$ redox couple follows the Nernstian behavior (–59 mV/pH unit), and therefore, at pH 14 the VB of *β*-Ni(OH)$_2$ will eventually be below the redox potential of $^{\bullet}OH/OH_{aq}^{-}$ pairs (i.e., 1.0–1.1 V *vs* NHE at pH = 14). On this basis, in solutions with pH ≥ 14, the photochemical oxidation of OH_{aq}^{-} species by the surface-reaching holes in the as-prepared Ni-CdS heterostructures is thermodynamically feasible. As a proof of concept, the production of $^{\bullet}OH$ radicals was assessed by fluorescence (FL) spectroscopy measurements, using terephthalic acid (TA) instead of ethanol in the photocatalytic water-reduction experiments on mesoporous CdS and 10% Ni-CdS NCAs catalysts. Note that TA readily reacts with hydroxyl radicals to produce the fluorescent 2-hydroxyterephthalic acid (HTA). The results from the photocatalytic experiments conducted at pH 14, all showed an emission peak at about 440 nm that gradually increased during the reaction, suggesting the formation of hydroxyl radicals (see **Figure 3-79a**). Notably, the production rate of $^{\bullet}OH$ radicals from the 10% Ni-CdS catalyst, which is defined by the time evolution of the FL intensity of HTA (**Figure 3-79b**), is almost 3-times higher than that for CdS NCAs at similar conditions. Thus, it is reasonable to assume that the observed higher OH_{aq}^{-} oxidation kinetics for the Ni-modified catalyst are a result of the efficient separation of photoexcited electron-hole pairs at the *β*-Ni(OH)$_2$/CdS junction. The separation and transport of photoexcited carriers have been manifested clearly in the above PL spectra and EIS results.

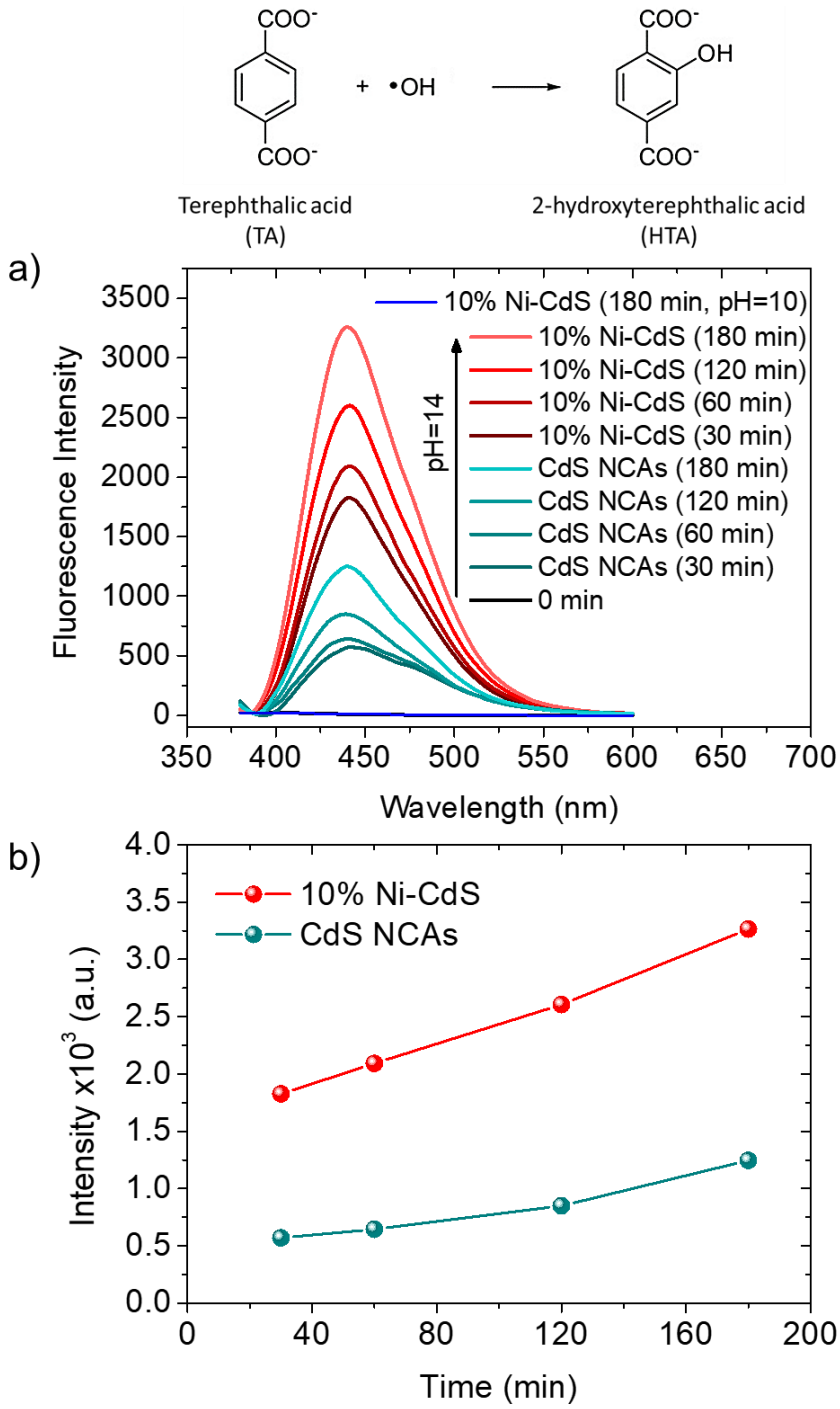

Figure 3-79: a) Comparison of ˙OH formation over the mesoporous CdS NCAs (cyan lines) and 10% Ni-CdS (red lines) samples, illustrated by fluorescence (FL) spectra of 2-hydroxyterephthalic acid (HTA). The increasing FL peak at 440 nm indicates the formation of HTA as a product of the reaction of terephthalic acid (TA) with the hydroxyl radicals. The FL spectrum of TA in the presence of 10% Ni-CdS NCAs catalyst in pH 10 aqueous solution after 3 h irradiation is also given for comparison (blue line). b) Time evolution of the HTA FL intensity at 440 nm for the CdS NCAs and 10% Ni- CdS NCAs samples. All the ˙OH radical formation tests were performed similarly to the photocatalytic H_2-evolution reactions, but with adding TA instead of ethanol as electron donor. The exact reaction conditions were as follows: 40 mg of catalyst dispersed in 20 mL NaOH aqueous solution (pH 14.0 or pH 10.0) containing 1.2 M terephthalic acid. Before irradiation, the mixture was purged with argon for at least 30 min to remove any dissolved air and then irradiated with a 440 nm LED light. Samples were collected using a syringe (1 mL) diluted with 9 mL DI water and centrifuged to remove the catalyst. The FL spectra were obtained at room temperature on a Jobin- Yvon Horiba FluoroMax-P (SPEX) spectrofluorometer using 320 nm excitation wavelength.

For comparison, FL spectroscopy analysis over the 10% Ni-CdS/OH^-/TA photocatalytic system at pH 10 was also conducted. As seen in **Figure 3-79a**, the FL spectrum does not show any emission peak at 440 nm after 3 h of photocatalytic reaction, indicating that no hydroxyl radicals are formed under these conditions. This means that at pH 10, the 10% Ni-CdS NCAs catalyst is not able to oxidize OH^- to $^{\bullet}OH$ radicals, thus resulting in lower photo-oxidation kinetics. The obtained FL results are in line with the low photocatalytic H_2-generation rate (~0.2 mmol h- 1) that was observed for the 10% Ni-CdS catalyst in the NaOH-ethanol (10% v/v) reaction solution with pH 10 (see **Figure 3-68b**); herein, the direct oxidation of ethanol from the photogenerated holes is considered to be the rate-determining step. Based on the above findings, it can be deduced that β-$Ni(OH)_2$ nanoparticles essentially serve as the oxidation active-sites (hole collectors) for the photo-oxidation of OH^- to $^{\bullet}OH$ radicals, thereby promoting electron-hole separation and greatly improving the photocatalytic efficiency. It is also noted that, during the course of irradiation, the transferred holes from the VB of CdS to β-$Ni(OH)_2$ could cause the oxidation of remaining Ni(0) clusters to Ni(II), yielding β-$Ni(OH)_2$ species, as has been suggested by the previous XPS measurements. Also, the β-$Ni(OH)_2$ nanoparticles are prone to further oxidation by the photoexcited holes, leading to the formation of nickel oxyhydroxide (NiOOH) species. [517] However, after 20-h photocatalytic reaction, no notable XPS peak corresponding to the NiOOH phase was detected in the examined catalyst. In the literature, the Ni $2p_{3/2}$ line of NiOOH has been reported to be in the binding energy range of 855.8–856.4 eV. [534-536] Thus, this further implies that β-$Ni(OH)_2$ behaves as an efficient hole-transfer mediator, that shuttles photogenerated holes from the catalyst to the ($^{\bullet}OH/OH^-$) redox species.

Overall, the remarkably improved H_2-evolution efficiency of this system stems from the strong electronic coupling between n-type CdS and p-type β-$Ni(OH)_2$ nanoparticles, which promotes the effective separation and transfer of photoinduced charge-carriers, as well as the permeable mesoporous structure, which provides more exposed active-sites for reaction and facilitates the fast transport of electrolytes between the nanoparticles. This work not only presents the possibility of using mesoporous networks of nanoscale p–n β-$Ni(OH)_2$/CdS junctions as a viable hydrogen evolution photocatalyst, but also can offer new opportunities for the development and in-depth understanding of noble metal-free photocatalysts for efficient solar-to-chemical energy conversion.

Conclusions

To summarize, a new and cost-effective synthetic method for preparing mesoporous networks of metal-chalcogenide NCs has been successfully developed and demonstrated in this work. This method utilizes a simple surfactant-assisted oxidative self-polymerization procedure, which entails a controlled destabilization of colloidal metal sulfide nanoparticles in the presence of nonionic surfactants. Remarkably, this new assembly process allows the construction of ordered mesoporous architectures with tailored characteristics, such as different composition (e.g., CdS and ZnS) and particle size (from 4 to 6.5 nm) of the chalcogenide nanobuilding blocks, as well as adjustable pore size by employing different structure-directing templates. Owing to the large surface area and three-dimensional open pore structure, the NC ensembles of CdS showed high activity and stability in visible-light-driven oxidation of 1-phenylethanol into acetophenone. Therefore, the proposed synthetic approach for assembling mesoporous structures with interconnected metal chalcogenide nanoparticles opens up great opportunities for developing new functional materials for technological applications, including catalysis and solar energy conversion to renewable fuels such as H_2.

To this end, this work also demonstrated that the surface of mesoporous CdS NCAs can be easily modified with effective co-catalysts, such as Pt nanoparticles, CuS NCs, and Ni-species, to develop new and efficient nanocomposite catalysts for photocatalytic water reduction and H_2 production under visible light. First, ordered mesoporous Pt-decorated CdS NCAs with different size of Pt nanoparticles (ranging from 1.8 to 3.3 nm) have been successfully prepared via this new method and a straightforward photodeposition process. The resulting materials are composed of a network structure of cross-linked CdS and Pt nanoparticles and exhibit accessible pore structure with high surface area. Photocatalytic studies revealed that these materials behave as highly efficient catalysts for H_2 evolution using visible-light irradiation. The enhanced activity is attributed to the decrease in the work function of Pt nanoparticles by increasing the particle size, and the increased number of surface edge sites of Pt nanoparticles. Thus, this decreases the height of the Schottky barrier created at the Pt/CdS junction and promotes the smooth electron transfer from photoactivated CdS to Pt. Moreover, critical for efficient H_2 evolution was the 3D open-pore structure and large accessible surface area. As a result of this, the Pt-CdS NCAs catalyst containing 5 wt% of Pt with 2.5–3 nm diameter particles exhibits the highest photocatalytic activity. This activity corresponds to a H_2-evolution rate of ~1.2 mmol h^{-1} (or 60 mmol h^{-1} g^{-1}) with an QY of 70% at $\lambda = 420 \pm 10$ nm, which is impressive considering that it is obtained by using only a Pt-CdS photocatalyst without any oxidation co-catalyst. Therefore, this study implies the promising potential of the mesoporous Pt-CdS NCAs to serve as an efficient and stable photocathode for water reduction under visible light.

Moreover, mesoporous networks of connected CuS and CdS NCs with high internal surface area and narrow pore-size distribution have also been synthesized, through a simple cation-exchange process, and investigated as photocatalysts for H_2 generation. The results demonstrated that controlling the chemical composition can lead to the formation of efficient charge separation interfaces along the binary CuS/CdS semiconductor, which greatly enhance the photocatalytic activity. As a result, mesoporous CuS/CdS NC assemblies, which contain ~5 mol% Cu, achieve an average H_2-evolution rate of 0.28 mmol h^{-1} with a QY of 12.6% at $\lambda = 420 \pm 10$ nm, while displaying good stability for at least 20 h of irradiation. The activity of this catalyst is about 5.3 times higher than that of pure mesoporous CdS assemblies, measured under identical reaction conditions. Using UV–vis/NIR, photoluminescence (PL) and electrochemical impedance spectroscopy, it is shown that the high H_2-production activity of the CuS/CdS NC-networks mainly arises from the proper alignment of the band-edge positions of the materials. The nanoscale p−n heterojunction negatively shifted the band-edge potentials, enhancing the separation of photoexcited electron-hole pairs and, thus, the H_2 evolution rate. These results suggest the great possibility for the implementation of this new mesoporous p-CuS/n-CdS heterojunctional photocatalyst as a sustainable and low-cost alternative in solar energy conversion applications.

Finally, surface modification with Ni-species, by a photochemical deposition process, resulted in the formation of mesoporous networks of β-$Ni(OH)_2$-modified CdS NCs with high internal surface area, that showed a very high photocatalytic activity and long-term stability for H_2 generation. By optimizing the loading of β-$Ni(OH)_2$, the Ni-modified CdS assemblies provide a high charge-carrier transfer and separation efficiency along the nanoheterojunctioned framework, in which β-$Ni(OH)_2$ and CdS NCs are in intimate contact, which results in a very high H_2-production rate in alkaline solution. Consequently, the Ni-CdS NCAs catalyst with 10 wt.% Ni loading achieved a H_2-evolution rate of 1.4 mmol h^{-1} under $\lambda \geq 420$ nm light irradiation with an apparent QY of 72% at $\lambda = 420$ nm, while demonstrating very good stability for at least 25 h in alkaline ethanol solution (5 M NaOH, 10% v/v ethanol). Notably, this is one of the highest so far reported efficiencies for nonprecious-metal CdS heterostructures. Using a combination of UV−vis/NIR, electrochemical impedance, and photoluminescence spectroscopy techniques, it was shown that the improved H_2-evolution efficiency of this system stems from the strong electrical coupling between n-type CdS and p-type β-$Ni(OH)_2$ NCs, which promotes efficient separation and transport of photoinduced carriers, as well as the pertinent mesoporous structure, which provides more exposed active sites for reaction and facilitates fast transport of electrolytes between the nanoparticles. Therefore, this study not only presents the possibility of using mesoporous networks of nanoscale p−n β-$Ni(OH)_2$/CdS junctions as a viable H_2-evolution photocatalyst, but also can offer new opportunities for the development and in-depth understanding of noble-metal-free photocatalysts for efficient solar-to-fuel conversion.

References

1. Lu, G.Q. and X.S. Zhao, *NANOPOROUS MATERIALS ? AN OVERVIEW*, in *Nanoporous Materials: Science and Engineering*. 2004, PUBLISHED BY IMPERIAL COLLEGE PRESS AND DISTRIBUTED BY WORLD SCIENTIFIC PUBLISHING CO. p. 1-13.
2. Rouquerol, J., et al., *Recommendations for the characterization of porous solids (Technical Report)*, in *Pure and Applied Chemistry*. 1994. p. 1739.
3. Harris, P.J.F., *Structure of non-graphitising carbons.* International Materials Reviews, 1997. **42**(5): p. 206-218.
4. Gelb, L.D., *Modeling Amorphous Porous Materials and Confined Fluids.* MRS Bulletin, 2009. **34**(8): p. 592-601.
5. Kowalczyk, P., et al., *Carbon Molecular Sieves: Reconstruction of Atomistic Structural Models with Experimental Constraints.* The Journal of Physical Chemistry C, 2014. **118**(24): p. 12996-13007.
6. Thompson, M.W., et al., *An Atomistic Carbide-Derived Carbon Model Generated Using ReaxFF-Based Quenched Molecular Dynamics.* C, 2017. **3**(4): p. 32.
7. Barton, T.J., et al., *Tailored Porous Materials.* Chemistry of Materials, 1999. **11**(10): p. 2633-2656.
8. Baerlocher, C., et al., *Preface*, in *Atlas of Zeolite Framework Types (Sixth Edition)*, C. Baerlocher, L.B. McCusker, and D.H. Olson, Editors. 2007, Elsevier Science B.V.: Amsterdam. p. 1-2.
9. Sherman, J.D., *Synthetic zeolites and other microporous oxide molecular sieves.* Proceedings of the National Academy of Sciences of the United States of America, 1999. **96**(7): p. 3471-3478.
10. Cheetham, A.K., G. Férey, and T. Loiseau, *Open-Framework Inorganic Materials.* Angewandte Chemie International Edition, 1999. **38**(22): p. 3268-3292.
11. Férey, G., *Microporous Solids: From Organically Templated Inorganic Skeletons to Hybrid Frameworks...Ecumenism in Chemistry.* Chemistry of Materials, 2001. **13**(10): p. 3084-3098.
12. Chiola, V., Ritsko, J.E., and Vanderpool, C.D., Process for Producing Low Bulk Density Silica, U.S. Patent 3, 556, 725, 1971.
13. Tsuneo, Y., et al., *The Preparation of Alkyltriinethylaininonium–Kaneinite Complexes and Their Conversion to Microporous Materials.* Bulletin of the Chemical Society of Japan, 1990. **63**(4): p. 988-992.
14. Inagaki, S., Y. Fukushima, and K. Kuroda, *Synthesis of highly ordered mesoporous materials from a layered polysilicate.* Journal of the Chemical Society, Chemical Communications, 1993(8): p. 680-682.
15. Shinji, I., et al., *Syntheses of Highly Ordered Mesoporous Materials, FSM-16, Derived from Kanemite.* Bulletin of the Chemical Society of Japan, 1996. **69**(5): p. 1449-1457.
16. Di Renzo, F., H. Cambon, and R. Dutartre, *A 28-year-old synthesis of micelle-templated mesoporous silica.* Microporous Materials, 1997. **10**(4): p. 283-286.

17. Kresge, C.T., et al., *Ordered mesoporous molecular sieves synthesized by a liquid-crystal template mechanism.* Nature, 1992. **359**(6397): p. 710-712.

18. Beck, J.S., et al., *A new family of mesoporous molecular sieves prepared with liquid crystal templates.* Journal of the American Chemical Society, 1992. **114**(27): p. 10834-10843.

19. Meynen, V., P. Cool, and E.F. Vansant, *Verified syntheses of mesoporous materials.* Microporous and Mesoporous Materials, 2009. **125**(3): p. 170-223.

20. Vartuli, J.C., et al., *Effect of Surfactant/Silica Molar Ratios on the Formation of Mesoporous Molecular Sieves: Inorganic Mimicry of Surfactant Liquid-Crystal Phases and Mechanistic Implications.* Chemistry of Materials, 1994. **6**(12): p. 2317-2326.

21. Kresge, C.T., et al., *The discovery of ExxonMobil's M41S family of mesoporous molecular sieves*, in *Studies in Surface Science and Catalysis*, O. Terasaki, Editor. 2004, Elsevier. p. 53-72.

22. Schwanke, A.J., R. Balzer, and S. Pergher, *Microporous and Mesoporous Materials from Natural and Inexpensive Sources*, in *Handbook of Ecomaterials*, L.M.T. Martínez, O.V. Kharissova, and B.I. Kharisov, Editors. 2017, Springer International Publishing: Cham. p. 1-22.

23. Zhao, D., et al., *Triblock Copolymer Syntheses of Mesoporous Silica with Periodic 50 to 300 Angstrom Pores.* Science, 1998. **279**(5350): p. 548-552.

24. Zhao, D., et al., *Nonionic Triblock and Star Diblock Copolymer and Oligomeric Surfactant Syntheses of Highly Ordered, Hydrothermally Stable, Mesoporous Silica Structures.* Journal of the American Chemical Society, 1998. **120**(24): p. 6024-6036.

25. Tanev, P.T. and T.J. Pinnavaia, *A Neutral Templating Route to Mesoporous Molecular Sieves.* Science, 1995. **267**(5199): p. 865-867.

26. Kleitz, F., S. Hei Choi, and R. Ryoo, *Cubic Ia3d large mesoporous silica: synthesis and replication to platinum nanowires, carbon nanorods and carbon nanotubes.* Chemical Communications, 2003(17): p. 2136-2137.

27. Bagshaw, S.A., E. Prouzet, and T.J. Pinnavaia, *Templating of Mesoporous Molecular Sieves by Nonionic Polyethylene Oxide Surfactants.* Science, 1995. **269**(5228): p. 1242-1244.

28. Moritz, M. and M. Geszke-Moritz, *Mesoporous materials as multifunctional tools in biosciences: Principles and applications.* Materials Science and Engineering: C, 2015. **49**: p. 114-151.

29. Di Renzo, F., et al., *Micelle-Templated Materials*, in *Handbook of Porous Solids*, F. Schüth, K. S. W. Sing, and J. Weitkamp, Editors. 2002, Wiley-VCH Verlag Gmb. p. 1311-1395.

30. Tadros, T., *Self-Assembly of Surfactants*, in *Encyclopedia of Colloid and Interface Science*, T. Tadros, Editor. 2013, Springer Berlin Heidelberg: Berlin, Heidelberg. p. 1044-1044.

31. Ying, J.Y., C.P. Mehnert, and M.S. Wong, *Synthesis and Applications of Supramolecular-Templated Mesoporous Materials.* Angewandte Chemie International Edition, 1999. **38**(1-2): p. 56-77.

32. Monnier, A., et al., *Cooperative Formation of Inorganic-Organic Interfaces in the Synthesis of Silicate Mesostructures.* Science, 1993. **261**(5126): p. 1299-1303.

33. Huo, Q., et al., *Organization of Organic Molecules with Inorganic Molecular Species into Nanocomposite Biphase Arrays.* Chemistry of Materials, 1994. **6**(8): p. 1176-1191.

34. Attard, G.S., J.C. Glyde, and C.G. Göltner, *Liquid-crystalline phases as templates for the synthesis of mesoporous silica.* Nature, 1995. **378**(6555): p. 366-368.

35. Brinker, C.J., et al., *Evaporation-Induced Self-Assembly: Nanostructures Made Easy.* Advanced Materials, 1999. **11**(7): p. 579-585.

36. Grosso, D., et al., *Fundamentals of Mesostructuring Through Evaporation-Induced Self-Assembly.* Advanced Functional Materials, 2004. **14**(4): p. 309-322.

37. Soler-Illia, G.J.A.A. and O. Azzaroni, *Multifunctional hybrids by combining ordered mesoporous materials and macromolecular building blocks.* Chemical Society Reviews, 2011. **40**(2): p. 1107-1150.

38. Wan, Y. and Zhao, *On the Controllable Soft-Templating Approach to Mesoporous Silicates.* Chemical Reviews, 2007. **107**(7): p. 2821-2860.

39. Firouzi, A., et al., *Cooperative organization of inorganic-surfactant and biomimetic assemblies.* Science, 1995. **267**(5201): p. 1138-1143.

40. Boissière, C., et al., *A New Synthesis of Mesoporous MSU-X Silica Controlled by a Two-Step Pathway.* Chemistry of Materials, 2000. **12**(10): p. 2902-2913.

41. Huo, Q., et al., *Generalized synthesis of periodic surfactant/inorganic composite materials.* Nature, 1994. **368**(6469): p. 317-321.

42. Sayari, A. and P. Liu, *Non-silica periodic mesostructured materials: recent progress.* Microporous Materials, 1997. **12**(4): p. 149-177.

43. Schüth, F., *Non-siliceous Mesostructured and Mesoporous Materials.* Chemistry of Materials, 2001. **13**(10): p. 3184-3195.

44. He, X. and D. Antonelli, *Recent Advances in Synthesis and Applications of Transition Metal Containing Mesoporous Molecular Sieves.* Angewandte Chemie International Edition, 2002. **41**(2): p. 214-229.

45. Attard, G.S., et al., *The True Liquid Crystal Approach to Mesoporous Silica.* MRS Proceedings, 1996. **425**: p. 179.

46. Göltner, C.G., et al., *Mesoporous Silica from Lyotropic Liquid Crystal Polymer Templates.* Angewandte Chemie International Edition, 1998. **37**(5): p. 613-616.

47. Göltner, C.G., et al., *Nanoporous Silicas by Casting the Aggregates of Amphiphilic Block Copolymers: The Transition from Cylinders to Lamellae and Vesicles.* Advanced Materials, 1999. **11**(5): p. 395-398.

48. Goltner, C.G. and M. Antonietti, *Mesoporous materials by templating of liquid crystalline phases.* Advanced Materials, 1997. **9**(5): p. 431-436.

49. Zhao, D.-D., et al., *Preparation of ordered mesoporous nickel oxide film electrodes via lyotropic liquid crystal templated electrodeposition route.* Electrochimica Acta, 2008. **53**(6): p. 2699-2705.

50. Luo, H., J. Zhang, and Y. Yan, *Electrochemical Deposition of Mesoporous Crystalline Oxide Semiconductor Films from Lyotropic Liquid Crystalline Phases.* Chemistry of Materials, 2003. **15**(20): p. 3769-3773.

51. Nelson, P.A., et al., *Mesoporous Nickel/Nickel Oxidea Nanoarchitectured Electrode.* Chemistry of Materials, 2002. **14**(2): p. 524-529.

52. H. Whitehead, A., et al., *Electrodeposition of mesoporous tin films.* Chemical Communications, 1999(4): p. 331-332.

53. Elliott, J.M., et al., *Nanostructured Platinum (HI-ePt) Films: Effects of Electrodeposition Conditions on Film Properties.* Chemistry of Materials, 1999. **11**(12): p. 3602-3609.

54. Çelik, Ö. and Ö. Dag, *A New Lyotropic Liquid Crystalline System: Oligo(ethylene oxide) Surfactants with [M(H2O)n]Xm Transition Metal Complexes.* Angewandte Chemie International Edition, 2001. **40**(20): p. 3799-3803.

55. Attard, G.S., et al., *Mesoporous Pt/Ru Alloy from the Hexagonal Lyotropic Liquid Crystalline Phase of a Nonionic Surfactant.* Chemistry of Materials, 2001. **13**(5): p. 1444-1446.

56. Attard, G.S., et al., *Liquid-Crystal Templates for Nanostructured Metals.* Angewandte Chemie International Edition in English, 1997. **36**(12): p. 1315-1317.

57. Attard, G.S., et al., *Mesoporous Platinum Films from Lyotropic Liquid Crystalline Phases.* Science, 1997. **278**(5339): p. 838-840.

58. Wolosiuk, A., O. Armagan, and P.V. Braun, *Double Direct Templating of Periodically Nanostructured ZnS Hollow Microspheres.* Journal of the American Chemical Society, 2005. **127**(47): p. 16356-16357.

59. Türker, Y. and Ö. Dag, *Synthesis of mesostructured metal sulfide films using [M(H2O)n](NO3)2:P85 (M = Cd(ii) and Zn(ii)) liquid crystalline mesophases.* Journal of Materials Chemistry, 2008. **18**(29): p. 3467-3473.

60. Nandhakumar, I.S., et al., *Optical properties of mesoporous II–VI semiconductor compound films.* Chemical Communications, 2004(12): p. 1374-1375.

61. Li, X., et al., *Electrodeposition of mesoporous CdTe films with the aid of citric acid from lyotropic liquid crystalline phases.* Journal of Materials Chemistry, 2006. **16**(31): p. 3207-3214.

62. Dag, Ö., et al., *Lyotropic Liquid-Crystalline Phase of Oligo(ethylene oxide) Surfactant/Transition Metal Salt and the Synthesis of Mesostructured Cadmium Sulfide.* Chemistry of Materials, 2003. **15**(14): p. 2711-2717.

63. Braun, P.V. and S.I. Stupp, *CdS mineralization of hexagonal, lamellar, and cubic lyotropic liquid crystals.* Materials Research Bulletin, 1999. **34**(3): p. 463-469.

64. Braun, P.V., et al., *Nanostructure Templating in Inorganic Solids with Organic Lyotropic Liquid Crystals.* Journal of the American Chemical Society, 1999. **121**(32): p. 7302-7309.

65. Innocenzi, P., et al., *Order−Disorder in Self-Assembled Mesostructured Silica Films: A Concepts Review.* Chemistry of Materials, 2009. **21**(13): p. 2555-2564.

66. Malfatti, L., et al., *Highly Ordered Self-Assembled Mesostructured Hafnia Thin Films: An Example of Rewritable Mesostructure.* Chemistry of Materials, 2006. **18**(19): p. 4553-4560.

67. Cagnol, F., et al., *Humidity-controlled mesostructuration in CTAB-templated silica thin film processing. The existence of a modulable steady state.* Journal of Materials Chemistry, 2003. **13**(1): p. 61-66.

68. Fan, J., et al., *Field-Directed and Confined Molecular Assembly of Mesostructured Materials: Basic Principles and New Opportunities.* Chemistry of Materials, 2008. **20**(3): p. 909-921.

69. Zhao, D., et al., *Continuous Mesoporous Silica Films with Highly Ordered Large Pore Structures.* Advanced Materials, 1998. **10**(16): p. 1380-1385.

70. Zhao, D., et al., *Synthesis of continuous mesoporous silica thin films with three-dimensional accessible pore structures.* Chemical Communications, 1998(22): p. 2499-2500.

71. Melosh, N.A., et al., *Molecular and Mesoscopic Structures of Transparent Block Copolymer−Silica Monoliths.* Macromolecules, 1999. **32**(13): p. 4332-4342.

72. Melosh, N.A., P. Davidson, and B.F. Chmelka, *Monolithic Mesophase Silica with Large Ordering Domains.* Journal of the American Chemical Society, 2000. **122**(5): p. 823-829.

73. Lu, Y., et al., *Aerosol-assisted self-assembly of mesostructured spherical nanoparticles.* Nature, 1999. **398**(6724): p. 223-226.

74. Yang, P., et al., *Block Copolymer Templating Syntheses of Mesoporous Metal Oxides with Large Ordering Lengths and Semicrystalline Framework.* Chemistry of Materials, 1999. **11**(10): p. 2813-2826.

75. Yang, P., et al., *Generalized syntheses of large-pore mesoporous metal oxides with semicrystalline frameworks.* Nature, 1998. **396**(6707): p. 152-155.

76. Feng, D., et al., *A general ligand-assisted self-assembly approach to crystalline mesoporous metal oxides.* NPG Asia Materials, 2018. **10**(8): p. 800-809.

77. Grosso, D., et al., *Highly Organized Mesoporous Titania Thin Films Showing Mono-Oriented 2D Hexagonal Channels.* Advanced Materials, 2001. **13**(14): p. 1085-1090.

78. Crepaldi, E.L., et al., *Nanocrystallised titania and zirconia mesoporous thin films exhibiting enhanced thermal stability.* New Journal of Chemistry, 2003. **27**(1): p. 9-13.

79. Grosso, D., et al., *Nanocrystalline Transition-Metal Oxide Spheres with Controlled Multi-Scale Porosity.* Advanced Functional Materials, 2003. **13**(1): p. 37-42.

80. Yang, H. and D. Zhao, *Synthesis of replica mesostructures by the nanocasting strategy.* Journal of Materials Chemistry, 2005. **15**(12): p. 1217-1231.

81. Lu, A.-H. and F. Schüth, *Nanocasting: A Versatile Strategy for Creating Nanostructured Porous Materials.* Advanced Materials, 2006. **18**(14): p. 1793-1805.

82. Schüth, F., *Endo- and Exotemplating to Create High-Surface-Area Inorganic Materials.* Angewandte Chemie International Edition, 2003. **42**(31): p. 3604-3622.

83. Ryoo, R., S.H. Joo, and S. Jun, *Synthesis of Highly Ordered Carbon Molecular Sieves via Template-Mediated Structural Transformation.* The Journal of Physical Chemistry B, 1999. **103**(37): p. 7743-7746.

84. Ryoo, R., et al., *Ordered Mesoporous Carbons.* Advanced Materials, 2001. **13**(9): p. 677-681.

85. Ryoo, R., et al., *07-O-01 - Ordered mesoporous carbon molecular, sieves by templated synthesis: the structural varieties*, in *Studies in Surface Science and Catalysis*, A. Galarneau, et al., Editors. 2001, Elsevier. p. 150.

86. Ryoo, R. and S. Hoon Joo, *Nanostructured carbon materials synthesized from mesoporous silica crystals by replication*, in *Studies in Surface Science and Catalysis*, O. Terasaki, Editor. 2004, Elsevier. p. 241-260.

87. Lu, A.H., D. Zhao, and Y. Wan, *Nanocasting: A Versatile Strategy for Creating Nanostructured Porous Materials*. Nanoscience Series. 2010: Royal Society of Chemistry.

88. Crepaldi, E.L., et al., *Controlled Formation of Highly Organized Mesoporous Titania Thin Films: From Mesostructured Hybrids to Mesoporous Nanoanatase TiO2.* Journal of the American Chemical Society, 2003. **125**(32): p. 9770-9786.

89. Kondo, J.N. and K. Domen, *Crystallization of Mesoporous Metal Oxides.* Chemistry of Materials, 2008. **20**(3): p. 835-847.

90. Puntes, V.F., K.M. Krishnan, and A.P. Alivisatos, *Colloidal Nanocrystal Shape and Size Control: The Case of Cobalt.* Science, 2001. **291**(5511): p. 2115-2117.

91. Park, J., et al., *Ultra-large-scale syntheses of monodisperse nanocrystals.* Nature Materials, 2004. **3**(12): p. 891-895.

92. Milliron, D.J., et al., *Colloidal nanocrystal heterostructures with linear and branched topology.* Nature, 2004. **430**(6996): p. 190-195.

93. Yin, Y. and A.P. Alivisatos, *Colloidal nanocrystal synthesis and the organic–inorganic interface.* Nature, 2005. **437**(7059): p. 664-670.

94. Jun, Y.-w., et al., *Recent advances in the shape control of inorganic nano-building blocks.* Coordination Chemistry Reviews, 2005. **249**(17): p. 1766-1775.

95. Jun, Y.-w., J.-s. Choi, and J. Cheon, *Shape Control of Semiconductor and Metal Oxide Nanocrystals through Nonhydrolytic Colloidal Routes.* Angewandte Chemie International Edition, 2006. **45**(21): p. 3414-3439.

96. Cozzoli, P.D., T. Pellegrino, and L. Manna, *Synthesis, properties and perspectives of hybrid nanocrystal structures.* Chemical Society Reviews, 2006. **35**(11): p. 1195-1208.

97. Buonsanti, R. and D.J. Milliron, *Chemistry of Doped Colloidal Nanocrystals.* Chemistry of Materials, 2013. **25**(8): p. 1305-1317.

98. Rao, C.N.R., P.J. Thomas, and G.U. Kulkarni, *Nanocrystals:: Synthesis, Properties and Applications*. 2007: Springer Berlin Heidelberg.

99. Rao, C.N.R., A. Müller, and A.K. Cheetham, *Nanomaterials Chemistry: Recent Developments and New Directions*. 2007: Wiley.

100. Schmid, G., *Nanoparticles: From Theory to Application*. 2011: Wiley.

101. Parak, W.J., et al., *Biological applications of colloidal nanocrystals.* Nanotechnology, 2003. **14**(7): p. R15-R27.

102. Osinski, M., T.M. Jovin, and K. Yamamoto, *Biomedical Applications of Colloidal Nanocrystals.* Journal of Biomedicine and Biotechnology, 2007. **2007**.

103. Zhu, J. and M. Zäch, *Nanostructured materials for photocatalytic hydrogen production.* Current Opinion in Colloid & Interface Science, 2009. **14**(4): p. 260-269.

104. Lohse, S.E. and C.J. Murphy, *Applications of Colloidal Inorganic Nanoparticles: From Medicine to Energy.* Journal of the American Chemical Society, 2012. **134**(38): p. 15607-15620.

105. Zhang, Q., et al., *Core–Shell Nanostructured Catalysts.* Accounts of Chemical Research, 2013. **46**(8): p. 1816-1824.

106. Liu, X. and M.T. Swihart, *Heavily-doped colloidal semiconductor and metal oxide nanocrystals: an emerging new class of plasmonic nanomaterials.* Chemical Society Reviews, 2014. **43**(11): p. 3908-3920.

107. Kovalenko, M.V., et al., *Prospects of Nanoscience with Nanocrystals.* ACS Nano, 2015. **9**(2): p. 1012-1057.

108. Sumanth Kumar, D., B. Jai Kumar, and H.M. Mahesh, *Chapter 3 - Quantum Nanostructures (QDs): An Overview*, in *Synthesis of Inorganic Nanomaterials*, S. Mohan Bhagyaraj, et al., Editors. 2018, Woodhead Publishing. p. 59-88.

109. Boles, M.A., et al., *The surface science of nanocrystals.* Nature Materials, 2016. **15**: p. 141.

110. Nie, Z., A. Petukhova, and E. Kumacheva, *Properties and emerging applications of self-assembled structures made from inorganic nanoparticles.* Nature Nanotechnology, 2009. **5**: p. 15.

111. Boles, M.A., M. Engel, and D.V. Talapin, *Self-Assembly of Colloidal Nanocrystals: From Intricate Structures to Functional Materials.* Chemical Reviews, 2016. **116**(18): p. 11220-11289.

112. Talapin, D.V., et al., *Prospects of Colloidal Nanocrystals for Electronic and Optoelectronic Applications.* Chemical Reviews, 2010. **110**(1): p. 389-458.

113. Ren, Z., et al., *Inorganic Ligand Thiosulfate-Capped Quantum Dots for Efficient Quantum Dot Sensitized Solar Cells.* ACS Applied Materials & Interfaces, 2017. **9**(22): p. 18936-18944.

114. Milliron, D.J., et al., *Constructing Functional Mesostructured Materials from Colloidal Nanocrystal Building Blocks.* Accounts of Chemical Research, 2014. **47**(1): p. 236-246.

115. Kovalenko, M.V., M. Scheele, and D.V. Talapin, *Colloidal Nanocrystals with Molecular Metal Chalcogenide Surface Ligands.* Science, 2009. **324**(5933): p. 1417-1420.

116. Lu, Z. and Y. Yin, *Colloidal nanoparticle clusters: functional materials by design.* Chemical Society Reviews, 2012. **41**(21): p. 6874-6887.

117. Kärger, J., D.M. Ruthven, and D.N. Theodorou, *Diffusion in Nanoporous Materials, 2 Volume Set*. 2012: Wiley.

118. Smarsly, B. and M. Antonietti, *Block Copolymer Assemblies as Templates for the Generation of Mesoporous Inorganic Materials and Crystalline Films.* European Journal of Inorganic Chemistry, 2006. **2006**(6): p. 1111-1119.

119. Bishop, K.J.M., et al., *Nanoscale Forces and Their Uses in Self-Assembly.* Small, 2009. **5**(14): p. 1600-1630.

120. Kao, J. and T. Xu, *Nanoparticle Assemblies in Supramolecular Nanocomposite Thin Films: Concentration Dependence.* Journal of the American Chemical Society, 2015. **137**(19): p. 6356-6365.

121. Williams, T.E., et al., *Nearest-neighbour nanocrystal bonding dictates framework stability or collapse in colloidal nanocrystal frameworks.* Chemical Communications, 2017. **53**(35): p. 4853-4856.

122. Yao, L., Y. Lin, and J.J. Watkins, *Ultrahigh Loading of Nanoparticles into Ordered Block Copolymer Composites.* Macromolecules, 2014. **47**(5): p. 1844-1849.

123. Song, D.-P., et al., *Controlled Supramolecular Self-Assembly of Large Nanoparticles in Amphiphilic Brush Block Copolymers.* Journal of the American Chemical Society, 2015. **137**(11): p. 3771-3774.

124. Lin, Y., et al., *Nanoparticle-Driven Assembly of Block Copolymers: A Simple Route to Ordered Hybrid Materials.* Journal of the American Chemical Society, 2011. **133**(17): p. 6513-6516.

125. Jang, S.G., E.J. Kramer, and C.J. Hawker, *Controlled Supramolecular Assembly of Micelle-Like Gold Nanoparticles in PS-b-P2VP Diblock Copolymers via Hydrogen Bonding.* Journal of the American Chemical Society, 2011. **133**(42): p. 16986-16996.

126. Jang, S.G., et al., *Morphology Evolution of PS-b-P2VP Diblock Copolymers via Supramolecular Assembly of Hydroxylated Gold Nanoparticles.* Macromolecules, 2012. **45**(3): p. 1553-1561.

127. Helms, B.A., et al., *Colloidal Nanocrystal Frameworks.* Advanced Materials, 2015. **27**(38): p. 5820-5829.

128. Warren, S.C., et al., *Ordered Mesoporous Materials from Metal Nanoparticle–Block Copolymer Self-Assembly.* Science, 2008. **320**(5884): p. 1748-1752.

129. Warren, S.C., F.J. DiSalvo, and U. Wiesner, *Nanoparticle-tuned assembly and disassembly of mesostructured silica hybrids.* Nature Materials, 2007. **6**: p. 156.

130. Velegraki, G., et al., *Mesoporous Copper Nanoparticle Networks Decorated by Graphite Layers for Surface-Enhanced Raman Scattering Detection of Trace Analytes.* ChemPlusChem, 2017. **82**(10): p. 1290-1297.

131. Corma, A., et al., *Hierarchically mesostructured doped CeO2 with potential for solar-cell use.* Nature Materials, 2004. **3**(6): p. 394-397.

132. Papadas, I.T., et al., *Templated assembly of BiFeO3 nanocrystals into 3D mesoporous networks for catalytic applications.* Nanoscale, 2015. **7**(13): p. 5737-5743.

133. Skliri, E., et al., *Assembly and photochemical properties of mesoporous networks of spinel ferrite nanoparticles for environmental photocatalytic remediation.* Applied Catalysis B: Environmental, 2018. **227**: p. 330-339.

134. Tamiolakis, I., et al., *One-pot synthesis of highly crystalline mesoporous TiO2 nanoparticle assemblies with enhanced photocatalytic activity.* Chemical Communications, 2012. **48**(53): p. 6687-6689.

135. Buonsanti, R., et al., *Assembly of Ligand-Stripped Nanocrystals into Precisely Controlled Mesoporous Architectures.* Nano Letters, 2012. **12**(7): p. 3872-3877.

136. Ong, G.K., et al., *Ordering in Polymer Micelle-Directed Assemblies of Colloidal Nanocrystals.* Nano Letters, 2015. **15**(12): p. 8240-8244.

137. Dong, A., et al., *A Generalized Ligand-Exchange Strategy Enabling Sequential Surface Functionalization of Colloidal Nanocrystals.* Journal of the American Chemical Society, 2011. **133**(4): p. 998-1006.

138. Rosen, E.L., et al., *Exceptionally Mild Reactive Stripping of Native Ligands from Nanocrystal Surfaces by Using Meerwein's Salt.* Angewandte Chemie International Edition, 2012. **51**(3): p. 684-689.

139. Rauda, I.E., et al., *General Method for the Synthesis of Hierarchical Nanocrystal-Based Mesoporous Materials.* ACS Nano, 2012. **6**(7): p. 6386-6399.

140. Papadas, I.T., et al., *Controllable Synthesis of Mesoporous Iron Oxide Nanoparticle Assemblies for Chemoselective Catalytic Reduction of Nitroarenes.* Chemistry – A European Journal, 2016. **22**(13): p. 4600-4607.

141. Skliri, E., et al., *Mesoporous Assembled Mn3O4 Nanoparticle Networks as Efficient Catalysts for Selective Oxidation of Alkenes and Aryl Alkanes.* ChemPlusChem, 2017. **82**(1): p. 136-143.

142. Velegraki, G., et al., *Fabrication of 3D mesoporous networks of assembled CoO nanoparticles for efficient photocatalytic reduction of aqueous Cr(VI).* Applied Catalysis B: Environmental, 2018. **221**: p. 635-644.

143. Velegraki, G., et al., *Boosting photochemical activity by Ni doping of mesoporous CoO nanoparticle assemblies.* Inorganic Chemistry Frontiers, 2019. **6**(3): p. 765-774.

144. Georgiou, Y., et al., *Mesoporous spinel CoFe2O4 as an efficient adsorbent for arsenite removal from water: high efficiency via control of the particle assemblage configuration.* Environmental Science: Nano, 2019. **6**(4): p. 1156-1167.

145. Talapin, D.V. and C.B. Murray, *PbSe Nanocrystal Solids for n- and p-Channel Thin Film Field-Effect Transistors.* Science, 2005. **310**(5745): p. 86-89.

146. Gur, I., et al., *Air-Stable All-Inorganic Nanocrystal Solar Cells Processed from Solution.* Science, 2005. **310**(5747): p. 462-465.

147. Wu, Y., et al., *Synthesis and Photovoltaic Application of Copper(I) Sulfide Nanocrystals.* Nano Letters, 2008. **8**(8): p. 2551-2555.

148. Xu, J., et al., *Large-Scale Synthesis of Long Crystalline Cu2-xSe Nanowire Bundles by Water-Evaporation-Induced Self-Assembly and Their Application in Gas Sensing.* Advanced Functional Materials, 2009. **19**(11): p. 1759-1766.

149. Dayal, S., et al., *Photovoltaic Devices with a Low Band Gap Polymer and CdSe Nanostructures Exceeding 3% Efficiency.* Nano Letters, 2010. **10**(1): p. 239-242.

150. Choi, J.J., et al., *Solution-Processed Nanocrystal Quantum Dot Tandem Solar Cells.* Advanced Materials, 2011. **23**(28): p. 3144-3148.

151. Qurashi, A., *Metal Chalcogenide Nanostructures for Renewable Energy Applications*. 2014: Wiley.

152. Kershaw, S.V., et al., *Materials aspects of semiconductor nanocrystals for optoelectronic applications.* Materials Horizons, 2017. **4**(2): p. 155-205.

153. Lai, C.-H., et al., *Direct growth of high-rate capability and high capacity copper sulfide nanowire array cathodes for lithium-ion batteries.* Journal of Materials Chemistry, 2010. **20**(32): p. 6638-6645.

154. Kibsgaard, J., et al., *Engineering the surface structure of MoS2 to preferentially expose active edge sites for electrocatalysis.* Nature Materials, 2012. **11**: p. 963.

155. Wilker, M.B., K.J. Schnitzenbaumer, and G. Dukovic, *Recent Progress in Photocatalysis Mediated by Colloidal II-VI Nanocrystals.* Israel Journal of Chemistry, 2012. **52**(11-12): p. 1002-1015.

156. Gadiyar, C., A. Loiudice, and R. Buonsanti, *Colloidal nanocrystals for photoelectrochemical and photocatalytic water splitting.* Journal of Physics D: Applied Physics, 2017. **50**(7): p. 074006.

157. Murray, C.B., D.J. Norris, and M.G. Bawendi, *Synthesis and characterization of nearly monodisperse CdE (E = sulfur, selenium, tellurium) semiconductor nanocrystallites.* Journal of the American Chemical Society, 1993. **115**(19): p. 8706-8715.

158. Hines, M.A. and P. Guyot-Sionnest, *Synthesis and Characterization of Strongly Luminescing ZnS-Capped CdSe Nanocrystals.* The Journal of Physical Chemistry, 1996. **100**(2): p. 468-471.

159. Peng, X., et al., *Epitaxial Growth of Highly Luminescent CdSe/CdS Core/Shell Nanocrystals with Photostability and Electronic Accessibility.* Journal of the American Chemical Society, 1997. **119**(30): p. 7019-7029.

160. Peng, X., et al., *Shape control of CdSe nanocrystals.* Nature, 2000. **404**(6773): p. 59-61.

161. Manna, L., E. C. Scher, and A. Paul Alivisatos, *Synthesis of Soluble and Processable Rod-, Arrow-, Teardrop-, and Tetrapod-Shaped CdSe Nanocrystals*. Vol. 122. 2000. 12700-12706.

162. Qi, L., H. Cölfen, and M. Antonietti, *Synthesis and Characterization of CdS Nanoparticles Stabilized by Double-Hydrophilic Block Copolymers.* Nano Letters, 2001. **1**(2): p. 61-65.

163. Li, L.-s., et al., *Band Gap Variation of Size- and Shape-Controlled Colloidal CdSe Quantum Rods.* Nano Letters, 2001. **1**(7): p. 349-351.

164. Yu, W.W. and X. Peng, *Formation of High-Quality CdS and Other II–VI Semiconductor Nanocrystals in Noncoordinating Solvents: Tunable Reactivity of Monomers.* Angewandte Chemie International Edition, 2002. **41**(13): p. 2368-2371.

165. Manna, L., et al., *Controlled growth of tetrapod-branched inorganic nanocrystals.* Nature Materials, 2003. **2**(6): p. 382-385.

166. Zhang, H., et al., *A Generic Method for Rational Scalable Synthesis of Monodisperse Metal Sulfide Nanocrystals.* Nano Letters, 2012. **12**(11): p. 5856-5860.

167. Murray, C.B., C.R. Kagan, and M.G. Bawendi, *Self-Organization of CdSe Nanocrystallites into Three-Dimensional Quantum Dot Superlattices.* Science, 1995. **270**(5240): p. 1335-1338.

168. Shevchenko, E.V., et al., *Structural diversity in binary nanoparticle superlattices.* Nature, 2006. **439**(7072): p. 55-59.

169. Shevchenko, E.V., et al., *Structural Characterization of Self-Assembled Multifunctional Binary Nanoparticle Superlattices.* Journal of the American Chemical Society, 2006. **128**(11): p. 3620-3637.

170. Luther, J.M., et al., *Structural, Optical, and Electrical Properties of Self-Assembled Films of PbSe Nanocrystals Treated with 1,2-Ethanedithiol.* ACS Nano, 2008. **2**(2): p. 271-280.

171. Law, M., et al., *Structural, Optical, and Electrical Properties of PbSe Nanocrystal Solids Treated Thermally or with Simple Amines.* Journal of the American Chemical Society, 2008. **130**(18): p. 5974-5985.

172. Zarghami, M.H., et al., *p-Type PbSe and PbS Quantum Dot Solids Prepared with Short-Chain Acids and Diacids.* ACS Nano, 2010. **4**(4): p. 2475-2485.

173. Tangirala, R., et al., *Modular Inorganic Nanocomposites by Conversion of Nanocrystal Superlattices.* Angewandte Chemie International Edition, 2010. **49**(16): p. 2878-2882.

174. Wang, R.Y., et al., *Ionic and Electronic Transport in Ag2S Nanocrystal–GeS2 Matrix Composites with Size-Controlled Ag2S Nanocrystals.* Advanced Materials, 2012. **24**(1): p. 99-103.

175. Jiang, C., J.-S. Lee, and D.V. Talapin, *Soluble Precursors for CuInSe2, CuIn1–xGaxSe2, and Cu2ZnSn(S,Se)4 Based on Colloidal Nanocrystals and Molecular Metal Chalcogenide Surface Ligands.* Journal of the American Chemical Society, 2012. **134**(11): p. 5010-5013.

176. van Westen, T. and R.D. Groot, *Effect of Temperature Cycling on Ostwald Ripening.* Crystal Growth & Design, 2018. **18**(9): p. 4952-4962.

177. Gommes, C.J., *Ostwald ripening of confined nanoparticles: chemomechanical coupling in nanopores.* Nanoscale, 2019. **11**(15): p. 7386-7393.

178. Yao, Q. and S.L. Brock, *Porous CdTe Nanocrystal Assemblies: Ligation Effects on the Gelation Process and the Properties of Resultant Aerogels.* Inorganic Chemistry, 2011. **50**(20): p. 9985-9992.

179. Yao, Q., I.U. Arachchige, and S.L. Brock, *Expanding the Repertoire of Chalcogenide Nanocrystal Networks: Ag2Se Gels and Aerogels by Cation Exchange Reactions.* Journal of the American Chemical Society, 2009. **131**(8): p. 2800-2801.

180. Nahar, L. and I.U. Arachchige, *Sol-Gel Methods for the Assembly of Metal and Semiconductor Nanoparticles*. Vol. 1. 2013. 1004.

181. Mohanan, J.L. and S.L. Brock, *A new addition to the aerogel community: unsupported CdS aerogels with tunable optical properties.* Journal of Non-Crystalline Solids, 2004. **350**: p. 1-8.

182. Mohanan, J.L., I.U. Arachchige, and S.L. Brock, *Porous Semiconductor Chalcogenide Aerogels.* Science, 2005. **307**(5708): p. 397-400.

183. Gaponik, N., et al., *Three-Dimensional Self-Assembly of Thiol-Capped CdTe Nanocrystals: Gels and Aerogels as Building Blocks for Nanotechnology.* Advanced Materials, 2008. **20**(22): p. 4257-4262.

184. Brock, S.L., I.U. Arachchige, and K.K. Kalebaila, *METAL CHALCOGENIDE GELS, XEROGELS AND AEROGELS.* Comments on Inorganic Chemistry, 2006. **27**(5-6): p. 103-126.

185. Arachchige, I.U. and S.L. Brock, *Sol–Gel Methods for the Assembly of Metal Chalcogenide Quantum Dots.* Accounts of Chemical Research, 2007. **40**(9): p. 801-809.

186. Arachchige, I.U. and S.L. Brock, *Highly Luminescent Quantum-Dot Monoliths.* Journal of the American Chemical Society, 2007. **129**(7): p. 1840-1841.

187. Arachchige, I.U. and S.L. Brock, *Sol−Gel Assembly of CdSe Nanoparticles to Form Porous Aerogel Networks.* Journal of the American Chemical Society, 2006. **128**(24): p. 7964-7971.

188. Rauda, I.E., et al., *Nanoporous Semiconductors Synthesized Through Polymer Templating of Ligand-Stripped CdSe Nanocrystals.* Advanced Materials, 2013. **25**(9): p. 1315-1322.

189. Ondry, J.C., et al., *A Room-Temperature, Solution Phase Method for the Synthesis of Mesoporous Metal Chalcogenide Nanocrystal-Based Thin Films with Precisely Controlled Grain Sizes.* Chemistry of Materials, 2016. **28**(17): p. 6105-6117.

190. Suni, T., et al., *The significance of land-atmosphere interactions in the Earth system—iLEAPS achievements and perspectives.* Anthropocene, 2015. **12**: p. 69-84.

191. Waters, C.N., et al., *The Anthropocene is functionally and stratigraphically distinct from the Holocene.* Science, 2016. **351**(6269).

192. Hartmann, T., *The last hours of ancient sunlight : the fate of the world and what we can do before it's too late*. 2004: Revised and updated. New York : Three Rivers Press, [2004] ©2004.

193. Goklany, Indur M., Humanity Unbound: How Fossil Fuels Saved Humanity from Nature and Nature from Humanity (December 19, 2012). Policy Analysis, No. 715, Cato Institute, Washington, DC. Available at SSRN: https://ssrn.com/abstract=2194659

194. United Nations, Department of Economic and Social Affairs, Population Division (2017). World Population Prospects: The 2017 Revision, Key Findings and Advance Tables. Working Paper No. ESA/P/WP/248.

195. Armaroli, N. and V. Balzani, *The Future of Energy Supply: Challenges and Opportunities.* Angewandte Chemie International Edition, 2007. **46**(1-2): p. 52-66.

196. International Energy Agency (IEA) - Key World Energy Statistics - 2017, https://www.iea.org/publications/freepublications/publication/KeyWorld2017.pdf

197. Lewis, N.S. and D.G. Nocera, *Powering the planet: Chemical challenges in solar energy utilization.* Proceedings of the National Academy of Sciences, 2006. **103**(43): p. 15729-15735.

198. International Energy Agency (IEA) - Global energy and CO2 status report - 2017, https://www.iea.org/geco/

199. Höök, M. and X. Tang, *Depletion of fossil fuels and anthropogenic climate change—A review.* Energy Policy, 2013. **52**: p. 797-809.

200. Davis, S.J., K. Caldeira, and H.D. Matthews, *Future CO₂ Emissions and Climate Change from Existing Energy Infrastructure.* Science, 2010. **329**(5997): p. 1330-1333.

201. Kampa, M. and E. Castanas, *Human health effects of air pollution.* Environmental Pollution, 2008. **151**(2): p. 362-367.

202. Jain, P.C., *Greenhouse effect and climate change: scientific basis and overview.* Renewable Energy, 1993. **3**(4): p. 403-420.

203. Thornes, J.E., *IPCC, 2001: Climate change 2001: impacts, adaptation and vulnerability, Contribution of Working Group II to the Third Assessment Report of the Intergovernmental Panel on Climate Change, edited by J. J. McCarthy, O. F. Canziani, N. A. Leary, D. J. Dokken and K. S. White (eds). Cambridge University Press, Cambridge, UK, and New York, USA, 2001. No. of pages: 1032. Price: £34.95, ISBN 0-521-01500-6 (paperback), ISBN 0-521-80768-9 (hardback).* International Journal of Climatology, 2002. **22**(10): p. 1285-1286.

204. Conte, M., et al., *Hydrogen economy for a sustainable development: state-of-the-art and technological perspectives.* Journal of Power Sources, 2001. **100**(1): p. 171-187.

205. Armaroli, N. and V. Balzani, *The Future of Energy Supply: Challenges and Opportunities.* Angewandte Chemie International Edition, 2006. **46**(1-2): p. 52-66.

206. Brundtland, G., et al., *Our Common Future ('Brundtland report')*. 1987: Oxford University Press, USA.

207. Omer, A.M., *Energy use and environmental impacts: A general review.* Journal of Renewable and Sustainable Energy, 2009. **1**(5): p. 053101.

208. Dincer, I. and C. Acar, *A review on clean energy solutions for better sustainability.* International Journal of Energy Research, 2015. **39**(5): p. 585-606.

209. Hoffmann, P., *Tomorrow's Energy: Hydrogen, Fuel Cells, and the Prospects for a Cleaner Planet*. 2002: MIT Press.

210. Dimitriou, P. and T. Tsujimura, *A review of hydrogen as a compression ignition engine fuel.* International Journal of Hydrogen Energy, 2017. **42**(38): p. 24470-24486.

211. Stambouli, A.B. and E. Traversa, *Solid oxide fuel cells (SOFCs): a review of an environmentally clean and efficient source of energy.* Renewable and Sustainable Energy Reviews, 2002. **6**(5): p. 433-455.

212. Preuster, P., A. Alekseev, and P. Wasserscheid, *Hydrogen Storage Technologies for Future Energy Systems.* Annual Review of Chemical and Biomolecular Engineering, 2017. **8**(1): p. 445-471.

213. Navlani-García, M., et al., *Recent strategies targeting efficient hydrogen production from chemical hydrogen storage materials over carbon-supported catalysts.* NPG Asia Materials, 2018. **10**(4): p. 277-292.

214. Cavendish, H., *XIX. Three papers, containing experiments on factitious air.* Philosophical Transactions, 1766. **56**: p. 141-184.

215. Haldane, J.B.S., *Daedalus : or, Science and the future. A paper read to the Heretics, Cambridge, on February 4th, 1923 / by J.B.S. Haldane*. 1924, London: Kegan Paul.

216. O'M. Bockris, J., *Energy: The Solar Hydrogen Alternative*. Vol. 123. 1975.

217. Hefner, R.A., *Toward sustainable economic growth: The age of energy gases.* International Journal of Hydrogen Energy, 1995. **20**(12): p. 945-948.

218. Dunn, S., *Hydrogen futures: toward a sustainable energy system.* International Journal of Hydrogen Energy, 2002. **27**(3): p. 235-264.

219. Mahmah, B., et al., *MedHySol: Future federator project of massive production of solar hydrogen.* International Journal of Hydrogen Energy, 2009. **34**(11): p. 4922-4933.

220. Momirlan, M. and T.N. Veziroglu, *The properties of hydrogen as fuel tomorrow in sustainable energy system for a cleaner planet.* International Journal of Hydrogen Energy, 2005. **30**(7): p. 795-802.

221. Kalamaras, C.M. and A.M. Efstathiou, *Hydrogen Production Technologies: Current State and Future Developments.* Conference Papers in Energy, 2013. **2013**: p. 9.

222. Dincer, I. and C. Acar, *Review and evaluation of hydrogen production methods for better sustainability.* International Journal of Hydrogen Energy, 2015. **40**(34): p. 11094-11111.

223. Ewan, B.C.R. and R.W.K. Allen, *A figure of merit assessment of the routes to hydrogen.* International Journal of Hydrogen Energy, 2005. **30**(8): p. 809-819.

224. da Silva Veras, T., et al., *Hydrogen: Trends, production and characterization of the main process worldwide.* International Journal of Hydrogen Energy, 2017. **42**(4): p. 2018-2033.

225. Zakkour, P. and G. Cook, *CCS Roadmap for Industry: High-purity CO2 sources Sectoral Assessment – Final Report*. 2010.

226. Woodward, J., et al., *Enzymatic Hydrogen Production: Conversion of Renewable Resources for Energy Production.* Energy & Fuels, 2000. **14**(1): p. 197-201.

227. Woodward, J., et al., *Enzymatic production of biohydrogen.* Nature, 2000. **405**: p. 1014.

228. E. Funk, J., *Thermochemical hydrogen production: past and present.* International Journal of Hydrogen Energy, 2001. **26**(3): p. 185-190.

229. Badwal, S.P.S., et al., *Emerging electrochemical energy conversion and storage technologies.* Frontiers in Chemistry, 2014. **2**(79).

230. Badwal, S.P.S., S. Giddey, and C. Munnings, *Hydrogen production via solid electrolytic routes.* Wiley Interdisciplinary Reviews: Energy and Environment, 2013. **2**(5): p. 473-487.

231. Akkerman, I., et al., *Photobiological hydrogen production: photochemical efficiency and bioreactor design.* International Journal of Hydrogen Energy, 2002. **27**(11): p. 1195-1208.

232. Yuan, Y.-P., et al., *Hetero-nanostructured suspended photocatalysts for solar-to-fuel conversion.* Energy & Environmental Science, 2014. **7**(12): p. 3934-3951.

233. Roger, I., M.A. Shipman, and M.D. Symes, *Earth-abundant catalysts for electrochemical and photoelectrochemical water splitting.* Nature Reviews Chemistry, 2017. **1**: p. 0003.

234. Hisatomi, T. and K. Domen, *Introductory lecture: sunlight-driven water splitting and carbon dioxide reduction by heterogeneous semiconductor systems as key processes in artificial photosynthesis.* Faraday Discussions, 2017. **198**(0): p. 11-35.

235. Bard, A.J. and M.A. Fox, *Artificial Photosynthesis: Solar Splitting of Water to Hydrogen and Oxygen.* Accounts of Chemical Research, 1995. **28**(3): p. 141-145.

236. Kondarides, D.I., et al., *Hydrogen Production by Photo-Induced Reforming of Biomass Components and Derivatives at Ambient Conditions.* Catalysis Letters, 2008. **122**(1): p. 26-32.

237. Kudo, A. and Y. Miseki, *Heterogeneous photocatalyst materials for water splitting.* Chemical Society Reviews, 2009. **38**(1): p. 253-278.

238. Fujishima, A. and K. Honda, *Electrochemical Photolysis of Water at a Semiconductor Electrode.* Nature, 1972. **238**(5358): p. 37-38.

239. Tachibana, Y., L. Vayssieres, and J.R. Durrant, *Artificial photosynthesis for solar water-splitting.* Nature Photonics, 2012. **6**: p. 511.

240. Walter, M.G., et al., *Solar Water Splitting Cells.* Chemical Reviews, 2010. **110**(11): p. 6446-6473.

241. Abdi, F.F., et al., *Efficient solar water splitting by enhanced charge separation in a bismuth vanadate-silicon tandem photoelectrode.* Nature Communications, 2013. **4**: p. 2195.

242. Ager, J.W., et al., *Experimental demonstrations of spontaneous, solar-driven photoelectrochemical water splitting.* Energy & Environmental Science, 2015. **8**(10): p. 2811-2824.

243. Yao, T., et al., *Photoelectrocatalytic Materials for Solar Water Splitting.* Advanced Energy Materials, 2018. **8**(21): p. 1800210.

244. Wrighton, M.S., P.T. Wolczanski, and A.B. Ellis, *Photoelectrolysis of water by irradiation of platinized n-type semiconducting metal oxides.* Journal of Solid State Chemistry, 1977. **22**(1): p. 17-29.

245. Nozik, A.J., *Photoelectrochemistry: Applications to Solar Energy Conversion.* Annual Review of Physical Chemistry, 1978. **29**(1): p. 189-222.

246. Bard, A.J., *Photoelectrochemistry and heterogeneous photo-catalysis at semiconductors.* Journal of Photochemistry, 1979. **10**(1): p. 59-75.

247. Bard, A.J., *Photoelectrochemistry.* Science, 1980. **207**(4427): p. 139.

248. Bard, A.J., *Design of semiconductor photoelectrochemical systems for solar energy conversion.* The Journal of Physical Chemistry, 1982. **86**(2): p. 172-177.

249. Osterloh, F.E., *Photocatalysis versus Photosynthesis: A Sensitivity Analysis of Devices for Solar Energy Conversion and Chemical Transformations.* ACS Energy Letters, 2017. **2**(2): p. 445-453.

250. Liao, C.-H., C.-W. Huang, and J.C.S. Wu, *Hydrogen Production from Semiconductor-based Photocatalysis via Water Splitting.* Catalysts, 2012. **2**(4): p. 490-516.

251. Takanabe, K. and K. Domen, *Photocatalysis in Generation of Hydrogen from Water*, in *Heterogeneous Catalysis at Nanoscale for Energy Applications*, F.F. Tao, W.F. Schneider, and P.V. Kamat, Editors. 2015, John Wiley & Sons, Ltd. p. 239-270.

252. James, B.D., et al., *Technoeconomic Analysis of Photoelectrochemical (PEC) Hydrogen Production.* 2009.

253. Pinaud, B.A., et al., *Technical and economic feasibility of centralized facilities for solar hydrogen production via photocatalysis and photoelectrochemistry.* Energy & Environmental Science, 2013. **6**(7): p. 1983-2002.

254. Chen, S., T. Takata, and K. Domen, *Particulate photocatalysts for overall water splitting.* Nature Reviews Materials, 2017. **2**: p. 17050.

255. Callister, W.D. and D.G. Rethwisch, *Materials Science and Engineering: An Introduction, 9th Edition: Ninth Edition*. 2013: John Wiley and Sons, Incorporated.

256. Hoffmann, M.R., et al., *Environmental Applications of Semiconductor Photocatalysis.* Chemical Reviews, 1995. **95**(1): p. 69-96.

257. Mills, A. and S. Le Hunte, *An overview of semiconductor photocatalysis.* Journal of Photochemistry and Photobiology A: Chemistry, 1997. **108**(1): p. 1-35.

258. Kittel, C., *Introduction to solid state physics*. 2005, Hoboken, NJ: Wiley.

259. Hernández-Ramírez, A. and I. Medina-Ramírez, *Semiconducting Materials*, in *Photocatalytic Semiconductors: Synthesis, Characterization, and Environmental Applications*, A. Hernández-Ramírez and I. Medina-Ramírez, Editors. 2015, Springer International Publishing: Cham. p. 1-40.

260. Yang, X. and D. Wang, *Chapter Two - Photophysics and Photochemistry at the Semiconductor/Electrolyte Interface for Solar Water Splitting*, in *Semiconductors and Semimetals*, Z. Mi, L. Wang, and C. Jagadish, Editors. 2017, Elsevier. p. 47-80.

261. Kahn, A., *Fermi level, work function and vacuum level.* Materials Horizons, 2016. **3**(1): p. 7-10.

262. Linsebigler, A.L., G. Lu, and J.T. Yates, *Photocatalysis on TiO2 Surfaces: Principles, Mechanisms, and Selected Results.* Chemical Reviews, 1995. **95**(3): p. 735-758.

263. Zhang, Z. and J.T. Yates, *Band Bending in Semiconductors: Chemical and Physical Consequences at Surfaces and Interfaces.* Chemical Reviews, 2012. **112**(10): p. 5520-5551.

264. Zhang, X.G., *Basic Theories of Semiconductor Electrochemistry*, in *Electrochemistry of Silicon and Its Oxide*. 2001, Springer US: Boston, MA. p. 1-43.

265. Carmichael, P; (2016) Materials and Devices for Photoelectrochemical and Photocatalytic Water Splitting. Doctoral thesis , UCL (University College London).

266. van de Krol, R., *Principles of Photoelectrochemical Cells*, in *Photoelectrochemical Hydrogen Production*, R. van de Krol and M. Grätzel, Editors. 2012, Springer US: Boston, MA. p. 13-67.

267. Bustos, E., et al., *Electrochemical Characterization of Photocatalytic Materials*, in *Photocatalytic Semiconductors: Synthesis, Characterization, and Environmental Applications*, A. Hernández-Ramírez and I. Medina-Ramírez, Editors. 2015, Springer International Publishing: Cham. p. 155-185.

268. Hagfeldt, A. and M. Graetzel, *Light-Induced Redox Reactions in Nanocrystalline Systems.* Chemical Reviews, 1995. **95**(1): p. 49-68.

269. Bard, A.J., et al., *The concept of Fermi level pinning at semiconductor/liquid junctions. Consequences for energy conversion efficiency and selection of useful solution redox couples in solar devices.* Journal of the American Chemical Society, 1980. **102**(11): p. 3671-3677.

270. Sato, N., *CHAPTER 5 - ELECTRIC DOUBLE LAYER AT ELECTRODE INTERFACES*, in *Electrochemistry at Metal and Semiconductor Electrodes*, N. Sato, Editor. 1998, Elsevier Science: Amsterdam. p. 119-199.

271. Ge, H., et al., *Influence of Surface States on the Evaluation of the Flat Band Potential of TiO2.* ACS Applied Materials & Interfaces, 2014. **6**(4): p. 2401-2406.

272. Guijarro, N., M.S. Prévot, and K. Sivula, *Surface modification of semiconductor photoelectrodes.* Physical Chemistry Chemical Physics, 2015. **17**(24): p. 15655-15674.

273. Wood, A., M. Giersig, and P. Mulvaney, *Fermi Level Equilibration in Quantum Dot−Metal Nanojunctions.* The Journal of Physical Chemistry B, 2001. **105**(37): p. 8810-8815.

274. Jakob, M., H. Levanon, and P.V. Kamat, *Charge Distribution between UV-Irradiated TiO2 and Gold Nanoparticles: Determination of Shift in the Fermi Level.* Nano Letters, 2003. **3**(3): p. 353-358.

275. Subramanian, V., E.E. Wolf, and P.V. Kamat, *Catalysis with TiO2/Gold Nanocomposites. Effect of Metal Particle Size on the Fermi Level Equilibration.* Journal of the American Chemical Society, 2004. **126**(15): p. 4943-4950.

276. Zhang, L. and M. Jaroniec, *Toward designing semiconductor-semiconductor heterojunctions for photocatalytic applications.* Applied Surface Science, 2018. **430**: p. 2-17.

277. Li, J. and N. Wu, *Semiconductor-based photocatalysts and photoelectrochemical cells for solar fuel generation: a review.* Catalysis Science & Technology, 2015. **5**(3): p. 1360-1384.

278. Fujishima, A., X. Zhang, and D.A. Tryk, *TiO2 photocatalysis and related surface phenomena.* Surface Science Reports, 2008. **63**(12): p. 515-582.

279. Emeline, A.V., et al., *Chapter 1 - Heterogeneous Photocatalysis: Basic Approaches and Terminology*, in *New and Future Developments in Catalysis*, S.L. Suib, Editor. 2013, Elsevier: Amsterdam. p. 1-47.

280. Kisch, H., *Semiconductor Photocatalysis—Mechanistic and Synthetic Aspects.* Angewandte Chemie International Edition, 2013. **52**(3): p. 812-847.

281. Blake, *Bibliography of Work on Photocatalytic Removal of Hazardous Compounds from Water and Air*. 1994.

282. Ravelli, D., et al., *Photocatalysis. A multi-faceted concept for green chemistry.* Chemical Society Reviews, 2009. **38**(7): p. 1999-2011.

283. Michelin, C. and N. Hoffmann, *Photocatalysis applied to organic synthesis – A green chemistry approach.* Current Opinion in Green and Sustainable Chemistry, 2018. **10**: p. 40-45.

284. Kou, J., et al., *Selectivity Enhancement in Heterogeneous Photocatalytic Transformations.* Chemical Reviews, 2017. **117**(3): p. 1445-1514.

285. Herrmann, J.M., et al., *Environmental green chemistry as defined by photocatalysis.* Journal of Hazardous Materials, 2007. **146**(3): p. 624-629.

286. Herrmann, J.-M., *Heterogeneous photocatalysis: fundamentals and applications to the removal of various types of aqueous pollutants.* Catalysis Today, 1999. **53**(1): p. 115-129.

287. Fox, M.A. and M.T. Dulay, *Heterogeneous photocatalysis.* Chemical Reviews, 1993. **93**(1): p. 341-357.

288. Cherevatskaya, M. and B. König, *Heterogeneous photocatalysts in organic synthesis.* Russian Chemical Reviews, 2014. **83**(3): p. 183-195.

289. Dincer, I. and C. Zamfirescu, *Chapter 5 - Hydrogen Production by Photonic Energy*, in *Sustainable Hydrogen Production*, I. Dincer and C. Zamfirescu, Editors. 2016, Elsevier. p. 309-391.

290. Bolts, J.M. and M.S. Wrighton, *Correlation of photocurrent-voltage curves with flat-band potential for stable photoelectrodes for the photoelectrolysis of water.* The Journal of Physical Chemistry, 1976. **80**(24): p. 2641-2645.

291. Morrison, S.R., *Electrochemistry at Semiconductor and Oxidized Metal Electrodes*. 2011: Springer US.

292. Li, X., et al., *Engineering heterogeneous semiconductors for solar water splitting.* Journal of Materials Chemistry A, 2015. **3**(6): p. 2485-2534.

293. Tang, J., J.R. Durrant, and D.R. Klug, *Mechanism of Photocatalytic Water Splitting in TiO2. Reaction of Water with Photoholes, Importance of Charge Carrier Dynamics, and Evidence for Four-Hole Chemistry.* Journal of the American Chemical Society, 2008. **130**(42): p. 13885-13891.

294. Marschall, R., *Semiconductor Composites: Strategies for Enhancing Charge Carrier Separation to Improve Photocatalytic Activity.* Advanced Functional Materials, 2014. **24**(17): p. 2421-2440.

295. Reza Gholipour, M., et al., *Nanocomposite heterojunctions as sunlight-driven photocatalysts for hydrogen production from water splitting.* Nanoscale, 2015. **7**(18): p. 8187-8208.

296. Osterloh, F.E., *Inorganic nanostructures for photoelectrochemical and photocatalytic water splitting.* Chemical Society Reviews, 2013. **42**(6): p. 2294-2320.

297. Li, L., P.A. Salvador, and G.S. Rohrer, *Photocatalysts with internal electric fields.* Nanoscale, 2014. **6**(1): p. 24-42.

298. Beydoun, D., et al., *Role of Nanoparticles in Photocatalysis.* Journal of Nanoparticle Research, 1999. **1**(4): p. 439-458.

299. Albery, W.J. and P.N. Bartlett, *The Transport and Kinetics of Photogenerated Carriers in Colloidal Semiconductor Electrode Particles.* Journal of The Electrochemical Society, 1984. **131**(2): p. 315-325.

300. Wang, Y. and N. Herron, *Nanometer-sized semiconductor clusters: materials synthesis, quantum size effects, and photophysical properties.* The Journal of Physical Chemistry, 1991. **95**(2): p. 525-532.

301. Holmes, M.A., T.K. Townsend, and F.E. Osterloh, *Quantum confinement controlled photocatalytic water splitting by suspended CdSe nanocrystals.* Chemical Communications, 2012. **48**(3): p. 371-373.

302. Zhang, Z., et al., *Role of Particle Size in Nanocrystalline TiO2-Based Photocatalyst.* Journal of Physical Chemistry B - J PHYS CHEM B, 1998. **102**: p. 10871-10878.

303. Serpone, N., D. Lawless, and R. Khairutdinov, *Size Effects on the Photophysical Properties of Colloidal Anatase TiO2 Particles: Size Quantization versus Direct Transitions in This Indirect Semiconductor?* The Journal of Physical Chemistry, 1995. **99**(45): p. 16646-16654.

304. Maeda, K. and K. Domen, *New Non-Oxide Photocatalysts Designed for Overall Water Splitting under Visible Light.* The Journal of Physical Chemistry C, 2007. **111**(22): p. 7851-7861.

305. Chen, X., et al., *Semiconductor-based Photocatalytic Hydrogen Generation.* Chemical Reviews, 2010. **110**(11): p. 6503-6570.

306. Yuan, L., et al., *Photocatalytic water splitting for solar hydrogen generation: fundamentals and recent advancements.* International Reviews in Physical Chemistry, 2016. **35**(1): p. 1-36.

307. Tee, S.Y., et al., *Recent Progress in Energy-Driven Water Splitting.* Advanced Science, 2017. **4**(5): p. 1600337.

308. Ran, J., et al., *Earth-abundant cocatalysts for semiconductor-based photocatalytic water splitting.* Chemical Society Reviews, 2014. **43**(22): p. 7787-7812.

309. Christoforidis, K.C. and P. Fornasiero, *Photocatalytic Hydrogen Production: A Rift into the Future Energy Supply.* ChemCatChem, 2017. **9**(9): p. 1523-1544.

310. Schneider, J. and D.W. Bahnemann, *Undesired Role of Sacrificial Reagents in Photocatalysis.* The Journal of Physical Chemistry Letters, 2013. **4**(20): p. 3479-3483.

311. Wagner, F.T. and G.A. Somorjai, *Photocatalytic and photoelectrochemical hydrogen production on strontium titanate single crystals.* Journal of the American Chemical Society, 1980. **102**(17): p. 5494-5502.

312. Kawai, T. and T. Sakata, *Photocatalytic decomposition of gaseous water over TiO2 and TiO2—RuO2 surfaces.* Chemical Physics Letters, 1980. **72**(1): p. 87-89.

313. Domen, K., et al., *Photocatalytic decomposition of water vapour on an NiO–SrTiO3 catalyst.* Journal of the Chemical Society, Chemical Communications, 1980(12): p. 543-544.

314. Domen, K., et al., *Photocatalytic decomposition of liquid water on a NiO・SrTiO3 catalyst.* Chemical Physics Letters, 1982. **92**(4): p. 433-434.

315. Moriya, Y., T. Takata, and K. Domen, *Recent progress in the development of (oxy)nitride photocatalysts for water splitting under visible-light irradiation.* Coordination Chemistry Reviews, 2013. **257**(13): p. 1957-1969.

316. Kudo, A., *Photocatalyst Materials for Water Splitting.* Catalysis Surveys from Asia, 2003. **7**(1): p. 31-38.

317. Sayama, K. and H. Arakawa, *Photocatalytic decomposition of water and photocatalytic reduction of carbon dioxide over zirconia catalyst.* The Journal of Physical Chemistry, 1993. **97**(3): p. 531-533.

318. Ikeda, S., et al., *Preparation of a high active photocatalyst, K2La2Ti3O10, by polymerized complex method and its photocatalytic activity of water splitting.* Journal of Materials Research, 1998. **13**(4): p. 852-855.

319. Kato, H. and A. Kudo, *New tantalate photocatalysts for water decomposition into H2 and O2.* Chemical Physics Letters, 1998. **295**(5): p. 487-492.

320. G. Kim, H., et al., *Highly donor-doped (110) layered perovskite materials as novel photocatalysts for overall water splitting.* Chemical Communications, 1999(12): p. 1077-1078.

321. Kato, H. and A. Kudo, *Water Splitting into H2 and O2 on Alkali Tantalate Photocatalysts ATaO3 (A = Li, Na, and K).* The Journal of Physical Chemistry B, 2001. **105**(19): p. 4285-4292.

322. Kato, H., K. Asakura, and A. Kudo, *Highly Efficient Water Splitting into H2 and O2 over Lanthanum-Doped NaTaO3 Photocatalysts with High Crystallinity and Surface Nanostructure.* Journal of the American Chemical Society, 2003. **125**(10): p. 3082-3089.

323. Ikeda, S., et al., *Overall Water Splitting on Tungsten-Based Photocatalysts with Defect Pyrochlore Structure.* Catalysis Letters, 2004. **98**(4): p. 229-233.

324. Inoue, Y., *Photocatalytic water splitting by RuO2-loaded metal oxides and nitrides with d0- and d10 -related electronic configurations.* Energy & Environmental Science, 2009. **2**(4): p. 364-386.

325. Scaife, D.E., *Oxide semiconductors in photoelectrochemical conversion of solar energy.* Solar Energy, 1980. **25**(1): p. 41-54.

326. Martha, S., P. Chandra Sahoo, and K.M. Parida, *An overview on visible light responsive metal oxide based photocatalysts for hydrogen energy production.* RSC Advances, 2015. **5**(76): p. 61535-61553.

327. Asahi, R., et al., *Visible-Light Photocatalysis in Nitrogen-Doped Titanium Oxides.* Science, 2001. **293**(5528): p. 269.

328. Williams, R., *Becquerel Photovoltaic Effect in Binary Compounds.* The Journal of Chemical Physics, 1960. **32**(5): p. 1505-1514.

329. Gerischer, H., *Electrochemical photo and solar cells principles and some experiments.* Journal of Electroanalytical Chemistry and Interfacial Electrochemistry, 1975. **58**(1): p. 263-274.

330. Ellis, A.B., et al., *Study of n-type semiconducting cadmium chalcogenide-based photoelectrochemical cells employing polychalcogenide electrolytes.* Journal of the American Chemical Society, 1977. **99**(9): p. 2839-2848.

331. Kisch, H., *Semiconductor Photocatalysis: Principles and Applications*. 2015: Wiley.

332. Kambe, S., et al., *Photocatalytic hydrogen production with Cd(S, Se) solid solution particles: Determining factors for the highly efficient photocatalyst.* Chemical Physics Letters, 1984. **109**(1): p. 105-109.

333. Frame, F.A. and F.E. Osterloh, *CdSe-MoS2: A Quantum Size-Confined Photocatalyst for Hydrogen Evolution from Water under Visible Light.* The Journal of Physical Chemistry C, 2010. **114**(23): p. 10628-10633.

334. Andrew Frame, F., et al., *First demonstration of CdSe as a photocatalyst for hydrogen evolution from water under UV and visible light.* Chemical Communications, 2008(19): p. 2206-2208.

335. Haug, A., et al., *How to use the world's scarce selenium resources efficiently to increase the selenium concentration in food.* Microbial Ecology in Health and Disease, 2007. **19**(4): p. 209-228.

336. Bradshaw Alex, M., B. Reuter, and T. Hamacher, *The Potential Scarcity of Rare Elements for the Energiewende*, in *Green*. 2013. p. 93.

337. Reber, J.F. and K. Meier, *Photochemical production of hydrogen with zinc sulfide suspensions.* The Journal of Physical Chemistry, 1984. **88**(24): p. 5903-5913.

338. Darwent, J.R. and G. Porter, *Photochemical hydrogen production using cadmium sulphide suspensions in aerated water.* Journal of the Chemical Society, Chemical Communications, 1981(4): p. 145-146.

339. Kalyanasundaram, K., et al., *Cleavage of Water by Visible-Light Irradiation of Colloidal CdS Solutions; Inhibition of Photocorrosion by RuO2.* Angewandte Chemie International Edition in English, 1981. **20**(11): p. 987-988.

340. Borgarello, E., et al., *Visible Light Induced Generation of Hydrogen from H2S in CdS-Dispersions, Hole Transfer Catalysis by RuO2.* Helvetica Chimica Acta, 1982. **65**(1): p. 243-248.

341. Buehler, N., K. Meier, and J.F. Reber, *Photochemical hydrogen production with cadmium sulfide suspensions.* The Journal of Physical Chemistry, 1984. **88**(15): p. 3261-3268.

342. Mills, A. and G. Williams, *Photosensitised oxidation of water by CdS-based suspensions.* Journal of the Chemical Society, Faraday Transactions 1: Physical Chemistry in Condensed Phases, 1989. **85**(3): p. 503-519.

343. Borrell, L., et al., *A comparative study of CdS-based semiconductor photocatalysts for solar hydrogen production from sulphide + sulphite substrates.* Solar Energy Materials and Solar Cells, 1992. **25**(1): p. 25-39.

344. Zhang, K. and L. Guo, *Metal sulphide semiconductors for photocatalytic hydrogen production.* Catalysis Science & Technology, 2013. **3**(7): p. 1672-1690.

345. Chen, X. and W. Shangguan, *Hydrogen production from water splitting on CdS-based photocatalysts using solar light.* Frontiers in Energy, 2013. **7**(1): p. 111-118.

346. Yuan, Y.-J., et al., *Cadmium sulfide-based nanomaterials for photocatalytic hydrogen production.* Journal of Materials Chemistry A, 2018. **6**(25): p. 11606-11630.

347. Cheng, L., et al., *CdS-Based photocatalysts.* Energy & Environmental Science, 2018. **11**(6): p. 1362-1391.

348. Mark, P., *Ambipolar Diffusion of Free Carriers in Insulating CdS Crystals.* Physical Review, 1965. **137**(1A): p. A203-A210.

349. Novikov, B.V., et al., *Determination of exciton diffusion length from photoconductivity low-temperature spectra.* physica status solidi (b), 1971. **48**(2): p. 473-480.

350. Ebothé, J., *Hole-diffusion length and transport parameters of thin CdS films from a Schottky barrier.* Journal of Applied Physics, 1986. **59**(6): p. 2076-2081.

351. Weber, C., et al., *Measurement of the diffusion-length of carriers and excitons in CdS using laser-induced transient gratings.* Zeitschrift für Physik B Condensed Matter, 1988. **72**(3): p. 379-384.

352. Yang, X., C. Xu, and N.C. Giles, *Intrinsic electron mobilities in CdSe, CdS, ZnO, and ZnS and their use in analysis of temperature-dependent Hall measurements.* Journal of Applied Physics, 2008. **104**(7): p. 073727.

353. Tong, H., et al., *Electronic coupling assembly of semiconductor nanocrystals: self-narrowed band gap to promise solar energy utilization.* Energy & Environmental Science, 2011. **4**(5): p. 1684-1689.

354. Xu, Y. and M.A.A. Schoonen, *The absolute energy positions of conduction and valence bands of selected semiconducting minerals.* American Mineralogist, 2000. **85**(3-4): p. 543-556.

355. Meissner, D., R. Memming, and B. Kastening, *Photoelectrochemistry of cadmium sulfide. 1. Reanalysis of photocorrosion and flat-band potential.* The Journal of Physical Chemistry, 1988. **92**(12): p. 3476-3483.

356. Wu, K., et al., *Hole Removal Rate Limits Photodriven H2 Generation Efficiency in CdS-Pt and CdSe/CdS-Pt Semiconductor Nanorod–Metal Tip Heterostructures.* Journal of the American Chemical Society, 2014. **136**(21): p. 7708-7716.

357. Berr, M.J., et al., *Hole scavenger redox potentials determine quantum efficiency and stability of Pt-decorated CdS nanorods for photocatalytic hydrogen generation.* Applied Physics Letters, 2012. **100**(22): p. 223903.

358. Simon, T., et al., *Redox shuttle mechanism enhances photocatalytic H2 generation on Ni-decorated CdS nanorods.* Nature Materials, 2014. **13**: p. 1013.

359. Liu, M., et al., *Manganese doped cadmium sulfide nanocrystal for hydrogen production from water under visible light.* International Journal of Hydrogen Energy, 2012. **37**(1): p. 730-736.

360. Huang, S., et al., *Enhanced photocatalytic activity and stability of semiconductor by Ag doping and simultaneous deposition: the case of CdS.* RSC Advances, 2013. **3**(43): p. 20782-20792.

361. Li, S., et al., *Construction of Shallow Surface States through Light Ni Doping for High-Efficiency Photocatalytic Hydrogen Production of CdS Nanocrystals.* Chemistry – A European Journal, 2014. **20**(1): p. 311-316.

362. Korake, P.V., S.N. Achary, and N.M. Gupta, *Role of aliovalent cation doping in the activity of nanocrystalline CdS for visible-light-driven H2 production from water.* International Journal of Hydrogen Energy, 2015. **40**(28): p. 8695-8705.

363. He, B., et al., *One-Step Solvothermal Synthesis of Petalous Carbon-Coated Cu+-Doped CdS Nanocomposites with Enhanced Photocatalytic Hydrogen Production.* Langmuir, 2017. **33**(27): p. 6719-6726.

364. Xing, C., et al., *Band structure-controlled solid solution of Cd1-x ZnxS photocatalyst for hydrogen production by water splitting.* International Journal of Hydrogen Energy, 2006. **31**(14): p. 2018-2024.

365. Ikeue, K., S. Shiiba, and M. Machida, *Novel Visible-Light-Driven Photocatalyst Based on Mn−Cd−S for Efficient H2 Evolution.* Chemistry of Materials, 2010. **22**(3): p. 743-745.

366. Liu, M., et al., *Twins in Cd1−xZnxS solid solution: Highly efficient photocatalyst for hydrogen generation from water.* Energy & Environmental Science, 2011. **4**(4): p. 1372-1378.

367. Liu, M., et al., *Twin-induced one-dimensional homojunctions yield high quantum efficiency for solar hydrogen generation.* Nature Communications, 2013. **4**: p. 2278.

368. Khan, M.M.T., R.C. Bhardwaj, and C.M. Jadhav, *Photocatalytic H2 and O2 generation from water using a CdS dispersion loaded with Pt, Ir, or Rh and RuO2. Use of [{Ru(OH)(edta)}2(O2)] as an electron relay (H4edta = ethylenediaminetetra-acetic acid).* Journal of the Chemical Society, Chemical Communications, 1985(23): p. 1690-1692.

369. Rufus, I.B., et al., *Cadmium sulfide with iridium sulfide and platinum sulfide deposits as a photocatalyst for the decomposition of aqueous sulfide.* Journal of Photochemistry and Photobiology A: Chemistry, 1995. **91**(1): p. 63-66.

370. Sathish, M., B. Viswanathan, and R.P. Viswanath, *Alternate synthetic strategy for the preparation of CdS nanoparticles and its exploitation for water splitting.* International Journal of Hydrogen Energy, 2006. **31**(7): p. 891-898.

371. Yan, H., et al., *Visible-light-driven hydrogen production with extremely high quantum efficiency on Pt–PdS/CdS photocatalyst.* Journal of Catalysis, 2009. **266**(2): p. 165-168.

372. Yang, J., et al., *Roles of cocatalysts in Pt–PdS/CdS with exceptionally high quantum efficiency for photocatalytic hydrogen production.* Journal of Catalysis, 2012. **290**: p. 151-157.

373. Wang, Y., Y. Wang, and R. Xu, *Photochemical Deposition of Pt on CdS for H2 Evolution from Water: Markedly Enhanced Activity by Controlling Pt Reduction Environment.* The Journal of Physical Chemistry C, 2013. **117**(2): p. 783-790.

374. Majeed, I., et al., *On the role of metal particle size and surface coverage for photo-catalytic hydrogen production: A case study of the Au/CdS system.* Applied Catalysis B: Environmental, 2016. **182**: p. 266-276.

375. Tada, H., et al., *All-solid-state Z-scheme in CdS–Au–TiO2 three-component nanojunction system.* Nature Materials, 2006. **5**(10): p. 782-786.

376. Savinov, E.N., Y.A. Gruzdkov, and V.N. Parmon, *Suspensions of semiconductors with microheterojunctions—A new type of highly efficient photocatalyst for dihydrogen production from solution of hydrogen sulfide and sulfide ions.* International Journal of Hydrogen Energy, 1989. **14**(1): p. 1-9.

377. Zhang, L.J., et al., *Noble-metal-free CuS/CdS composites for photocatalytic H2 evolution and its photogenerated charge transfer properties.* International Journal of Hydrogen Energy, 2013. **38**(27): p. 11811-11817.

378. Cheng, F. and Q. Xiang, *A solid-state approach to fabricate a CdS/CuS nano-heterojunction with promoted visible-light photocatalytic H2-evolution activity.* RSC Advances, 2016. **6**(80): p. 76269-76272.

379. Zong, X., et al., *Enhancement of Photocatalytic H2 Evolution on CdS by Loading MoS2 as Cocatalyst under Visible Light Irradiation.* Journal of the American Chemical Society, 2008. **130**(23): p. 7176-7177.

380. Zong, X., et al., *Photocatalytic H2 Evolution on MoS2/CdS Catalysts under Visible Light Irradiation.* The Journal of Physical Chemistry C, 2010. **114**(4): p. 1963-1968.

381. Zong, X., et al., *Photocatalytic H2 Evolution on CdS Loaded with WS2 as Cocatalyst under Visible Light Irradiation.* The Journal of Physical Chemistry C, 2011. **115**(24): p. 12202-12208.

382. Wang, H., et al., *Nickel nanoparticles modified CdS – A potential photocatalyst for hydrogen production through water splitting under visible light irradiation.* International Journal of Hydrogen Energy, 2015. **40**(1): p. 340-345.

383. Chen, S., et al., *Promotion effect of nickel loaded on CdS for photocatalytic H2 production in lactic acid solution.* Applied Surface Science, 2014. **316**: p. 590-594.

384. Zhukovskyi, M., et al., *Efficient Photocatalytic Hydrogen Generation from Ni Nanoparticle Decorated CdS Nanosheets.* ACS Catalysis, 2015. **5**(11): p. 6615-6623.

385. Ran, J., J. Yu, and M. Jaroniec, *Ni(OH)2 modified CdS nanorods for highly efficient visible-light-driven photocatalytic H2 generation.* Green Chemistry, 2011. **13**(10): p. 2708-2713.

386. Khan, Z., et al., *Hierarchical 3D NiO–CdS heteroarchitecture for efficient visible light photocatalytic hydrogen generation.* Journal of Materials Chemistry, 2012. **22**(24): p. 12090-12095.

387. Chen, X., et al., *In situ photodeposition of NiOX on CdS for hydrogen production under visible light: Enhanced activity by controlling solution environment.* Applied Catalysis B: Environmental, 2014. **152-153**: p. 68-72.

388. Zhang, J., et al., *Fabrication of NiS modified CdS nanorod p–n junction photocatalysts with enhanced visible-light photocatalytic H2-production activity.* Physical Chemistry Chemical Physics, 2013. **15**(29): p. 12088-12094.

389. Guan, S., et al., *β-NiS modified CdS nanowires for photocatalytic H2 evolution with exceptionally high efficiency.* Chemical Science, 2018. **9**(6): p. 1574-1585.

390. Zhang, W., et al., *Highly efficient and noble metal-free NiS/CdS photocatalysts for H2 evolution from lactic acid sacrificial solution under visible light.* Chemical Communications, 2010. **46**(40): p. 7631-7633.

391. Li, Q., et al., *Highly Efficient Visible-Light-Driven Photocatalytic Hydrogen Production of CdS-Cluster-Decorated Graphene Nanosheets.* Journal of the American Chemical Society, 2011. **133**(28): p. 10878-10884.

392. Gao, P., et al., *High quality graphene oxide–CdS–Pt nanocomposites for efficient photocatalytic hydrogen evolution.* Journal of Materials Chemistry, 2012. **22**(5): p. 2292-2298.

393. Wang, J.-J., et al., *Enhanced visible-light-driven hydrogen generation by in situ formed photocatalyst RGO–CdS–NixS from metal salts and RGO–CdS composites.* Journal of Materials Chemistry A, 2017. **5**(20): p. 9537-9543.

394. Yan, Z., et al., *Cadmium sulfide/graphitic carbon nitride heterostructure nanowire loading with a nickel hydroxide cocatalyst for highly efficient photocatalytic hydrogen production in water under visible light.* Nanoscale, 2016. **8**(8): p. 4748-4756.

395. Yue, X., et al., *Cadmium Sulfide and Nickel Synergetic Co-catalysts Supported on Graphitic Carbon Nitride for Visible-Light-Driven Photocatalytic Hydrogen Evolution.* Scientific Reports, 2016. **6**: p. 22268.

396. Bao, N., et al., *Self-Templated Synthesis of Nanoporous CdS Nanostructures for Highly Efficient Photocatalytic Hydrogen Production under Visible Light.* Chemistry of Materials, 2008. **20**(1): p. 110-117.

397. Yu, J.C., X. Wang, and X. Fu, *Pore-Wall Chemistry and Photocatalytic Activity of Mesoporous Titania Molecular Sieve Films.* Chemistry of Materials, 2004. **16**(8): p. 1523-1530.

398. Rossetti, R., et al., *Size effects in the excited electronic states of small colloidal CdS crystallites.* The Journal of Chemical Physics, 1984. **80**(9): p. 4464-4469.

399. Rossetti, R., et al., *Excited electronic states and optical spectra of ZnS and CdS crystallites in the ≅15 to 50 Å size range: Evolution from molecular to bulk semiconducting properties.* The Journal of Chemical Physics, 1985. **82**(1): p. 552-559.

400. Li, H., W.Y. Shih, and W.-H. Shih, *Synthesis and Characterization of Aqueous Carboxyl-Capped CdS Quantum Dots for Bioapplications.* Industrial & Engineering Chemistry Research, 2007. **46**(7): p. 2013-2019.

401. Liji Sobhana, S.S., et al., *CdS quantum dots for measurement of the size-dependent optical properties of thiol capping.* Journal of Nanoparticle Research, 2011. **13**(4): p. 1747-1757.

402. Vamvasakis, I., et al., *Template-Directed Assembly of Metal–Chalcogenide Nanocrystals into Ordered Mesoporous Networks.* ACS Nano, 2015. **9**(4): p. 4419-4426.

403. Dukovic, G., et al., *Photodeposition of Pt on Colloidal CdS and CdSe/CdS Semiconductor Nanostructures.* Advanced Materials, 2008. **20**(22): p. 4306-4311.

404. Vamvasakis, I., B. Liu, and G.S. Armatas, *Size Effects of Platinum Nanoparticles in the Photocatalytic Hydrogen Production Over 3D Mesoporous Networks of CdS and Pt Nanojunctions.* Advanced Functional Materials, 2016. **26**(44): p. 8062-8071.

405. Vamvasakis, I., et al., *Enhanced visible-light photocatalytic hydrogen production activity of three-dimensional mesoporous p-CuS/n-CdS nanocrystal assemblies.* Inorganic Chemistry Frontiers, 2017. **4**(3): p. 433-441.

406. Vamvasakis, I., et al., *Visible-Light Photocatalytic H2 Production Activity of β-Ni(OH)2-Modified CdS Mesoporous Nanoheterojunction Networks.* ACS Catalysis, 2018. **8**(9): p. 8726-8738.

407. Hammersley, F. A. P., in ESRF98HA01T: FIT2D V9.129 Reference Manual V3.1, ESRF Internal Report, France, 1998.

408. Sequeira, A.D., J.S. Pedersen, and G. Kostorz, *The Anisotropy of Metallic Systems — Analysis of Small-Angle Scattering Data*, in *Modern Aspects of Small-Angle Scattering*, H. Brumberger, Editor. 1995, Springer Netherlands: Dordrecht. p. 267-297.

409. Scherrer, P., *Bestimmung der inneren Struktur und der Größe von Kolloidteilchen mittels Röntgenstrahlen*, in *Kolloidchemie Ein Lehrbuch*. 1912, Springer Berlin Heidelberg: Berlin, Heidelberg. p. 387-409.

410. Scherrer, P., *Bestimmung der Größe und der inneren Struktur von Kolloidteilchen mittels Röntgenstrahlen.* Nachrichten von der Gesellschaft der Wissenschaften zu Göttingen, Mathematisch-Physikalische Klasse, 1918. **1918**: p. 98-100.

411. Patterson, A.L., *The Scherrer Formula for X-Ray Particle Size Determination.* Physical Review, 1939. **56**(10): p. 978-982.

412. Sing, K.S.W., *Reporting physisorption data for gas/solid systems with special reference to the determination of surface area and porosity (Recommendations 1984).* Pure and Applied Chemistry, 1985. **57**: p. 603 - 619.

413. Brunauer, S., et al., *On a Theory of the van der Waals Adsorption of Gases.* Journal of the American Chemical Society, 1940. **62**(7): p. 1723-1732.

414. Ravikovitch, P.I., et al., *Evaluation of Pore Structure Parameters of MCM-41 Catalyst Supports and Catalysts by Means of Nitrogen and Argon Adsorption.* The Journal of Physical Chemistry B, 1997. **101**(19): p. 3671-3679.

415. Kubelka, P., *New Contributions to the Optics of Intensely Light-Scattering Materials. Part I.* Journal of the Optical Society of America, 1948. **38**(5): p. 448-457.

416. Tauc, J., *Optical Properties of Amorphous Semiconductors*, in *Amorphous and Liquid Semiconductors*, J. Tauc, Editor. 1974, Springer US: Boston, MA. p. 159-220.

417. Brus, L., *Electronic wave functions in semiconductor clusters: experiment and theory.* The Journal of Physical Chemistry, 1986. **90**(12): p. 2555-2560.

418. Kuehnel, M.F., et al., *Photocatalytic Formic Acid Conversion on CdS Nanocrystals with Controllable Selectivity for H2 or CO.* Angewandte Chemie, 2015. **127**(33): p. 9763-9767.

419. Baslak, C., et al., *Photocatalytic hydrogen evolution based on mercaptopropionic acid stabilized CdS and CdTeS quantum dots.* International Journal of Hydrogen Energy, 2016. **41**(45): p. 20523-20528.

420. Gacoin, T., L. Malier, and J.-P. Boilot, *Sol–gel transition in CdS colloids.* Journal of Materials Chemistry, 1997. **7**(6): p. 859-860.

421. Gacoin, T., L. Malier, and J.-P. Boilot, *New Transparent Chalcogenide Materials Using a Sol−Gel Process.* Chemistry of Materials, 1997. **9**(7): p. 1502-1504.

422. Arachchige, I.U., J.L. Mohanan, and S.L. Brock, *Sol−Gel Processing of Semiconducting Metal Chalcogenide Xerogels: Influence of Dimensionality on Quantum Confinement Effects in a Nanoparticle Network.* Chemistry of Materials, 2005. **17**(26): p. 6644-6650.

423. Pala, I.R., et al., *Reversible Gelation of II–VI Nanocrystals: The Nature of Interparticle Bonding and the Origin of Nanocrystal Photochemical Instability.* Angewandte Chemie, 2010. **122**(21): p. 3743-3747.

424. Gacoin, T., et al., *Transformation of CdS Colloids: Sols, Gels, and Precipitates.* The Journal of Physical Chemistry B, 2001. **105**(42): p. 10228-10235.

425. Choi, J.J., et al., *Controlling Nanocrystal Superlattice Symmetry and Shape-Anisotropic Interactions through Variable Ligand Surface Coverage.* Journal of the American Chemical Society, 2011. **133**(9): p. 3131-3138.

426. THOMMES, M., *PHYSICAL ADSORPTION CHARACTERIZATION OF ORDERED AND AMORPHOUS MESOPOROUS MATERIALS*, in *Nanoporous Materials: Science and Engineering*, G.Q. Lu and X.S. Zhao, Editors. 2004, Imperial College Press: London, U.K. p. 317-364.

427. Rouquerol, F., J. Rouquerol, and K.S.W. Sing, *Adsorption by Powders and Porous Solids: Principles, Methodology and Applications*. 1999, London, U.K.: Academic Press.

428. Brus, L.E., *Electron–electron and electron-hole interactions in small semiconductor crystallites: The size dependence of the lowest excited electronic state.* The Journal of Chemical Physics, 1984. **80**(9): p. 4403-4409.

429. Alivisatos, A.P., *Semiconductor Clusters, Nanocrystals, and Quantum Dots.* Science, 1996. **271**(5251): p. 933-937.

430. Koole, R., et al., *Electronic Coupling and Exciton Energy Transfer in CdTe Quantum-Dot Molecules.* Journal of the American Chemical Society, 2006. **128**(32): p. 10436-10441.

431. Choi, J.J., et al., *Photogenerated Exciton Dissociation in Highly Coupled Lead Salt Nanocrystal Assemblies.* Nano Letters, 2010. **10**(5): p. 1805-1811.

432. Okamoto, S. and Y. Kanemitsu, *Photoluminescence properties of surface-oxidized Ge nanocrystals: Surface localization of excitons.* Physical Review B, 1996. **54**(23): p. 16421-16424.

433. Pala, I.R., et al., *Reversible Gelation of II–VI Nanocrystals: The Nature of Interparticle Bonding and the Origin of Nanocrystal Photochemical Instability.* Angewandte Chemie International Edition, 2010. **49**(21): p. 3661-3665.

434. Zhang, Y., et al., *Transforming CdS into an efficient visible light photocatalyst for selective oxidation of saturated primary C–H bonds under ambient conditions.* Chemical Science, 2012. **3**(9): p. 2812-2822.

435. Kornarakis, I., et al., *Efficient visible-light photocatalytic activity by band alignment in mesoporous ternary polyoxometalate–Ag2S–CdS semiconductors.* Nanoscale, 2014. **6**(15): p. 8694-8703.

436. Zhang, N., et al., *Assembly of CdS Nanoparticles on the Two-Dimensional Graphene Scaffold as Visible-Light-Driven Photocatalyst for Selective Organic Transformation under Ambient Conditions.* The Journal of Physical Chemistry C, 2011. **115**(47): p. 23501-23511.

437. Bonde, J., et al., *Hydrogen evolution on nano-particulate transition metal sulfides.* Faraday Discussions, 2009. **140**(0): p. 219-231.

438. Zhang, J., et al., *Visible Light Photocatalytic H2-Production Activity of CuS/ZnS Porous Nanosheets Based on Photoinduced Interfacial Charge Transfer.* Nano Letters, 2011. **11**(11): p. 4774-4779.

439. Hou, Y., et al., *Layered Nanojunctions for Hydrogen-Evolution Catalysis.* Angewandte Chemie International Edition, 2013. **52**(13): p. 3621-3625.

440. Staszak-Jirkovský, J., et al., *Design of active and stable Co–Mo–Sx chalcogels as pH-universal catalysts for the hydrogen evolution reaction.* Nature Materials, 2015. **15**: p. 197.

441. Jing, D. and L. Guo, *A Novel Method for the Preparation of a Highly Stable and Active CdS Photocatalyst with a Special Surface Nanostructure.* The Journal of Physical Chemistry B, 2006. **110**(23): p. 11139-11145.

442. Jang, J.S., U.A. Joshi, and J.S. Lee, *Solvothermal Synthesis of CdS Nanowires for Photocatalytic Hydrogen and Electricity Production.* The Journal of Physical Chemistry C, 2007. **111**(35): p. 13280-13287.

443. Li, Y., et al., *Synthesis of CdS Nanorods by an Ethylenediamine Assisted Hydrothermal Method for Photocatalytic Hydrogen Evolution.* The Journal of Physical Chemistry C, 2009. **113**(21): p. 9352-9358.

444. Kamat, P.V., *Manipulation of Charge Transfer Across Semiconductor Interface. A Criterion That Cannot Be Ignored in Photocatalyst Design.* The Journal of Physical Chemistry Letters, 2012. **3**(5): p. 663-672.

445. Mongin, D., et al., *Ultrafast Photoinduced Charge Separation in Metal–Semiconductor Nanohybrids.* ACS Nano, 2012. **6**(8): p. 7034-7043.

446. Eastman, D.E., *Photoelectric Work Functions of Transition, Rare-Earth, and Noble Metals.* Physical Review B, 1970. **2**(1): p. 1-2.

447. Xin, G., et al., *Highly Efficient Deposition Method of Platinum over CdS for H2 Evolution under Visible Light.* The Journal of Physical Chemistry C, 2014. **118**(38): p. 21928-21934.

448. Reber, J.F. and M. Rusek, *Photochemical hydrogen production with platinized suspensions of cadmium sulfide and cadmium zinc sulfide modified by silver sulfide.* The Journal of Physical Chemistry, 1986. **90**(5): p. 824-834.

449. Achermann, M., *Exciton−Plasmon Interactions in Metal−Semiconductor Nanostructures.* The Journal of Physical Chemistry Letters, 2010. **1**(19): p. 2837-2843.

450. Hao, Q., et al., *Effects of Intrinsic Fano Interference on Surface Enhanced Raman Spectroscopy: Comparison between Platinum and Gold.* The Journal of Physical Chemistry C, 2010. **114**(42): p. 18059-18066.

451. Manchon, D., et al., *Plasmonic coupling with most of the transition metals: a new family of broad band and near infrared nanoantennas.* Nanoscale, 2015. **7**(3): p. 1181-1192.

452. Tang, W.Z. and C.P. Huang, *Photocatalyzed oxidation pathways of 2,4-dichlorophenol by CdS in basic and acidic aqueous solutions.* Water Research, 1995. **29**(2): p. 745-756.

453. Kalisman, P., Y. Nakibli, and L. Amirav, *Perfect Photon-to-Hydrogen Conversion Efficiency.* Nano Letters, 2016. **16**(3): p. 1776-1781.

454. Amirav, L. and A.P. Alivisatos, *Photocatalytic Hydrogen Production with Tunable Nanorod Heterostructures.* The Journal of Physical Chemistry Letters, 2010. **1**(7): p. 1051-1054.

455. Popczun, E.J., et al., *Highly Active Electrocatalysis of the Hydrogen Evolution Reaction by Cobalt Phosphide Nanoparticles.* Angewandte Chemie International Edition, 2014. **53**(21): p. 5427-5430.

456. Voiry, D., J. Yang, and M. Chhowalla, *Recent Strategies for Improving the Catalytic Activity of 2D TMD Nanosheets Toward the Hydrogen Evolution Reaction.* Advanced Materials, 2016. **28**(29): p. 6197-6206.

457. Finlayson, M.F., et al., *Determination of flat-band position of cadmium sulfide crystals, films, and powders by photocurrent and impedance techniques, photoredox reaction mediated by intragap states.* The Journal of Physical Chemistry, 1985. **89**(26): p. 5676-5681.

458. Swank, R.K., *Surface Properties of II-VI Compounds.* Physical Review, 1967. **153**(3): p. 844-849.

459. Michaelson, H.B., *The work function of the elements and its periodicity.* Journal of Applied Physics, 1977. **48**(11): p. 4729-4733.

460. Wood, D.M., *Classical Size Dependence of the Work Function of Small Metallic Spheres.* Physical Review Letters, 1981. **46**(11): p. 749-749.

461. Shiraishi, Y., et al., *Platinum Nanoparticles Supported on Anatase Titanium Dioxide as Highly Active Catalysts for Aerobic Oxidation under Visible Light Irradiation.* ACS Catalysis, 2012. **2**(9): p. 1984-1992.

462. Nakato, Y., et al., *Effect of microscopic discontinuity of metal overlayers on the photovoltages in metal-coated semiconductor-liquid junction photoelectrochemical cells for efficient solar energy conversion.* The Journal of Physical Chemistry, 1988. **92**(8): p. 2316-2324.

463. Peng, T., et al., *Hydrothermal Preparation of Multiwalled Carbon Nanotubes (MWCNTs)/CdS Nanocomposite and Its Efficient Photocatalytic Hydrogen Production under Visible Light Irradiation.* Energy & Fuels, 2011. **25**(5): p. 2203-2210.

464. De Trizio, L. and L. Manna, *Forging Colloidal Nanostructures via Cation Exchange Reactions.* Chemical Reviews, 2016. **116**(18): p. 10852-10887.

465. Mondal, C., et al., *Preformed ZnS nanoflower prompted evolution of CuS/ZnS p–n heterojunctions for exceptional visible-light driven photocatalytic activity.* New Journal of Chemistry, 2015. **39**(7): p. 5628-5635.

466. Bhide, V.G., et al., *Depth profile composition studies of thin film CdS:Cu2S solar cells using XPS and AES.* Journal of Physics D: Applied Physics, 1981. **14**(9): p. 1647-1656.

467. Li, T.-L., Y.-L. Lee, and H. Teng, *High-performance quantum dot-sensitized solar cells based on sensitization with CuInS2 quantum dots/CdS heterostructure.* Energy & Environmental Science, 2012. **5**(1): p. 5315-5324.

468. Ye, M., et al., *In situ growth of CuS and Cu1.8S nanosheet arrays as efficient counter electrodes for quantum dot-sensitized solar cells.* Journal of Materials Chemistry A, 2015. **3**(18): p. 9595-9600.

469. Amri, A., et al., *Solar absorptance of copper–cobalt oxide thin film coatings with nano-size, grain-like morphology: Optimization and synchrotron radiation XPS studies.* Applied Surface Science, 2013. **275**: p. 127-135.

470. Naşcu, C., et al., *Spray pyrolysis deposition of CuS thin films.* Materials Letters, 1997. **32**(2): p. 73-77.

471. Dias Filho, N.L., *Adsorption of Cu(II) and Co(II) complexes on a silica gel surface chemically modified with 2-mercaptoimidazole.* Microchimica Acta, 1999. **130**(4): p. 233-240.

472. Lang, D., F. Cheng, and Q. Xiang, *Enhancement of photocatalytic H2 production activity of CdS nanorods by cobalt-based cocatalyst modification.* Catalysis Science & Technology, 2016. **6**(16): p. 6207-6216.

473. Chen, Y., et al., *Noble-metal-free Cu2S-modified photocatalysts for enhanced photocatalytic hydrogen production by forming nanoscale p–n junction structure.* RSC Advances, 2015. **5**(23): p. 18159-18166.

474. Zhang, K., et al., *Significantly improved photocatalytic hydrogen production activity over Cd1-xZnxS photocatalysts prepared by a novel thermal sulfuration method.* International Journal of Hydrogen Energy, 2007. **32**(18): p. 4685-4691.

475. Yu, J., J. Zhang, and M. Jaroniec, *Preparation and enhanced visible-light photocatalytic H2-production activity of CdS quantum dots-sensitized Zn1−xCdxS solid solution.* Green Chemistry, 2010. **12**(9): p. 1611-1614.

476. Liu, G., et al., *Photocatalytic H2 evolution under visible light irradiation on a novel CdxCuyZn1−x−yS catalyst.* Catalysis Communications, 2008. **9**(1): p. 126-130.

477. Zhang, W., et al., *Doped Solid Solution: (Zn0.95Cu0.05)1−xCdxS Nanocrystals with High Activity for H2 Evolution from Aqueous Solutions under Visible Light.* The Journal of Physical Chemistry C, 2008. **112**(45): p. 17635-17642.

478. Li, Y., et al., *Hierarchical ZnS-In2S3-CuS Nanospheres with Nanoporous Structure: Facile Synthesis, Growth Mechanism, and Excellent Photocatalytic Activity.* Advanced Functional Materials, 2010. **20**(19): p. 3390-3398.

479. Shen, Z., et al., *Sonochemistry synthesis and enhanced photocatalytic H2-production activity of nanocrystals embedded in CdS/ZnS/In2S3 microspheres.* Nanoscale, 2012. **4**(6): p. 2010-2017.

480. Li, Y., et al., *A simple template-free synthesis of nanoporous ZnS–In2S3–Ag2S solid solutions for highly efficient photocatalytic H2 evolution under visible light.* Chemical Communications, 2009(15): p. 2020-2022.

481. Vegelius, J.R., et al., *X-ray Spectroscopic Study of Cu2S, CuS, and Copper Films Exposed to Na2S Solutions.* The Journal of Physical Chemistry C, 2012. **116**(42): p. 22293-22300.

482. Xu, W., et al., *Nanoporous CuS with excellent photocatalytic property.* Scientific Reports, 2015. **5**: p. 18125.

483. Lee, M. and K. Yong, *Highly efficient visible light photocatalysis of novel CuS/ZnO heterostructure nanowire arrays.* Nanotechnology, 2012. **23**(19): p. 194014.

484. Johansson, J., et al., *Growth of conductive copper sulfide thin films by atomic layer deposition.* Journal of Materials Chemistry, 2002. **12**(4): p. 1022-1026.

485. Sabah, F.A., et al., *High performance CuS p-type thin film as a hydrogen gas sensor.* Sensors and Actuators A: Physical, 2016. **249**: p. 68-76.

486. Sabah, F.A., et al., *CuS p- type thin film characterization deposited on Ti, ITO and glass substrates using spray pyrolysis deposition (SPD) for light emitting diode (LED) application.* AIP Conference Proceedings, 2016. **1733**(1): p. 020021.

487. Gupta, S., et al., *Study of charge separation and interface formation in a single nanorod CdS–CuxS heterojunction solar cell using Kelvin probe force microscopy.* Nanotechnology, 2013. **24**(25): p. 255703.

488. Mulliken, R.S., *A New Electroaffinity Scale; Together with Data on Valence States and on Valence Ionization Potentials and Electron Affinities.* The Journal of Chemical Physics, 1934. **2**(11): p. 782-793.

489. Hong, E., D. Kim, and J.H. Kim, *Heterostructured metal sulfide (ZnS–CuS–CdS) photocatalyst for high electron utilization in hydrogen production from solar water splitting.* Journal of Industrial and Engineering Chemistry, 2014. **20**(5): p. 3869-3874.

490. Khan, Z., et al., *Hierarchical 3D NiO-CdS heteroarchitecture for efficient visible light photocatalytic hydrogen generation.* Journal of Materials Chemistry, 2012. **22**(24): p. 12090-12095.

491. Chai, Z., et al., *Efficient Visible Light-Driven Splitting of Alcohols into Hydrogen and Corresponding Carbonyl Compounds over a Ni-Modified CdS Photocatalyst.* Journal of the American Chemical Society, 2016. **138**(32): p. 10128-10131.

492. Wang, J.J., et al., *Photocatalytic Hydrogen Evolution from Glycerol and Water over Nickel-Hybrid Cadmium Sulfide Quantum Dots under Visible-Light Irradiation.* ChemSusChem, 2014. **7**(5): p. 1468-1475.

493. Zhang, J., et al., *Fabrication of NiS modified CdS nanorod p-n junction photocatalysts with enhanced visible-light photocatalytic H2-production activity.* Physical Chemistry Chemical Physics, 2013. **15**(29): p. 12088-12094.

494. Guan, S., et al., *[small beta]-NiS modified CdS nanowires for photocatalytic H2 evolution with exceptionally high efficiency.* Chemical Science, 2018. **9**(6): p. 1574-1585.

495. Wang, J.-J., et al., *Enhanced visible-light-driven hydrogen generation by in situ formed photocatalyst RGO-CdS-NixS from metal salts and RGO-CdS composites.* Journal of Materials Chemistry A, 2017. **5**(20): p. 9537-9543.

496. Chen, X., et al., *In situ photodeposition of nickel oxides on CdS for highly efficient hydrogen production via visible-light-driven photocatalysis.* Catalysis Communications, 2013. **36**: p. 104-108.

497. Medway, S.L., et al., *In situ studies of the oxidation of nickel electrodes in alkaline solution.* Journal of Electroanalytical Chemistry, 2006. **587**(1): p. 172-181.

498. Hall, D.S., C. Bock, and B.R. MacDougall, *The Electrochemistry of Metallic Nickel: Oxides, Hydroxides, Hydrides and Alkaline Hydrogen Evolution.* Journal of The Electrochemical Society, 2013. **160**(3): p. F235-F243.

499. Yuan, J., et al., *Amorphous Co3O4 modified CdS nanorods with enhanced visible-light photocatalytic H2-production activity.* Dalton Transactions, 2015. **44**(4): p. 1680-1689.

500. Barreca, D., et al., *Nanostructured Cadmium Sulfide Thin Films by XPS.* Surface Science Spectra, 2002. **9**(1): p. 46-53.

501. Ma, L., et al., *Catalyst- and template-free low-temperature in situ growth of n-type CdS nanowire on p-type CdTe film and p-n heterojunction properties.* Scientific Reports, 2016. **6**: p. 38858.

502. Wang, X., et al., *Visual monitoring of laser power and spot profile in micron region by a single chip of Zn-doped CdS nanobelts.* RSC Advances, 2014. **4**(94): p. 52550-52554.

503. Wang, J., et al., *Solution-phase catalytic synthesis, characterization and growth kinetics of Ag2S–CdS matchstick-like heteronanostructures.* Dalton Transactions, 2014. **43**(10): p. 3990-3998.

504. Yan, J., et al., *Advanced Asymmetric Supercapacitors Based on Ni(OH)2/Graphene and Porous Graphene Electrodes with High Energy Density.* Advanced Functional Materials, 2012. **22**(12): p. 2632-2641.

505. Su, Y.-Z., et al., *Amorphous Ni(OH)2 @ three-dimensional Ni core–shell nanostructures for high capacitance pseudocapacitors and asymmetric supercapacitors.* Journal of Materials Chemistry A, 2014. **2**(34): p. 13845-13853.

506. Biesinger, M.C., et al., *X-ray photoelectron spectroscopic chemical state quantification of mixed nickel metal, oxide and hydroxide systems.* Surface and Interface Analysis, 2009. **41**(4): p. 324-332.

507. Wei, W., et al., *Construction of hierarchical three-dimensional interspersed flower-like nickel hydroxide for asymmetric supercapacitors.* Nano Research, 2017. **10**(11): p. 3726-3742.

508. Gao, M.Y., et al., *Nitrate-induced and in situ electrochemical activation synthesis of oxygen deficiencies-rich nickel/nickel (oxy)hydroxide hybrid films for enhanced electrocatalytic water splitting.* Nanoscale, 2018. **10**(37): p. 17546-17551.

509. Kamran, M.A., et al., *Near Infrared Emission Band and Origin in Ni(II)-Doped CdS Nanoribbons by CVD Technique.* The Journal of Physical Chemistry C, 2013. **117**(34): p. 17777-17785.

510. Gopi, C.V.V.M., et al., *Improving the performance of quantum dot sensitized solar cells through CdNiS quantum dots with reduced recombination and enhanced electron lifetime.* Dalton Transactions, 2016. **45**(20): p. 8447-8457.

511. Hall, D.S., et al., *Nickel hydroxides and related materials: a review of their structures, synthesis and properties.* Proceedings. Mathematical, physical, and engineering sciences, 2015. **471**(2174): p. 20140792-20140792.

512. Hermet, P., et al., *Dielectric, magnetic, and phonon properties of nickel hydroxide.* Physical Review B, 2011. **84**(23): p. 235211.

513. Overend, R. and G. Paraskevopoulos, *Rates of hydroxyl radical reactions. 4. Reactions with methanol, ethanol, 1-propanol, and 2-propanol at 296 K.* The Journal of Physical Chemistry, 1978. **82**(12): p. 1329-1333.

514. Liu, M., et al., *Photocatalytic hydrogen production using twinned nanocrystals and an unanchored NiSx co-catalyst.* Nature Energy, 2016. **1**(11): p. 16151.

515. Xu, Y. and R. Xu, *Nickel-based cocatalysts for photocatalytic hydrogen production.* Applied Surface Science, 2015. **351**: p. 779-793.

516. Liu, M., et al., *Photocatalytic hydrogen production using twinned nanocrystals and an unanchored NiSx co-catalyst.* Nature Energy, 2016. **1**: p. 16151.

517. Han, K., et al., *Transient Behavior of Ni@NiOx Functionalized SrTiO3 in Overall Water Splitting.* ACS Catalysis, 2017. **7**(3): p. 1610-1614.

518. Macdonald, J.R., *Impedance spectroscopy.* Annals of Biomedical Engineering, 1992. **20**(3): p. 289-305.

519. Cheong, A.K., A. Lasia, and J. Lessard, *Hydrogen Evolution Reaction at Composite-Coated Raney Nickel Electrodes in Aqueous and Aqueous-Methanolic Solutions.* Journal of The Electrochemical Society, 1993. **140**(10): p. 2721-2725.

520. Da Silva, L.M., L.A. De Faria, and J.F.C. Boodts, *Electrochemical impedance spectroscopic (EIS) investigation of the deactivation mechanism, surface and electrocatalytic properties of Ti/RuO2(x)+Co3O4(1−x) electrodes.* Journal of Electroanalytical Chemistry, 2002. **532**(1): p. 141-150.

521. Da Silva, L.M., et al., *Electrochemical impedance spectroscopy study during accelerated life test of conductive oxides: Ti/(Ru + Ti + Ce)O2-system.* Electrochimica Acta, 2004. **49**(27): p. 4893-4906.

522. Bisquert, J., H. Randriamahazaka, and G. Garcia-Belmonte, *Inductive behaviour by charge-transfer and relaxation in solid-state electrochemistry.* Electrochimica Acta, 2005. **51**(4): p. 627-640.

523. Harrington, D.A. and P. van den Driessche, *Mechanism and equivalent circuits in electrochemical impedance spectroscopy.* Electrochimica Acta, 2011. **56**(23): p. 8005-8013.

524. Kim, J.Y., et al., *Highly Conformal Deposition of an Ultrathin FeOOH Layer on a Hematite Nanostructure for Efficient Solar Water Splitting.* Angewandte Chemie International Edition, 2016. **55**(36): p. 10854-10858.

525. Matsumoto, Y., et al., *Photoelectrochemical Properties of the Zn-Ti-Fe Spinel Oxides.* Journal of The Electrochemical Society, 1986. **133**(4): p. 711-716.

526. Ishikawa, A., et al., *Oxysulfide Sm2Ti2S2O5 as a Stable Photocatalyst for Water Oxidation and Reduction under Visible Light Irradiation (λ ≤ 650 nm).* Journal of the American Chemical Society, 2002. **124**(45): p. 13547-13553.

527. Greiner, M.T., et al., *Effects of Processing Conditions on the Work Function and Energy-Level Alignment of NiO Thin Films.* The Journal of Physical Chemistry C, 2010. **114**(46): p. 19777-19781.

528. Digdaya, I.A., et al., *Interfacial engineering of metal-insulator-semiconductor junctions for efficient and stable photoelectrochemical water oxidation.* Nature Communications, 2017. **8**(1): p. 15968.

529. Chen, P., et al., *Phase-Transformation Engineering in Cobalt Diselenide Realizing Enhanced Catalytic Activity for Hydrogen Evolution in an Alkaline Medium.* Advanced Materials, 2016. **28**(34): p. 7527-7532.

530. Irwin, M.D., et al., *p-Type semiconducting nickel oxide as an efficiency-enhancing anode interfacial layer in polymer bulk-heterojunction solar cells.* Proceedings of the National Academy of Sciences, 2008. **105**(8): p. 2783-2787.

531. Schulz, P., et al., *NiOX/MoO3 Bi-Layers as Efficient Hole Extraction Contacts in Organic Solar Cells.* Advanced Functional Materials, 2014. **24**(5): p. 701-706.

532. Wardman, P., *Reduction Potentials of One-Electron Couples Involving Free Radicals in Aqueous Solution.* Journal of Physical and Chemical Reference Data, 1989. **18**(4): p. 1637-1755.

533. Anderson, R.L., *Germanium-Gallium Arsenide Heterojunctions [Letter to the Editor].* IBM Journal of Research and Development, 1960. **4**(3): p. 283-287.

534. Grosvenor, A.P., et al., *New interpretations of XPS spectra of nickel metal and oxides.* Surface Science, 2006. **600**(9): p. 1771-1779.

535. Ratcliff, E.L., et al., *Evidence for near-Surface NiOOH Species in Solution-Processed NiOx Selective Interlayer Materials: Impact on Energetics and the Performance of Polymer Bulk Heterojunction Photovoltaics.* Chemistry of Materials, 2011. **23**(22): p. 4988-5000.

536. Weidler, N., et al., *X-ray Photoelectron Spectroscopic Investigation of Plasma-Enhanced Chemical Vapor Deposited NiOx, NiOx(OH)y, and CoNiOx(OH)y: Influence of the Chemical Composition on the Catalytic Activity for the Oxygen Evolution Reaction.* The Journal of Physical Chemistry C, 2017. **121**(12): p. 6455-6463.

537. Zeng, M. and Y. Li, *Recent advances in heterogeneous electrocatalysts for the hydrogen evolution reaction.* Journal of Materials Chemistry A, 2015. **3**(29): p. 14942-14962.

APPENDIX

A.1 Surface-State Induced Band Bending

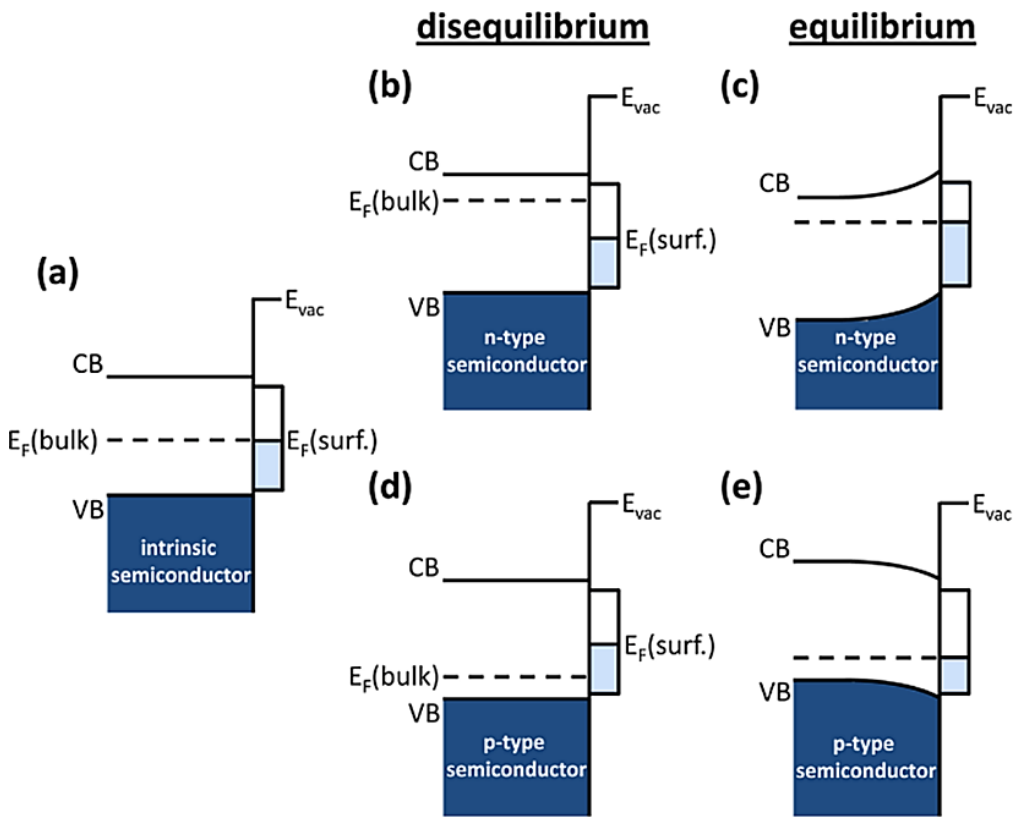

Figure A-1: Schematic illustration of surface-state induced band bending: (a) undoped (intrinsic) semiconductor, where the Fermi level of the bulk semiconductor [E_F(bulk)] is located at the mid-gap and is equal in energy to the surface Fermi level [E_F(surf.)]. In this case the bands remain flat; (b) disequilibrium and (c) equilibrium between the bulk of n-type semiconductor and its surface, where initially E_F(bulk) > E_F(surf.) and thus under equilibrium the bands shift upwards (upward band-bending); (d) disequilibrium and (e) equilibrium between the bulk of p-type semiconductor and its surface, where equilibrium causes the bands to bend downwards (downward band-bending) because initially E_F(bulk) is lower than E_F(surf.). In every case, the semiconductor Fermi level will be pinned at the energy level of the surface states after equilibrium (i.e., Fermi level pinning). Reproduced with permission from ref. [263]. Copyright © 2012, American Chemical Society.

A.2 Metal/Semiconductor Junction

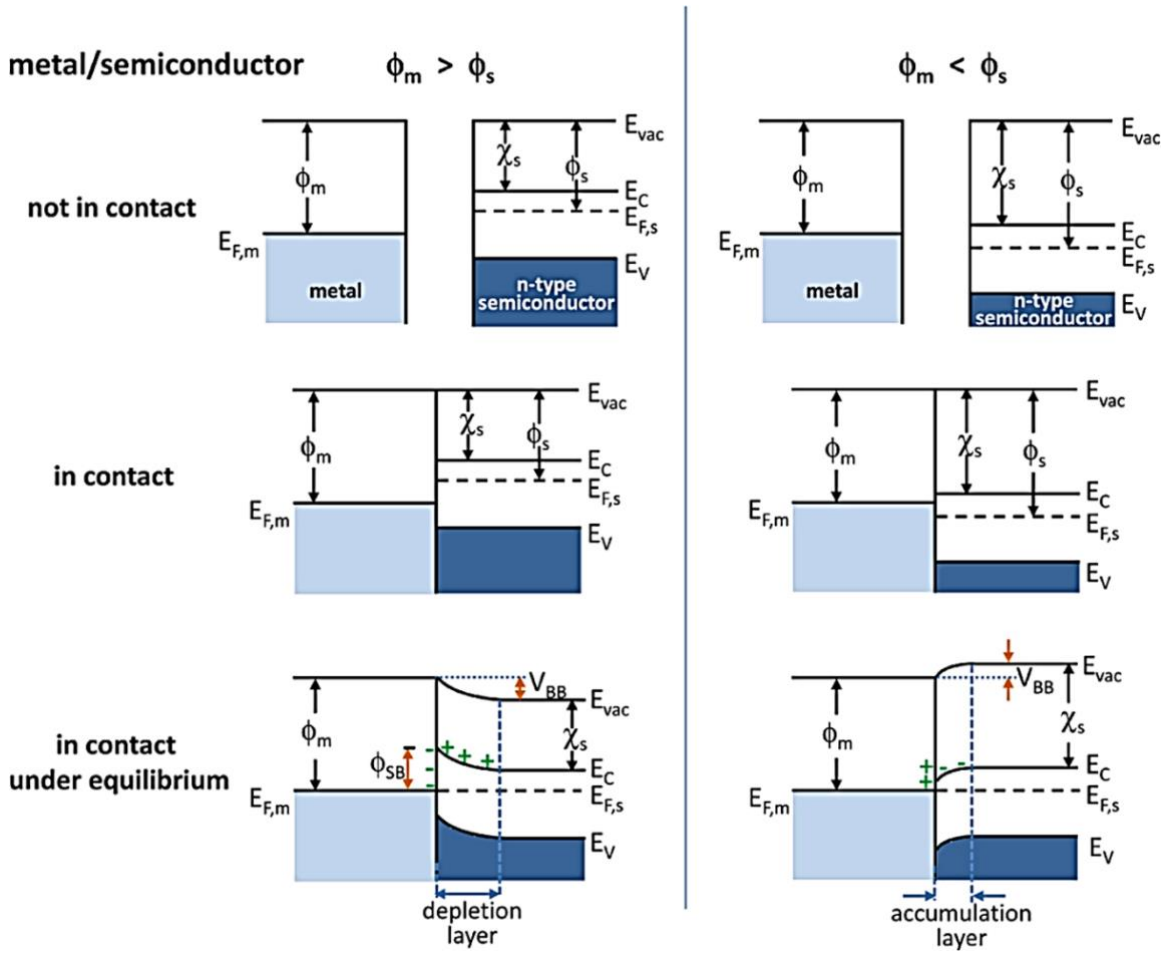

Figure A-2: Energy band diagrams of metal and n-type semiconductor contacts, where E_{vac} = vacuum energy; E_C = energy of conduction band; E_V = energy of valence band; $E_{F,m}$ = Fermi level of metal; $E_{F,s}$ = Fermi level of semiconductor; Φ_m = metal work function; Φ_s = semiconductor work function; χ_s = semiconductor electron affinity; V_{BB} = degree of semiconductor band-bending. If the metal work function (Φ_m) is higher than that of the semiconductor (Φ_s), that is, $\Phi_m > \Phi_s$ as shown on the left panel, electrons will flow from the semiconductor to the metal. Under equilibrium, a charge double-layer and a build-in electric field will be established at the metal/semiconductor interface, where the metal is negatively charged and the semiconductor is positively charged near the surface, due to the depletion of electrons in the space charge region; forming a depletion layer. When $\Phi_m < \Phi_s$, as shown in the right panel, electrons are accumulated in the semiconductor space-charge region due to the electron transfer from the metal to the semiconductor, thus forming an accumulation layer in the semiconductor and a positively charged surface layer in the metal side of the interface. In general, when the Fermi level of the metal is below that of the semiconductor, charge will flow to the metal causing the semiconductor Fermi level to decrease, and vice versa. Because of the electric field at the interface, the energy band edges in the semiconductor will also shift continuously, causing band-bending across the space-charge layer. The energy bands bend upwards toward the interface when $\Phi_m > \Phi_s$, while the edges bend downwards when $\Phi_m < \Phi_s$. In each case, the semiconductor Fermi level will be pinned to that of the metal after equilibrium, creating a fixed band-bending. Reproduced with permission from ref. [263]. Copyright © 2012, American Chemical Society.

A.3 Semiconductor/Semiconductor Heterojunction

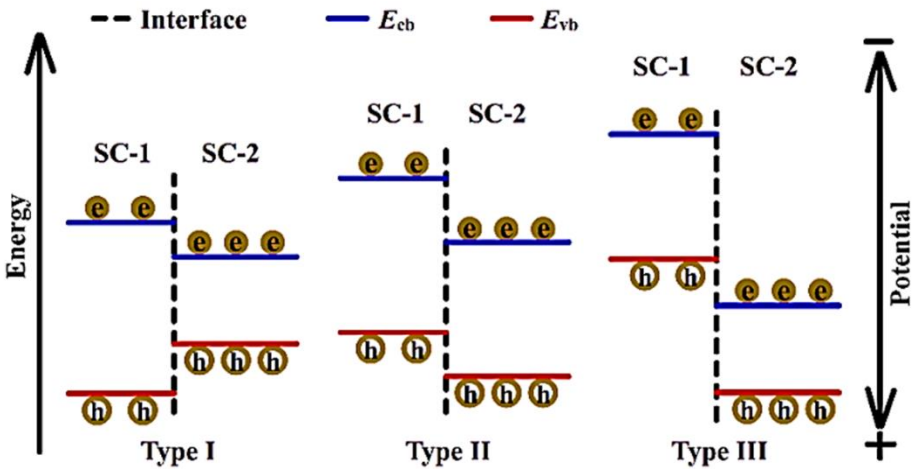

Figure A-3: Possible types of band alignments for two semiconductors in a heterojunction. Blue lines represent the energy level of the CB (E_{cb}) and red lines the position of the VB (E_{cb}). In Type I, the CB of SC-1 is more negative than that of SC-2, and its VB is more positive than that of SC-2. In Type II, the CB of SC-1 is more negative than that of SC-2, while the VB of SC-2 is more positive than that of SC-1. In Type III, both the CB and the VB of SC-2 are lower (more positive) than the VB of SC-1. Reproduced with permission from ref. [276]. Copyright © 2017 Elsevier B.V. All rights reserved.

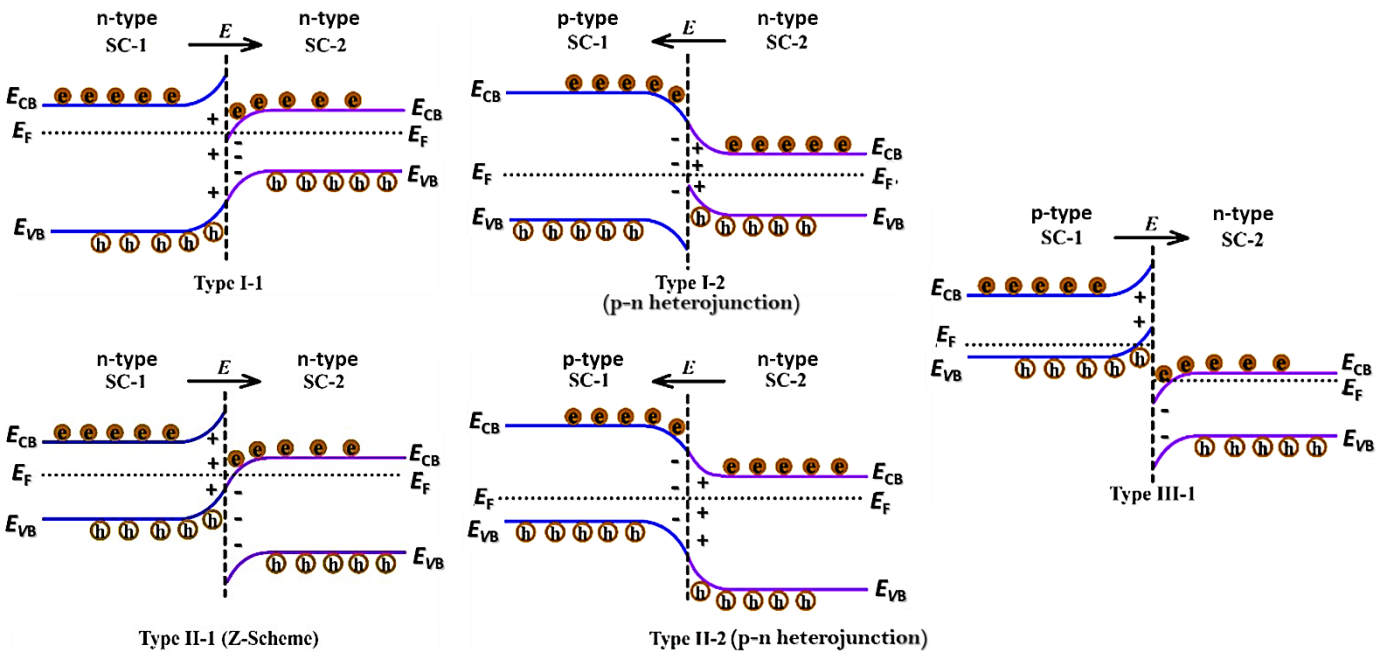

Figure A-4: Possible situations of electrostatic interactions and band-bending in SC/SC hetero-junctions based on the three different types of band-alignment of Figure A-3. Adapted with permission from ref. [276]. Copyright © 2017 Elsevier B.V. All rights reserved.

A.4 Classification of Physisorption Isotherms

The majority of physisorption isotherms may be grouped into six types according to IUPAC classification, as shown in **Figure A-5a.**

- Type I isotherms are given by microporous solids having relatively small external surfaces, such as activated carbons and zeolitic molecular sieves, the limiting uptake being governed by the accessible micropore volume rather than by the internal surface area.
- Type II isotherms are typical of non-porous or macroporous solids, on the surface of which unrestricted monolayer-multilayer adsorption takes place. Point B, is often taken to indicate the stage at which monolayer coverage is complete and multilayer adsorption about to begin.
- Type III isotherms are not common. They are convex to the relative pressure (P/P_0) axis over their entire range, and therefore does not exhibit a point B. In such cases, the adsorbent-adsorbate interactions play an important role.
- Type IV isotherms are given by many mesoporous industrial adsorbents. Their characteristic feature is the hysteresis loop, which is associated with capillary condensation taking place in mesopores, and the limiting uptake over a range of high (P/P_0).
- Type V isotherms are uncommon and related to type III isotherms: the adsorbent-adsorbate interactions are weak.
- Type VI isotherms represent stepwise multilayer adsorption on a uniform non-porous surface, in which the sharpness of the steps depends on the system and the temperature.

A.5 Hysteresis Classification

Hysteresis appearing in the multilayer range of physisorption isotherms is usually associated with capillary condensation in mesopore structures. Such hysteresis loops may exhibit a wide variety of shapes and important for determining the pore geometry and structure of the material. According to IUPAC recommendations, there are four types of hysteresis loops, as shown in **Figure A-5b.**

- Type H1 hysteresis is often associated with porous materials known to consist of compact agglomerates of uniform spherical particles in fairly regular array, hence having narrow pore size distributions.

- Type H2 is given by more complex pore structures in which network effects are important. The very steep desorption branch, which is a characteristic feature of H2 loops, can be attributed either to pore-blocking/percolation in ink-bottle-shaped pores (narrow range of pore necks) or to cavitation-induced evaporation. H2 hysteresis loops are given by many porous adsorbents, for instance: inorganic oxide gels, porous glasses, as well as ordered mesoporous materials.
- Type H3 hysteresis is observed with non-rigid aggregates of plate-like particles giving rise to slit-shaped pores, but also if the pore network consists of macropores which are not completely filled with pore condensate.
- Type H4 loop is often associated with narrow slit-like pores, but in this case the absorption branch is a composite of Types I and II character, which is indicative of microporosity. The H4 loops are often found with aggregated crystals of zeolites, some mesoporous zeolites, and micro-mesoporous carbons.

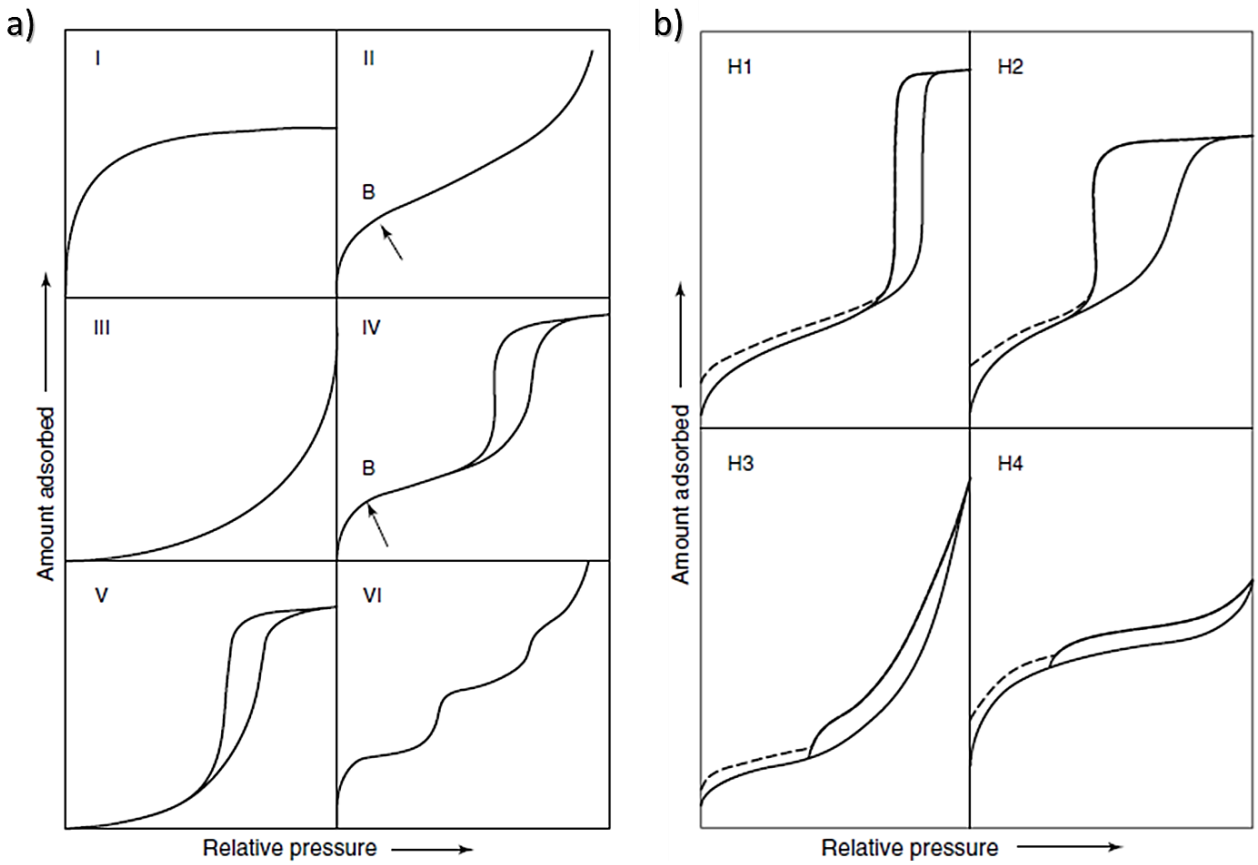

Figure A-5: (a) Physisorption isotherm types and (b) hysteresis classification according to the IUPAC recommendations. Adapted from ref. [412]

A.6 Volcano Plot for Metal Hydrogen Evolution Catalysts

The established free-energy diagram of the Hydrogen evolution activity over various metal catalysts, the so-called volcano plot as shown in **Figure A-6**, provides a quantitative relationship between measured electrochemical activity and theoretical free energy of hydrogen adsorption, to evaluate the electrocatalytic properties of typical metallic catalysts. The catalyst's performance can be quantitatively evaluated by the position of its j_0 and ΔG_{H^*} values relative to the volcano peak (the closer the position of these values to the peak, the better is the catalyst).

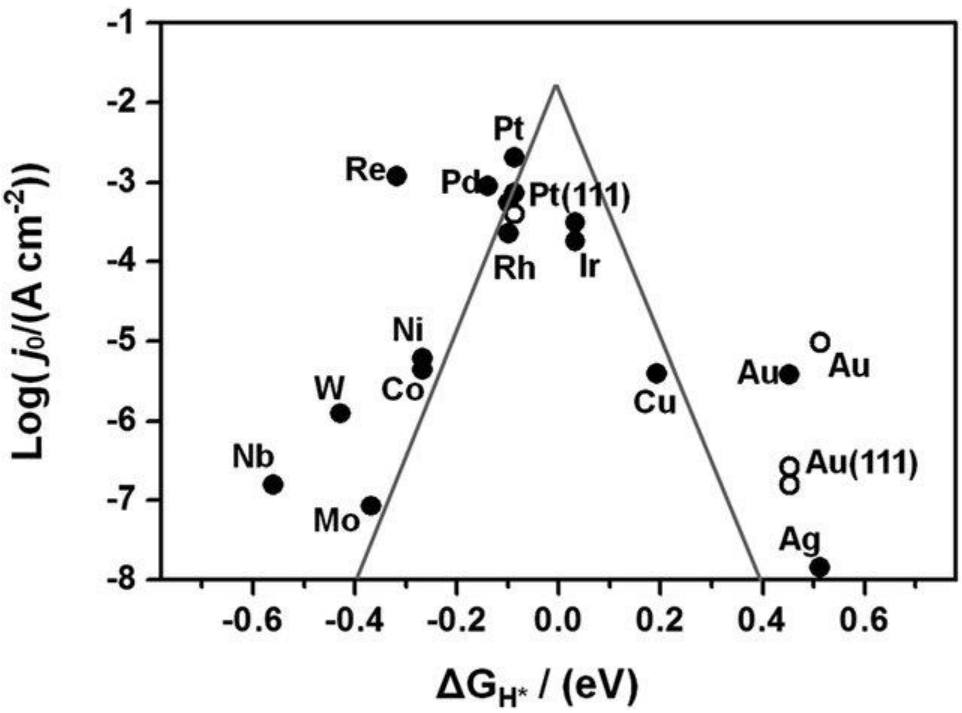

Figure A-6: Volcano plot of exchange current density (j_0) as a function of DFT-calculated Gibbs free energy (ΔG_{H^*}) of adsorbed atomic hydrogen on pure metals. Metal Pt, with slightly negative hydrogen adsorption energy, has the highest Hydrogen evolution activity. Reproduced from ref. [537] with permission from The Royal Society of Chemistry.

A.7 pH Dependence of CdS Band Edge Potentials for Hydroxyl Radical Formation

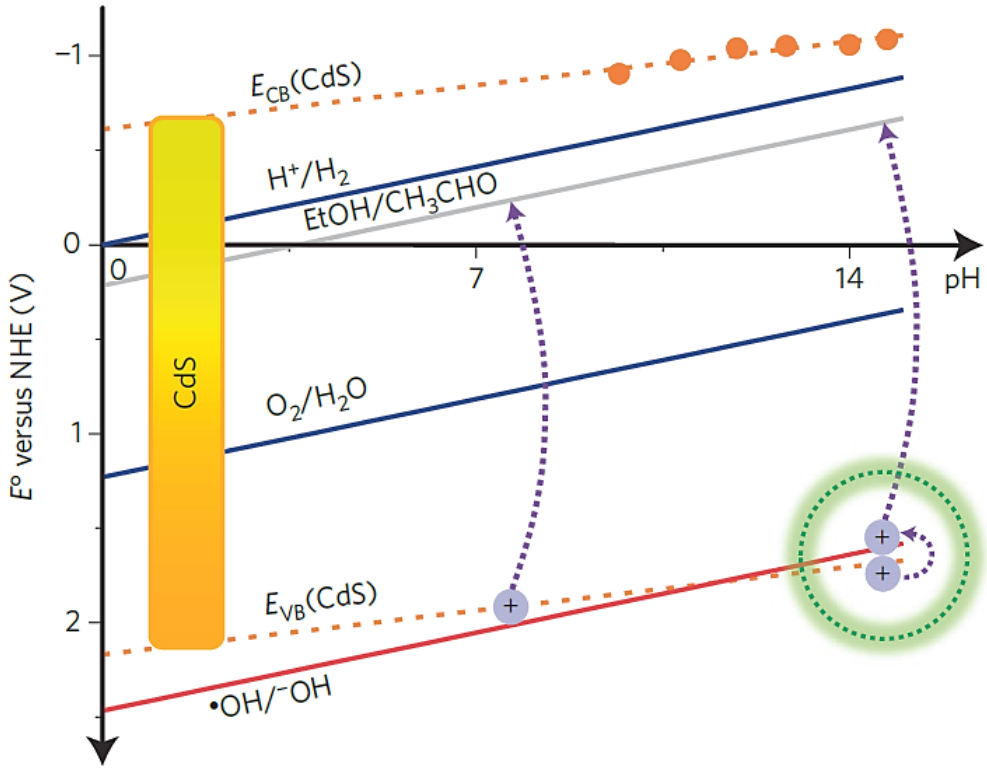

Figure A-7: Energy diagram for the two-step oxidation reaction. The electrochemical potentials of water reduction and oxidation, hydroxyl anion and ethanol oxidation follow Nernstian behavior (slope −59 mV/pH), but the dependence of CdS conduction band (E_{CB}) and valence band (E_{VB}) on pH is only −33 mV/pH. The green circle marks the region where E_{VB}(CdS) is more positive than E^o (•OH/⁻OH); the violet arrows denote the possibility of a two-step oxidation pathway at high pH versus a single-step process at lower pH. Reproduced with permission from ref. [358]. Copyright © 2014, Springer Nature.